

Fast SLM-based linear and nonlinear structured illumination microscopy



seit 1558

Kumulative Dissertation

zur Erlangung des akademischen Grades
doktor rerum naturalium (Dr. rer. nat.)

vorgelegt dem Rat der Chemisch-Geowissenschaftlichen Fakultät
der Friedrich-Schiller-Universität Jena

eingereicht von M. Sc. Hui-Wen Lu-Walther

geboren am 26.01.1981 in Taichung City, Taiwan

1. Gutachter: Prof. Dr. rer. nat. Rainer Heintzmann

2. Gutachter: Prof. Dr. rer. nat. Jürgen Popp

Tag der öffentlichen Verteidigung: 10.08.2016

Contents

Abstract	1
Zusammenfassung.....	3
Acknowledgements	5
1. Introduction	7
1.1. Superresolution in fluorescence microscopy	7
1.2. Fluorescence – Incoherent imaging	9
1.3. The diffraction limit in microscopy	10
2. Structured illumination microscopy (SIM)	11
2.1. Spatial light modulator	15
2.2. The evolution of the fast structured illumination microscope setup	18
2.2.1. Isotropic resolution improvement	23
2.2.2. The need for fast acquisition.....	26
2.3. Going beyond: Synchronized updates	30
2.4. Computation of grating patterns - Changes in the software	33
2.5. Vibrations and air fluctuations in the environment.....	36
3. Nonlinear structured illumination microscopy (NL-SIM) – Gaining further spatial resolution	38
3.1. Nonlinear photo-response from photoswitchable proteins	38
4. Conclusion.....	44
5. Outlook.....	45
5.1. Dual-colors 3D SIM imaging	45
5.2. Further resolution improvement in NL-SIM	46
Reference	49
Publication list	54
Publications	55
Appendix	131
Selbständigkeitserklärung	152
Erklärungen	152

List of Abbreviations

AOTF	Acousto-optical tunable filter
APSF	Amplitude point spread function
FWHM	Full width at half maximum
fastSIM	Fast structured illumination microscope
FFU	Filter fan unit
fps	Frame per second
LCoS	Liquid crystal on silicon
LSIM	Linear Structured Illumination Microscopy
NA	Numerical aperture
NL-SIM	Nonlinear structured Illumination Microscopy
OTF	Optical transfer function
PALM	Photo-Activated Localization Microscopy
PSF	Point spread function
PUA	Polyunsaturated aldehyde
QWP	Quarter wave plate
ROI	Region of interest
RSFPs	Reversibly photoswitchable fluorescent proteins
sCMOS	Scientific CMOS
SIM	Structured Illumination Microscopy
SLM	Spatial light modulator
SNR	Signal-to-noise
STED	Stimulated Emission Depletion
STORM	Stochastic Optical Reconstruction Microscopy

Abstract

Fluorescent microscopy becomes an essential tool for medical and biological investigations due to its major advantages of allowing for minimally invasive observation and rapid optical imaging. It is also a highly desirable tool to study the three dimensional interior of living specimens at a small scale. However, the resolution of optical systems is fundamentally limited by the diffraction of light, which consequently coins the development of super-resolution imaging methods.

Structured illumination microscopy (SIM) is one of the super-resolution techniques. SIM provides a two-fold lateral resolution improvement for those types of samples where the fluorescence emission intensity depends linearly on the intensity of the illumination pattern. The concept of SIM is based on the Moiré effect. A structured illumination pattern is projected into the sample and high spatial frequency components of the biological sample, which are normally above the cut-off frequency of the optical transfer function and therefore lost, are then down-modulated to low spatial frequencies that reside inside the passband of the optical transfer function of the microscope. Typically, a lateral resolution of 100 nm becomes achievable in SIM. SIM is a wide-field technique and thus allows fast acquisition of large fields of view.

This work discusses methods to improve the acquisition speed of SIM and to further enhance the resolution beyond the usual factor of two using nonlinear SIM (NL-SIM). Improvement of the acquisition speed is achieved by exploiting the advantages of a ferroelectric spatial light modulator (SLM) which offers fast switching of the illumination pattern, a modern sCMOS camera which provides fast readout and a novel synchronization approach between the different opto-electronical components.

Zusammenfassung

Fluoreszenzmikroskopie entwickelt sich zu einem essentiellen Instrument für medizinische und biologische Untersuchungen dank seiner wesentlichen Vorzüge hinsichtlich minimal-invasiver Beobachtungsmöglichkeiten und schneller optischer Bildgebung. Zudem ist sie ein vielversprechendes Werkzeug für das Studium der feinsten Details im dreidimensionalen Inneren von lebenden Proben. Jedoch ist die Auflösung optischer Systeme durch die Lichtbeugung fundamental begrenzt, was zur Entwicklung super-auflösender Bildgebungsverfahren führt.

Strukturiert-beleuchtende Mikroskopie, (Abk.: SIM, von engl. „structured illumination microscopy“), ist eine dieser super-auflösenden Techniken. Für Proben, bei denen die Fluoreszenzemissionsintensität linear von der Intensität des Beleuchtungsmusters abhängt, lässt sich durch den Einsatz von SIM die laterale Auflösung verdoppeln. Das Prinzip von SIM basiert dabei auf dem Moiré-Effekt. Ein strukturiertes Beleuchtungsmuster wird in die Probe projiziert, und hohe Ortsfrequenzkomponenten der biologischen Probe, welche normalerweise oberhalb der Frequenzgrenze der optischen Transferfunktion lägen und damit verloren gingen, werden so zu niederen Ortsfrequenzen heruntermoduliert, die noch im Durchlassbereich der optischen Transferfunktion des Mikroskops liegen. Typischerweise kann mit SIM eine laterale Auflösung von 100 nm erzielt werden. Als Weitfeld-Mikroskopieverfahren erlaubt SIM zugleich die schnelle Aufnahme eines großen Sichtbereiches.

In dieser Arbeit werden Methoden dargelegt, mit welchen die Aufnahmegeschwindigkeit von SIM verbessert sowie durch die Verwendung von nichtlinearer SIM (NL-SIM) die Auflösung noch über den üblichen Faktor zwei hinaus gesteigert werden kann. Die Erhöhung der Aufnahmegeschwindigkeit erfolgt dabei durch Ausnutzung der Vorteile eines

ferro-elektrischen, räumlichen Modulators für Licht (Abk.: SLM, von engl. „spatial light modulator“), welcher einen schnelle Wechsel des Beleuchtungsmusters erlaubt, einer modernen sCMOS-Kamera, welche schnelles Auslesen der Daten ermöglicht, sowie einem neuartigen Synchronisationsverfahren zwischen den beteiligten opto-elektronischen Komponenten.

Acknowledgements

I would like to thank Prof. Rainer Heintzmann for giving me the opportunity to do my PhD project in his research group in Leibniz Institute of Photonic Technology, Jena. I thank him for his support and advice whenever I needed it, and for providing abundant resources to proceed with this project.

My special thanks to Dr. Martin Kielhorn, who helped me tremendously in the optical lab, offered practical advice for my experimental work and productive discussions on structured illumination microscopy and helped me to solve many technical problems during the experiment.

To Dr. Wenya Hou, who helped me with the molecular biology work and supplied numerous samples of transfected cells. To Dr. Christian Hoischen and his colleagues, who helped with the DNA construction, DNA amplification, and assisted me with the cell cultures in the biology lab.

I thank all my colleagues for their professional technical support in the lab, fruitful discussions about science and microscopy and for the pleasant atmosphere in the office. Thanks to Dr. Kai Wicker for helping me in scientific understanding as well as support in the lab. Thanks to Ronny Förster who set up the first prototype of the fastSIM system and the development of the grating design algorithm, Aurélie Jost and Sapna Shukla who were always ready to help, proofread my thesis and offered productive discussions, Ivana Šumanovac Šestak who helped me with the sample preparation, Marie Walde who shared NL-SIM research experience and lab notes from her previous work with me and Walter Müller who offered helpful discussion on imaging processing. Thanks to Florian Blase for electronics assistance. Thanks to Dr. Elen Tolstik and Dr. Tatiana Tolstik for all the help and assistance in the biology lab.

Many thanks to Robert Kretschmer for comprehensive support with the development of a motorized z-stage, developing the Arduino code for controlling the z-stage, a GUI to manage it via serial interface and many general practical help in the optical lab and biology lab.

I thank my family for their unconditional support. Thanks to my mother Mei-Fen and my sister Hui-Ling for taking care of everything for me and my family in Taiwan. Thanks to my son Mika whose smile delights my daily life. Lastly, my deep gratitude goes to my husband, Benny, for irreplaceable understanding and support. He makes it possible for me to finish my studies.

1. Introduction

Wide-field fluorescence microscopy is an essential tool for biologists to study functions and dynamic processes in living organisms since it offers high contrast, background-free imaging and minimally invasive contact during observation. The resolution of an aberration-free light microscope is fundamentally limited by the wavelength of light and the numerical aperture (NA) of a microscope objective. Consequently, finer details are not resolvable as the corresponding high spatial frequencies are outside the region of support of the optical transfer function. A conventional wide-field light microscope generally has a lateral resolution of ~ 200 nm and an axial resolution of ~ 500 nm. In recent years, several techniques in fluorescence microscopy have been developed to overcome the diffraction barrier.

This thesis contains research results for improving the lateral resolution in structured illumination microscopy (SIM), increasing the acquisition speed of SIM using both hardware and software modifications, and gaining further resolution improvement by employing the nonlinear photo response of photoswitchable fluorescent proteins in nonlinear structured illumination microscopy (NL-SIM).

1.1. Superresolution in fluorescence microscopy

The general idea of confocal microscopy is to use a pinhole placed in the plane conjugated to the focal plane of an objective in the detection pathway to achieve optical sectioning in specimens, i.e. discard the blurry background that comes from out-of-focus planes. The lateral resolution improvement in a confocal microscope is minor due to the limited size of the pinhole. By using an extremely small pinhole, the lateral resolution can be improved; however the trade-off cost is a strongly reduced light from the in-focus plane. Also, confocal microscopy is a point-scanning technique and thus the acquisition is time-

consuming. To increase the acquisition speed, spinning disc systems were introduced to acquire multiple spot-scanning data in parallel [1-3].

Stimulated emission depletion (STED) microscopy is another point-scanning technique. STED microscopy typically uses two lasers for the excitation and depletion of fluorophores, respectively. One laser is focused into the sample and excites the fluorophores. The second laser beam used for depletion is formed in a doughnut shape with zero intensity in its center, coinciding with the center position of the excitation beam. The stimulated emission process consequently reduces the size of the equivalent fluorescence emission spot so that the resulting lateral resolution is of ~ 20 nm [4]. In addition, the axial resolution can be improved by a factor of 3.5 in STED by employing a confocal pinhole or a phase plate pair to form an axial doughnut [5]. In 4Pi-STED microscopy, a better axial resolution of down to 30-50 nm is achieved [6]. In recent years, photoswitchable fluorophores have been widely employed in STED microscopy to achieve the same depletion effect [7, 8].

Another approach to superresolution is pointillistic microscopy [9], such as Photo-activated localization microscopy (PALM) [10] and stochastic optical reconstruction microscopy (STORM) [11]. In localization microscopy, photoswitchable fluorophores are sparsely turned on, and fluorophores can be localized consecutively with a precise estimation in nanometer accuracy. Hence, a superresolved image can be constructed with those individually localized emitters with a lateral resolution down to ~ 20 nm.

SIM is one of the subwavelength imaging techniques which have been developed to acquire images at a resolution beyond the diffraction limit [13, 15]. SIM is a wide-field technique which offers a large field of view and fast acquisition. The principle is to project a spatially patterned illumination, usually a periodic grating pattern, on the sample such that Moiré fringes are created. The recorded Moiré fringes contain the frequency of the illumination structure and the spatial frequencies of the sample. High spatial frequency information of the sample which was outside the passband of the optical

transfer function is now down-modulated into the passband of the OTF. By acquiring several images, each for a different position of the illumination pattern, the sample information can be retrieved, and a superresolved SIM image can be created through computational reconstruction. In the linear SIM (LSIM) method, a two-fold resolution improvement is achieved.

In order to gain further resolution enhancement in a conventional SIM system, the use of photoswitchable fluorescent proteins that can produce a nonlinear fluorescent response is introduced. In general, photoswitchable fluorophores can be switched by light of a specific wavelength between a fluorescent “on state” and a nonfluorescent “off state” and this switching process is reversible. Nonlinearity can be introduced by saturating the transition state of photoswitchable fluorophores such that the effective fluorescence emission pattern contains higher-order harmonics outside the passband of the OTF of the illumination objective [12,13]. The sample information is attached to all these additional higher-order harmonics as well as to the zeroth order. Theoretically, the resolution improvement is unlimited in NL-SIM. However, only the higher-order harmonics whose intensity is above the noise level can be detected and used in the image reconstruction [16-19].

1.2. Fluorescence – Incoherent imaging

Due to the Stokes shift, light emitted from fluorophores is at different wavelengths. In contrast to coherent imaging, where the light is of a single wavelength only, fluorescence produces a broad wavelength spectrum and therefore incoherent light.

In coherent imaging cases, light emanating from different point sources can interfere. The intensity measured by a detector is proportional to the averaged absolute square of the electric field strength. The electric field at the image plane is described via a convolution of the amplitude at the sample plane with the amplitude point spread function (APSF). The measured intensity is then obtained by calculating the absolute squared magnitude of this amplitude

distribution. In incoherent imaging case, such as fluorescence, light emanating from different fluorophores does not interfere. Thus, the fluorescence emission intensity distribution in the image plane can be directly calculated as the sum of the individual point spread function (PSF) images of all points in the sample, which is a convolution of the fluorophore distribution with the PSF.

In the following sections, we only discuss the incoherent image case. Thus, the imaging process can be sufficiently described as a convolution with a PSF.

1.3. The diffraction limit in microscopy

Light emerging from an object can be described as a superposition of many spherical waves coming from lots of point emitters and propagating in all spatial directions. When imaging a point-like object with a microscope objective lens, the limited acceptance angle of the circular aperture of the objective lens cannot collect all of this light. Due to the loss of light, the image of the point-like object is not a perfect copy of the object. It becomes a blurry spot with a finite size, called the PSF. Two point-like objects next to each other will be imaged as the superposition of two corresponding point spread functions. When two point-like objects are too close to each other, they cannot be resolved as separate points. One possible way to define the resolution of an optical system is thus by determining the minimum resolvable distance between two point-like objects in the image.

Sparrow Limit	Rayleigh Limit	Abbe Limit
$d_{Sparrow} \approx 0.47 \cdot \frac{\lambda}{NA}$	$d_{Rayleigh} \approx 0.61 \cdot \frac{\lambda}{NA}$	$d_{Abbe} \approx 0.5 \cdot \frac{\lambda}{NA}$

Table 1 **Various resolution criteria and the corresponding definitions.** d is the minimum resolvable distance, λ is the wavelength of light in vacuum and NA is the numerical aperture of the objective lens that collects light [20].

The image of a point-like object produced by an optical system can be described as an Airy pattern [4]. There are different ways to define the lateral

resolution of an optical system that directly relate to properties of the PSF (see Table 1) [20]. The Sparrow limit is the distance between two point-like objects of equal intensity for which a central dip between their images is visible [21]. The Rayleigh limit is the distance between two point-like objects when the first minimum of the Airy pattern of one point-like object is at the first maximum of the other when using a low NA objective [22].

Another way to define the resolution more precisely is by means of the optical transfer function (OTF). The OTF is the Fourier transform of the PSF. The resolution of a light microscope is determined by the cut-off frequency of the OTF. Only those spatial frequencies coming from the object that are inside the support of the OTF, i.e. smaller than the cut-off-frequency, are detectable. The support of an OTF is closely related to the Abbe limit [23]:

$$d_{min} \approx \frac{\lambda}{2NA} = \frac{1}{f_{cut-off}}$$

Where $f_{cut-off}$ is the cut-off-frequency of the OTF, NA is the numerical aperture of the objective lens and λ is the wavelength of light in vacuum. The Abbe limit defines the resolution of a light microscope based on the diffraction from a periodical diffraction grating. The minimum resolvable distance between the lines of the grating is such that the first diffraction order can pass through the objective lens. Therefore, its propagation angle must be smaller than the acceptance angle of the objective lens, which is $\arcsin(NA/n)$, where n is the refractive index of the system.

2. Structured illumination microscopy (SIM)

Structured illumination microscopy offers resolution beyond the Abbe limit by employing a spatially patterned illumination on the sample. The combination of the structured illumination pattern and the sample structure creates Moiré fringes (see Fig. 1) which are recorded in the raw image. Thanks to the Moiré effect, high spatial frequencies which were outside the passband of the OTF are

now down-modulated to lower frequencies and can be transmitted by the objective.

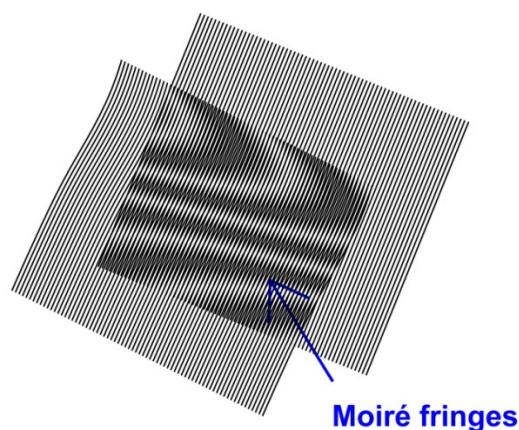


Fig. 1 Demonstration of the Moiré fringes. When two high-frequency pattern overlap with each other, Moiré fringes appear. The Moiré fringes are the product of the two original patterns and exhibit both fine and coarse patterns with corresponding high and low spatial frequencies, respectively.

To realize the idea of structured illumination in a conventional light microscope, it is straightforward to place a physical grating at the conjugate plane of a microscope objective in the illumination path such that an interference pattern is projected on the sample (see Fig. 2). The Fourier transform of the recorded image contains the zeroth and $\pm 1^{\text{st}}$ components. The $\pm 1^{\text{st}}$ components from the sinusoidal illumination pattern appear at a spatial frequency of $\pm \vec{k}_b$ (see Fig. 3b). The high spatial frequencies of the sample information that would normally lie outside the support of the OTF (\vec{k}_0) are now attached to the $\pm 1^{\text{st}}$ components and shifted into the passband of the OTF. Fig. 3c shows the multiplication of each component with the OTF. By separating each component in Fourier space and shifting the zeroth object frequency back to the zero coordinate of Fourier space (Fig. 3d, e), the maximum observable region is extended to approximately $(k_0 + |\vec{k}_b|)$, at which k_0 is the cut-off frequency in the wide-field case (see the enlargement of the OTF in Fig. 3f) [16, 24, 25].

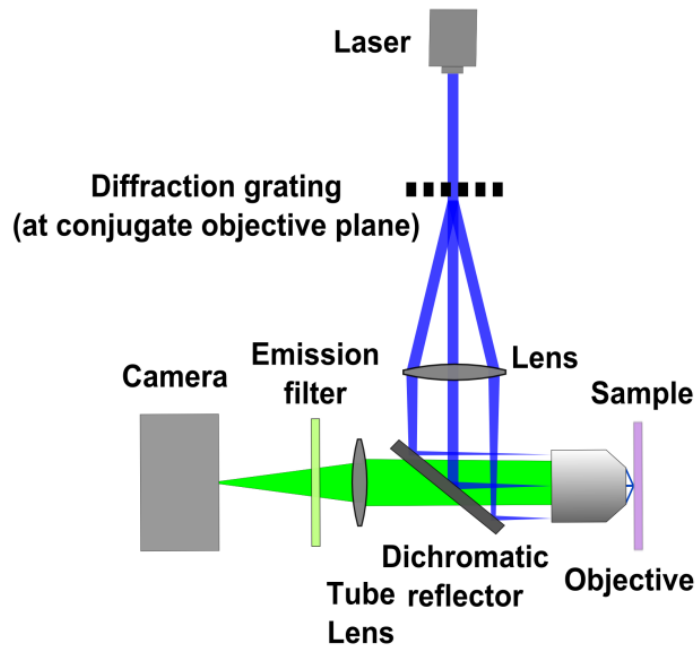


Fig. 2 A schematic diagram of the setup for structured illumination microscope.

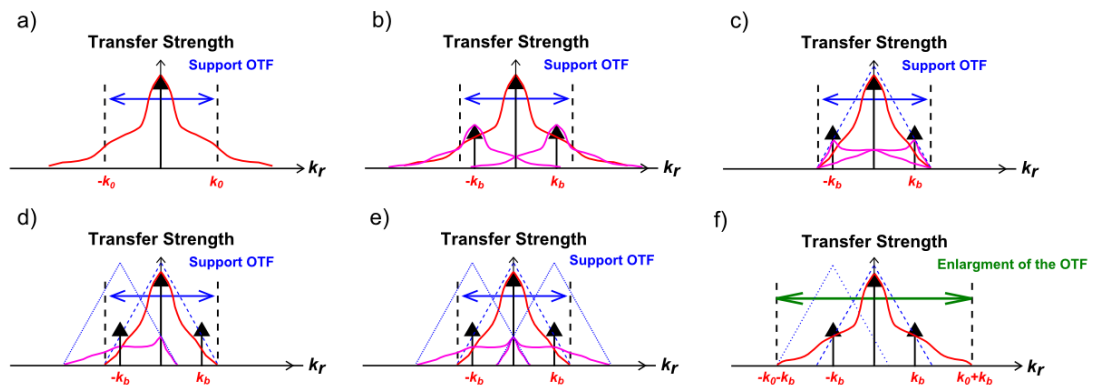


Fig. 3 **Fundamental concept of SIM theory.** a) The Fourier transform of the sample with uniform illumination (red curves). Only the spatial frequency below this cut-off frequency $\overline{k_0}$ is detectable. b) When the sample is illuminated with a periodic grating pattern, two side components (the $\pm 1^{\text{st}}$ components with spatial frequencies of $\pm \overline{k_b}$) are created in Fourier space. The sample information is attached to each component. c) Multiplication of each component with the OTF. The OTF marked as blue dotted line has a cut-off frequency $\overline{k_0}$. d) and e) Recombination of all components by separating the individual components, shifting both side components back to the zero coordinate in Fourier space and using a weighted averaging. f) The Fourier transform of the final reconstructed image shows an extended passband of the OTF to $k_0 + |\overline{k_b}|$ and consequently, resolution improvement is achieved.

An object imaged by a conventional fluorescence microscope is fundamentally a convolution of the PSF of the optical system with the fluorescence emission distribution of the sample:

$$I_{im}(\vec{r}) = PSF(\vec{r}) \otimes I_{em}(\vec{r}), \quad (1)$$

where the convolution operator is denoted by \otimes . $I_{im}(\vec{r})$ is the intensity distribution of the image, $I_{em}(\vec{r})$ is the fluorescence emission distribution of the sample. The fluorescence emission distribution of the sample is the multiplication of the intensity of the illumination $I_{illu}(\vec{r})$ with the local density of fluorophores $\rho(\vec{r})$:

$$I_{em}(\vec{r}) = \rho(\vec{r}) \cdot I_{illu}(\vec{r}). \quad (2)$$

Thus, the fluorescence emission distribution of the sample can be expressed as

$$I_{im}(\vec{r}) = PSF(\vec{r}) \otimes [\rho(\vec{r}) \cdot I_{illu}(\vec{r})]. \quad (3)$$

The OTF is the Fourier transform of the PSF, thus in Fourier space (3) becomes

$$\widetilde{I}_{im}(\vec{k}) = OTF(\vec{k}) \cdot [\widetilde{\rho}(\vec{k}) \otimes \widetilde{I}_{illu}(\vec{k})]. \quad (4)$$

In SIM, the illumination intensity is a two-dimensional harmonic pattern, and hence for two-beam SIM can be described as

$$I_{illu}(\vec{r}) = I_0 \cdot [1 + m \cos(\vec{k}_b \cdot \vec{r} + \phi_0)], \quad (5)$$

where I_0 is the intensity in the uniform illumination case, m is the modulation depth, \vec{k}_b is the spatial frequency of the harmonic pattern and ϕ_0 is the initial phase. The Fourier transform of Eq. (5) is

$$\widetilde{I}_{illu}(\vec{k}) = I_0 \cdot [\delta(\vec{k}) + \frac{m}{2} (e^{i\phi_0} \delta(\vec{k} - \vec{k}_b) + e^{-i\phi_0} \delta(\vec{k} + \vec{k}_b))], \quad (6)$$

where $\delta(\vec{k})$ is a Dirac's delta function. Combining Eq. (4) and Eq. (6) yields:

$$\widetilde{I}_m(\vec{k}) = OTF(\vec{k}) \cdot \tilde{\rho}(\vec{k}) \otimes I_0 \cdot \left\{ [\delta(\vec{k}) + \frac{m}{2} e^{i\phi_0} \delta(\vec{k} - \vec{k}_b) + \frac{m}{2} e^{-i\phi_0} \delta(\vec{k} + \vec{k}_b)] \right\} \quad (7)$$

In order to separate the different information components and to achieve isotropic resolution enhancement, several raw images with different illumination pattern phases and orientations are required. In a two-beam LSIM system, typically nine images with three phase steps for each three different illumination pattern orientations, separated by 60° , are acquired for reconstructing one 2D superresolved image with a two-fold resolution improvement. Ideally, based on the symmetry of the diffraction orders, the minimum number of required images can be reduced to five. In a three-beam LSIM system, the zeroth order illumination beam is not blocked and forms an interference pattern together with the $\pm 1^{\text{st}}$ diffraction orders in the sample plane. Fifteen images with five phase steps for each of the three different grating orientations are required for image reconstruction, since there are five components in Fourier space, including the DC term. The advantage of the three-beam SIM is optical sectioning and has enhanced resolution also in z, thus being the preferred method for 3D-SIM [24, 26].

2.1. Spatial light modulator

Many early SIM systems which use a mechanically moving, physical grating to generate the spatial patterned illumination cannot guarantee the precise shift of the illumination pattern during image acquisition [15]. The spatial light modulator based SIM system arose in the need of a fast illumination pattern switching and an accurate pattern shift for video rate observation in living cells [26, 27].

A ferroelectric-liquid-crystal-on-silicon (LCoS) display used as a spatial light modulator (SLM) has two stable crystal axes driven by an applied voltage. A two-dimensional harmonic pattern, hereafter referred to as grating pattern, is uploaded to the SLM and diffracts the illumination light. The specific grating

pattern design is presented in [HWLW1, HWLW2] and in chapter 2.4. Due to the pixelated structure of the display, additional unwanted diffraction orders are created and lead to a jagged edge in the illumination pattern in the sample plane [28]. In SIM, a Fourier filter is used to block those unwanted diffraction orders [16-18, 24, 26-28].

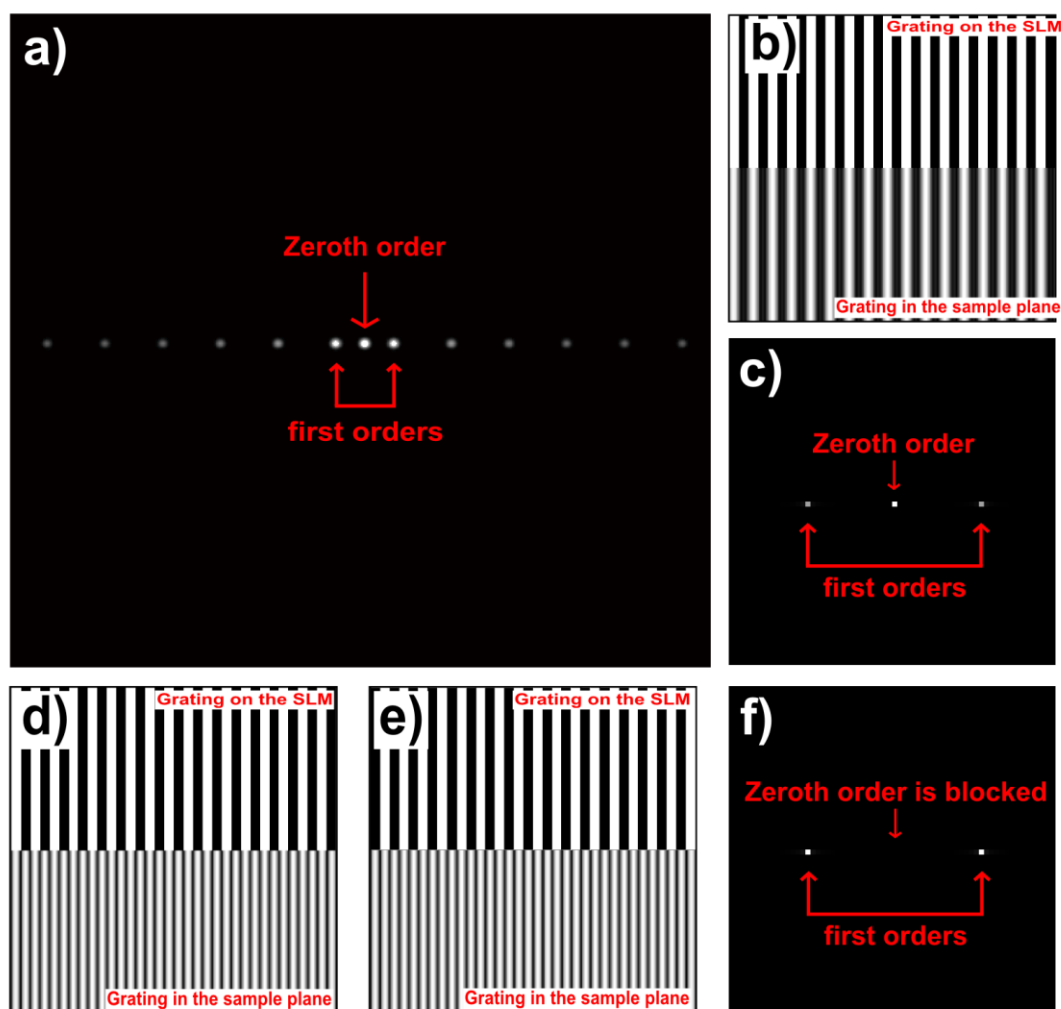


Fig. 4 **Simulation of two-beam interference and three-beam interference in the sample plane.** a) The Fourier transform of a periodic pattern displayed on the SLM. b) The displayed pattern on the SLM (top) and the corresponding three-beam interference in the sample plane (bottom) where only the zeroth and $\pm 1^{\text{st}}$ diffraction orders are transferred through a Fourier filter c). d) The displayed pattern on the SLM (top) and the corresponding two-beam interference in the sample plane (bottom) where only the $\pm 1^{\text{st}}$ diffraction orders are transferred through a Fourier filter f). e) The displayed pattern on the SLM (top) as in d) but with a phase shift of π and the corresponding two-beam interference in the sample plane (bottom).

To prevent damage of the LCoS, the SLM displays the inverse image of the previous grating pattern. In the two-beam SIM system, the zeroth illumination order is blocked (see Fig. 4f). Only the $\pm 1^{\text{st}}$ diffraction orders pass through the objective and form an interference pattern in the sample plane. This leads to the same interference pattern in the sample plane for both grating pattern and its inverse image displayed on the SLM (see Fig. 4d and e).

In NL-SIM, the criteria to achieve perfect ON/OFF photoswitching of the fluorophores are demanding. Fig. 5 shows the three-beam interference and two-beam interference. In three-beam interference, there is an extra small peak between two high peaks. This will introduce unwanted photoswitching of fluorophores. Hence, a two-beam SIM system is preferable for NL-SIM as it offers better contrast modulation. NL-SIM will be discussed in chapter 3.

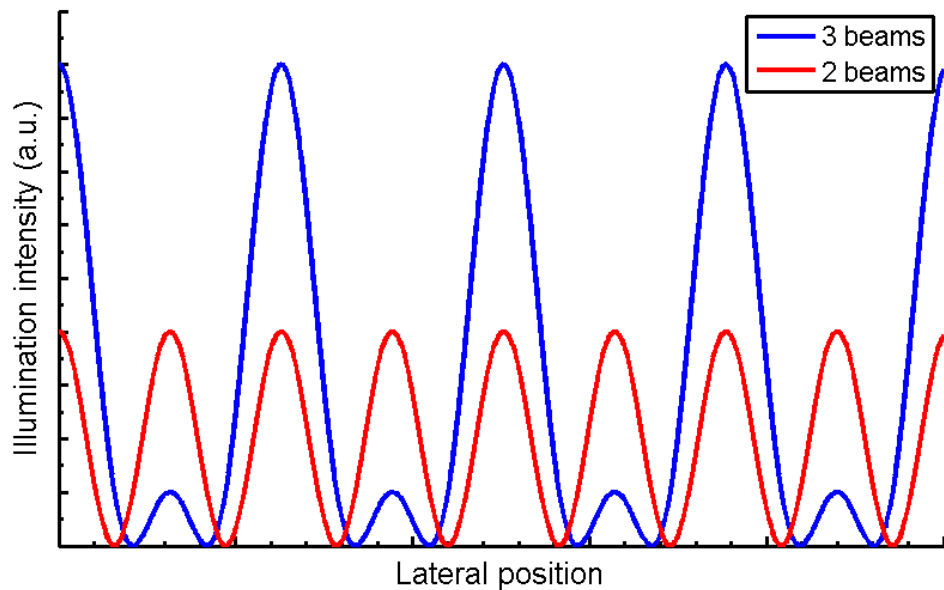


Fig. 5 Illustration of intensity distribution of the illumination pattern resulting from three-beam interference (blue) and two-beam interference (red).

2.2. The evolution of the fast structured illumination microscope setup

Ferroelectric SLMs offer fast switching up to several kHz. However, low diffraction efficiency is a major drawback. Nevertheless, as the required illumination intensity for acquiring raw SIM images is relatively low it is preferable to use a ferroelectric SLM to modulate the illumination light. The equipment which limits the acquisition speed in a conventional SIM system is the camera. Unlike any camera with a CMOS or CCD-based sensor, a scientific CMOS (sCMOS) camera is superior with its extremely high frame rate, low noise, large field of view and wide dynamic range. By employing an sCMOS camera and a ferroelectric SLM in a SIM system, the acquisition speed can be improved significantly with respect to other conventional SIM systems [HWLW1, HWLW2]. The lately reported fastest SIM acquisition rate is demonstrated with a raw frame rate of 714 frames per second (fps) and a superresolved frame rate of 79 fps [HWLW3].

The design of the fast structured illumination microscope (fastSIM) is inspired by Fiolka et al [29]. The fastSIM setup was upgraded several times in order to achieve faster acquisition rates and to gain further resolution improvement. The main changes that have been done in the fastSIM setup concerned the camera and the acquisition configuration. Using a different laser wavelength which is at the excitation maximum of the used fluorophores also reduces the exposure time.

The simplified sketch of the first prototype of the fastSIM setup is shown in Fig. 6. A laser with a wavelength of 442 nm (CW laser, LRS405NL-200, LASEVER, China) was used for excitation. An acousto-optical tunable filter (AOTF) right behind the 442 nm CW laser ensures precise and fast switching of the illumination light. An illumination grating pattern is generated by an SLM placed in the intermediate image plane and is projected on the sample. The

general idea of the design of the grating patterns is presented in [HWLW1, HWLW2] and will be further discussed in 2.4. In order to achieve high contrast of the illumination grating in the sample plane, a quarter wave plate (QWP) and a customized azimuthally patterned polarizer (pizza polarizer) are placed after the SLM to achieve azimuthal polarization. A passive mask as a Fourier filter is used to block all unwanted diffraction orders except the $\pm 1^{\text{st}}$ diffraction orders. Fluorescence is collected by a sCMOS camera (Orca Flash 2.8, Hamamatsu, Japan). The electronic circuit sketch can be found in [HWLW1].

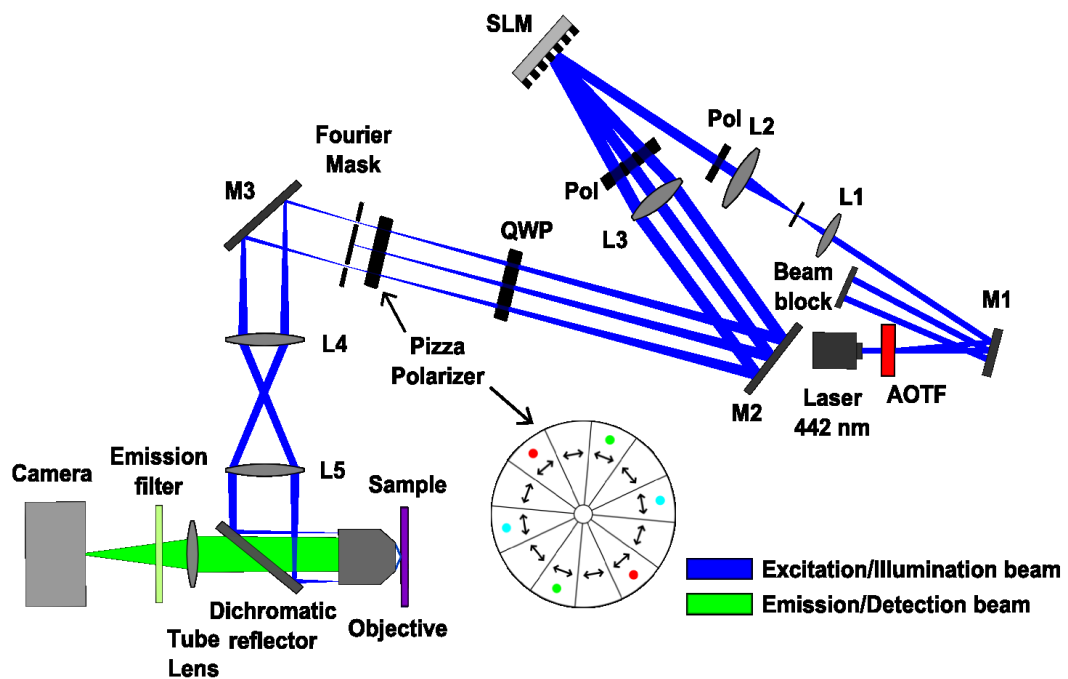


Fig. 6 **A schematic diagram of the fastSIM prototype.** A laser wavelength of 442 nm is used for excitation. The AOTF switches the laser beam on and off. The polarizer before the SLM controls the polarization of the incident beam onto the SLM. The second polarizer after the SLM ensures the linear polarization of the diffracted beam. The SLM displays grating patterns. The quarter wave plate (QWP) converts the linearly polarized beams to circular polarized. The pizza polarizer converts the beams of circular polarization to azimuthal polarization. The Fourier mask is used to block all the unwanted diffraction orders except the $\pm 1^{\text{st}}$ diffraction orders. Two $\pm 1^{\text{st}}$ diffraction orders are focused at the back focal plane of an objective and form plane waves which interfere and lead to the illumination grating pattern on the sample. The sCMOS camera collects fluorescence filtered by an emission filter.

The trigger timing of synchronization between each electronic component is shown in Fig. 7. A microcontroller (Arduino Uno, Arduino, Italy) is responsible for synchronizing the AOTF, the SLM and the camera. All triggers are on the low-to-high edge. The camera is the master and is operated in Global Exposure Level Trigger Mode.

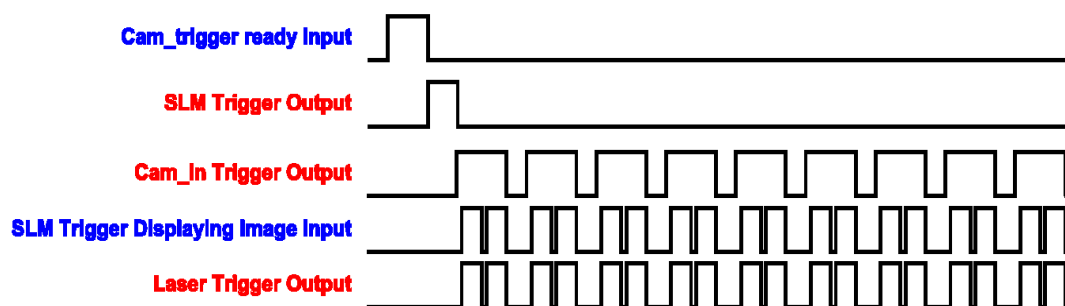


Fig. 7 A schematic diagram of the synchronization in the fastSIM prototype. The sCMOS camera is operated in a Global Exposure Level Trigger Mode. The diagram shows the trigger timing of an Arduino synchronizing the AOTF (Laser ON/OFF), the SLM and the sCMOS camera. The TTL signals being sent to the Arduino are marked in blue and the signals from the Arduino are marked in red.

The strength of the fastSIM setup is its simplicity. Passive components, like the pizza polarizer and the Fourier filter, greatly reduce the time and work for synchronization. However, the design of this prototype is not optimal. Fig. 8 shows that the grating contrast depends on the orientation of the illumination grating. This is due to the flawed polarization control of the illumination light. Therefore, the resolution improvement is not isotropic in all lateral directions [28]. First of all, mirrors create unexpected changes in the polarization of the illumination light. Some mirrors placed in the optical path are not designed for maintaining the polarization and thus change the polarization of the illumination light. Secondly, as described in [HWLW2], a conventional dichromatic reflector contributes different phase changes at arbitrary polarization (except in s- and p-polarization). Therefore, the polarization of a linearly polarized beam along s- and p-polarization remains linear and others at arbitrary orientations are converted to elliptical, which diminishes the

illumination grating contrast. Consequently, the contrast of the illumination is degraded along other orientations. Moreover, the residual addressing structure on the SLM display was not found and taken into account in the first version of the grating generation algorithm, which leads to the breakdown of diffraction order selection in the Fourier plane of the SLM when we later tried to use more grating orientations for the NL-SIM experiment (see chapter 3).

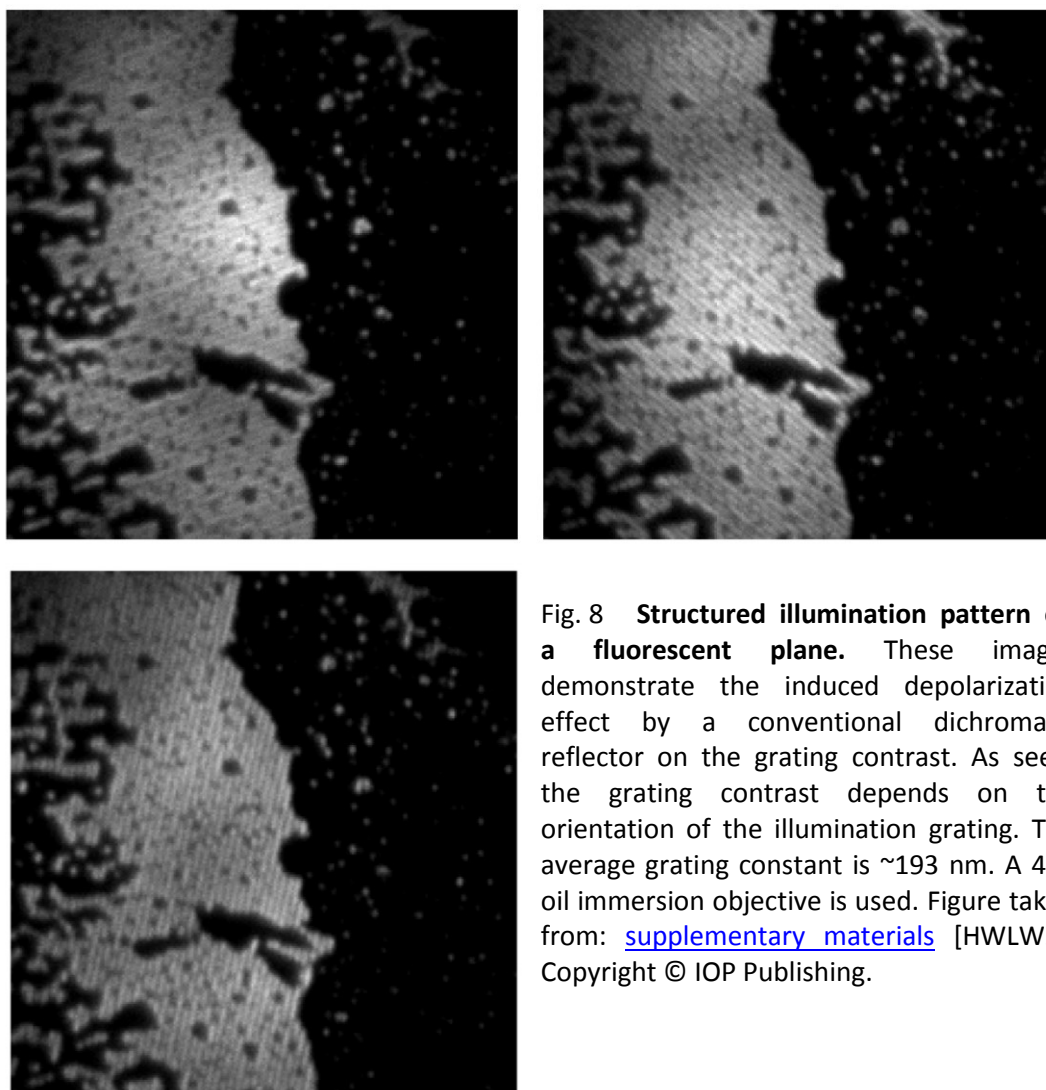


Fig. 8 Structured illumination pattern on a fluorescent plane. These images demonstrate the induced depolarization effect by a conventional dichromatic reflector on the grating contrast. As seen, the grating contrast depends on the orientation of the illumination grating. The average grating constant is ~ 193 nm. A 40 \times oil immersion objective is used. Figure taken from: [supplementary materials](#) [HWLW2]. Copyright © IOP Publishing.

To demonstrate the performance of the fastSIM setup, fluorescent microspheres (PCFP-0252, Kisker Biotech GmbH & Co. KG, Germany) with an approximate diameter of 100 nm were imaged. The wide-field and SIM results

are shown in Fig. 9 a) and b). The average full width at half maximum (FWHM) in the wide-field and the SIM images are 224.8 ± 21.2 nm and 114.2 ± 9.5 nm, respectively. Nine raw images were acquired in 131.4 ms for reconstructing one 2D SIM image with a region of interest (ROI) of $27.92 \times 13.70 \mu\text{m}^2$ and thereby we first achieved a superresolved frame rate of 7.6 fps with the fastSIM system.

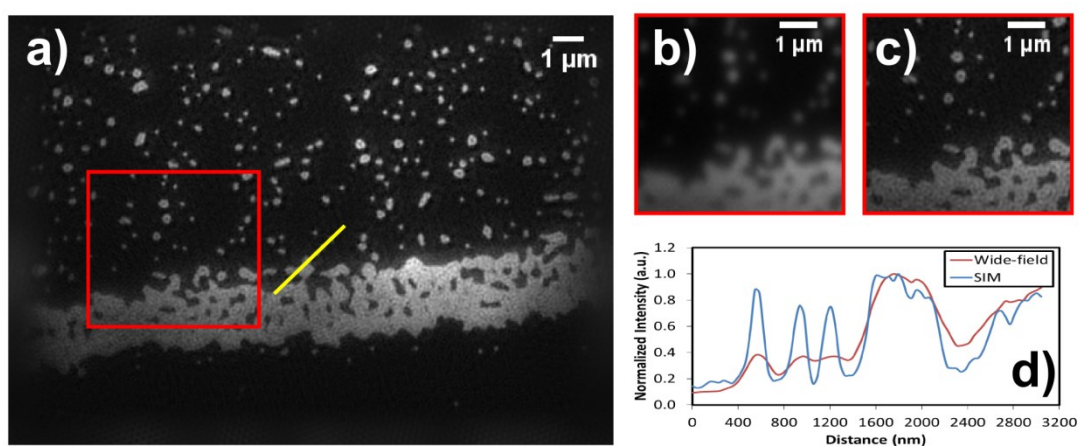


Fig. 9 **Superresolved image of fluorescent microspheres.** a) SIM image of fluorescent microspheres with average diameter of ~ 100 nm. Magnifications of the red-boxed region represent wide-field b) and SIM c) results. d) Normalized intensity profiles along the yellow line in a). Note: The resolution improvement is not isotropic [28]. Figure taken from: [HWLW1]. Copyright © OSA Publishing.

In the fastSIM prototype, the wavelength of the illumination light is not at the excitation maximum of the used fluorophores which results in longer exposure times. Moreover, the acquisition rate is also limited by the Orca Flash 2.8 sCMOS camera hardware which offers only one trigger output and thus limits the fast synchronization between each electronic component. Furthermore, the illumination grating constant chosen in the experiment was 193 nm which is far larger than the diffraction limit ($\lambda_{ex}/(2 \times NA) = 442/(2 \times 1.4) = 158$ nm). By using a smaller illumination grating constant the resolution improvement will be more promising.

2.2.1. Isotropic resolution improvement

In order to achieve nearly isotropic resolution improvement, the illumination grating pattern in the sample plane has to be orientated in different directions. In LSIM, three different grating directions are sufficient. Besides, the contrast of the illumination grating in the sample plane affects signal strength. Thus, illumination light with azimuthal polarization at the sample plane is required. In the upgraded version of the fastSIM setup, several mirrors were removed from the optical path to avoid phase changes on the polarization. One polarization-maintaining mirror placed before the SLM and the SLM itself are used as reflectors. The SLM displays grating patterns and diffracts the incoming illumination light.

The SLM (FLCoS, SXGA-3DM, 1280 × 1024 pixels, Forth Dimension Displays, UK) used in the fastSIM setup is originally designed for a wavelength of 532 nm. Two stable birefringent axes, hereafter referred to as *on* and *off*, separated by an angle of $\Delta\theta$ are given by the direction of the liquid crystal inside the ferroelectric LCoS, which is driven by an applied voltage. Thus, the SLM acts as a locally rotatable waveplate.

In [30], Martínez-García *et al.* presented the derivations of the polarization of light diffracted by a binary polarization gratings displaying on a ferroelectric SLM. The SLM acts as a typical half-wave plate to all odd diffraction orders which is independent on the wavelength of the illumination light if the polarization of the incident beam on the SLM is linearly polarized with arbitrary orientation. This is ideal in our case as we only use the $\pm 1^{\text{st}}$ diffraction orders to form the illumination grating on the sample. However, due to phase mismatch the zeroth diffraction order will be elliptically polarized if an illumination wavelength not designed for the SLM is used, which results in reduced diffraction efficiency.

The illustration of the polarization of the diffraction orders (only zeroth and the $\pm 1^{\text{st}}$ diffraction orders) along the optical path is shown in Fig. 10. By employing two identical dichromatic reflectors, the phase change on the

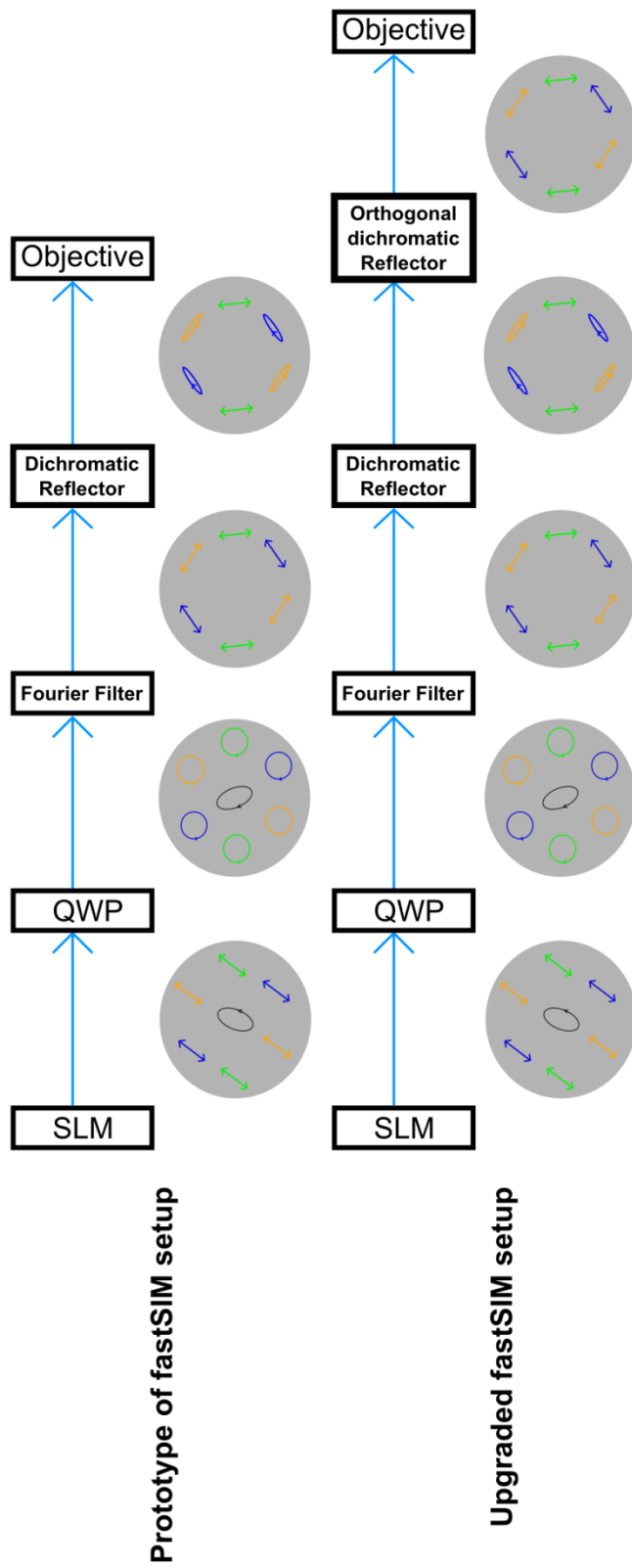


Fig. 10 **Illustration of the polarization of the diffraction orders along the optical path.** The incident illumination beam onto the SLM has linear polarization in between the fast and slow axis of the SLM. The polarization of the zeroth beam (marked in black) is elliptical due to the mismatch of the illumination wavelength to the SLM. The polarization of the $\pm 1^{\text{st}}$ diffraction beams diffracted by the SLM is linear. Three pairs of the $\pm 1^{\text{st}}$ diffraction beams from different grating orientations are marked in green, blue and yellow, respectively. The zeroth beam is blocked by the Fourier filter. The QWP and the azimuthal polarizer convert the $\pm 1^{\text{st}}$ diffraction beams to azimuthal polarization. In the upgraded fastSIM setup, two identical but orthogonally orientated dichromatic reflectors are used to compensate the phase change and preserve the azimuthal polarization of $\pm 1^{\text{st}}$ diffraction beams.

polarization induced by the first dichromatic reflector can be compensated by the second dichromatic reflector which imparts opposite phase shift to the beam.

Fig. 11 shows that the contrast of the illumination grating is now more homogeneous in all grating orientations. Grating patterns with six orientations were displayed on the SLM. The angle between each orientation is ~ 30 degrees and the average grating constant is ~ 267.3 nm in the sample plane. A $63\times$ objective with an NA of 1.46 was used.

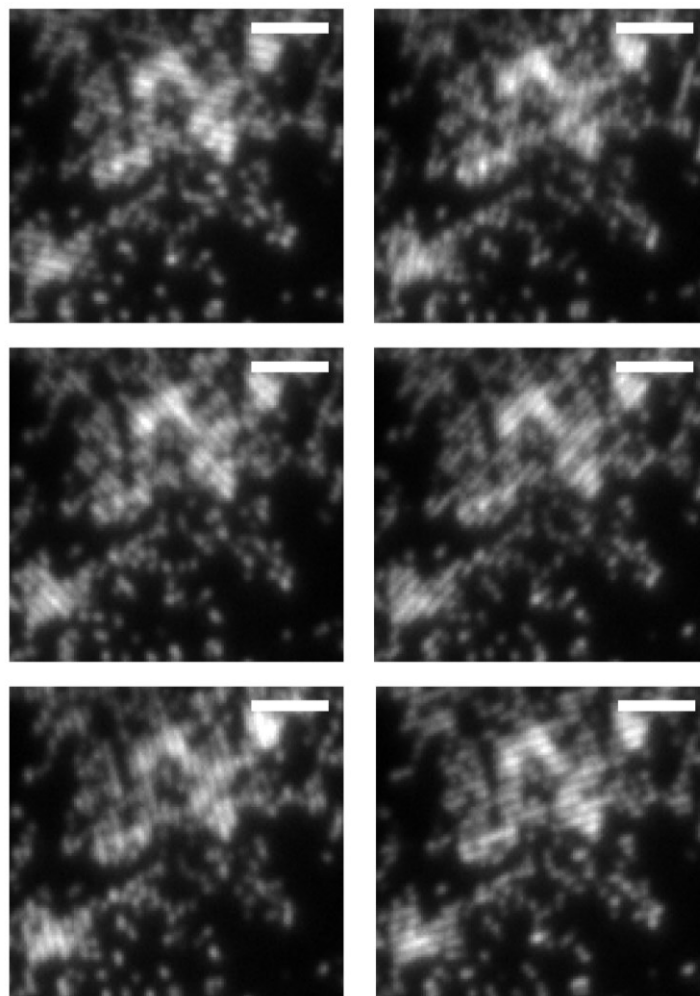


Fig. 11 **Structured illumination pattern on the fluorescent plane.** These images demonstrate the homogeneous grating contrast in all orientations of the illumination grating. The induced depolarization effect is compensated by the second dichromatic reflector, which is identical to the first dichromatic reflector. The average grating constant is ~ 267.3 nm. A $63\times$ oil immersion objective was used. The global scale bar is $2\ \mu\text{m}$.

2.2.2. The need for fast acquisition

In order to improve the acquisition speed and thereby follow fast dynamics of moving objects, we upgraded the camera to a modern sCMOS camera (Orca Flash 4.0, Hamamatsu, Japan) which offers fast readout and three trigger outputs for better synchronization controlling. We also changed the illumination light to a 488 nm laser (CW laser, LuxX 488-200 Omicron, Germany) which is close to the excitation maximum of the most often used fluorophores and thus shortened the exposure time. The upgraded version of the fastSIM setup sketch is shown in Fig. 12. The electronic circuit sketch can be found in Appendix A.1.

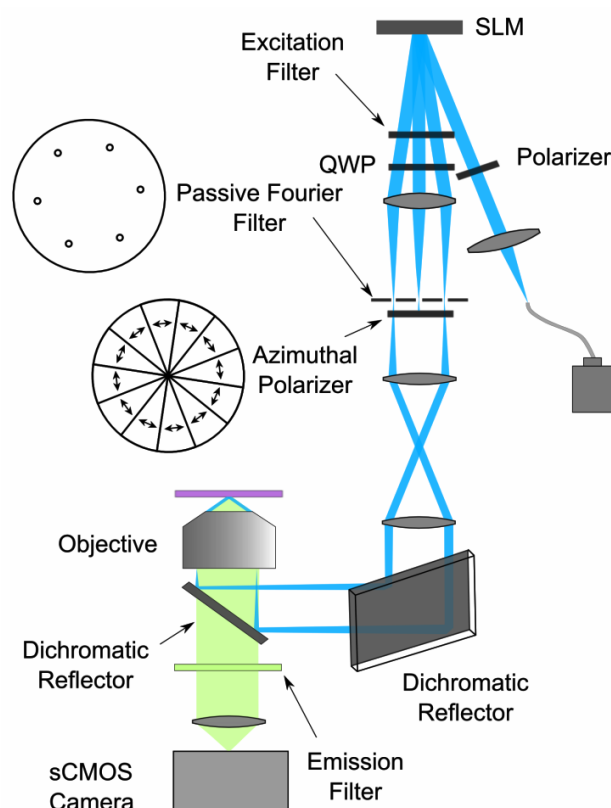


Fig. 12 **A schematic diagram of the upgraded fastSIM system.** A 488 nm laser is used for excitation. The $\pm 1^{\text{st}}$ diffraction orders are reflected by two identical dichromatic reflectors which ensure an azimuthally arranged linear polarization of all illumination beams. The illumination beams are refocused at the very edge of the back focal plane of the objective (63 \times , NA 1.46) and form an illumination grating pattern on the sample. The sCMOS camera collects fluorescence filtered by an emission filter. Figure adapted from: [HWLW2]

The signal readout from the Orca Flash 4.0 sCMOS camera is more than three times faster compared with the Orca Flash 2.8 sCMOS version. The camera is operated in “Free Running Mode” in which the illumination time and readout timing can be set by software command (see Fig. 13). During acquisition the illumination light is on when all pixels in a chosen ROI are ready for global exposure. Moreover, in order to avoid double exposure on the same pixels, the next exposure does not start before the last raw image has been read out. The acquisition rate can be up to 162.07 fps with a ROI of $16.5 \times 16.5 \mu\text{m}^2$. The length of the internal exposure time in the software setting is equal to the sum of the readout time, the illumination time, and the image loading time onto the SLM. We used a logic analyzer to measure the exact length of the internal exposure time for arbitrary ROIs (see Table 2).

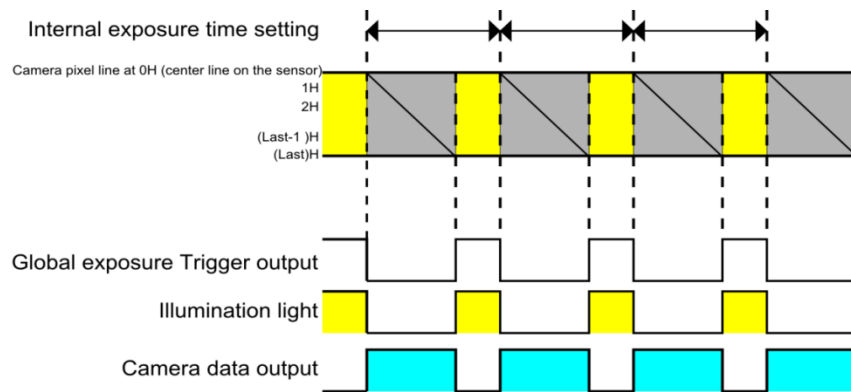


Fig. 13 Illustration of the free running mode readout method of the Orca Flash 4.0 sCMOS camera. The illumination light is on when all pixels in a chosen ROI are ready for global exposure (region marked in yellow). All triggers are on the low-to-high edge.

Illumination Time		4 ms		
Region of Interest (ROI)		Internal Exposure Time Setting (ms)	Raw Data Frame Rate (fps)	SIM Frame Rate (fps)
(pixels)	(μm)			
1536×1536	49.5 × 49.5	8.67	115.34	12.82
1024×1024	33.0 × 33.0	7.38	135.50	15.06
512×512	16.5 × 16.5	6.17	162.07	18.01
256×256	8.3 × 8.3	5.52	181.16	20.13

Table 2 Acquisition raw frame rate and superresolved SIM frame rate according to different ROIs in a reconstructed SIM image in the upgraded fastSIM system. Table taken from: [HWLW2]. Copyright © IOP Publishing.

The 488 nm laser can be switched with 10 ns rise time. The laser is guided via a single-mode polarization-maintaining fiber which yields a clean Gaussian beam profile at the fiber exit. Therefore, the AOTF and the telescope right behind the AOTF could be removed from the system, making it even more compact.

We observed the Brownian motion of beads in a 3D volume sample of the fluorescent microspheres over 60 time points with an excitation wavelength of 488 nm. The average grating constant is ~ 181 nm in the sample plane. Videos for wide-field and SIM can be found in the [supplementary materials](#) in [HWLW2], respectively. One single SIM frame of a time series is shown in Fig. 14 [HWLW2]. The superresolved frame rate is 18.01 fps. The speed of the fastSIM system is at least improved by a factor of 2.4 compared to the former fastSIM system. Fig. 14 d) and e) show the mean FWHM of 50 fluorescent microspheres in both wide-field and SIM images which are 222.3 ± 38.5 nm and 93.6 ± 15.1 nm, respectively.

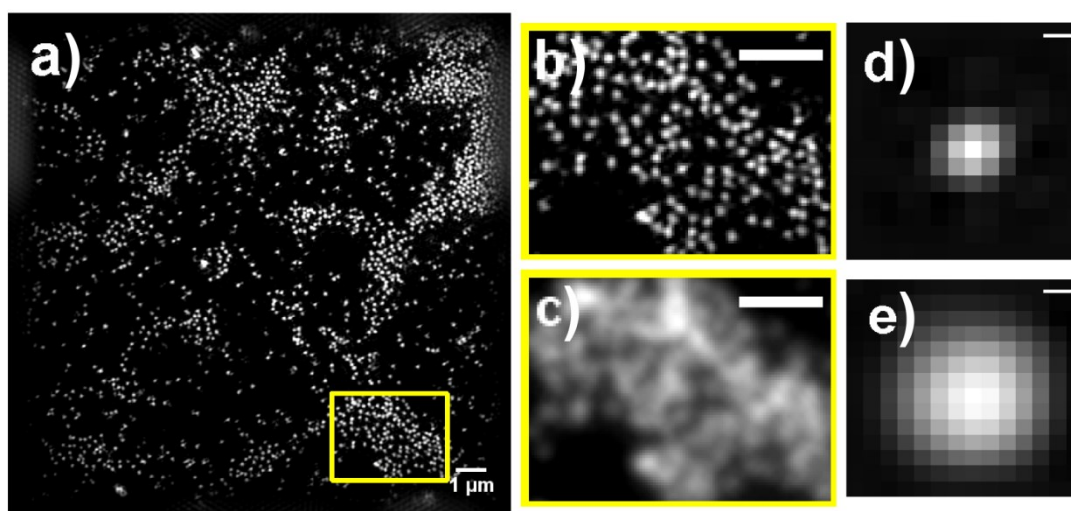


Fig. 14 **Single superresolved frame of fluorescent microspheres in a 3D volume specimen.** The average diameter of fluorescent microspheres is ~ 100 nm. a) SIM image of fluorescent microspheres in a large field of view. b) Magnifications of the yellow-boxed region in a) represent SIM b) and wide-field c) results. 50 selected microspheres were used to calculate the mean FWHM in both SIM and wide-field image (shown in d) and e)). Scale bar in b) and c) is $1 \mu\text{m}$. Scale bar in d) and e) is 100 nm. Figure taken from: [HWLW2]. Copyright © IOP Publishing.

Fig. 15 shows actin filaments of bovine pulmonary artery endothelial (BPAE) cells (FluoCells® Prepared Slide #1, Invitrogen) labelled with Alexa Fluor® 488 phalloidin imaged with SIM. The excitation wavelength is 488 nm and the maximum emission wavelength is 510 nm [HWLW2].

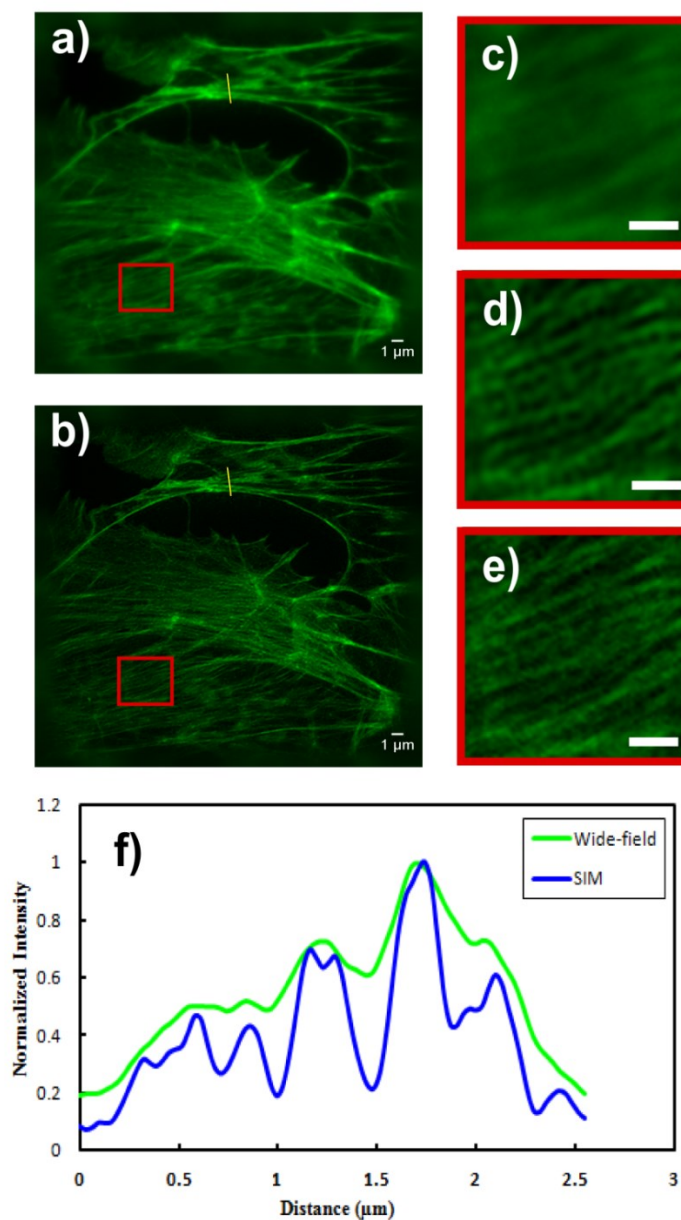


Fig. 15 **BPAE cell labelled with Alexa 488 phalloidin.** a) The wide-field image. b) SIM image. Magnifications of the red-boxed region represent wide-field c), conventional deconvolution d) and SIM e) results. f) Normalized intensity profiles along the yellow line in both a) and b). Global scale bar is 1 μm. Figure taken from: [HWLW2]. Copyright © IOP Publishing.

2.3. Going beyond: Synchronized updates

In the Orca Flash 4.0 sCMOS camera, the highest raw frame rate of 802.0 fps with a ROI of 256×256 pixels can be achieved if the exposure time is equal to the readout time, i.e. with continuous acquisition. In continuous acquisition mode, the sCMOS camera's rolling shutters move upward and downward from the middle of the camera chip continuously. However, the former synchronization configuration in the fastSIM system limits the speed, since the data readout process starts after the global exposure of all pixels in a selected ROI in order to prevent double exposure by the current and next illumination patterns. This results in a discontinuous acquisition configuration as the next exposure starts when the camera finishes the previous data readout. To overcome this limit, we acquired data with continuous running exposure and readout lines of the camera by employing segmented frames displayed on the SLM instead of full frame grating patterns (see Fig. 16).

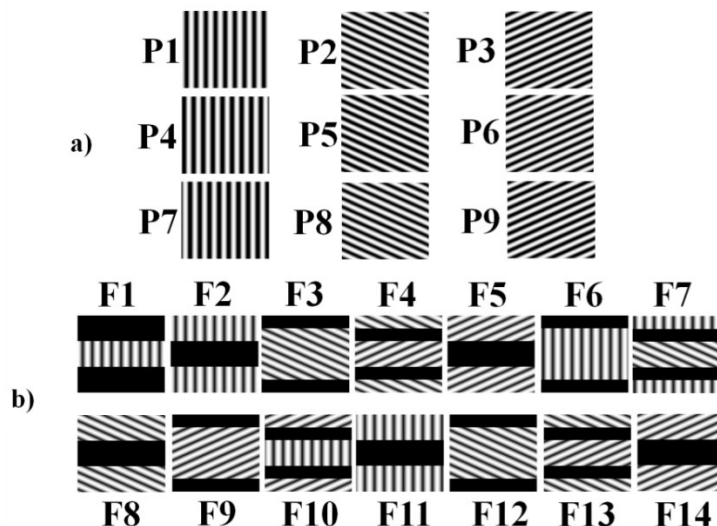


Fig. 16 **Grating patterns displayed on the SLM.** a) 9 single full frames grating patterns used in the previous experimental configuration in [HWLW2]. b) 14 segmented frames with fractions of the 9 full frames grating patterns in a) are displayed sequentially on the SLM. Figure taken from: [HWLW3]. Copyright © IOP Publishing.

We divided the patterns displayed on the SLM into several segments along the direction of the sCMOS camera's rolling shutters. Thus, instead of displaying full frame grating patterns on the SLM, 14 segmented frames showing fractions of the 9 full frame grating patterns are displayed. Each segmented frame contains dark regions for the purpose described below.

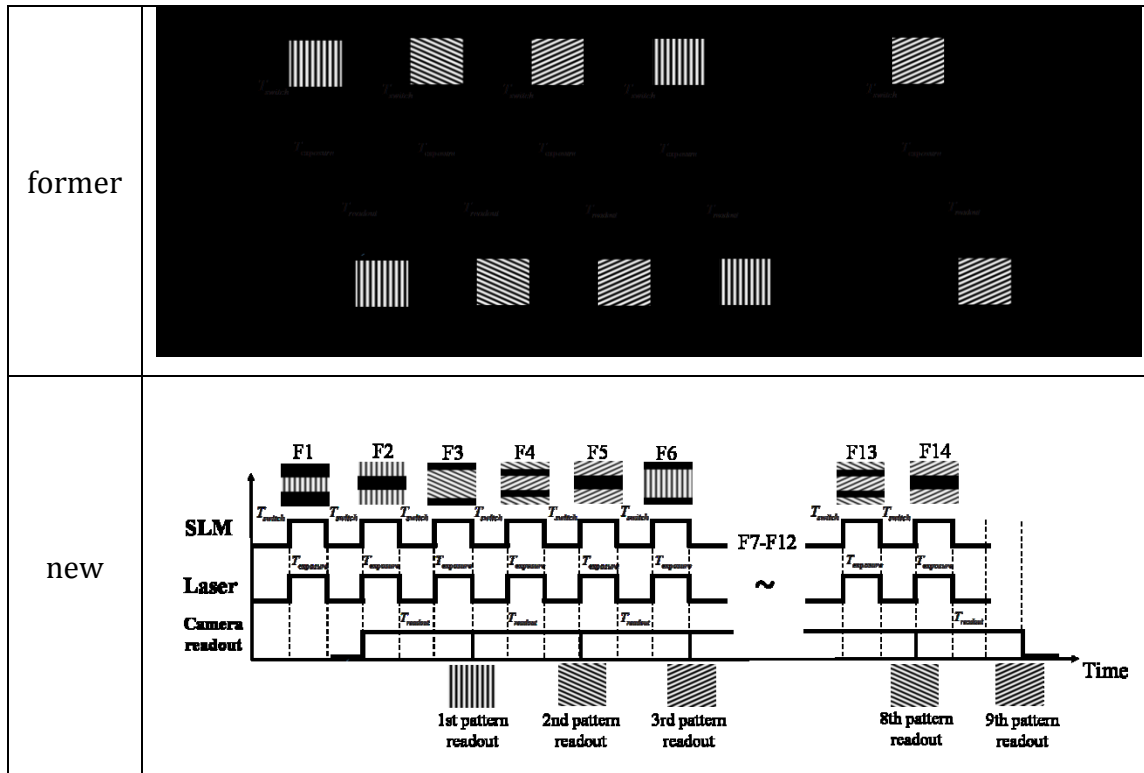


Fig. 17 **Synchronization configuration sketch** in the former fastSIM system [HWLW2] and in [HWLW3]. Figure taken from: [HWLW3]. Copyright © IOP Publishing.

The laser is off while the frame is uploading to the SLM. This switching time between two frames is ~ 0.434 ms. In the continuous acquisition, the camera readout lines which reset the pixel to zero immediately are always in the dark region of the adjacent displayed frame on the SLM. The camera exposure lines move continuously behind the readout lines. In order to ensure continuous readout, the exposure time of each frame is chosen roughly the same as the frame switching time on the SLM which is 0.5 ms in this acquisition configuration. An animation visualizes the acquisition process including the

displayed SLM frames and the positions of the start-exposure and readout lines can be fine in the [supplementary materials](#) in [HWLW3]. This new approach can achieve a very high raw frame rate of 714 fps and a very high superresolved frame rate of 79 fps with a ROI of $16.5 \times 16.5 \mu\text{m}^2$. The comparison between the former acquisition method in [HWLW2] and the new acquisition method in [HWLW3] is shown in Fig. 17.

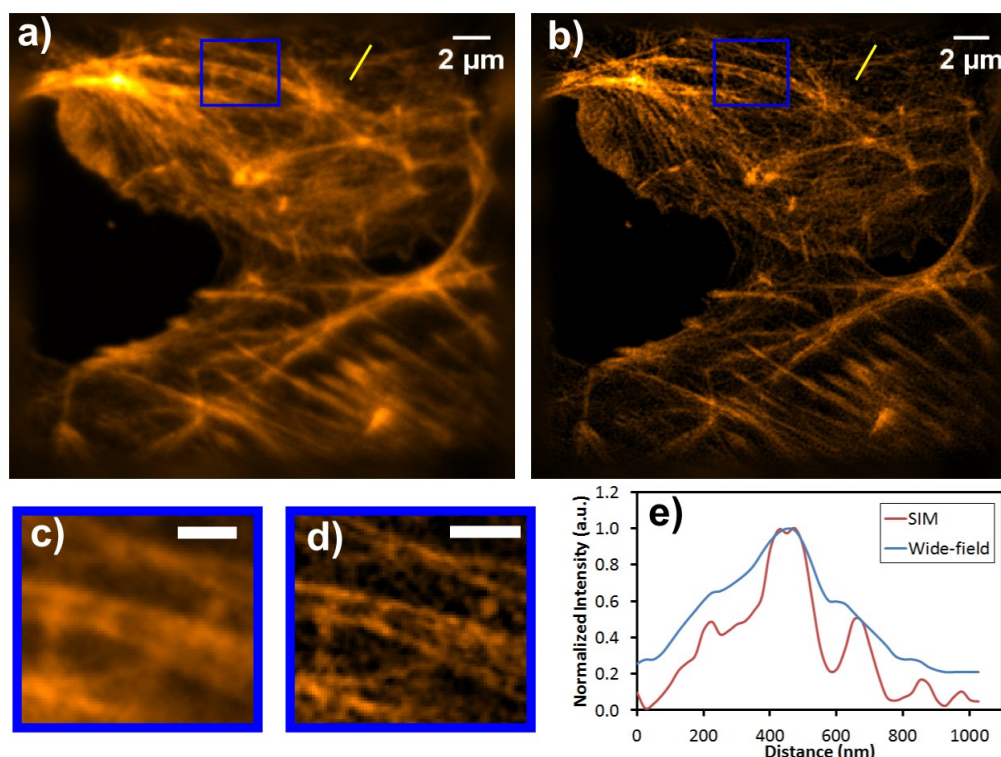


Fig. 18 **Superresolved imaging with the new acquisition method described in [HWLW3].** BPAE cell labelled with Alexa 4.Fluor® 488 phalloidin. a) Wide-field image. b) SIM image. Magnifications of the blue-boxed region represent c) wide-field and d) SIM results. The scale bar in c) and d) is $1 \mu\text{m}$. e) Normalized intensity profiles along the yellow line in both a) and b). Figure taken from: [HWLW3]. Copyright © IOP Publishing.

We imaged actin filaments of BPAE cells, the same prepared cell slide from Invitrogen® as before, using the new acquisition configuration in the fastSIM setup. The wide-field and superresolved SIM images are shown in Fig. 18. The effective illumination time of each segmented frame displayed on the SLM is 0.5 ms. 14 segmented frames were displayed on the SLM and 9 camera readout images were acquired for reconstructing one 2D superresolved SIM

image. The total acquisition time is 12.6 ms which corresponds to a superresolved acquisition frame rate of 79 fps.

The characteristic of each fastSIM system version as well as the achieved results is shown in Table 3. We demonstrated the improvement of the acquisition speed in the fastSIM system by modifying the hardware configuration or changing the synchronization routine. The new acquisition method can achieve the fastest acquisition speed till now. However, in this synchronization configuration, the exposure time is no longer adjustable. Thus, the sample must show strong fluorescence or a higher laser power is needed if the sample is not bright enough. Nevertheless, the switching between two acquisition methods, in [HWLW2] and in [HWLW3], is flexible and can be carried out without changing the setup's hardware configuration.

FastSIM System Version	[HWLW1]	[HWLW2]	[HWLW3]
Acquisition Speed	7.6 fps	18.01 fps	79 fps
Excitation light	442 nm	488 nm	488 nm
Mean FWHM of Microspheres in Wide-field (nm)	224.8 ± 21.2	222.3 ± 38.5	282 ± 25.2
Mean FWHM of Microspheres in SIM (nm)	114.2 ± 9.5	93.6 ± 15.1	108 ± 19.2
Azimuthal Polarization of the Illumination Light in the Sample Plane	No	Yes	Yes
Adjustable Exposure Time	Yes	Yes	No
Cell Imaging	No	Yes	Yes
Fast Dynamics Imaging Result	No	Yes	Not yet

Table 3 **Characteristics of the fastSIM system among each version.**

2.4. Computation of grating patterns - Changes in the software

The concept of the design of the grating patterns displayed on the SLM has been presented in [HWLW1] and [HWLW2]. Here, only few concepts shall be

introduced. As we use a passive Fourier filter to select only the $\pm 1^{\text{st}}$ diffraction orders in the Fourier plane of the SLM to form the structured illumination in the sample plane, a simulation is useful for us to understand the distribution of all diffraction orders in Fourier space. In [HWLW1], we presented the first version of the grating pattern generation algorithm, only considering the effect of the pixelated grating pattern on the SLM. This algorithm seemed to work well for the gratings pairs chosen at that time, and the passive Fourier filter successfully selected only the $\pm 1^{\text{st}}$ diffraction orders. Later, we observed extra diffraction orders from the SLM display structure that caused a breakdown of this algorithm when we tried to do SIM imaging with more grating orientations. These residual diffraction orders come from the existence of the periodicity of the square pixels and the internal distribution of vias in the display structure (see Fig. 19 a). Thus, the diffraction orders originating from the pixelated grating pattern itself convolve with these residual diffraction orders in Fourier space.

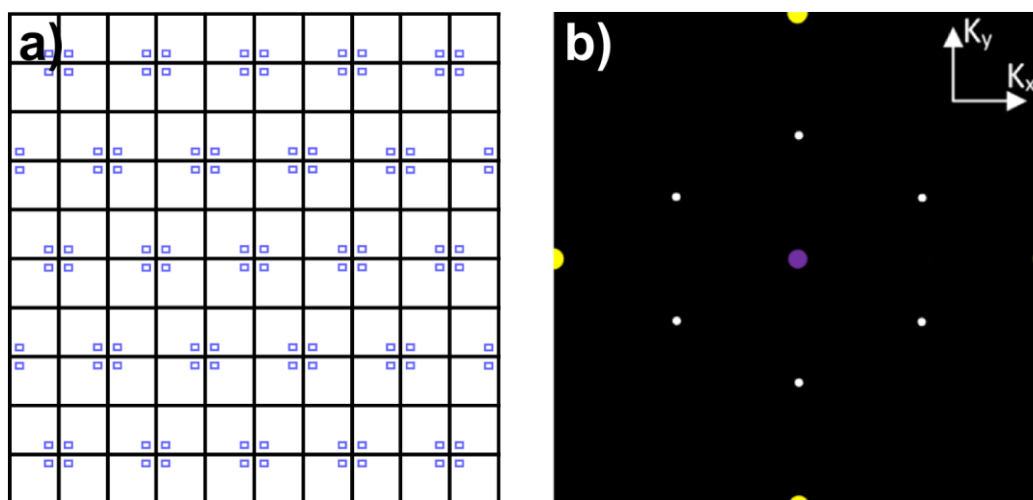


Fig. 19 **A schematic sketch of the residual structure of the SLM display (theory).** a) The pixelated SLM display and the vias underneath the display are marked in blue. b) Fourier transform of the residual structure of the SLM display. The periodicity of the square pixels contributes to four diffraction orders marked in yellow. The internal distribution of the via structures introduce another six diffraction orders marked in white. Figure b) taken from: [HWLW2]. Copyright © IOP Publishing.

A unit cell is defined by two vectors \vec{V}_a and \vec{V}_b as shown in Fig. 20 a). The grating pattern is then the multiple replication of the unit cell. A set of parameters are given to define the grating constant, the grating orientations and the unit cell vectors. Two phase step vectors are introduced to calculate the equidistant phase step. Fig. 20 shows one frame of a pixelated grating pattern displayed on the SLM and the corresponding diffraction orders in the Fourier plane of the SLM in a real case with all three orientations of grating patterns display. In Fig. 20 b), the six yellow rings indicate the holes on the passive Fourier filter. By adopting this new grating search algorithm, six orientations of grating pattern pairs can be found and the passive Fourier filter can still successfully block all unwanted diffraction orders except the $\pm 1^{\text{st}}$ diffraction orders which we used in [HWLW4] for the NL-SIM experiment.

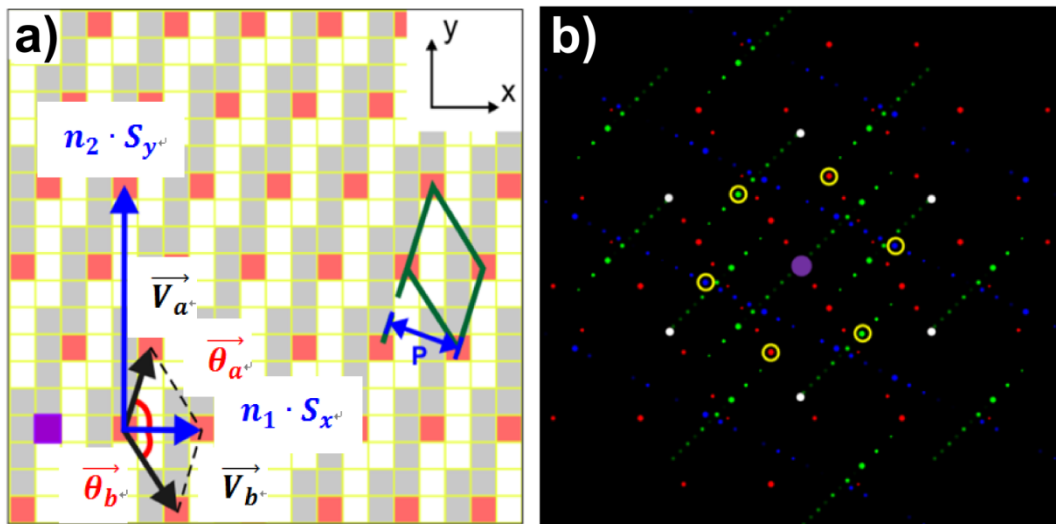


Fig. 20 **A schematic sketch of the concept of spatial frequency filtering in the Fourier space.** a) A grating pattern displayed on the SLM. Lattice points are pixels marked in red. \vec{V}_a and \vec{V}_b are unit cell vectors. P denotes grating constant. S_x and S_y are two components of a phase step vector. b) The Fourier transform of the grating pattern orientated in three directions separated by $\sim 60^\circ$. Figure taken from: [HWLW2]. Copyright © IOP Publishing.

2.5. Vibrations and air fluctuations in the environment

Vibrations come from everywhere. Influences from the building transferred through the optical table, the cooling fan of the laser, the filter fan unit (FFU) above the optical table, even persons walking near the optical table may fluctuate and their effects on the surrounding air might all be sources of vibrations that may shake the illumination grating pattern during image acquisition. Thus, a closed cage around a superresolution microscope is necessary.

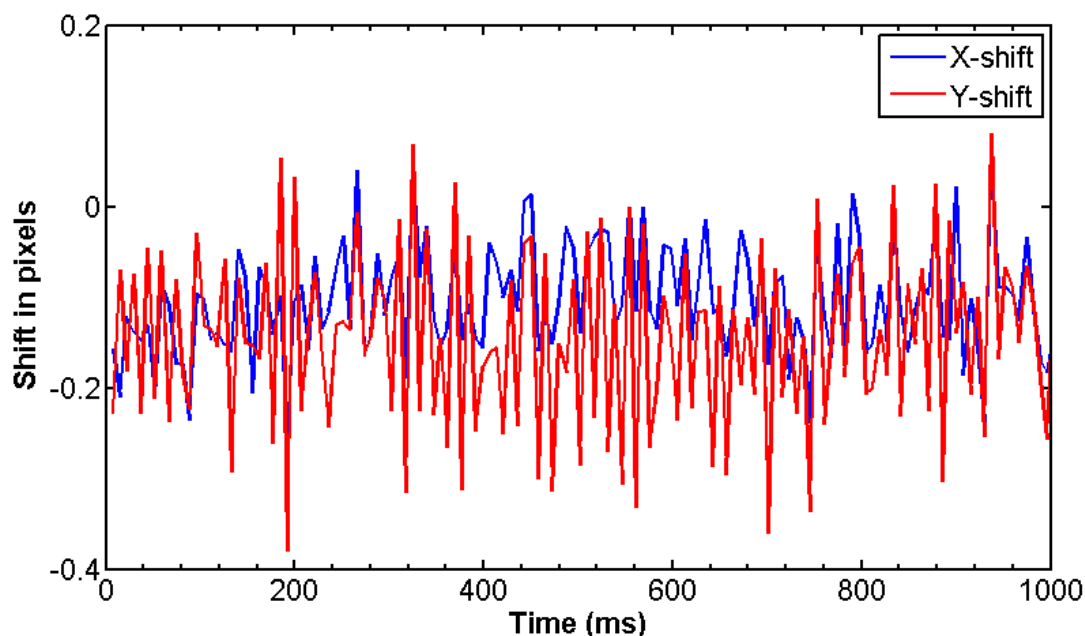


Fig. 21 **Vibration test in the fastSIM setup.** The sCMOS camera is operated in the air-cooling mode.

To ensure a stable structured illumination, we put the laser body outside the main optical path section as the fan on the laser body may cause air fluctuation. Furthermore, we shut down FFU above the optical table during the data acquisition. Moreover, an external z-axis nanopositioning system is placed on the microscope body as a stabilized sample holder. This holder is fixed with four clamps to the microscope body. The vibration test is done by acquiring 150

images of fluorescent microspheres with wide field illumination of 488 nm laser. The shift in x and y direction is shown in Fig. 21. The standard deviations of the shift are 3.87 nm and 6.45 nm in x direction and in y direction, respectively.

We observed that this vibration mainly comes from the fan on the camera when we use the air-cooling mode to cool down the camera chip. Thus, we changed to the water-cooling mode to cool down the camera instead. A water cooling system (Ultra Titan 150, Hailea) is attached to the camera for this purpose. In order to avoid extra vibration from the cooling system, the water pipes connected to the camera and the cooling system are fixed on the ground and the cooling system is placed on shock absorbing foam. Fig. 22 shows that the standard deviations of the shift are 1.94 nm and 1.94 nm in x direction and in y direction, respectively for the water cooling mode.

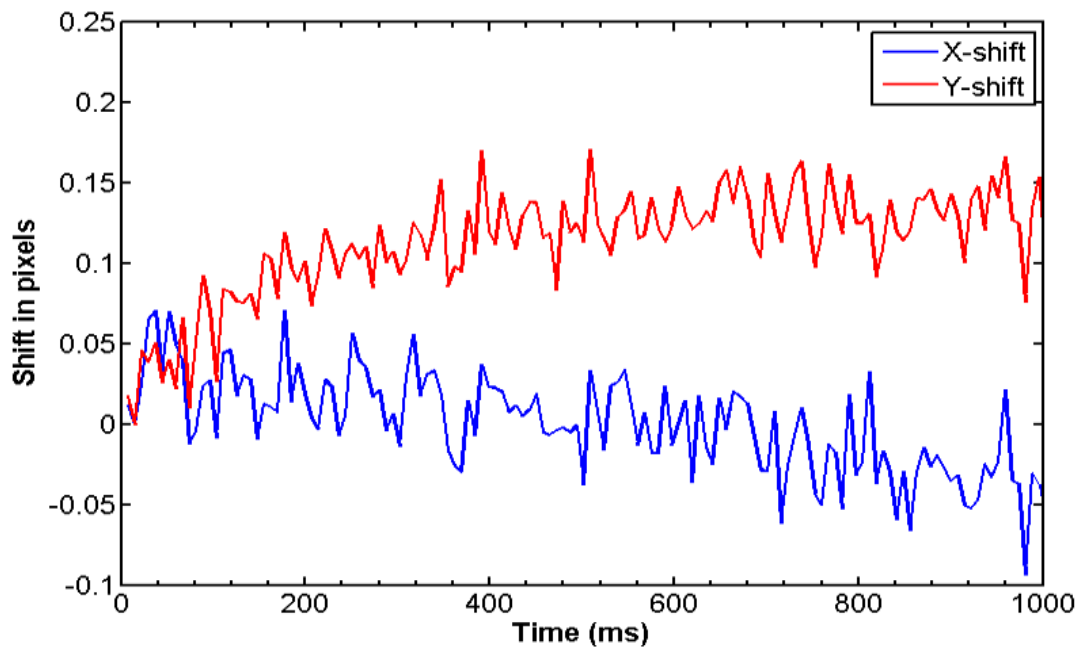


Fig. 22 **Vibration test in the fastSIM setup.** The sCMOS camera is operated in the water-cooling mode. An external water cooling system is attached.

3. Nonlinear structured illumination microscopy (NL-SIM) – Gaining further spatial resolution

Apart from improving the acquisition rate of SIM, we also worked on gaining further resolution improvement through nonlinear structured illumination microscopy (NL-SIM). The linear dependence of the fluorophore emission rate on the illumination intensity can be changed to a non-linear dependence by saturating either the fluorescent excited state (S_1) or the nonfluorescent off-state (S_{off}) of a photoswitchable fluorescent protein (see Fig. 23). In the past years, many scientists dedicated their efforts to develop reversibly photoswitchable fluorescent proteins (RSFPs), e.g. Dronpa [16, 17], mIrisFP [31, 32], mIrisGFP, rsEGFP [33] etc. However, acquiring sufficient fluorescence for reconstructing a NL-SIM image is problematic with these RSFPs as they either offer low photostability after a few switching cycles, long relaxation time or low quantum yield. Some newly developed RSFPs, like SkyIris-NS [34] and Kohinoor [35], overcome these problems.

3.1. Nonlinear photo-response from photoswitchable proteins

When the nonlinear dependence of the fluorescence emission rate on the illumination intensity is created, the effective fluorescence emission pattern contains higher-order harmonics ($\pm 2\vec{k}_b, \pm 3\vec{k}_b$ etc., which are multiples of $\pm\vec{k}_b$) in Fourier space (see Fig. 23 e). The object information attaches to all higher-order harmonics as to the zeroth component in Fourier space. The achievable resolution is restricted by the signal-to-noise (SNR) ratio and thus only the frequency orders above the noise level are detectable and therefore suitable for NL-SIM image reconstruction.

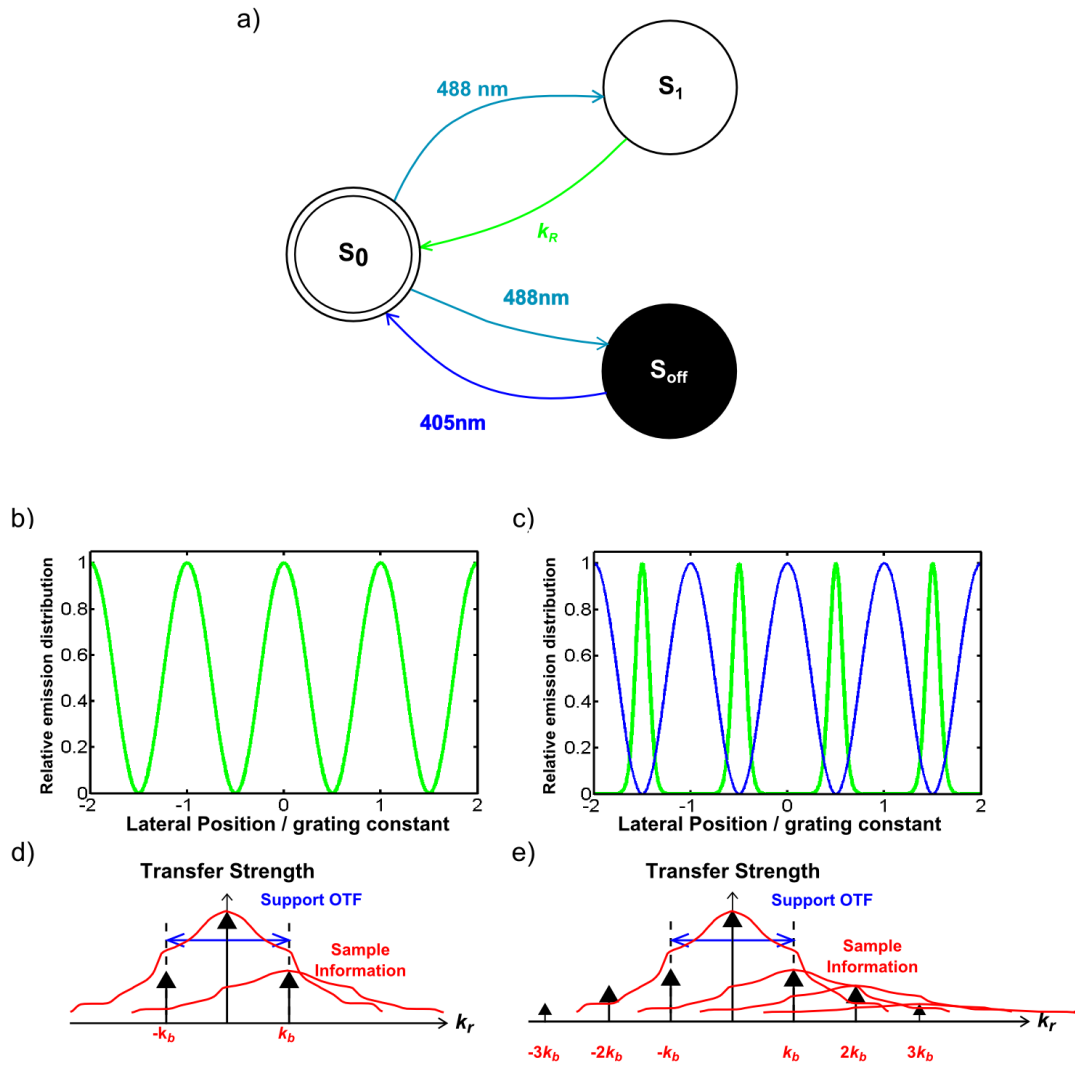


Fig. 23 **Simulation of fluorescence emission distribution in a two-beam LSIM and a NL-SIM scheme.** a) Switching behavior of photoswitchable proteins, such as Dronpa, mIrisGFP, rsEGFP and Skyran-NS. Excitation λ : 488 nm, photodeactivation λ : 488 nm, photoactivation λ : 405 nm. S_{OFF} , S_0 , S_1 and k_R denote the dark state, the fluorescent ground state, the fluorescent excited state and the rate constant of fluorescence, respectively. b) Fluorescence emission distribution in a two-beam LSIM system. c) Fluorescence emission distribution (green curve) in a two-beam NL-SIM system where there is fluorophore saturation in the dark state. The deactivation is done by the 488 nm laser (blue curve). d) A scheme of the fluorescence emission pattern of b) in Fourier space. e) A scheme of the fluorescence emission pattern of c) in Fourier space.

Fig. 23 b) shows the LSIM case when the fluorescence emission pattern (green curve) is linearly dependent on the excitation intensity. Note that the

excitation pattern is at the same lateral position as the emission pattern. The corresponding zeroth and the $\pm 1^{\text{st}}$ components are shown in Fig. 23 d) for this sinusoidal fluorescence emission pattern. One of the approaches to create a nonlinear dependence of the fluorescence emission pattern on the illumination intensity is to saturate the nonfluorescent off-state of the fluorophore. For example, an illumination wavelength of 488 nm can be used for deactivating SkyJan-NS and for excitation as well. A 405 nm laser drives these RSFPs to the on state (S_0). Fig. 23 c) shows the remaining fluorophores in the on state (green curve) after deactivation by the spatially patterned illumination of 488 nm (blue curve). Thus, the fluorescence emission pattern is no longer sinusoidal (see green curve in Fig. 23 c) which leads to the appearance of higher-order harmonics (see Fig. 23 e) at high saturation level. Moreover, in order to obtain enough fluorescence from the remaining fluorophores in the on-state and thus push up the intensity of higher-order harmonics, it is preferable to use the same spatially patterned illumination of 405 nm with a $\pi/2$ phase shift with respect to the deactivation wavelength of 488 nm. This requires an accurate design of the grating pattern to produce a perfect 405 nm illumination pattern that is very precisely aligned to the 488 nm illumination pattern at every position to overcome the achromatic aberration in an objective [18].

We chose the photoswitchable fluorescent protein Kohinoor to perform the NL-SIM experiments due to its property of positive photoswitchability (see Fig. 24 a), as we can deactivate Kohinoor with 405 nm over a large field of view and activate Kohinoor with 488 nm patterned illumination simultaneously to generate the nonlinear fluorescence emission rate to the illumination intensity (see Fig. 24 b). This greatly simplifies the NL-SIM acquisition method as the acquisition method to the same scheme we used for LSIM and avoids illuminating the SLM with the 405 nm laser since 405 nm lie outside its recommended safe working range of wavelength. A schematic diagram of the NL-SIM setup is shown in Fig. 25. The electronic circuit sketch can be found in Appendix A.2.

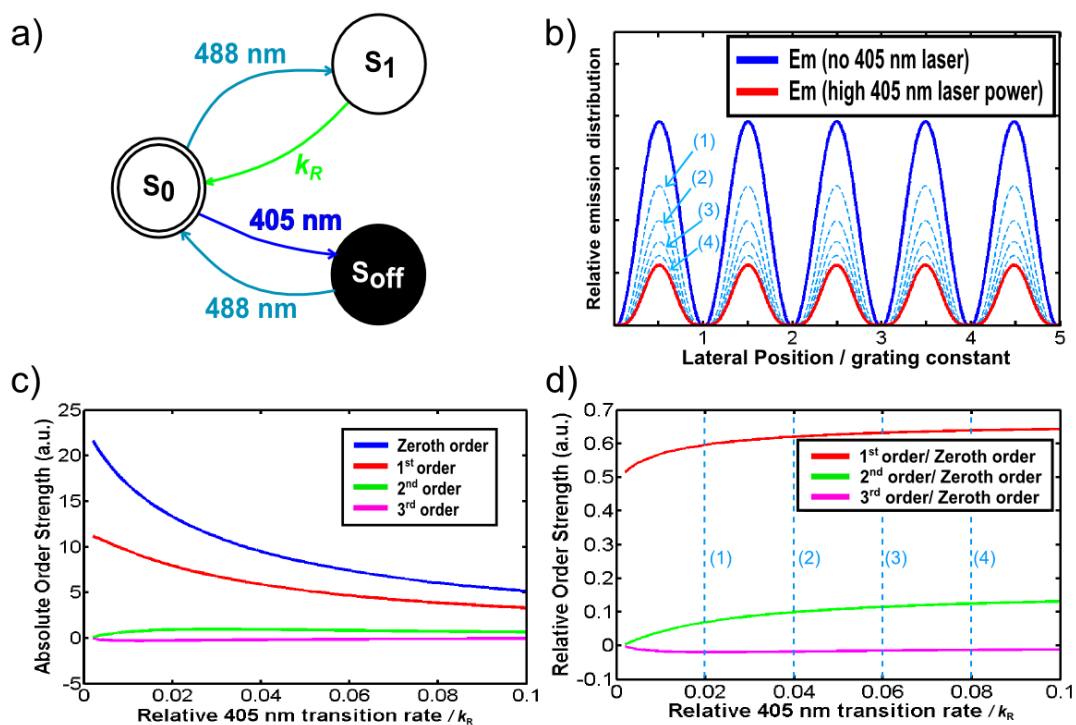


Fig. 24 **Simulation of nonlinear fluorescence emission characteristics in a two-beam NL-SIM scheme.** a) Illustration of switching behavior of Kohinoor. Excitation λ : 488 nm, photoactivation λ : 488 nm, photodeactivation λ : 405 nm. S_{OFF} , S_0 , S_1 and k_R denote the dark state, the fluorescent ground state, the fluorescent excitation state and the rate constant of fluorescence, respectively. b) Simulated dependence of the fluorescence emission distribution in a steady state with no simultaneous photodeactivation (blue solid line) and photodeactivation with high powered 405 nm illumination (red solid line) over a large field of view in which the relative transition rate of the 405 nm laser is equal to $0.1k_R$. c) Absolute component strength. d) Relative component strength. Figure taken from: [HWLW4].

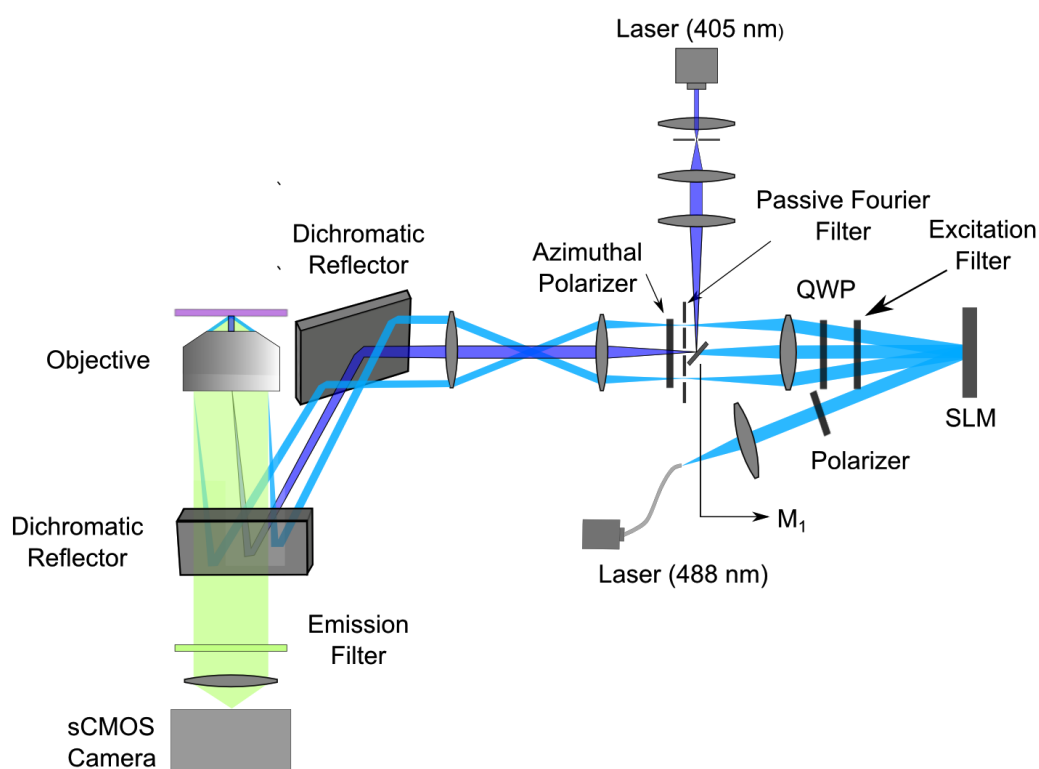


Fig. 25 **A schematic diagram of the fast nonlinear structured illumination microscope setup.** The NL-SIM setup is upgraded from the former setup described in [HWLW2]. A 405 nm laser and a small mirror are integrated into the system. The zero diffraction order of the 488 nm laser is blocked by the backside of a small mirror (M_1) used to reflect the 405 nm laser into the system near the Fourier plane of the SLM. Both 405 nm and 488 nm laser are sent to the sample plane through a 63 \times oil immersion objective. The 405 nm laser illuminates the sample over a large field of view for photodeactivation while the $\pm 1^{\text{st}}$ diffraction orders of the 488 nm laser form an interference pattern on the sample for excitation and photoactivation. Figure taken from: [HWLW4].

However, there are two constraints on generating the nonlinearity by this method. First, the saturation level achievable by this method is limited. With a higher intensity of the deactivation laser, the nonlinearity is stronger (see Fig. 24 b). However, it also pushes down the general grating contrast, as the deactivation happens everywhere in the illuminated region. Fig. 24 d) shows the simulation of the relative diffraction order strengths which indicates that only the first higher-order harmonics (the $\pm 2^{\text{nd}}$ diffraction orders) are slightly above the noise level. Secondly, the molecular switching perturbs the

overall emission pattern and leads to artefacts in the SIM reconstruction, even if many photons can be detected from a single fluorophore. Since the concentration of fluorophores is not very far from the single-molecule regime, we solved this problem by opting for several switching cycles contributing to a single detected image by applying both activation and deactivation simultaneously. The direct consequence will be a decrease in acquisition speed. The resolution in our NL-SIM result is slightly better than in the LSIM image (see Fig. 26).

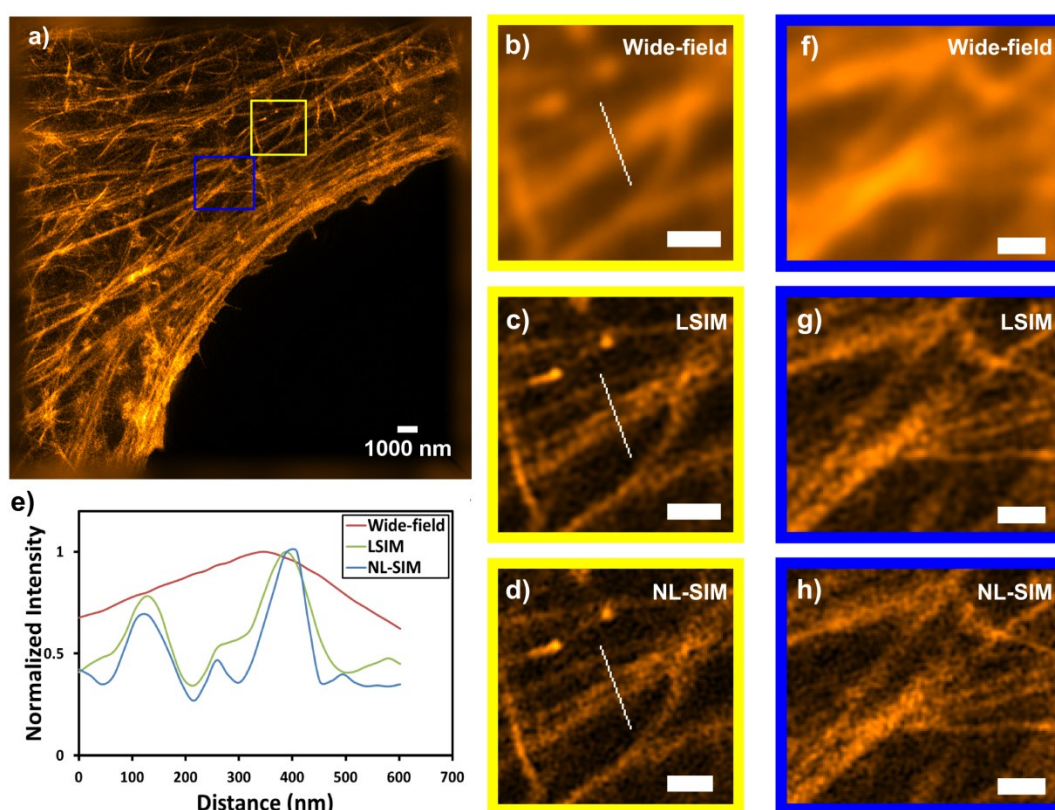


Fig. 26 **NL-SIM imaging of a HeLa cell expressing Kohinoor-actin.** a) NL-SIM image in a large field of view. Magnified view of the yellow-boxed region and blue-boxed region represent conventional wide-field microscopy image b) and f), LSIM image c) and g), and NL-SIM image d) and h), respectively. Scale bar in magnified images is 500 nm. e) Normalized intensity profiles along the white line in b), c) and d). Part of figures taken from: [HWLW4].

4. Conclusion

The construction of the first fastSIM setup prototype as well as the grating design for the pixelated display of the SLM was demonstrated in [HWLW1]. A superresolved SIM image of fluorescent microspheres was presented to prove the state-of-the-art implementation of the fastSIM system. In [HWLW2], we upgraded the fastSIM system to a faster acquisition scheme by employing a laser with a wavelength fitting to the maximum excitation of the fluorophore and by adopting the free running mode of the novel sCMOS camera, which offers faster readout. The isotropic resolution improvement was achieved by employing two identical dichromatic reflectors, where the second dichromatic reflector compensates for the phase changes of the polarization induced by the first dichromatic reflector. We modified the grating search algorithm by exploring the residual structures on the SLM display and optimized it for advanced grating pattern design with more grating orientations and the required accurate phase steps. SIM is a superior method for fast acquisition of large fields of view which we demonstrated in a recorded time-lapse video (see [supplementary materials](#) in [HWLW2]). We showed that the attainable acquisition speed in our fastSIM system is suited to imaging fast dynamics of fluorescent microspheres diffusing in a 3D volume sample. In [HWLW3], we achieved the fastest acquisition rate up to this day by adopting a new synchronization configuration where the 14 segmented grating patterns displayed on the SLM are synchronized with the rolling shutter position of the sCMOS camera.

For achieving a nearly perfect superresolved NL-SIM image, a stable structured illumination and drift-free imaging is required. Therefore, several methods were employed to reduce air fluctuations and vibrations from the environment and from the equipment in the setup. The construction of the fast NL-SIM setup and the study of fluorophore saturation were demonstrated in

[HWLW4]. Further resolution improvement was achieved with the help of Kohinoor, a photoswitchable fluorescent protein using the NL-SIM system.

Additional applications of SIM imaging in biological studies were demonstrated in [HWLW5] in the localization of the mycobacteria position inside macrophages and as a comparison to Raman microspectroscopy imaging. In [HWLW6], the 3D SIM image demonstrated the uptake of the polyunsaturated aldehyde (PUA) probe into cells of the diatom *Phaeodactylum tricornutum* to reveal protein targets of PUAs and to study the affected metabolic pathways.

5. Outlook

5.1. Dual-colors 3D SIM imaging

The current fastSIM setup offers an illumination pattern formed by two-beam interference. There is a trade-off between the grating contrast in the sample plane and the optical sectioning along the z direction when the zeroth order from the SLM is blocked by a Fourier filter. This is a general problem in a conventional light microscope due to the “missing cone” in the wide-field OTF. In a two-beam SIM system, the missing cone can be filled substantially if the modulation frequency is close to half the limit frequency. However, the lateral resolution gain will only be 1.5 [36]. By employing three-beam interference to form the illumination pattern in SIM, the optical sectioning is optimal and results in the removal of out-of-focus light [24, 36, 37]. The challenge lies in the rapid control of the azimuthal polarization of the zeroth and the $\pm 1^{\text{st}}$ diffraction orders, as the contrast of the illumination grating depends on the polarization of the illumination beams. The azimuthal polarizer currently used in the fastSIM setup has an undefined region in the center, and thus it has to be replaced by a tunable polarization rotator which can modulate all diffraction orders, such as a liquid crystal cell (SWIFT; Meadowlark). However, the

shortcoming of the Meadowlark device is its temperature depended drift of the liquid crystal cell which requires frequent recalibration.

Another future aim of our fastSIM system is to employ dual-color illumination. By mounting the Fourier filter on a motorized rotator, a flexible diffraction order selection can be realized. In order to achieve the same resolution improvement in dual-color SIM, grating patterns with different grating constants, corresponding to the laser wavelengths, need to be applied.

5.2. Further resolution improvement in NL-SIM

The current NL-SIM acquisition method offers only very little resolution improvement with respect to LSIM as the nonlinearity of the fluorescence emission pattern does not push up the strength of the first higher-order harmonics significantly. Besides, the noise effect of the single-molecule switching coming from the simultaneous photoactivation and photodeactivation of the fluorophore creates artefacts in the SIM reconstruction. Two alternative acquisition methods might help to avoid the single-molecule switching and gain further resolution improvement in NL-SIM:

Method A: Pre-photoactivation with patterned illumination of the 488 nm laser

As photoactivation of Kohinoor can be done with the 488 nm laser, pre-photoactivation before acquiring NL-SIM data to achieve higher nonlinearity of the fluorescence emission pattern is possible. First, all fluorophores in a large field of view are deactivated using the 405 nm laser and then ~20% of fluorophores are activated with patterned illumination of the 488 nm laser. Then the NL-SIM data is acquired with a π phase shift of the patterned illumination of the 488 nm laser. This will lead to saturation in the fluorescent excited state. Fig. 27 c) shows that the absolute value of the relative diffraction strength of the first higher-order harmonics is pushed up to ~30%, which can contribute significantly to the signal for the NL-SIM image reconstruction.

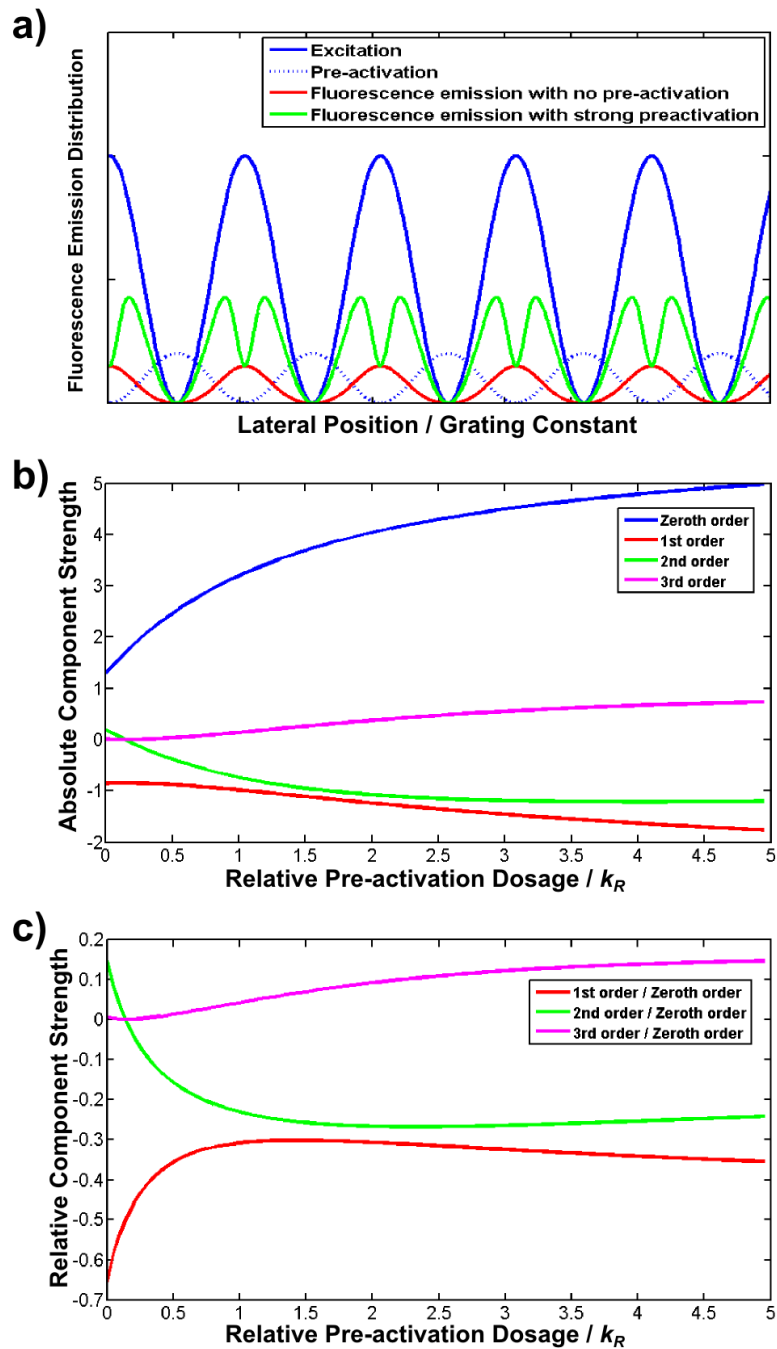


Fig. 27 **Simulation of nonlinear fluorescence emission characteristics in a two-beam NL-SIM scheme.** a) Simulated dependence of the fluorescence emission distribution with pre-photodeactivation (green solid line) and with no photodeactivation (red solid line). The patterned illumination for pre-photodeactivation is shown as the blue dashed line. The patterned illumination for excitation is shown as the blue solid line. b) Absolute component order strength calculated from the green curve in a). c) Relative component order strength calculated from the green curve in a).

Method B: Introducing photodeactivation with patterned illumination of the 405 nm laser

The other alternative method is to use photoactivation with patterned illumination of the 405 nm laser instead of a wide-field activation. This requires a perfect calibration of the position of the illumination grating in the sample plane with both the 488 nm and the 405 nm laser, as an optical lens introduces chromatic aberration. The chromatic aberration introduces a phase shift of the interference pattern, i.e. illumination grating, and as well as a grating constant difference between different wavelengths of light. Consequently, it will lead to an unexpected region of photoactivation/photodeactivation of the fluorophores.

Reference

- [1] Ichihara A, Tanaami T, Isozaki K, Sugiyama Y, Kosugi Y, Mikuriya K, Abe M, Uemura I. High-speed confocal fluorescence microscopy using a Nipkow scanner with microlenses for 3-D imaging of single fluorescence molecule in real time. *Bioimages*. 1996; 4: 57–62
- [2] Juškaitis R, Wilson T, Neil M A A, Kozubek M. Efficient realtime confocal microscopy with white light sources. *Nature*. 1996; 383: 804–806
- [3] Petráň M, Hadravsky M, Egger M D, Galambos R. Tandemscanning reflected-light microscope. *Journal of the Optical Society of America*. 1968; 58: 661–664
- [4] Heintzmann R, Ficz G. Breaking the resolution limit in light microscopy. *Briefings in Functional Genomics*. 2006; 5: 289–301
- [5] Willig K I, Harke B, Medda R, Hell S W. STED microscopy with continuous wave beams. *Nature Methods*. 2007; 4: 915–918
- [6] Dyba M, Jakobs S, Hell S W. Immunofluorescence stimulated emission depletion microscopy. *Nature Biotechnology*. 2003; 21: 1303–1304
- [7] Rittweger E, Han K Y, Irvine S E, Eggeling C, Hell S W. STED microscopy reveals crystal colour centres with nanometric resolution. *Nature Photonics*. 2009; 3: 144–147
- [8] Grotjohann T, Testa I, Leutenegger M, Bock H, Urban N T, Lavoie-Cardinal F, Willig K I, Eggeling C, Jakobs S, Hell S W. Diffraction-unlimited all-optical imaging and writing with a photochromic GFP. *Nature*. 2011; 478: 204–208
- [9] Lidke K A, Rieger B, Jovin T M, Heintzmann R. Superresolution by localization of quantum dots using blinking statistics. *Optics Express*. 2005; 13: 7052-7062. doi: 10.1364/OPEX.13.007052
- [10] Betzig E, Patterson G H, Sougrat R, Lindwasser W, Olenych S, Bonifacino J S, Davidson M W, Lippincott-Schwartz J, Hess H F. Imaging intracellular

- fluorescent proteins at nanometer resolution. *Science*. 2006; 313: 1642–1645
- [11] Rust M J, Bates M, Zhuang X. Sub-diffraction-limit imaging by stochastic optical reconstruction microscopy (STORM). *Nature Methods*. 2006; 3: 793–796
- [12] Heintzmann R, Cremer C. Verfahren zur Erhöhung der Auflösung optischer Abbildung; German Patent Nr. 199 08 883 A1, September 7, 2000, priority Mar. 2nd, 1999; Heintzmann R, Cremer C. Method and Device for Representing an Object, WO 0052512, Patent Applicant: Max-Planck Society, priority (see above), 1999.
- [13] Heintzmann R, Cremer C. Laterally modulated excitation microscopy: improvement of resolution by using a diffraction grating. in *Proceedings of the Society of Photographic Instrumentation Engineers*. 1999; 3568: 185–196
- [14] Heintzmann R, Jovin T M. Saturated patterned excitation microscopy—a concept for optical resolution improvement. *Journal Optical Society of America*. 2002; 19: 1599–1609
- [15] Gustafsson M G L. Surpassing the lateral resolution limit by a factor of two using structured illumination microscopy. *Journal of Microscopy*. 2000; 198: 82–87
- [16] Hirvonen L, Mandula O, Wicker K, Heintzmann R. Structured illumination microscopy using photoswitchable fluorescent proteins. in *Proceedings of the Society of Photographic Instrumentation Engineers*. 2008; 6861: 68610L
- [17] Rego E H, Shao L, Macklin J J, Winoto L, Johansson G A, Kamps-Hughes N, Davidson M W, Gustafsson M G. Nonlinear structured-illumination microscopy with a photoswitchable protein reveals cellular structures at 50-nm resolution. *Proceedings of the National Academy of Sciences* 2012; 109: E135–E143. doi: 10.1073/pnas.1107547108; pmid: 22160683

- [18] Li D, Shao L, Chen B-C, Zhang X, Zhang M, Moses B, Milkie D E, Beach J R, Hammer J A III, Pasham M, Kirchhausen T, Baird M A, Davidson M W, Xu P, Betzig E. Extended-resolution structured illumination imaging of endocytic and cytoskeletal dynamics. *Science*. 2015; 349: aab3500. doi: 10.1126/science.aab3500
- [19] Hirvonen L. Structured illumination microscopy using photoswitchable fluorescent proteins. PhD thesis, King's college London, 2008
- [20] Schermelleh L, Heintzmann R, Leonhardt H. A guide to super-resolution fluorescence microscopy. *The Journal of Cell Biology*. 2010; 190: 165–175. doi: www.jcb.org/cgi/doi/10.1083/jcb.201002018
- [21] Sparrow C M. On spectroscopic resolving power, *Astrophysical Journal*. 1916; 44: 76–86
- [22] Rayleigh L. Investigations in optics with special reference to the spectroscope. *Philosophical Magazine*. 1879; 8: 261
- [23] Abbe E. Beiträge zur Theorie des Mikroskops und der mikroskopischen Wahrnehmung. in *Arkiv Mikroskopische Anatomie*. 1873; 9: 413–418
- [24] Gustafsson M G L, Shao L, Carlton P M, Wang C J R, Golubovskaya I N, Cande W Z, Agard D A, and Sedat J W. Three-dimensional resolution doubling in wide-field fluorescence microscopy by structured illumination. *Biophysical Journal*. 2008; 94: 4957–4970
- [25] Mandula O. Pattern excitation microscopy. diploma's thesis, Charles University in Prague, King's college London. 2008
- [26] Hirvonen L, Wicker K, Mandula O, and Heintzmann R. Structured illumination microscopy of a living cell. *European Biophysics Journal*. 2009; 38: 807–812
- [27] Kner P, Chhun B B, Griffis E R, Winoto L, and Gustafsson M G L. Super-resolution video microscopy of live cells by structured illumination. *Nature Methods*. 2009; 6: 339–342
- [28] Förster R. Fast Structured Illumination Microscopy. master's thesis, Friedrich Schiller University Jena. 2012

- [29] Fiolka R, Shao L, Rego E H, Davidson M W, Gustafsson M G L. Time-lapse two-color 3D imaging of live cells with doubled resolution using structured illumination. *Proceedings of the National Academy of Sciences*. 2012; 109: 5311–5315
- [30] Martínez-García A, Moreno I, Sánchez-López M M, García-Martínez P. Operational modes of a ferroelectric LCoS modulator for displaying binary polarization, amplitude, and phase diffraction gratings. *Applied Optics*. 2009; 48: 2903–2914
- [31] Fuchs J, Böhme S, Oswald F, Hedde P N, Krause M, Wiedenmann J, Nienhaus G U. A photoactivatable marker protein for pulse-chase imaging with superresolution. *Nature Methods*. 2010; 7: 627–630 doi:10.1038/nmeth.1477
- [32] Wiedenmann J, Gayda S, Adam V, Oswald F, Nienhaus K, Bourgeois D, Nienhaus G U. From EosFP to mIrisFP: structure-based development of advanced photoactivatable marker proteins of the GFP-family. *Journal Biophotonics*. 2011; 4: 377–390. doi: 10.1002/jbio.201000122
- [33] Grotjohann T, Testa I, Leutenegger M, Bock H, Urban N T, Lavoie-Cardinal F, Willig K I, Eggeling C, Jakobs S, Hell S W. Diffraction-unlimited all-optical imaging and writing with a photochromic GFP. *Nature*. 2011; 478: 204–208. doi:10.1038/nature10497
- [34] Zhang X, Chen X, Zeng Z, Zhang M, Sun Y, Xi P, Peng J, Xu P. Development of a reversibly switchable fluorescent protein for super-resolution optical fluctuation imaging (SOFI). *ACS Nano*. 2015; 9: 2659–2667. doi: 10.1021/nn5064387; pmid: 25695314
- [35] Tiwari D K, Arai Y, Yamanaka M, Matsuda T, Agetsuma M, Nakano M, Fujita K, Nagai T. A fast- and positively photoswitchable fluorescent protein for ultralow-laser-power RESOLFT nanoscopy. *Nature Methods*. 2015; 12: 515–518. doi: 10.1038/nmeth.3362
- [36] Wicker K. Increasing resolution and light efficiency in fluorescence microscopy. PhD thesis, King's college London, 2010

- [37] Neil M A A, Juškaitis R , Wilson T. Method of obtaining optical sectioning by using structured light in a conventional microscope. Optics Letters. 1997; 22: 1905-1907

Publication list

- [HWLW1] Förster R, Lu-Walther H-W, Jost A, Kielhorn M, Wicker K, Heintzmann R. Simple structured illumination microscope setup with high acquisition speed by using a spatial light modulator. *Optics Express*. 2014; 22: 20663-20677. doi: <http://dx.doi.org/10.1364/OE.22.020663>
- [HWLW2] Lu-Walther H-W, Kielhorn M, Förster R, Jost A, Wicker K, Heintzmann R. fastSIM: a practical implementation of fast structured illumination microscopy. *Methods and Applications in Fluorescence*. 2015; 3: 014001. doi: <http://dx.doi.org/10.1088/2050-6120/3/1/014001>
- [HWLW3] Song L, Lu-Walther H-W, Förster R, Jost A, Kielhorn M, Zhou J, Heintzmann R. Fast structured illumination microscopy using rolling shutter cameras. *Measurement Science and Technology*. 2016; 27: 055401. doi: <http://dx.doi.org/10.1088/0957-0233/27/5/055401>
- [HWLW4] Lu-Walther H-W, Hou W, Kielhorn M, Arai Y, Nagai T, Kessels M M, Qualman B, Heintzmann R. Structured illumination microscopy: gaining further resolution improvement by nonlinear photo-response from photoswitchable fluorescent protein. *PLoS ONE*. 16 April 2016; submitted.
- [HWLW5] Silge A, Abdou E, Schneider K, Meisel S, Bocklitz T, Lu-Walther H-W, Heintzmann R, Rösch P and Popp J. Shedding light on host niches: label-free in situ detection of *Mycobacterium gordonae* via carotenoids in macrophages by Raman microspectroscopy. *Cellular Microbiology*. 2015; 17:832–842. doi: <http://dx.doi.org/10.1111/cmi.12404>
- [HWLW6] Wolfram S, Wielsch N, Hupfer Y, Mönch B, Lu-Walther H-W, Heintzmann R, Werz O, Svatoš A and Pohnert G. A Metabolic Probe-Enabled Strategy Reveals Uptake and Protein Targets of Polyunsaturated Aldehydes in the Diatom *Phaeodactylum tricornutum*. *PLoS ONE*. 2015; 10: e0140927. doi: <http://dx.doi.org/10.1371/journal.pone.0140927>

Poster list

- [PP1] Lu-Walther H-W, Kielhorn M, Heintzmann R. Fast High-Resolution Fluorescence Microscopy by Nonlinear Structured Illumination. Best poster prize in *Winter Seminar-Biophysical Chemistry, Molecular Biology and Cybernetics of Cell Functions*. 2014.
- [PP2] Lu-Walther H-W, Song L, Förster R, Kielhorn M, Heintzmann R. Fast High-Resolution Fluorescence Microscopy by Structured Illumination. Best poster prize in *International OSA Network of Students*. 2015.

Publications

Publication 1

Simple structured illumination microscope setup with high acquisition speed by using a spatial light modulator

Förster R, Lu-Walther H-W, Jost A, Kielhorn M, Wicker K, Heintzmann R.

[HWLW1] Förster R, Lu-Walther H-W, Jost A, Kielhorn M, Wicker K, Heintzmann R. Simple structured illumination microscope setup with high acquisition speed by using a spatial light modulator. Optics Express. 2014; 22: 20663-20677. <http://dx.doi.org/10.1364/OE.22.020663>

Beteiligt an (*Zutreffendes ankreuzen*)

Author	Förster R	Lu-Walther H-W
Konzeption des Forschungsansatzes		
Planung der Untersuchungen	×	
Datenerhebung	×	×
Datenanalyse und -interpretation	×	×
Schreiben des Manuskripts	×	×
Vorschlag Anrechnung Publikationsäquivalente	N.A.	0,5

All authors revised, edited and proof read the final manuscript.

Reprinted with kind permission from the OSA publishing group.

Simple structured illumination microscope setup with high acquisition speed by using a spatial light modulator

Ronny Förster,^{1,2} Hui-Wen Lu-Walther,¹ Aurélie Jost,^{1,2} Martin Kielhorn,^{1,3} Kai Wicker,^{1,2,4} and Rainer Heintzmann^{1,2,3,*}

¹Leibniz Institute of Photonic Technology, Jena, Germany

²Institute of Physical Chemistry, Abbe Center of Photonics, Friedrich-Schiller-University Jena, Germany

³Randall Division of Cell and Molecular Biophysics, King's College London, London, UK

⁴Currently at Carl Zeiss AG, Corporate Research and Technology, Jena, Germany

heintzmann@gmail.com

Abstract: We describe a two-beam interference structured illumination fluorescence microscope. The novelty of the presented system lies in its simplicity. A programmable spatial light modulator (ferroelectric LCoS) in an intermediate image plane enables precise and rapid control of the excitation pattern in the specimen. The contrast of the projected light pattern is strongly influenced by the polarization state of the light entering the high NA objective. To achieve high contrast, we use a segmented polarizer. Furthermore, a mask with six holes blocks unwanted components in the spatial frequency spectrum of the illumination grating. Both these passive components serve their purpose in a simpler and almost as efficient way as active components. We demonstrate a lateral resolution of 114.2 ± 9.5 nm at a frame rate of 7.6 fps per reconstructed 2D slice.

©2014 Optical Society of America

OCIS codes: (100.6640) Superresolution; (180.2520) Fluorescence microscopy; (180.0180) Microscopy; (070.6120) Spatial light modulators; (230.3720) Liquid-crystal devices.

References and links

1. J. B. Pawley, "Handbook of biological confocal microscopy, Third Edition," *J. Bio-Med. Opt.* **35**, 2765 (2008).
2. E. Betzig, G. H. Patterson, R. Sougrat, O. W. Lindwasser, S. Olenych, J. S. Bonifacino, M. W. Davidson, J. Lippincott-Schwartz, and H. F. Hess, "Imaging intracellular fluorescent proteins at nanometer resolution," *Science* **313**(5793), 1642–1645 (2006).
3. M. J. Rust, M. Bates, and X. Zhuang, "Sub-diffraction-limit imaging by stochastic optical reconstruction microscopy (STORM)," *Nat. Methods* **3**(10), 793–796 (2006).
4. S. T. Hess, T. P. K. Girirajan, and M. D. Mason, "Ultra-high resolution imaging by fluorescence photoactivation localization microscopy," *Biophys. J.* **91**(11), 4258–4272 (2006).
5. S. W. Hell and J. Wichmann, "Breaking the diffraction resolution limit by stimulated emission: stimulated-emission-depletion fluorescence microscopy," *Opt. Lett.* **19**(11), 780–782 (1994).
6. G. Donnert, J. Keller, R. Medda, M. A. Andrei, S. O. Rizzoli, R. Lührmann, R. Jahn, C. Eggeling, and S. W. Hell, "Macromolecular-scale resolution in biological fluorescence microscopy," *Proc. Natl. Acad. Sci. U.S.A.* **103**(31), 11440–11445 (2006).
7. K. Lidke, B. Rieger, T. Jovin, and R. Heintzmann, "Superresolution by localization of quantum dots using blinking statistics," *Opt. Express* **13**(18), 7052–7062 (2005).
8. R. Heintzmann and C. Cremer, "Laterally modulated excitation microscopy: improvement of resolution by using a diffraction grating," *Proc. SPIE* **3568**, 185–196 (1999).
9. M. G. L. Gustafsson, "Surpassing the lateral resolution limit by a factor of two using structured illumination microscopy," *J. Microsc.* **198**(2), 82–87 (2000).
10. K. Wicker, O. Mandula, G. Best, R. Fiolka, and R. Heintzmann, "Phase optimisation for structured illumination microscopy," *Opt. Express* **21**(2), 2032–2049 (2013).
11. R. Heintzmann and M. G. L. Gustafsson, "Subdiffraction resolution in continuous samples," *Nat. Photonics* **3**(7), 362–364 (2009).
12. E. H. Rego, L. Shao, J. J. Macklin, L. Winoto, G. A. Johansson, N. Kamps-Hughes, M. W. Davidson, and M. G. Gustafsson, "Nonlinear structured-illumination microscopy with a photoswitchable protein reveals cellular structures at 50-nm resolution," *Proc. Natl. Acad. Sci. U.S.A.* **109**(3), E135–E143 (2012).

13. R. Fiolka, L. Shao, E. H. Rego, M. W. Davidson, and M. G. L. Gustafsson, "Time-lapse two-color 3D imaging of live cells with doubled resolution using structured illumination," *Proc. Natl. Acad. Sci. U.S.A.* **109**(14), 5311–5315 (2012).
14. Zeiss, "ELYRA Enter the World of Superresolution," 1-24 (2012).
15. P. Kner, B. B. Chhun, E. R. Griffis, L. Winoto, and M. G. L. Gustafsson, "Super-resolution video microscopy of live cells by structured illumination," *Nat. Methods* **6**(5), 339–342 (2009).
16. A. Martínez-García, I. Moreno, M. M. Sánchez-López, and P. García-Martínez, "Operational modes of a ferroelectric LCoS modulator for displaying binary polarization, amplitude, and phase diffraction gratings," *Appl. Opt.* **48**(15), 2903–2914 (2009).
17. L. Shao, P. Kner, E. H. Rego, and M. G. L. Gustafsson, "Super-resolution 3D microscopy of live whole cells using structured illumination," *Nat. Methods* **8**(12), 1044–1046 (2011).
18. M. M. Sánchez-López, I. Moreno, and A. Martínez-García, "Teaching diffraction gratings by means of a phasor analysis," Conference Paper, Education and Training in Optics and Photonics, St. Asaph, North Wales, United Kingdom, June 5-7, Session 4 (EMA) (2009).
19. Forth Dimension Displays, *Introduction to the -3DM System* (2011).
20. W. Demtröder, *Experimentalphysik 3: Atome, Moleküle Und Festkörper* (Springer, 2010).
21. J. Mertz, *Introduction to Optical Microscopy* (Roberts and Company Publishers, 2010).

1. Introduction

Fluorescence microscopy is a well-established method in life science. Unfortunately, its resolution is fundamentally limited by diffraction and details that are smaller than the diffraction limit are unresolved. The resolution of a classical microscope is defined by $\sin(\theta)\lambda/(2n)$ in the lateral plane and $(1-\cos\theta)\lambda/n$ in the axial direction [1]. There are several methods to improve the resolution of wide-field microscopy [2–7].

One of them is structured illumination microscopy (SIM). Here, a periodically modulated illumination pattern is projected into the sample. The whole region of interest is acquired in one image. Thus, SIM has the capability of super resolution with high frame rates even in a large region of interest (ROI), because it is a wide-field technique.

In SIM, objective information with a high spatial frequency is down-modulated by the frequency of the illumination grating in the Fourier domain. Thus, frequencies higher than the Abbe limit can be shifted into the pass-band of the optical transfer function (OTF) and are transferred by the microscope. The resolution enhancement is limited to a factor of two, in the case where the illumination grating itself is generated by the objective [8,9]. Several raw images for different pattern positions as well as image processing are necessary to undo the frequency modulation and to compute the final high-resolution image out of the raw SIM images [10]. This procedure has to be repeated in several directions because the down modulation is along one direction only. If a living cell moves between individual raw images, the reconstruction will exhibit artifacts. The shorter the acquisition time, the fewer motion artifacts will be in the final image.

The reconstruction algorithm needs precise knowledge about the shape of the illumination pattern. In our setup a sinusoidally modulated pattern is used. This is achieved by the interference of two plane waves (two-beam interference) originating from two focused spots in the back focal plane (BFP) of the objective. These are the plus and minus first diffraction orders of a grating positioned in an intermediate image plane. As a result, the fundamental sinusoidal component of the diffraction grating is projected into the sample plane.

Lateral and axial resolution can be further enhanced by illuminating with different patterns. If the zero diffraction order is also used (three-beam illumination), the illumination pattern is modulated additionally along the axial direction. With this illumination, axial and lateral resolution can be improved by a factor of two compared to wide-field. Furthermore, optical sectioning is achieved by filling the missing cone.

Further improvements have been made to the SIM technique by the invention of non-linear SIM (NL-SIM) [11]. In this case, saturation processes lead to an effective sub-diffraction illumination grating, thus enabling only noise limited resolution. Rego *et al.* have demonstrated a resolution of 50 nm for fixed nuclear pore complexes [12]. However, the

number of raw images necessary for the reconstruction is increased nearly by one order of magnitude. Therefore, acquisition speed and frame rate are substantially decreased.

Current Fast-SIM setups achieve an accurate illumination pattern and precise phase stepping, by controlling the illumination beam and using a number of active components [13]. These include a spatial light modulator (SLM) for pattern stepping, an active pupil aperture for blocking unwanted diffraction orders and an active polarization rotator for ensuring high pattern contrast. All of these need a precise characterization, before the challenging alignment can be done. Some devices are not commercially available but are custom-built. Additionally, synchronization is necessary. Based on the advanced setup by Fiolka *et al.* [13], we replaced complex active devices by unsophisticated passive components. Therefore, our setup needs less synchronization and is simplified.

The speed of our system makes it an ideal candidate for NL-SIM. We discuss if our newly introduced components can theoretically fulfill the more stringent demands of NL-SIM.

Although SIM is a wide-field technique, it is slower than conventional microscopy because several raw images for different illumination patterns have to be acquired. Shifting and rotating the projected grating by moving the diffraction grating in the intermediate image plane itself is time-consuming. In commercial systems, like the Elyra S.1 (Zeiss, Germany), it takes approximately 1.4 s to acquire a single plane 2D high resolution image (512×512 pixel; three-beam illumination) [14]. Thus, it is prone to motion artifacts and it is impossible to record biological processes which happen in less than a second.

Kner *et al.* published a method to reduce the acquisition time by producing the gratings with a SLM. The SLM can switch faster and more precisely between two different illumination grating positions than a physical grating, because the displayed pixel values simply has to be changed [15]. However, replacing the diffraction grating with the SLM is complex. Some additional elements have to be inserted to the setup to remove the drawbacks [16].

The grating displayed on the SLM is pixelated and binary. Therefore, its Fourier transform exhibits more than the two desired first diffraction orders. To have a sinusoidal illumination pattern in the sample, the additionally appearing ‘unwanted orders’ have to be blocked in a pupil plane. The approach from Fiolka *et al.* is a “rotating-slit”. It is a narrow mechanical slit, centered on the zero order. The slit is rotated to the direction of the first orders so that they can pass. The filtering always works perfectly because the patterns displayed on the SLM are designed in such a way that no unwanted order can lie on the slit, as theory shows. The drawbacks of the slit are that it is not commercially available, needs to be synchronized and consumes 1.5 ms to rotate to the next direction [13].

A second issue is that only the azimuthally polarized components of the two beams interfere and form a grating. The rest forms an offset and is lost for the application of SIM. The interference of azimuthally polarized orders never has an offset and has therefore a perfect contrast and the best signal-to-noise ratio (SNR) for all grating directions. Unfortunately, the diffracted orders from the SLM all have the same linear polarization [16]. Fiolka *et al.* used an active “polarization-rotator” (SWIFT, Meadowlark, USA) to rotate the polarization in each order into the specific direction. The device needs a very precise adjustment, synchronization and ~ 1 ms to get ready for the next polarization direction [13].

Polarization-rotator and rotating-slit perform very well in practice. Both devices correct the drawbacks of the SLM and lead to a sinusoidally modulated illumination pattern of high contrast [13].

2. Materials and methods

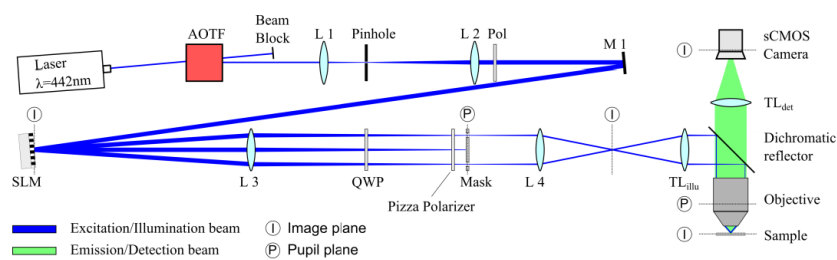


Fig. 1. The AOTF switches the illumination beam on and off. Mode cleaning and beam expansion is performed by the lenses L1 & L2 and a pinhole. The SLM is illuminated and the light is diffracted into different orders. L3, L4, the illumination tube lens and the objective project the grating from the SLM in the sample plane. A “pizza polarizer” and a mask accomplish a sinusoidal illumination grating of high contrast in the sample. Emitted light goes through the dichromatic reflector and is imaged with the detection tube lens to the sCMOS camera

We have built a simple Fast-SIM setup, as depicted in Fig. 1. The design is a simplified version of the setup of Fiolka *et al.* [13]. The excitation laser (442 nm/70 mW) is controlled by an acousto-optic tunable filter (AOTF_nC-VIS, AA Opto-Electronic, France). A beam collimator consisting of a pinhole ($\varnothing = 25 \mu\text{m}$, Thorlabs, USA) and two lenses ($f_1 = 35 \text{ mm}$ and $f_2 = 100 \text{ mm}$, Thorlabs, USA) achieves mode cleaning and beam expansion.

The SLM (ferroelectric LCOS, SXGA-3DM, Forth Dimension Displays, UK) is placed in an image plane. It displays a grating which diffracts the light [16]. Section 2.1 explains the grating properties and how the precise patterns are calculated, based on ideas from Shao *et al.* [17]. In theory a perfect binary phase grating diffracts $\sim 80\%$ of the light into the first orders [18]. We measured the reflectivity of the SLM to be only 46% in the all-on state. The SLM is designed to work in reflection akin to a $\lambda/2$ plate (at 532 nm) rotating its c-axis by ~ 35 degrees. At ± 17 degrees c-axis rotation this yields a light efficiency of only 33% predicting $\sim 12\%$ overall efficiency. Finally we operated the device at 442 nm, far from its design wavelength explaining the observed low overall efficiency of 3% of the light in the first orders.

A polarizer in the illumination beam (22 CA 25, Comar, UK) ensures that the diffracted orders are also linearly polarized [16]. This is necessary for the subsequent polarization control. The beam illuminates the SLM under an angle of incidence of 2° . This separates the diffracted beams from the illumination beam. A beam splitter is not required [15]. In the setup, the beam diameter is roughly one third of the shorter side of the SLM. This ensures that the beam does not illuminate the scattering mounting of the SLM. On the other hand, the beam is big enough to illuminate a large field of view in the sample.

The spatial frequency domain of the displayed grating is projected into the BFP of lens 3 ($f_3 = 750 \text{ mm}$, Thorlabs, USA). Here we use a mask to block unwanted orders (see section 2.1). It is a fixed cardboard with six little holes at the positions of the desired first diffraction orders [15]. We verified in a simulation that no unwanted orders can pass the mask through one of the holes. Thus, our mask filters as efficiently as the rotating slit. But unlike the rotating slit can only accommodate the diffraction orders for a single fixed wavelength. However, using the mask saves effort and time. Two passive optical components guarantee azimuthally polarized light. The first one is a quarter wave plate (QWP), which realizes circular polarization in all diffraction orders. The second element is a customized patterned polarizer (Codixx, Germany). Twelve identical angular polarizers are glued together to the nearly azimuthal polarizer of Fig. 2. The transmission axis of each individual section is parallel to its chord. Because of its shape, we termed it “pizza polarizer”. Six segments are usually sufficient for SIM. Nevertheless, we are using twelve segments for increased

flexibility and to enable subsequential Nonlinear-SIM experiments. The pizza polarizer is located close to a pupil plane where the diffraction orders are focused and traverse the right segment. To avoid scattering of unwanted orders on the glue which connects two segments, the pizza polarizer should be located behind the mask. Due to a lack of space we had to place them the other way round. However, we saw no negative effect of this order in the experiment. Half of the light is lost using this combination of QWP pizza polarizer. However, it is easy to adjust, does not require any synchronization, control or loading time.

Lens 4 ($f_4 = 150$ mm, Thorlabs, USA) and the illumination tube lens ($f_{TL-illu} = 125$ mm, Thorlabs, USA), image the pupil plane into the BFP of the objective. The objective (Plan-Apochromat $\times 63/1.4$ oil DIC, Zeiss, Germany) generates the two-beam interference in the sample plane. The grating constant in the sample is 193 nm. The field of view in sample space is $19.5 \times 13.8 \mu\text{m}^2$. The emitted fluorescent light is imaged by the objective and the detection tube lens ($f_{TL-det} = 164.5$ mm, Zeiss, Germany) onto a modern camera with sCMOS technology and fast readout (Orca Flash 2.8, Hamamatsu, Japan). We run the camera in the 'global exposure level trigger' mode, which operates with a time-saving permanently opened shutter. The AOTF prevents the camera from being illuminated during readout.

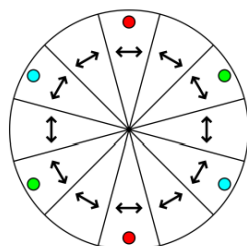


Fig. 2. Twelve circular segments of linear polarizers form one azimuthally polarizer – termed pizza polarizer. The position of the two first orders is shown for each grating direction in different colors.

Camera, AOTF and SLM are synchronized by a microcontroller (Arduino Uno, Arduino, Italy). Thus, for each raw image, the same sample area is illuminated with a different grating. The camera integrates when the SLM displays a grating. The SLM can display a grating only up to 2 ms. Keeping its liquid crystals longer in one state lead to accumulation of ions on the electrodes and the long-term destruction of the device. Thus the SLM had to display a grating and its inverse successively before loading the next grating [19], which is automatically ensured by the SLM driver software. In case of two-beam illumination, the grating and its inverse lead to the same projected pattern in the sample. Therefore, each raw image is illuminated by both. The AOTF switches off the illumination beam while the SLM is loading a grating image which takes ~ 0.434 ms.

Due to the losses in the optical components, foremost the SLM, less than 1% of the laser output intensity reaches the sample. Additionally, the laser wavelength of 442 nm is not at the excitation maxima of the used fluorophores (470 - 490 nm). Thus, an exposure time of 8 ms per raw image was necessary to have an acceptable SNR in the image. Therefore, the SLM displays each grating four times for 2 ms (two positive-negative image pairs). Furthermore, the SLM displays a non-illuminated grating during the readout of the camera. The SLM runs continuously to avoid unpredictable time delays when it starts or stops.

2.1 Grating design (after Shao *et al.*)

The gratings used in the experiments are designed and characterized based on the ideas from Shao *et al.* [17]. Figure 3 shows an example grating. White pixels are in the on state and black pixels are off. The 2D periodic pixel pattern forms a grating.

The theory of crystal structures with lattice vectors is suitable to describe the patterns [20]. The lattice points are marked in red. The lattice vectors \vec{a} connect two lattice points. Two different lattice vectors describe the two-dimensional grating pattern P completely:

$$P = \{\vec{a}_H; \vec{a}_\theta\} \quad \text{with} \quad \vec{a}_H = \begin{pmatrix} h \\ 0 \end{pmatrix} \quad \text{and} \quad \vec{a}_\theta = \begin{pmatrix} \theta_x \\ \theta_y \end{pmatrix} \quad (1)$$

The lattice vector \vec{a}_H is always horizontal and defines the horizontal grating period. The grating direction is only defined by \vec{a}_θ (see blue dotted line in Fig. 3). The range of search for a useful grating is given by:

$$\begin{aligned} h &\in \{1, 2, \dots, h_{\max}\} \\ \theta_x &\in \{1, 2, \dots, \theta_{x_{\max}}\} \\ \theta_y &\in \{-\theta_{y_{\max}}, -\theta_{y_{\max}} + 1, \dots, \theta_{y_{\max}} - 1, \theta_{y_{\max}}\} \end{aligned} \quad (2)$$

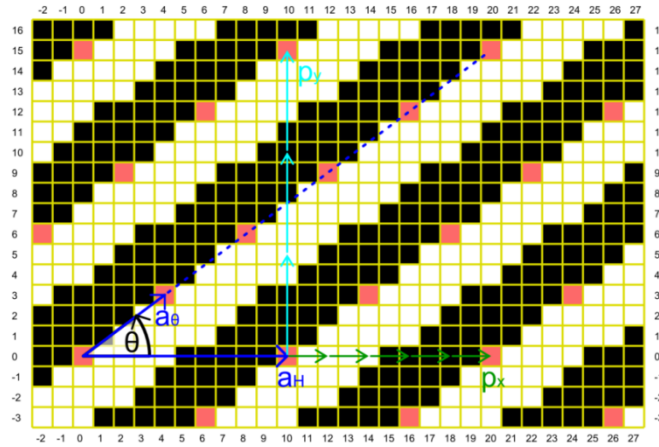


Fig. 3. Grating on a SLM. White and red pixels are on, black pixels are off. The red pixels are lattice points, which are connected by the lattice vectors \vec{a}_θ and \vec{a}_H . The grating direction θ is only defined by \vec{a}_θ . The grating constant has to be calculated with both lattice vectors. Five equidistant phase steps (three-beam illumination) are provided by a horizontal shift (green). Three such phase steps (two-beam illumination) are done vertically (cyan).

The characteristic grating parameters, orientation θ and grating period g , can be calculated with:

$$\theta(P) = \theta(\vec{a}_\theta) = \begin{cases} \frac{\pi}{2} & \text{for } \theta_x = 0 \\ \arctan\left(\frac{\theta_y}{\theta_x}\right) \in [0, \pi] & \text{for } \theta_x \neq 0 \end{cases} \quad (3)$$

$$g(P) = g(\vec{a}_H, \vec{a}_\theta) = h \sin(\theta) \quad (4)$$

Three gratings P form a triplet $T = \{P_1; P_2; P_3\}$. A brute-force algorithm searches systematically for three matching gratings. Therefore, the triplet has to pass three tests before being accepted.

1. The angles $\alpha(T)$ between the gratings must be close to 60° . We accept a triplet if the angular deviation is smaller than 5° :

$$\alpha(T) = \{|\theta(P_1) - \theta(P_2)|; |\theta(P_1) - \theta(P_3)|; |\theta(P_2) - \theta(P_3)|\} \quad (5)$$

$$\Delta\alpha(T) = \max\{\alpha(T) - 60^\circ\} < 5^\circ$$

2. All three grating constants should be similar. To check this, we define the average grating constant of the triplet $\bar{g}(T)$. The mismatch $\Delta g(T)$ between a single grating constant and this average value has to be smaller than 2%:

$$g(T) = \{g(P_1); g(P_2); g(P_3)\} \quad (6)$$

$$\bar{g}(T) = \frac{\max(g(T)) + \min(g(T))}{2} \quad (7)$$

$$\Delta g(T) = \frac{\max\{\bar{g}(T) - g(T)\}}{\bar{g}(T)} < 2\% \quad (8)$$

3. The mask, as a Fourier filter in the experiment, can only operate if no unwanted order is at the position of any desired first diffraction order. Therefore, we calculate the Fourier transform of all three gratings and assign each of them to one channel of a RGB-image. A gamma correction of 0.3 is applied to enhance the visibility of the weaker unwanted orders. Six yellow circles around the first diffraction orders represent the holes in the mask. Our algorithm maximizes the diameter of the holes, such that no unwanted orders fall in the circles – see Fig. 4. The triplet with the largest circle, passing tests 1 and 2, is finally used in our experiment. The white spot in the middle is the zero order.

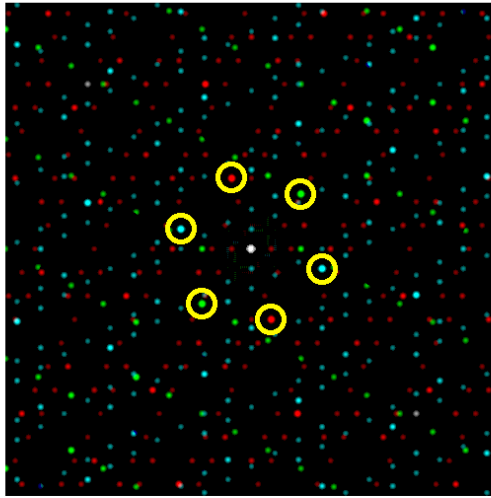


Fig. 4. All three Fourier transforms of the gratings in one RGB image. The yellow circles represent the holes in the mask. The triplet is useless if unwanted orders are in the circle. Gamma correction of 0.30 is applied for a better visibility.

An additional step can test the possibility of homogeneous phase steps. In this case, the intensity patterns of all grating steps add up to a homogeneous distribution. Thus the

illumination beam does not bleach any grating into the sample in time. We found out that homogeneous phase steps occur, when h or θ_y are multiples of the number of phase steps. Unfortunately, this advantage significantly reduces the number of matching gratings a lot. We do not have homogeneous phase step because it is not necessary for the reconstruction algorithm and our laser is not powerful enough to bleach a grating into the sample.

In our experiment we used the following three grating parameters (see Table 1):

Table 1. Grating Parameters of Three Different Gratings Separated by $\sim 60^\circ$

	Grating 1	Grating 2	Grating 3
h [Px]	7	10	25
θ_x [Px]	7	10	25
θ_y [Px]	25	-9	7
$\bar{g}(T)$ [Px]	$6.72 \pm 0.03 \rightarrow \Delta g(T) = 0.4\%$		
$\bar{g}(T)$ [μm]	91.5 ± 0.4		
θ [°]	74.4	138.0	15.6
$\alpha(T)$ [°]	63.6	57.6	58.8

In comparison to Shao *et al.* [17] our gratings have almost the same amount of on and off pixels, which leads to a higher diffraction efficiency.

2.2 Future grating design (after Fiolka *et al.*)

The new gratings are designed and characterized based on the ideas from Fiolka *et al.* and intended for NL-SIM [13]. Figure 5 shows an example grating. White and red pixels are in the on state and black pixels are off. Two lattice vectors completely describe the two-dimensional grating pattern P :

$$P = \{\vec{a}_H, \vec{a}_\theta\} \quad \text{with} \quad \vec{a}_H = \begin{pmatrix} h_x \\ h_y \end{pmatrix} \quad \text{and} \quad \vec{a}_\theta = \begin{pmatrix} \theta_x \\ \theta_y \end{pmatrix} \quad (9)$$

There exist more gratings to choose from, because \vec{a}_H is not restricted anymore to be horizontal. Grating orientation θ and period g can be calculated with:

$$\theta(P) = \theta(\vec{a}_\theta) = \begin{cases} \frac{\pi}{2} & \text{for } \theta_x = 0 \\ \arctan\left(\frac{\theta_y}{\theta_x}\right) \in [0, \pi] & \text{for } \theta_x \neq 0 \end{cases} \quad (10)$$

$$g(P) = \sqrt{h_x^2 + h_y^2} \left| \sin(\theta(\vec{a}_\theta) - \theta(\vec{a}_H)) \right| = \frac{h_x \theta_y - h_y \theta_x}{\sqrt{h_x^2 + h_y^2}} \quad (11)$$

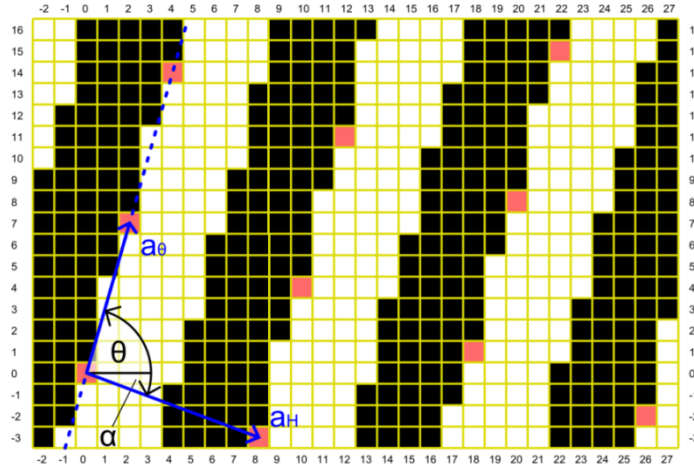


Fig. 5. Grating on the SLM based on Fiolka's approach. White and red pixels are on, black pixels are off. The red pixels are lattice points, which are connected by the lattice vectors \vec{a}_θ and \vec{a}_H . The grating direction is still only defined by \vec{a}_θ . The second lattice vector \vec{a}_H does not have to be horizontal anymore.

The algorithm is extended to six directions. It is still a brute-force algorithm, which searches systematically for the matching gratings. Each sextet $S = \{P_1; P_2; P_3; P_4; P_5; P_6\}$ has to pass four tests before being accepted. The angles $\alpha(S)$ between the gratings have to be close to 30° . We accept a sextet if the angular deviation is always smaller than 1° . All six grating constants should be similar. We define the average grating constant of the sextet $g(S)$ again as the mid-range value. The mismatch $\Delta g(S)$ between a single grating constant and this average value has to be smaller than 1%. The algorithm automatically checks if a mask can block all unwanted orders. A square of several pixels is defined around each first order. The intensity of all unwanted orders in this square is summed and compared to that of the first order. The sextet is rejected if the intensity of the first order is not at least 100 times that of the unwanted orders.

Homogeneous phase steps are favorable in non-linear SIM because the saturation processes might lead to bleaching artifacts. Seven phase steps enable the reconstruction of the first and second higher-order harmonic to double the lateral resolution of SIM [12]. We check if either a horizontal or vertical phase step is possible (*mod* – modulo and *lcm* – least common multiple):

Vertical phase step test ($\theta_x \neq 0$ required):

$$\begin{aligned}
 & \text{If:} \\
 & h_x = 0: \quad h_y \bmod 7 = 0 \quad (12) \\
 & \text{Else:} \quad \left(\text{lcm}(|h_x|, |\theta_x|) \frac{\theta_y}{\theta_x} - \frac{h_y}{h_x} \right) \bmod 7 = 0
 \end{aligned}$$

Horizontal phase step test ($\theta_y \neq 0$ required):

$$\begin{aligned}
 & \text{If:} \\
 & h_y = 0: \quad h_x \bmod 7 = 0 \\
 & \text{Else:} \quad \left(\text{lcm}(|h_y|, |\theta_y|) \frac{\theta_x}{\theta_y} - \frac{h_x}{h_y} \right) \bmod 7 = 0
 \end{aligned} \tag{13}$$

The sextet we used for our first experiments is in Table 2:

Table 2. Grating Parameters of Six Different Gratings Separated by $\sim 30^\circ$

	Grating 1	Grating 2	Grating 3	Grating 4	Grating 5	Grating 6
θ_x [Px]	1	13	24	27	21	13
θ_y [Px]	-27	-21	-13	1	13	24
h_x [Px]	2	12	7	4	14	6
h_y [Px]	23	-14	-7	3	12	17
$g(S)$ [Px]	2.850	2.834	2.821	2.850	2.834	2.821
$\overline{g(s)}$ [Px]	$2.835 \pm 0.015 \rightarrow \Delta g(S) = 0.6\%$					
$\overline{g(s)}$ [μm]	38.61 ± 0.21					
θ [$^\circ$]	2.12	31.76	61.56	92.12	121.76	151.56
$\Delta\alpha(S)$ [$^\circ$]	29.64	29.80	30.56	29.64	29.80	30.56

3. Results

We took a picture of a plane close to the pupil plane with a simple web camera from the side (Fig. 6). The picture is intentionally overexposed to aid the visibility of the dim but disturbing undesired orders. The left side shows this plane without any filtering. The unwanted orders are clearly visible. The right image shows the same plane after insertion of the mask. No unwanted orders pass the mask through one of its six holes making it suitable for all three grating directions. The simple idea of a mask works quite well.

We illuminated a 110 nm beads sample with the grating. Figure 7 shows the image of one single bead. While shifting the grating laterally, we observed that the emission is bright when a bead is on a maximum intensity (left) and very dim when it is at the minimum (right). The measured modulation depth is 80% at a bead size of 110 nm. Note that the bead is not completely extinguished on the right because it is wider than the dark fringe itself, and therefore still slightly excited.

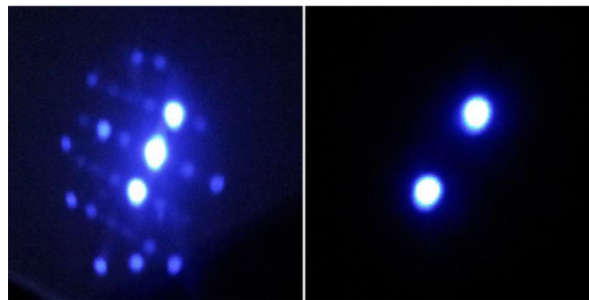


Fig. 6. Illumination orders close to the pupil plane after the order selection mask with and without the mask. Left: Unwanted orders are present. Right: The used mask blocks unwanted orders except the first orders.

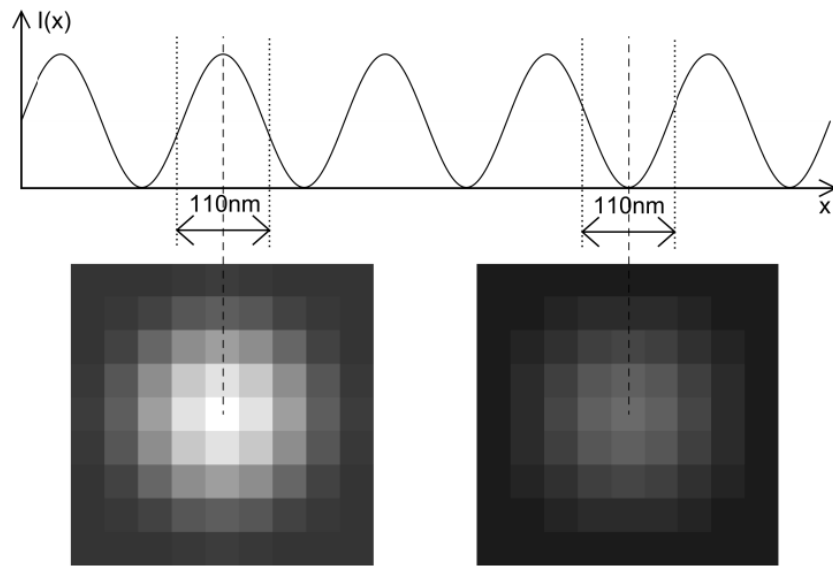


Fig. 7. 110 nm bead with different brightness resulting from the high illumination grating contrast (left: maximum, right: minimum). The gray values are non-linear ($\gamma = 0.4$).

To demonstrate and characterize the performance of our Fast-SIM system in practice, we imaged a sample consisting of 110 nm fluorescent beads. Figure 8 shows a comparison of conventional wide-field microscopy with SIM, which has a clearly improved lateral resolution (for a fair comparison, linear image deconvolution has been applied to both images [21]). Figure 9 shows a profile along the yellow line in Fig. 8. SIM clearly resolves the three beads on the right (green), while they are nearly unresolved in wide-field (blue dotted). On top of that, edges are steeper in SIM than in wide-field.

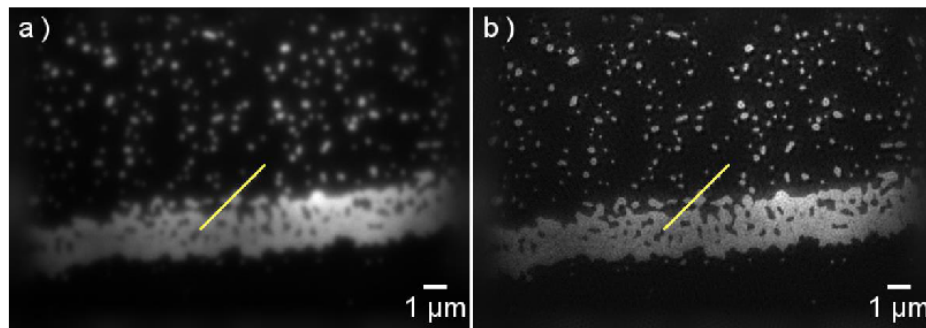


Fig. 8. Comparison of wide-field (a) and SIM (b) with a 110 nm bead sample

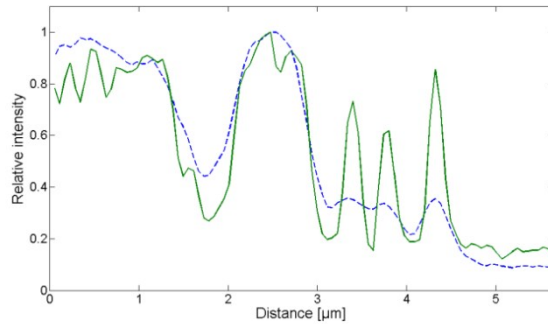


Fig. 9. Wide-field (blue dotted) and SIM (green) profile along the yellow line from Fig. 8 beginning at the left bottom.

50 beads that appear bright and well-isolated in wide-field and SIM were selected in both wide-field and SIM images to determine the full width at half maximum (FWHM) of the effective PSF (Fig. 10). This average bead size in wide-field image has an FWHM of 224.8 ± 21.2 nm. In SIM, the FWHM is reduced to 114.2 ± 9.5 nm. The enhancement could be improved further, by bringing the grating constant (currently 193 nm) closer to the diffraction limit ($\lambda_{ex} / (2 \times \text{NA}) = 442 / (2 \times 1.4) = 158$ nm).

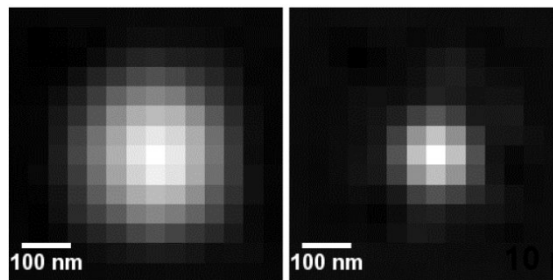


Fig. 10. Average point spread function of wide-field (left) and SIM (right) from Fig. 8

The acquisition time for one raw image is 14.6 ms, i.e. 68.5 frames per second (fps). This figure of the raw data rate has to be divided by the total number of acquired images, here nine, to get the final high-resolution imaging rate of 7.6 fps. The setup is ten times faster than the commercial system Elyra S.1, which provides 0.7 fps.

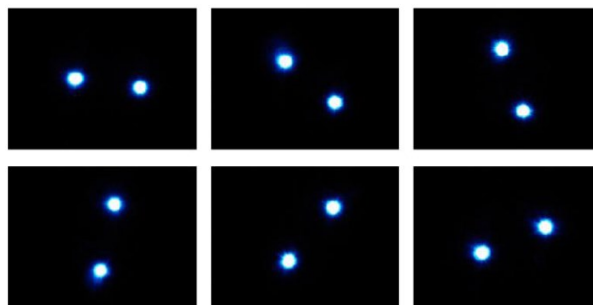


Fig. 11. Six different grating directions filtered by a mask in a pupil plane. All unwanted orders are blocked.

4. Discussion

We have built a Fast-SIM system which uses passive and unsophisticated components for selecting the illumination orders and controlling their polarization. The use of a passive mask for order selection requires the calculation of unique grating patterns, which guarantees the separation of wanted from unwanted orders between all orientations. Since we have found a triplet of matching gratings, our mask perfectly filters the illumination beam and made the rotating slit method superfluous. However, a rotating slit has potential advantages when working with multiple wavelengths as otherwise the holes in our mask will have to be elongated or repeated for each wavelength leading to potential unwanted order crosstalk. The “pizza polarizer” guarantees in a very simple way for an illumination pattern of high contrast for all directions. Exposure time or laser power has to be increased because of overall low transmittance. The light efficiency of the polarization rotator (>90% according to the manufacturer’s specification) is above our pizza polarizer, which is bound to have a theoretical transmittance of below 50% when illuminated with circular polarization. The greatest advantage using a mask and a pizza polarizer is simplifying the system setup and synchronization.

The exposure time of 8 ms per raw image is still comparatively long. The main reason is that our excitation wavelength does not match the excitation maximum of the fluorophores. The exposure time could be reduced significantly by using a 488 nm laser. On the other side, the exposure time for cell imaging is usually 2-10 times longer than for beads.

5. Outlook

The setup can be expanded to a nonlinear SIM system. Rego *et al.* used nine grating directions to achieve an isotropic resolution of 50 nm [12]. We think that using six directions will be sufficient for this purpose. We therefore extended our grating search algorithm by three directions. Additionally, we updated the grating design for even smaller and more precise gratings [13]. We found six gratings which can be filtered by a mask (see Fig. 11) and have a grating period of roughly 39 μm on the SLM (reduction of 58%). This will enlarge the ROI over five times and the system will be shortened by the higher diffraction angle on the SLM. The deviations from the desired 30° angle ($180^\circ / 6$ directions) are less than 1°. The algorithm and the new gratings are attached in section 2.2. NL-SIM needs a high illumination contrast [12]. This can be provided by our pizza polarizer with 12 segments. With further improvement in system efficiency and laser power, we expect the system to be suitable for non-linear SIM experiments using photo-switchable fluorophores.

To expand the current system to 3D-SIM the zero order has to pass the order selection mask. This is achieved by another hole at its center. However, the required rotation of the linear polarization in the zero order cannot be achieved with the passive pizza-polarizer. The manufacturer Codixx of our pizza polarizer also provides a version where the center does not modify the polarization state. Thus 3D SIM is possible with this passive device at a 50% loss of contrast of the 1st intensity order when the zero order stays circularly polarized, whereas the 2nd intensity order remains at 100% contrast.

The use of passive components for order selection and polarization control significantly simplifies the setup. In order to facilitate the construction of such a home-built system for other labs, we provide detailed instructions on how to synchronize the remaining components and generate patterns suitable for passive filtering in section 2.1 and 2.2.

Appendix

A. SLM software

Our SLM (SXGA-3DM) is controlled via the Software MetroCon 2.0 from ForthDD. First, the user has to upload his gratings. Afterwards, a schedule (called ‘repertoire’) has to be created, which defines the succession of the gratings and how long they are displayed. These

repertoires can be saved as a 'repz' file. It is a simple zip file which includes the gratings (in png-format), their schedule and some internal files which define exposure time and trigger behavior. If many gratings or complicated schedules are required, it might be useful to produce this repertoire by hand instead of using the slow MetroCon2.0.

B. How to rebuild the Fast-SIM

We believe that our Fast-SIM setup is an easy-to-reproduce solution to whoever wants to build a high-resolution microscope for imaging of biological samples. This is why we indicate here a short manual and made our files for SLM and Arduino online available.

How to connect the devices (see also Appendix C with Fig. 12):

1. Connect the SLM via USB to a PC
2. Connect wires to J3 port of the SLM (20 way, 2 rows, Molex, 2.54 mm Pitch)
 - a. Solder load resistor on the SLM input signal and the ADUM (quad-channel digital isolator – ADUM 1402 (Analog Devices, Norwood, USA)) on the SLM output signal
- b. Connect the cables to the specified Arduino pins
3. Connect the Camera to the PC and the trigger in and output via an BNC cable to the Arduino
4. Connect the AOTF control device to the power supply and the two signal cables to the Arduino
5. Connect the AOTF itself and its control unit to the control box

Settings/Programs:

1. Arduino

Load the attached program to the Arduino ("ArduinoCode"). The software for uploading is available at www.ardunio.cc.

2. SLM

Starting the SLM with MetroCon 2.0 and upload our repertoire (" {25 10 7; 7 -9 25}_phases_3_rep_3.repz")

3. Camera:

- a. We used "HC image live" from the company to use the camera
- b. Chose external "Level trigger mode" → "Global exposure level trigger mode"
- c. Set the polarity of in- and output signals to "positive"

Mask

Fix a stable cardboard on a holder and put it in the pupil plane of the SLM. Mark with a pen the position of the first orders. Take the cardboard out and prick it with a needle at the marked positions. Use a sharp knife to remove the burr from the backside of the cardboard.

Hints

A logic analyzer (Saleae, San Francisco, CA, USA) is helpful to understand, debug and repair the electronic circuit. Camera and the laser switch can be replaced by other models. However, it is important to remember that the Arduino operate with 5V logic. Changing the repertoires might require changing the Arduino code and vice versa.

C. Electronic circuit

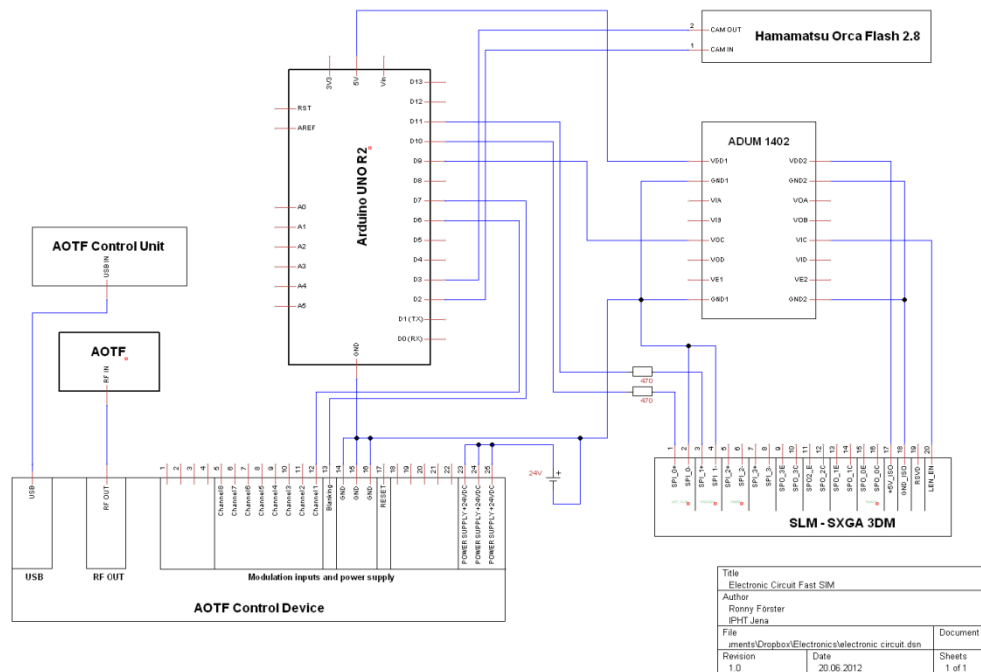


Fig. 12. Electronic circuit to synchronize SLM, Camera and AOTF with an Arduino.

D. Overview over the online available files (<https://github.com/nanoimaging/Appendix-E>)

File/Folder name	Info
ArduinoCode	Arduino code for synchronization of Fast-SIM system
[25 10 7;7 -9 25]_phases_3_rep_3	Repz file for the SLM with our gratings Load it in MetroCon and send it to the SLM
repertoire	Used gratings, sequences and schedule for SIM
electronic circuit	Used electronic circuit for connecting the devices
gratings NL SIM	New gratings for NL SIM

Acknowledgments

We thank Robert Kretschmer for the technical support.

Publication 2

fastSIM: a practical implementation of fast structured illumination microscopy

Lu-Walther H-W, Kielhorn M, Förster R, Jost A, Wicker K, Heintzmann R.

[HWLW2] Lu-Walther H-W, Kielhorn M, Förster R, Jost A, Wicker K, Heintzmann R. fastSIM: a practical implementation of fast structured illumination microscopy. *Methods and Applications in Fluorescence*. 2015; 3: 014001. doi: <http://dx.doi.org/10.1088/2050-6120/3/1/014001>

Beteiligt an (*Zutreffendes ankreuzen*)

Author	Lu-Walther H-W
Konzeption des Forschungsansatzes	×
Planung der Untersuchungen	×
Datenerhebung	×
Datenanalyse und -interpretation	×
Schreiben des Manuskripts	×
Vorschlag Anrechnung Publikationsäquivalente	1,0

All authors revised, edited and proof read the final manuscript.

Reprinted with kind permission from the *IOP Publishing*.

Copyright © IOP Publishing. Reproduced with permission. All rights reserved.

fastSIM: a practical implementation of fast structured illumination microscopy

This content has been downloaded from IOPscience. Please scroll down to see the full text.

View [the table of contents for this issue](#), or go to the [journal homepage](#) for more

Download details:

IP Address: 141.35.29.154

This content was downloaded on 04/01/2016 at 10:24

Please note that [terms and conditions apply](#).

Methods and Applications in Fluorescence



PAPER

fastSIM: a practical implementation of fast structured illumination microscopy

RECEIVED
26 June 2014

REVISED
24 September 2014

ACCEPTED FOR PUBLICATION
13 October 2014

PUBLISHED
16 January 2015

Hui-Wen Lu-Walther¹, Martin Kielhorn¹, Ronny Förster¹, Aurélie Jost^{1,2}, Kai Wicker^{1,2,3} and Rainer Heintzmann^{1,2,4}

¹ Leibniz Institute of Photonic Technology, Jena, Germany


² Institute of Physical Chemistry, Abbe Center of Photonics, Friedrich-Schiller-University Jena, Jena, Germany

³ Carl Zeiss AG, Corporate Research and Technology, Carl-Zeiss-Promenade 10, 07743 Jena, Germany

⁴ King's College London, Randall Division of Cell and Molecular Biophysics, London, UK

E-mail: heintzmann@gmail.com

Keywords: structured illumination microscopy, superresolution, fluorescence microscopy, spatial light modulators, liquid-crystal devices

 Online supplementary data available from stacks.iop.org/MAF/01/014001

Abstract

A significant improvement in acquisition speed of structured illumination microscopy (SIM) opens a new field of applications to this already well-established super-resolution method towards 3D scanning real-time imaging of living cells. We demonstrate a method of increased acquisition speed on a two-beam SIM fluorescence microscope with a lateral resolution of ~ 100 nm at a maximum raw data acquisition rate of 162 frames per second (fps) with a region of interest of $16.5 \times 16.5 \mu\text{m}^2$, free of mechanically moving components. We use a programmable spatial light modulator (ferroelectric LCOS) which promises precise and rapid control of the excitation pattern in the sample plane. A passive Fourier filter and a segmented azimuthally patterned polarizer are used to perform structured illumination with maximum contrast. Furthermore, the free running mode in a modern sCMOS camera helps to achieve faster data acquisition.

1. Introduction

Wide-field fluorescence microscopy offers minimally invasive observation of dynamic processes within cells and is an essential tool for studying biological samples. Unfortunately, the resolution of an optical microscope is fundamentally limited by diffraction and hence, finer details stay invisible [1]. A conventional wide-field fluorescence microscope generally has a lateral resolution of ~ 230 nm. The axial resolution is even lower and is approximately 1000 nm. Several approaches have been demonstrated which overcome this barrier and thus enhance the resolution [2].

Stimulated emission depletion (STED) microscopy promises a lateral resolution of 20 nm, thanks to a process of doughnut-shaped de-excitation around the center of the excitation beam [2]. An improved axial resolution has been demonstrated by introducing several approaches, e.g. implementing a confocal pinhole or using a phase plate pair to achieve an axial-doughnut [3]. 4Pi-STED microscopy gives an axial resolution of 30–50 nm [4]. However, since STED is a point-scanning method, enlarging the region of interest (ROI) would dramatically decrease the acquisition speed. Moreover,

high illumination intensity is needed. A commercially available system delivers a spatial resolution of 50–70 nm (Leica TCS STED, Leica Camera AG, Wetzlar, Germany [5]).

A different approach to high resolution is localization microscopy. With this technique fluorophores are imaged individually and the central position of a single fluorophore is precisely estimated. To create a final image, all fluorophores have to be localized sequentially. Thus, numerous raw images and long acquisition time are required. A commercially available system of the photoactivated localization microscopy (PALM) promises resolutions down to 20 nm laterally and 50 nm axially (Elyra P.1, Zeiss, Jena, Germany [6]).

Linear structured illumination microscopy (LSIM) is a wide-field technique. It provides fast data acquisition with a large field of view at a lateral resolution of ~ 100 nm [7]. A sinusoidal illumination pattern, hereafter referred to as the illumination grating, is projected onto the sample plane. High-frequency object information is down-modulated into the limited support region of the optical transfer function (OTF) [7–9]. Image processing is mostly done in the Fourier space. For reconstructing the high-resolution image, several

raw images with different illumination grating phases are required, in order to separate the different information components. The maximal lateral resolution enhancement is achieved only in the direction of the k -vector of the grating. Hence for near isotropic resolution improvement, the illumination grating has to be rotated into several directions. The grating is typically rotated to 3 orientations, separated by 60° . For each grating orientation, three images at phases 0 , $2\pi/3$ and $4\pi/3$ are recorded in a two-beam SIM system. Based on these images, three object components can be separated. These three components correspond to shifted Fourier object information attached to the zero and the ± 1 st illumination orders. These separated components are shifted in Fourier space such that the zero object frequency coincides with the zero coordinate of Fourier space, adjusted for global phase and joined by a weighted averaging process [10]. This results in an image with approximately twice the region of the support of the effective OTF, hence twice the lateral resolution.

An axially modulated illumination pattern can be produced by three-beam interference. This also allows for a twofold enhancement of the axial region of the support of the OTF. Five images at phases 0 , $2\pi/5$, $4\pi/5$, $6\pi/5$ and $8\pi/5$ are usually required for separating five object components in frequency space. This type of system is generally called a 3D-SIM system [9, 11]. Note that the missing cone which prevents optical sectioning is filled substantially already in a two-beam SIM system by the two higher orders shifting sufficiently inward when not at the very limit (detection) spatial frequency. Thus optical sectioning can also be achieved in a two-beam SIM system (2D-SIM) as ours. If the modulation frequency is close to half the limit frequency this sectioning is optimal, but the lateral resolution gain will only be 1.5.

1.1. Existing SIM systems

The sinusoidal structured illumination pattern is obtained by the interference of two plane waves coming from two beams focused on the periphery of the back focal plane of an objective. Placing a physical grating in an intermediate image plane in a conventional wide-field fluorescent microscope is a straightforward way to build a SIM system. The physical grating diffracts light and forms the required zero and ± 1 st diffraction order beams. However, the acquisition speed and precision in a SIM system using a physical grating is limited by the mechanical movement of the physical grating. With long acquisition time, artefacts may occur through sample drift or the motion of a living cell. It is difficult to record biological processes which happen in the time span of raw image acquisition.

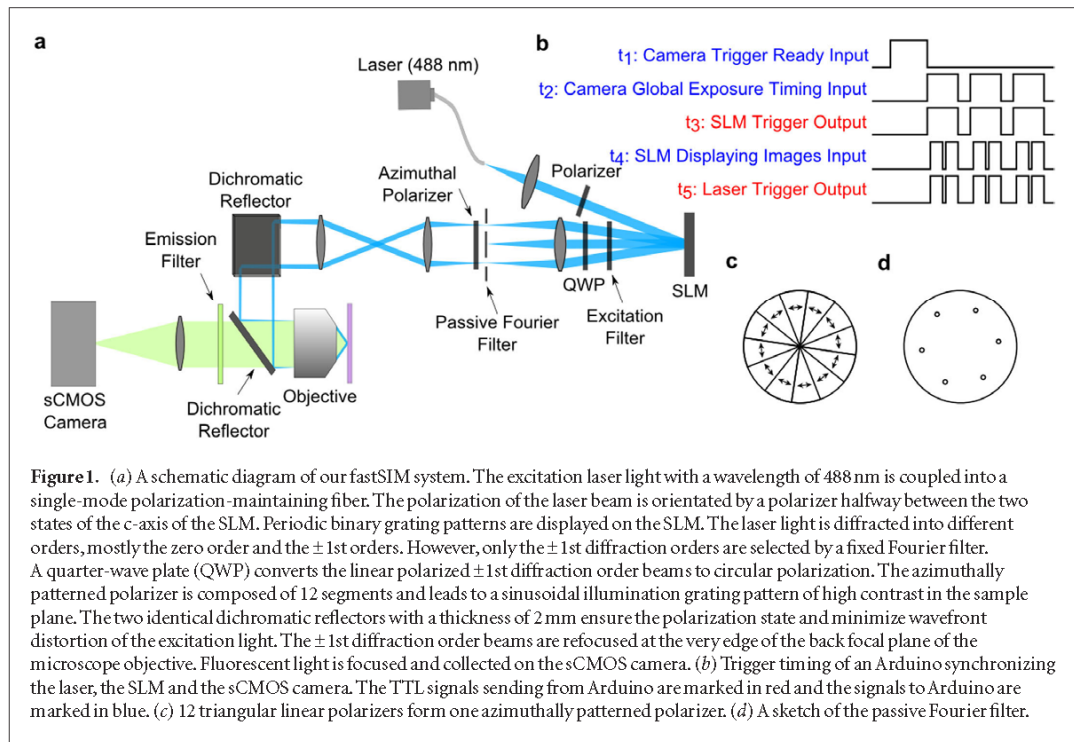
Fiolka *et al* used a ferroelectric spatial light modulator (SLM) to produce gratings and thus sped up the acquisition time. The volume acquisition rate of this SIM system is 1.4 s ($1\ \mu\text{m}$ thickness $\times 51\ \mu\text{m} \times 51\ \mu\text{m}$ [12]). The ferroelectric liquid crystal can be driven at a

frame rate above 1 kHz which allows a fast and precise switching between grating transfers and orientations. However, replacing a physical grating by a pixelated SLM is not trivial and has some trade-off. The pixelated SLM display introduces additional unwanted diffraction orders which deflect illumination laser power and form a jagged edge in the illumination pattern. Using a simple mask or a rotating-slit can filter the spatial frequency spectrum and yield a sinusoidal illumination grating [12, 13]. A rotating-slit is preferable for multi-color applications. However, the mechanical slit requires 1.5 ms for switching between different grating orientations. Additionally, Fiolka *et al* used a liquid crystal cell (SWIFT, Meadowlark, USA) and a quarter wave plate (QWP) as a tuneable polarization rotator to maintain s-polarized light. Thus, maximum illumination grating contrast can be achieved in all grating orientations. This device needs approximately 1 ms for switching the polarization orientation. The adjustment of this device is more challenging, and temperature depended drift of the liquid crystal cell is a problem requiring frequent recalibration. An active component limits the acquisition speed and requires synchronization with other devices. Another possibility of implementing the desired high-contrast grating structure is based on an interferometric scheme, where the two (or three) required orders are generated by splitting light by a beam splitter and tilting them with respect to each other by adjustable motorized mirrors [14]. However, a disadvantage here is the need for mechanical movement which is required for phase shifting (potentially fast) and for changing the pattern direction (slow). A commercial 3D-SIM system using a mirror galvanometer and several physical gratings is available (OMX, Applied Precision, Washington, USA). The acquisition frame rate of the OMX system is 100 fps for an image size of 512×512 pixels [15]. In this paper, we demonstrate the SLM-based improvement of acquisition speed in a conventional two-beam SIM system.

2. Materials and methods

2.1. fastSIM setup

The present fastSIM system is an improved version of the system described in [16]. We plan to expand the fastSIM setup to a non-linear SIM (NLSIM) system. The contrast of the illumination grating in NLSIM is critical for performing high nonlinear photo-response, and consequently determines the lateral resolution enhancement. Thus, a two-beam SIM system becomes our choice, even though a three-beam SIM system provides better optical sectioning. In NLSIM, saturation processes lead to sub-diffraction effective illumination gratings and enable a resolution improvement even better than a factor of two, which is only limited by the non-linearity and photon shot noise and thereby mostly dependent on the fluorophore's switching properties. Gustafsson *et al* demonstrated a resolution of 50 nm with NLSIM. For reconstruction,



around six times more raw images than for a 2D-LSIM image are required [17]. Therefore, the frame rate is further decreased by nearly an order of magnitude.

Considering cost-effectiveness, we built a simple fastSIM setup with fast acquisition but relative low cost (see figure 1(a)). The excitation laser with a wavelength of 488 nm (CW laser, LuxX 488-200 Omicron, Germany) can be switched with 10 ns rise time. Moreover, using a single-mode polarization-maintaining fiber allows multi-colour laser coupling and yields a clean Gaussian beam profile. However, loss of laser intensity in the fiber is a drawback. Later, we use a polarizer to ensure linear polarization after the fiber.

To avoid wavefront distortion and spurious reflections, the laser beam is directed onto an SLM at a small incident angle ($\sim 3^\circ$) instead of using a beamsplitter. Note that a large incident angle leads to a distortion of the illumination grating in the sample plane. The size of the excitation laser beam is a trade-off between illumination intensity and the size of the ROI. Additionally, over-illuminating the edge of the SLM diffracts the light in an uncontrolled manner and should be avoided. In the setup, the FWHM of the illumination beam is roughly one third of the SLM's height. The possible fluorescence from the liquid crystals of the SLM is blocked by a bandpass excitation filter. The SLM (SXGA-3DM, 1280×1024 pixels, Forth Dimension Displays, UK) displays a binary grating pattern that diffracts the light. This ferroelectric SLM is essentially a binary device with two possible orientations of the optical axis with close to $\lambda/2$ retardance in reflection configuration. When the SLM is operated under the design wavelength, i.e. 532 nm, it behaves as a half-wave plate (HWP). As we use it at 488 nm wavelength, the liquid crystal layer

introduces a phase shift φ different from the ideal value of 180° . The zero diffraction order thus has elliptical polarization. However, as long as the input beam is linear polarized, the ± 1 st diffraction orders are independent of this phase shift [18]. Thus, in a two-beam SIM system, the SLM can still work as a HWP, i.e. the ± 1 st diffraction orders are linear polarized, but with reduced diffraction efficiency.

The reflectivity of the SLM is low. Even when all pixels are off (the SLM works like a common mirror), less than half of the light is reflected. When a grating pattern is displayed, only 5% of the incident light is diffracted into the ± 1 st diffraction order beams. The residual 95% of light is discarded before reaching the specimen.

We place a fixed mask as a Fourier filter in the Fourier plane of the SLM. The Fourier filter removes spurious diffraction orders to ensure a perfectly sinusoidal illumination grating in the sample plane. For one illumination wavelength a Fourier filter with six holes is enough (see figure 1(d)). The contrast of the illumination grating in the sample plane is determined by the polarization of the illumination beam. Only the field components polarized in the transversal plane interfere to form the illumination grating. The electric field with axial polarization forms an offset and destroys the signal-to-noise ratio. This effect is critical for objectives with high numerical aperture. We use a QWP and a customized azimuthally patterned polarizer (Codixx, Germany, see figure 1(c)) to achieve an s-polarized beam for all grating orientations. The QWP orientated at 45° converts the linearly polarized ± 1 st diffraction order beams to circular polarization. The azimuthally patterned polarizer is composed of twelve identical segments. As shown in figure 1(c), the arrow in each

individual section indicates the direction of the transmission axis.

We place the azimuthally patterned polarizer close to the Fourier plane of the SLM where the diffraction orders are well separated. The drawback of the azimuthally patterned polarizer is that at least 50% of the light is discarded here. Nevertheless, compared to an active liquid crystal polarization rotator, this device needs no synchronisation and greatly simplifies the system.

The state of the light polarization after being reflected by a dichromatic reflector is determined by s- and p-polarization components. A dichromatic reflector imparts different phases to these two different components. Consequently, it converts a linear polarized beam, at arbitrary polarization (except in s- and p-polarization), to elliptical polarization and diminishes the illumination grating contrast (see figure S1 (stacks.iop.org/MAF/01/014001) in Supplementary Material for experimental data). Two identical dichromatic reflectors can be arranged in 3D such that the second dichromatic reflector compensates for the phase change induced by the first one (previous s- becomes p- and p- becomes s-polarization). The other alternative is using a customized dichromatic reflector which is specifically designed for polarization conservation for all orientations. Moreover, a conventional thin (1 mm) dichromatic reflector is generally bent by its dielectric coating and thus causes wavefront distortion. This wavefront distortion leads to significant aberration in the interference in the sample plane. To avoid this, we use two custom-made identical dichroic reflectors (H488 LPXR, 45 deg., AHE, Germany) both with a substrate thickness of 2 mm.

The two ± 1 st diffraction order beams interfere again after the objective (Plan-Apochromat $\times 63/1.46$ oil, Korr TIRF, Zeiss, Germany), forming an illumination grating with a grating period of ~ 184 nm close to the diffraction limit $\lambda_{\text{ex}} / (2 \times \text{NA}) = 488 \text{ nm} / (2 \times 1.46) = 167$ nm in the sample plane. The pattern spacing in the sample should be chosen as close as possible to this limit. This assures the maximal achievable resolution. As a sidenote, the usable field of view with high grating contrast can sometimes be influenced by vignetting effects inside the objective, when very close to the limit frequency. This can often be amended as follows: block sequentially one order and observe the uniform illumination position in the sample, while the SLM displays a pattern only within a wide disk-shaped region of interest. If there is a shift between the illumination from each order, adjust (if available) the correction collar on the objective or the SLM and/or illumination lens position. If asymmetric vignetting is observed in an order, the orders probably do not focus exactly to the correct back focal plane and the orders are not centered correctly. Due to the losses on the optical components, less than 3% of the laser power reaches the sample. The emitted fluorescent light is deflected and imaged on a sCMOS camera (Orca Flash 4, Hamamatsu, Japan).

2.2. Grating pattern generation algorithm for SLM

The SLM generating the grating is composed of square pixels. The grating pattern shows a jagged edge when the grating direction is not parallel to the axes of the pixels (see figure 2(a)). This jagged edge causes additional diffraction orders in frequency space. When the SLM displays a white image, i.e. all pixels are ON, we observed some residual diffraction orders from the SLM display structure (see figure 2(e)). The periodicity of the square pixels contributes to four diffraction orders marked in yellow. Moreover, there are another six significant diffraction orders, marked in white in figure 2(e). According to the manufacturer, they originate from the internal distribution of vias in the display structure. The via is the connection from a pixel to the next pixel and drives circuitry underneath the mirror. The vias are grouped as shown in figure 2(d). Hence, when the SLM displays a grating, the diffraction orders originating from the grating convolve with these residual diffraction orders in frequency space (see figure 2(f)). Plenty of diffraction orders emerge in frequency space, which makes the selection of only the ± 1 st diffraction orders difficult. Those four diffraction orders contributed from the periodicity of the square pixels are far away from the center. Therefore, in our grating-search algorithm, we only consider the effect of the via structure and the grating displayed on the SLM.

Now we discuss the generation of binary gratings with different orientations and phases. We describe an algorithm to search for a set of gratings by determining grating patterns with a specific grating constant, orientations and required phase steps, as well as simulate a Fourier filter in the Fourier plane of the SLM for filtering unwanted orders (see figure 3). The code was written in Matlab using the DipImage toolbox (Delft University of Technology, Delft, Netherlands) which is freely available at https://github.com/nanoimaging/fastSIM_GratingSearchforSLM.

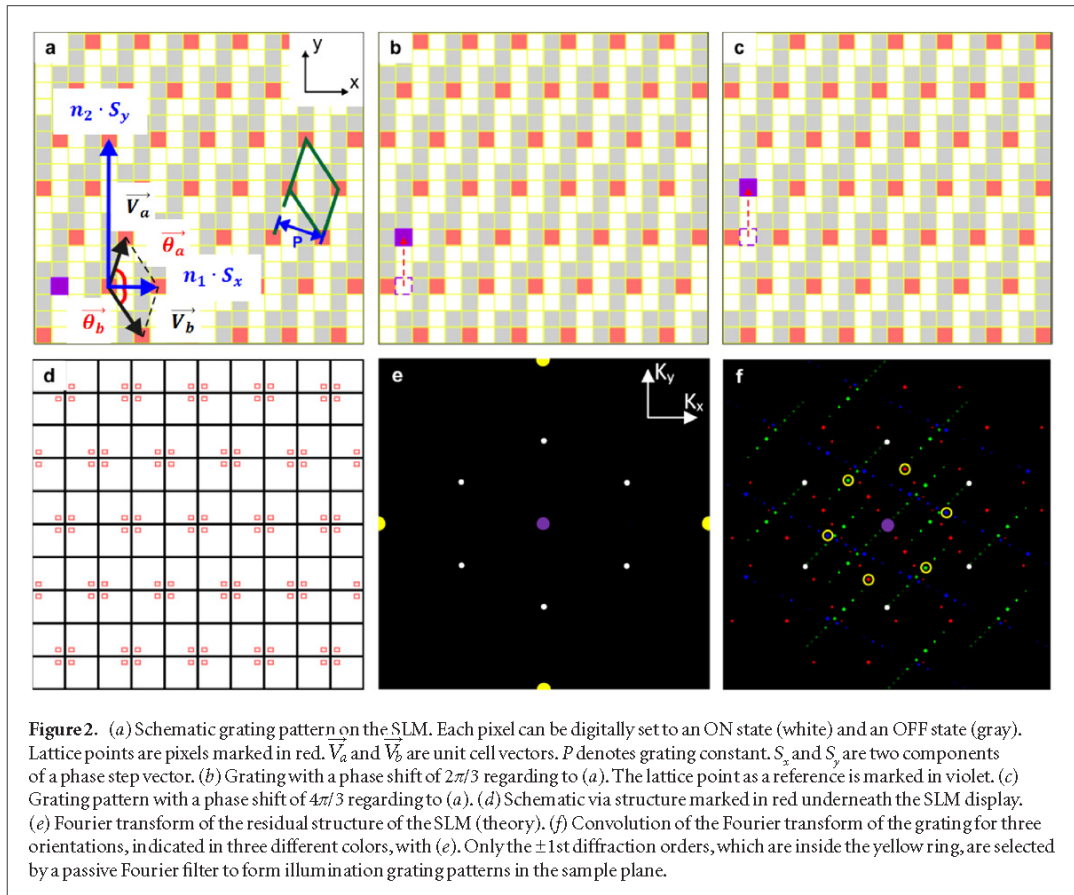
The way the grating patterns on the SLM are defined and characterized is inspired by Shao *et al* [9, 12]. The grating pattern represented on the pixelated SLM display is the multiple replication of a unit cell which is defined by vectors $\vec{V}_a = (a_x, a_y)$ and $\vec{V}_b = (b_x, b_y)$ as shown in figure 2(a). The grating orientation θ_a (orthogonal to the grating vector \vec{K}) is defined by \vec{V}_a :

$$\tan \theta_a = \frac{a_y}{a_x}.$$

The grating constant, P , equals to:

$$P = \sqrt{b_x^2 + b_y^2} \cdot \sin(\theta_a - \theta_b), \text{ where } \tan \theta_b = \frac{b_y}{b_x}.$$

With a given tolerance for the grating constant, a given tolerance for the grating orientation and a range of parameters a_x, a_y, b_x and b_y , plenty of unit cells with matched grating constant can be found. From these unit cells, we select three which are separated by $60 \pm 1^\circ$



and verify that three equidistant phase steps can be realized with all three unit cells.

We vary the phase of the unit cell by translating the unit cell on the SLM display. Equidistant phase steps ensure that the grating pattern is always shifted with the same phase step to the next grating position. We introduce a phase step vector $\vec{S} = (S_x, S_y)$ that has integer components due to the pixelated display (see figure 2(a)). These components, S_x and S_y , equal to:

$$S_x = \frac{\left| \text{lcm}(a_y, b_y) \cdot \left(\frac{a_x}{a_y} - \frac{b_x}{b_y} \right) \right|}{n_1}$$

$$S_y = \frac{\left| \text{lcm}(a_x, b_x) \cdot \left(\frac{a_y}{a_x} - \frac{b_y}{b_x} \right) \right|}{n_2}$$

where lcm means least common multiple. S_x and S_y are the equidistant phase steps in horizontal and in vertical, respectively. After n_x phase steps in horizontal (the phase step vector $\vec{S} = (S_x, 0)$), or n_y phase steps in vertical (the phase step vector $\vec{S} = (0, S_y)$), the phase of the grating is identical to the one at the initial position. Thus, each lattice point is shifted to the position of another one. By applying grating translation along in both horizontal and vertical directions yields more flexibilities of finding matched grating patterns. In figure 2(a), $\vec{V}_a = (1, 3)$ and $\vec{V}_b = (2, -3)$, thus $n_1 \cdot S_x = 3$ which

allows 3 equi-phase steps, and $n_2 \cdot S_y = 9$ which allows 3 and 9 equi-phase steps.

To fill the unit cell we threshold a sin function to form a pixelwise binary grating pattern (see figure 2(a)).

$$\text{Value}(\vec{r}) = \sin(\vec{K} \cdot \vec{r} + \varphi) > 0,$$

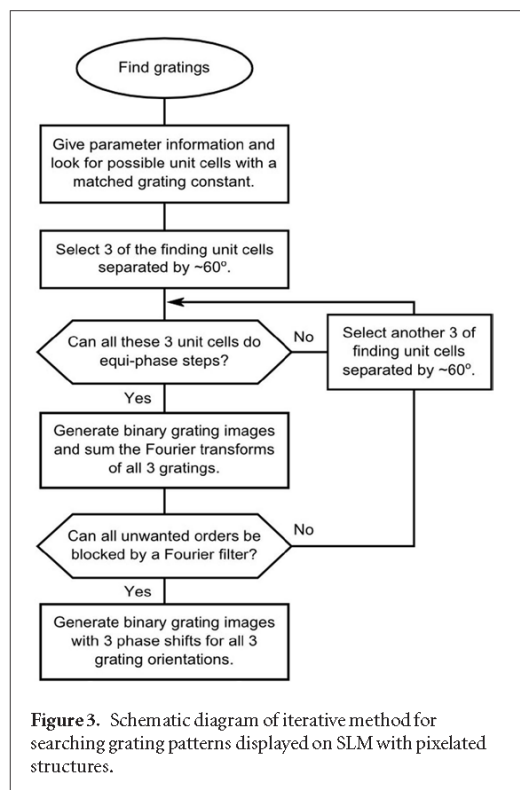
$$\vec{K} = \vec{K}_x + \vec{K}_y = \left(\frac{2\pi}{P} \cdot \sin \theta_a \right) \vec{x} + \left(\frac{2\pi}{P} \cdot \cos \theta_a \right) \vec{y},$$

where φ is the phase of the grating. Three pixelwise binary grating patterns at three different orientations are used in the next step to simulate the sum of diffraction orders in frequency space.

We simulate the distribution of the diffraction orders in the Fourier plane of the SLM considering the convolution of the diffraction orders from the via structure and those from grating patterns at three different orientations displaying on the SLM (see figure 2(f)). We then search for grating patterns to minimize unwanted contributions in the yellow circles. When grating patterns at three different orientations fulfills the former criteria, we generate three images at phases 0, $2\pi/3$ and $4\pi/3$ for each orientation.

2.3. Synchronization in fastSIM

At the heart of our setup is a microcontroller (Arduino Uno, Arduino, Italy), which is responsible for synchronizing the laser, the SLM and the camera.



Before loading a new grating pattern image, the SLM displays the inverse grating image of the previous one to prevent damage to the LCOS. These two images have a phase difference of π . In the case of two beam interference, the phase shift of the projected grating in the sample plane is 2π when the phase shift of the grating image displayed on the SLM is π . Accordingly, the projections of two grating images with a phase difference of π are identical in the sample plane. Therefore, both displayed gratings are used during one camera integration.

The Orca Flash 4 sCMOS camera promises high speed readout due to its split readout scheme, whereby the top and bottom halves of the sensor are readout simultaneously. Each time, two horizontal lines are read in parallel from the center to the side (upward and downward). Secondly, in the free running mode, the exposure and readout timing are controlled by an internal microprocessor and can be set by a software command. We illuminated only at the timing while all pixels of the camera inside the desired ROI are ready for global exposure, right after the readout process finishes. The length of the exposure time in the software setting is equal to the sum of readout time, illumination time, and image loading time onto the SLM (see table 1). Each grating image is displayed for 2 ms on the SLM and the same to its inverse image. When the SLM is displaying a grating, the laser is ON. Each time the SLM is loading an image, which roughly takes $440 \mu\text{s}$, the laser is OFF. Thus, the illumination time in each raw image is 4 ms. The readout time depends on the size of a ROI.

The synchronization process during data acquisition is shown in figure 1(b). When an acquisition starts, the Arduino first receives a trigger ready signal from the camera indicating that the camera shutter is now opening. After all the pixels in the selected ROI are ready for global exposure, a camera global exposure signal is sent to the Arduino which then triggers the SLM to display the gratings.

The sum of all individual raw images is equivalent to a wide-field image, which we used for comparison.

2.4. Sample preparation

Best resolution is achieved closest to the coverslip. Due to the aberrations caused by refractive index mismatch, the resolution degrades as we move away from the coverslip. To achieve best quality of the super-resolution images, we characterize the PSF of the optical system and apply the experimental PSF in the image processing, whenever it is necessary. Several factors affecting the quality of the result need to be considered during sample preparation. When preparing a sample for SIM imaging, it is preferable that the sample is deposited on the coverslip. A coverslip with a thickness of $170 \pm 5 \mu\text{m}$ is highly recommended. Moreover, a sample should be ideally embedded in a medium with an index of refraction close to the immersion oil (usually 1.518), when using an oil immersion objective which allows for highest resolution. However, this embedding medium is not suitable for preparing a living cell sample.

Drops of fluorescent microspheres (PCFP-0252, Kisker Biotech GmbH & Co. KG, Germany) with an approximate diameter of 100 nm were diluted in distilled water in concentration of 1:2. A few drops of diluted microspheres solution were dried on a coverslip and mounted in the embedding medium. For preparing a fluorescent microspheres volume specimen, the diluted fluorescent microspheres were mixed with the embedding medium with an index of refraction of 1.50, relatively close to the index of the immersion oil ($n = 1.518$). Later, drops of this mixture were placed on a coverslip which was then placed on a slide and sealed with nail polish.

The embedding medium we used to prepare a fluorescent microspheres sample is a mixture of 2 solutions with a ratio of 3:1 that are generally stored separately at 4°C :

Solution 1: 100 mL Poly (vinylalcohol) 20%, 50 mL Glycerine 87%, 19.5 mg NaN_3 (2 mM).

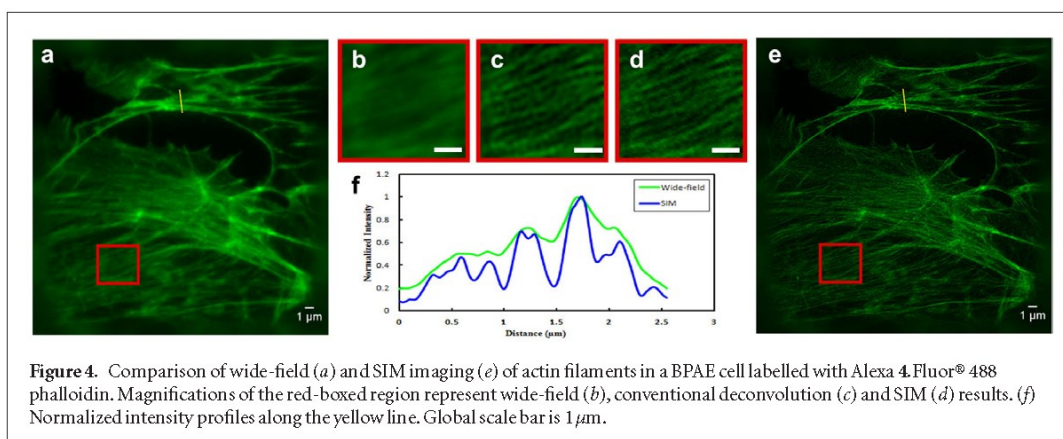
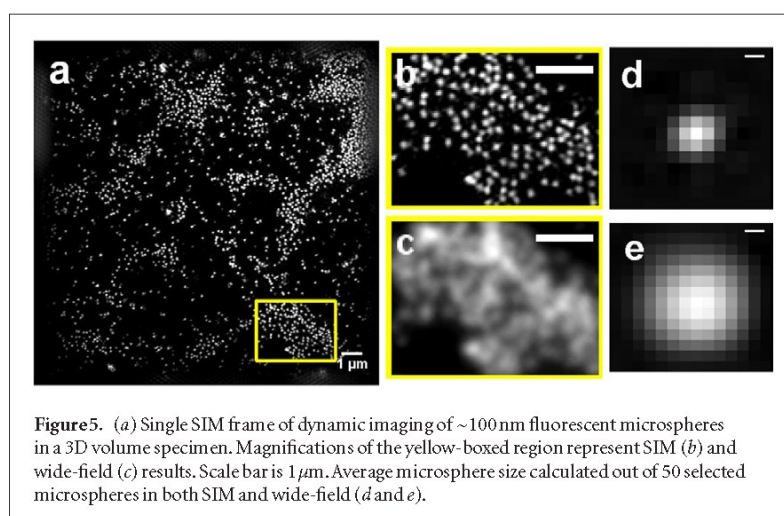
Solution 2: 2.5 g Propylgallate / 100 mL solution, 50 mL PBS + 50 mL Glycerine, pH 7.3.

3. Results

To demonstrate the resolution performance on the fastSIM system, we imaged actin filaments of bovine pulmonary artery endothelial cells (BPAE, Invitrogen) labelled with Alexa Fluor® 488 phalloidin with excitation wavelength of 488 nm and emission

Table 1. Acquisition raw frame rate and one super-resolution SIM frame rate according to different ROIs in a reconstructed SIM image.

Illumination time 4 ms				
Region of interest (ROI)		Exposure time setting (ms)	Raw data frame rate (fps)	SIM frame rate (fps)
(pixels)	(μm)			
1536×1536	49.5×49.5	8.67	115.34	12.82
1024×1024	33.0×33.0	7.38	135.50	15.06
512×512	16.5×16.5	6.17	162.07	18.01
256×256	8.3×8.3	5.52	181.16	20.13

**Figure 4.** Comparison of wide-field (*a*) and SIM imaging (*e*) of actin filaments in a BPAE cell labelled with Alexa 4.Fluor® 488 phalloidin. Magnifications of the red-boxed region represent wide-field (*b*), conventional deconvolution (*c*) and SIM (*d*) results. (*f*) Normalized intensity profiles along the yellow line. Global scale bar is $1\mu\text{m}$.**Figure 5.** (*a*) Single SIM frame of dynamic imaging of $\sim 100\text{ nm}$ fluorescent microspheres in a 3D volume specimen. Magnifications of the yellow-boxed region represent SIM (*b*) and wide-field (*c*) results. Scale bar is $1\mu\text{m}$. Average microsphere size calculated out of 50 selected microspheres in both SIM and wide-field (*d* and *e*).

wavelength of 510 nm (see figure 4). Nine raw images were acquired for reconstructing one 2D-SIM image with a ROI of $33.0 \times 33.0\mu\text{m}$ within 66.6 ms.

Imaging moving objects is always a challenge for a conventional SIM system when the acquisition is slow and the ROI becomes too large. Here, we demonstrated that our fastSIM system is capable of imaging fast moving objects with a resolution of approximately 100 nm. We observed Brownian motion in a 3D volume sample of fluorescent microspheres over 60 time points. 540 raw images in total were recorded within 3.34 s with excitation wavelength of 488 nm and emission wavelength of 520 nm. All images were recorded with a ROI of $16.5 \times 16.5\mu\text{m}$ at a raw frame rate of 162.07 fps. One single SIM frame of a time series is shown in figure 5.

90% of the fluorescent microspheres were immobile on the coverslip. However, some diffusing microspheres close to the coverslip can still be resolved individually over time. Videos for wide-field and SIM can be found in Movie S1 and Movie S2, stacks.iop.org/MAF/01/014001 respectively. Additionally, 50 fluorescent microspheres were selected in both wide-field and SIM images to calculate mean FWHM which are $222.3 \pm 38.5\text{ nm}$ and $93.6 \pm 15.1\text{ nm}$, respectively.

When the emitted fluorescence is low, which often happens in a sparse specimen, it is then difficult to extract enough information from raw images to reconstruct a SIM image. There are approaches to deal with this. It can be useful to perform the parameter estimation on a sufficiently dense region. In our case, this

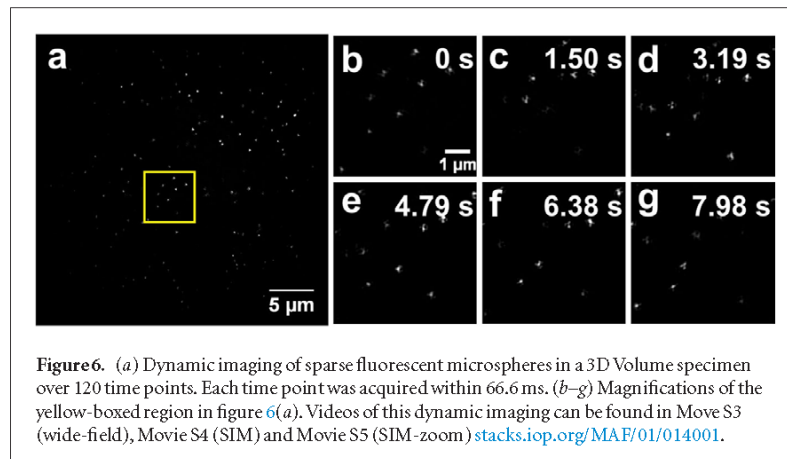


Figure 6. (a) Dynamic imaging of sparse fluorescent microspheres in a 3D Volume specimen over 120 time points. Each time point was acquired within 66.6 ms. (b–g) Magnifications of the yellow-boxed region in figure 6(a). Videos of this dynamic imaging can be found in Movie S3 (wide-field), Movie S4 (SIM) and Movie S5 (SIM-zoom) stacks.iop.org/MAF/01/014001.

was done after the estimation steps [10, 19]. Once all the required parameters are calculated (e.g. the grating constant, grating phases, grating directions etc), we later apply the same parameters to process images acquired in the region of freely diffusing beads.

We imaged diffusing fluorescent microspheres deeper inside the specimen, where the distribution of microspheres is thin. All images were acquired with a ROI of $33.0 \times 33.0 \mu\text{m}$. 1080 raw images were recorded within 7.98 s, i.e. 120 time points (see figure 6, Movie S4 stacks.iop.org/MAF/01/014001). The result shows slight artefacts appearing around the microspheres originating mainly from the fast movement of the microspheres and from the poor information for reconstruction in a sparse specimen.

4. Discussion and conclusion

We have demonstrated the acquisition speed enhancement of super-resolution microscopy based on a conventional two-beam SIM system. We applied two passive devices, a fixed Fourier filter and an azimuthally patterned polarizer, to simplify the system synchronization during the acquisition. We also demonstrated that driving an sCMOS camera under an internal running mode yields the fastest frame rate. The present fastSIM system is capable of time series imaging with a relatively large ROI for both dense and sparse specimen. It also provides promising results with lateral resolution better than 100 nm. Based on the findings of Brunstein *et al* [20], we extrapolate (not accounting for experimental differences) the maximal tolerable speed of the moving beads to be about $1.045 \mu\text{m s}^{-1}$. This corresponds to about 8 nm movement per raw-data frame and a maximum phase mismatch between raw-data frames of 15° . By tracing the wide-field images of 10 diffusing beads, which show relatively minor artefacts, we estimated their movement to be around 732 nm s^{-1} . Thus the bead displacement is $\sim 49 \text{ nm}$ per one SIM frame which induces artefact.

Efforts to further improve the acquisition speed without modifying the current system configuration can involve shortening the exposure time by applying

higher illumination laser power on the sample and synchronizing the running shutter with the display of partial SLM patterns taking advantage of the usage of the readout timing on camera. This system has been tested with illumination time of 2 ms which achieves a raw frame rate of 239.81 fps with a ROI of $16.5 \times 16.5 \mu\text{m}$.

Removing unnecessary optical components, e.g. mirrors, beamsplitters and etc, in the optical path yields better polarization conserving and minimizing wavefront distortion. In return, the system alignment also becomes easier.

This setup is now expanded for NLSIM application. For reconstructing one single slice in a 2D NLSIM image, more raw data images are required, e.g. six different orientations of grating, each with nine equidistant phase steps. With the help of the grating pattern generation algorithm, it is possible to find a series grating pattern images for both conventional SIM and NLSIM. Therefore, applying both techniques on the same system without modifying or realigning any optical components is feasible.

We are aiming at real time living cell imaging with fastSIM system as well as putting more efforts on further resolution improvement, which will contribute greatly to the study of the life science.

Acknowledgments

We thank Elena Tolstik for fluorescent microspheres specimen assistance; Robert Kretschmer and Florian Blase for electronics assistance and general practical help; Sarmiza Stanca for embedding medium preparation; Reto Fiolka for useful discussions related to optics, physics and image processing; Ivana Šumanovac Šestak for discussions and suggestions related to biology; and Sapna Shukla for proofreading this manuscript. This research work was funded in part by the Federal Ministry of Education and Research, Germany (BMBF, grant no. 13N13140).

References

- [1] Pawley J B 2008 Handbook of biological confocal microscopy *J. Bio-Med. Opt.* **13** 29902–3

- [2] Heintzmann R and Ficz G 2006 Breaking the resolution limit in light microscopy *Brief. Funct. Genomic Proteomic* **5** 289–301
- [3] Willig KI, Harke B, Medda R and Hell S W 2007 STED microscopy with continuous wave beams *Nat. Methods* **4** 915–8
- [4] Dyba M, Jakobs S and Hell S W 2003 Immunofluorescence stimulated emission depletion microscopy *Nat. Biotechnol.* **21** 1303–4
- [5] Leica Microsystems 2014 Production information for leica TCS STED (<http://www.leica-microsystems.com/products/confocal-microscopes/leica-tcs-sp8-configurable-confocal/details/product/leica-tcs-sp8-sted-3x/>)
- [6] Zeiss 2014 Product information for #elyra P.1 (http://www.zeiss.com/microscopy/en_de/products/elyra-superresolution.html#elyra-p-1)
- [7] Heintzmann R and Cremer C 1997 Laterally modulated excitation microscopy *Proc. SPIE* **3568** 185–96
- [8] Gustafsson M G L 2000 Surpassing the lateral resolution limit by a factor of two using structured illumination microscopy *J. Microsc.* **198** 82–7
- [9] Shao L, Kner P, Rego E H and Gustafsson M G L 2011 Super-resolution 3D microscopy of live whole cells using structured illumination *Nat. Methods* **8** 1044–6
- [10] Wicker K, Mandula O, Best G, Fiolka R and Heintzmann R 2013 Phase optimization for structured illumination microscopy *Opt. Express* **21** 2032–49
- [11] Gustafsson M G L, Shao L, Carlton P M, Wang C J R, Golubovskaya I N, Cande W Z, Agard D A and Sedat J W 2008 3D resolution doubling in wide-field fluorescence microscopy by structured illumination *Biophys. J.* **94** 4957–70
- [12] Fiolka R, Shao L, Rego E H, Davidson M W and Gustafsson M G L 2012 Time-lapse two-color 3D imaging of live cells with doubled resolution using structured illumination *Proc. Natl Acad. Sci.* **109** 5311–5
- [13] Kner P, Chhun B B, Griffis E R, Winoto L and Gustafsson M G L 2009 Super-resolution video microscopy of live cells by structured illumination *Nat. Methods* **6** 339–42
- [14] Best G, Amberger R, Baddeley D, Ach T, Dithmar S, Heintzmann R and Cremer C 2011 Structured illumination microscopy of autofluorescent aggregations in human tissue *Micron* **42** 330–5
- [15] Light Microscopy Facility 2014 Product information: Applied Precision OMX (<http://microscopy.lifesci.dundee.ac.uk/omx/>)
- [16] Förster R, Lu-Walther H-W, Jost A, Kielhorn M, Wicker K and Heintzmann R 2014 Simple structured illumination microscope setup with high acquisition speed by using a spatial light modulator *Opt. Express* **22** 20663–77
- [17] Rego E H, Shao L, Macklin J J, Winoto L, Johansson G A, Kamps-Hughes N, Davidson M W and Gustafsson M G L 2012 Nonlinear structured-illumination microscopy with a photoswitchable protein reveals cellular structures at 50 nm resolution *Proc. Natl Acad. Sci.* **109** E135–43
- [18] Martínez-García A, Moreno I, Sánchez-López M M and García-Martínez P 2009 Operational modes of a ferroelectric LCoS modulator for displaying binary polarization, amplitude, and phase diffraction gratings *Appl. Opt.* **48** 2903–14
- [19] Wicker K 2013 Non-iterative determination of pattern phase in structured illumination microscopy using auto-correlations in Fourier space *Opt. Express* **21** 24692–701
- [20] Brunstein M, Wicker K, Herault K, Heintzmann R and Oheim M 2013 Full-field dual-color 100 nm super-resolution imaging reveals organization and dynamics of mitochondrial and ER networks *Opt. Express* **21** 26162–73

Publication 3

Fast structured illumination microscopy using rolling shutter cameras

Song L, Lu-Walther H-W, Förster R, Jost A, Kielhorn M, Zhou J, Heintzmann R.

[HWLW3] Song L, Lu-Walther H-W, Förster R, Jost A, Kielhorn M, Zhou J, Heintzmann R. Fast structured illumination microscopy using rolling shutter cameras. Measurement Science and Technology. 2016; 27: 055401. doi: <http://dx.doi.org/10.1088/0957-0233/27/5/055401>

Beteiligt an (*Zutreffendes ankreuzen*)

Author	Song L	Lu-Walther H-W
Konzeption des Forschungsansatzes	×	×
Planung der Untersuchungen	×	×
Datenerhebung	×	×
Datenanalyse und -interpretation	×	×
Schreiben des Manuskripts	×	×
Vorschlag Anrechnung Publikationsäquivalente	1,0	1,0

Both authors contributed equally to this work.

All authors revised, edited and proof read the final manuscript.

Reprinted with kind permission from the IOP publishing group.

Copyright © IOP Publishing. Reproduced with permission. All rights reserved.

Fast structured illumination microscopy using rolling shutter cameras

Liyan Song^{1,2,5}, Hui-Wen Lu-Walther^{1,5}, Ronny Förster^{1,3}, Aurélie Jost^{1,3}, Martin Kielhorn^{1,3,6}, Jianying Zhou^{2,4} and Rainer Heintzmann^{1,3}

¹ Leibniz Institute of Photonic Technology, Jena, Germany

² State Key laboratory of optoelectronic Materials and Technologies, Sun Yat-sen University, Guangzhou 510275, People's Republic of China

³ Institute of Physical Chemistry, Abbe Center of Photonics, Friedrich-Schiller-University Jena, Jena, Germany

⁴ SYSU-CMU Shunde international Joint Research Institute, Shunde 528300, People's Republic of China

E-mail: heintzmann@gmail.com

Received 29 December 2015, revised 6 March 2016

Accepted for publication 15 March 2016

Published 6 April 2016



Abstract

Spatial light modulators (SLM) update in a synchronous manner, whereas the data readout process in fast structured illumination systems is usually done using a rolling shutter camera with asynchronous readout. In structured illumination microscopy (SIM), this leads to synchronization problems causing a speed limit for fast acquisition. In this paper we present a configuration to overcome this limit by exploiting the extremely fast SLM display and dividing it into several segments along the direction of the rolling shutter of the sCMOS camera and displaying multiple SLM frames per camera acquisition. The sCMOS runs in continuous rolling shutter mode and the SLM keeps the readout-line always inside a dark region presenting different SIM patterns before and after the readout/start-exposure line.

Using this approach, we reached a raw frame rate of 714 frames per second (fps) resulting in a two-beam SIM acquisition rate of 79 fps with a region of interest (ROI) of $16.5 \times 16.5 \mu\text{m}^2$.

Keywords: structured illumination microscopy, superresolution, video rate, spatial light modulators, synchronization

 Online supplementary data available from stacks.iop.org/MST/27/055401/mmedia

(Some figures may appear in colour only in the online journal)

1. Introduction

Video rate observation is one of the aims super-resolution technology is working towards. It is of vital importance for biologists to have fast imaging with resolution down to molecular level to see the interaction and migration of molecular targets within the cell or other biological samples. Currently, details down to several tens of nanometer can be resolved by fluorescence based microscopy such as STED (stimulated emission depletion microscopy) [1, 2], PALM (photoactivated localization microscopy), dSTORM (direct stochastic optical

reconstruction microscopy) [3, 4] and linear [5, 6] and non-linear [7–10] structured illumination microscopy (SIM).

In STED, the excitation light is focused to a diffraction-limited spot onto the sample. A doughnut-shaped beam within the range of emission frequencies centers on this focus, leading to a decay of the excited molecules via the stimulated emission process. Hence, the spontaneous fluorescence emission does not happen at the periphery but only in a much thinner sub-diffraction region close to the focal point. The overlap of the excitation beam and the STED doughnut beam is then scanned over the whole region of interest. The direct consequence is a trade-off between acquisition speed and field of view as it is usually the case for point-scanning techniques. Typically, several tens of seconds are needed for

⁵ Both authors contributed equally to this work.

⁶ Currently at eZono AG, 07743 Jena, Germany.

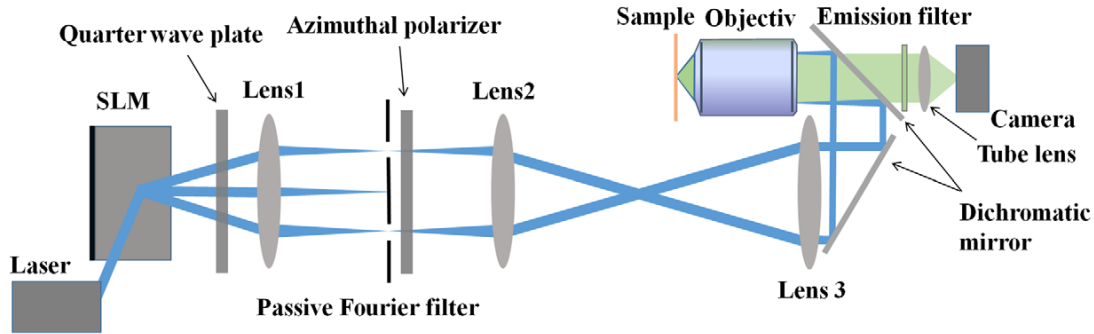


Figure 1. Simplified sketch of our two-beam based fastSIM setup. The second dichromic mirror is identical and oriented perpendicular to the first one, to compensate for polarization effects.

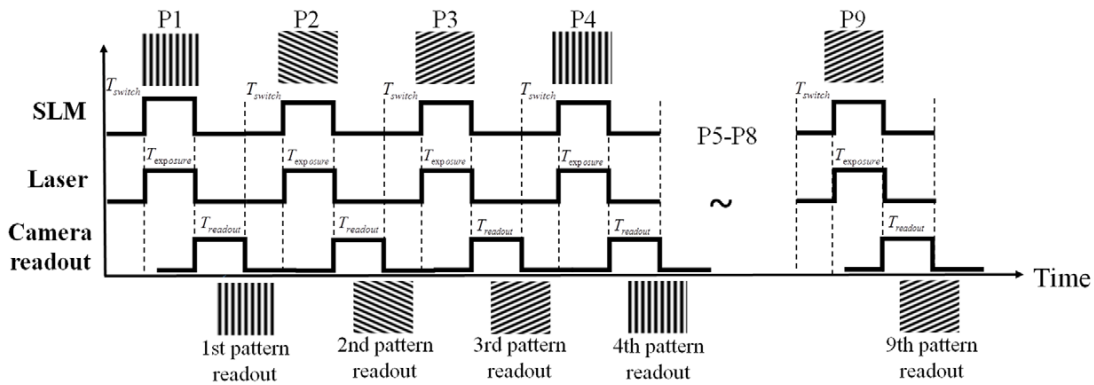


Figure 2. Conventional synchronization among SLM, laser and camera readout process to acquire 9 raw images, P = pattern (corresponding to the patterns in figure 3). During the readout time, the laser is switched off, which decreases the exposure duty-cycle and slows down the acquisition process.

one acquisition of a superresolved image of 512×512 pixels [2]. This can be improved by using optical lattices to acquire data faster [11]. Live imaging with STED is being performed to solve current questions in biology [12]. Localization-based methods such as PALM and *d*STORM exploit the blinking property of certain molecules. In a single camera frame, only a sub-set of the labeled molecules are emitting their diffraction-limited fluorescence signal. A processing algorithm is applied and can determine the probable localizations of the emitters. Many frames are acquired sequentially and the localization procedure is applied to each different sub-set, until a localization map of high accuracy is produced. Usually, many thousands of raw images are needed, thus yielding global recording times of seconds to even minutes [13]. STORM imaging can also be used to image processes in live cells [14]. SIM, on the other hand, is a wide-field method and requires only a few raw images to reconstruct the final super-resolution image. Thus, it has a great potential to realize fast acquisition speed.

Based on the Moiré Effect between the finely structured illumination grating and the object, object information outside the passband of the optical transfer function is mixed into the passband and transmitted to the image plane. In SIM, a computational reconstruction is then able to retrieve this high-frequency information and reconstruct a superresolved image.

In a typical SIM system, the interference is formed by beams of diffraction orders from a grating. First a physical grating was used to generate the interfering beams [5, 6]. Hirvonen *et al* [15] replaced this physical grating with a spatial light modulator (SLM), and Fiolka *et al* [16] used a fast version which generates diffraction patterns based on a ferroelectric liquid crystal (LC).

2. Method

In previous work [17, 18], we successfully demonstrated a fastSIM system and achieved an acquisition rate of 18 super-resolved fps with a lateral resolution of ~ 100 nm for a region of interest (ROI) of 512×512 pixel ($16.5 \times 16.5 \mu\text{m}^2$). This was realized by adopting a fast switchable (~ 1 kHz) SLM as a diffraction grating and by synchronizing this element with a laser source and a modern sCMOS camera running in free running mode [17, 18]. The setup sketch is shown in figure 1. The first diffraction (± 1 st) orders are selected by a passive Fourier filter [18] to form a sinusoidal interference pattern in the sample plane and the emission of excited fluorescence is imaged by the camera through the same illumination objective, a dichromic mirror (H488 LPXR, 45 deg., AHF, Germany) and a tube lens. To obtain a series of 9 raw images, a typical synchronizing configuration among laser (CW laser,

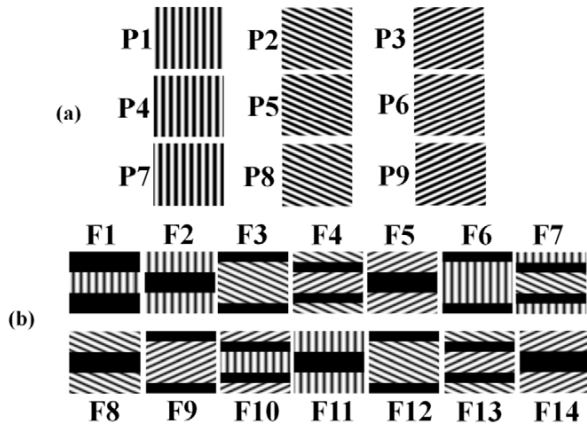


Figure 3. Grating patterns displayed on the SLM. (a) 9 single full frames grating patterns used in the previous experiment configuration [12], with $P\# = \text{SIM illumination pattern number}$; (b) new scheme with 14 segmented frames displaying parts of the 9 full frames grating patterns in (a) are designed based on the moving of camera readout line with $F\# = \text{frame number}$. In F1, there is a grating pattern (a segment of P1) in $\sim 1/3$ of the frame in the middle and the rest of $2/3$ area is dark. In F2, $\sim 1/3$ of the frame in the middle is dark while on the top and bottom area display the same grating pattern (segments of P1) as in F1, completing the display of P1. In F3, two sections on the top and also at the bottom which is $\sim 1/6$ of the frame size are dark and the other $2/3$ of the frame display the next grating pattern (a segment of P2). In F4, the same pattern (segments of P2) display within $\sim 1/6$ on the top and bottom while in the middle ($\sim 1/3$ full frame) display a third pattern (a segment of P3). F5-F14 are designed under the same configuration. Note that some frames (e.g. F4) simultaneously expose two readout frames, each with different patterns. Hence, the 14 $F\#$ correspond to the 14 combinations of partial gratings which are displayed sequentially on the SLM.

LuxX 488-200 Omicron, Germany), SLM (SXGA-3DM, 1280×1024 pixels, Forth Dimension Displays, UK) and camera (Orca Flash 4.0, Hamamatsu, Japan) was previously used as shown in figure 2.

Nine illumination patterns with different grating orientations and phase shifts are required to reconstruct a 2D SIM super-resolved image with a near-isotropic resolution improvement. The camera acquires one frame—referred to as a single SIM raw image—for each of these 9 illumination patterns. For the sake of presentation, the patterns are enlarged and shown in figure 3(a). The angle between each orientation is ~ 60 degree and the phase difference between each pattern in the same orientation is $2\pi/3$.

In the previously used scheme, we displayed a full frame grating pattern on the SLM for each of the 9 required raw images. Each time the SLM switches between two grating patterns, its state is undefined during $\sim 434 \mu\text{s}$ and there should be no exposure to the sample [19]. In order to homogeneously expose the sample, the full field exposure starts right after the pattern is uploaded and the readout process can only begin right after the whole pattern finished exposing, yielding an effective exposure duty-cycle of

$$\eta = \frac{T_{\text{exposure}}}{T_{\text{exposure}} + T_{\text{readout}} + T_{\text{switch}}} \quad (1)$$

with T_{exposure} , T_{readout} and T_{switch} denoting the timespan for exposure, readout and switching, respectively (see figure 2). By adopting a similar configuration as shown in reference [18], a 2D SIM frame rate of 18 fps was realized with a ROI of 512×512 pixels. However, the acquisition rate as well as the duty cycle can be improved significantly by allowing exposure also during the readout time.

Whereas previously used interline or frame-transfer CCDs can expose a new frame while the previously exposed frame is being read out, current sCMOS technology employs a rolling shutter consisting of continuously running start and stop/readout lines. The Orca Flash 4.0 sCMOS camera hardware instruction states that the fastest acquisition rate is achieved in a free running mode with a ROI of 256×256 pixels is 802 fps when the exposure time is equal to one frame readout time. When run in this configuration, two camera start-exposure lines move upwards and downwards from the center of the camera sensor. When the start-exposure lines reach the outer border of the frame, two camera readout lines then start from the center upwards and downwards while the exposure lines return to the center and keep moving behind the readout lines. By adopting this characteristic, we present a faster configuration by dividing each acquisition frame and thus each single grating pattern into several SLM display frames. The direct consequence is an increase of the total number of frames displayed on the SLM. In total, 14 segmented frames are now displayed on the SLM as shown in figure 3(b), for a total of 9 acquired raw images corresponding to the nine SIM patterns. The dark regions of each segmented grating pattern prevent double exposure by the current pattern and next pattern. In order to ensure continuous readout, we designed the display time of each frame roughly to be the same as the frame switching time on the SLM ($434 \mu\text{s}$), i.e. $T_{\text{exposure}} \cong T_{\text{switch}}$. One full acquired image is combined from two segmented parts of consecutive display frames. The reason for the mirror symmetry of the displayed area as shown in figure 3(b) is that the sCMOS camera is reading out data simultaneously using two readout lines running upwards and downwards from the center.

The synchronization is shown in figure 4. When the camera sends the Trigger-Ready output signal (at time t_0 in figure 4), the start-exposure lines start from the middle of the frame and the SLM begins to upload the first segmented frame (F1) which takes T_{switch} . After the SLM finishes uploading the first frame (at t_1), the laser is switched on for T_{exposure} , but the start-exposure line has already passed the area now displaying a grating in F1 (see figure 3(b)) and continues to move in the dark while the emission from the illumination pattern shown in F1 is being integrated on the detector. At t_2 the laser is turned off for the time T_{switch} while the second frame (F2) is transferred onto the SLM display. At t_3 the readout lines (which also stops the exposure and reset the pixels to zero) start from the middle of the frame and the start-exposure lines have also returned to the middle after reaching the outer lines of the frame and keep moving right behind the readout line. Thus the exposure starts immediately on the lines which have been cleared by the readout lines yet nothing is being displayed in the area where the readout line moves, whereas other parts of

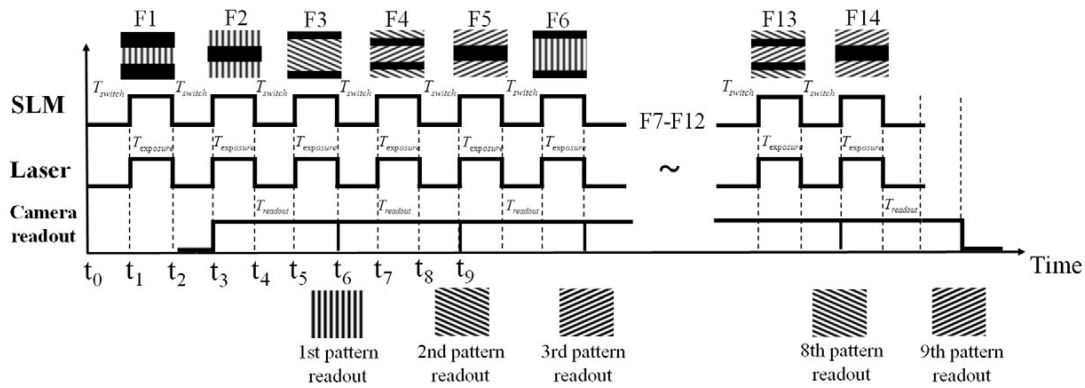


Figure 4. The modified synchronization configuration corresponding to segmented frame, $F\# =$ SLM display frame number. See figure 3 for details on the displayed patterns.

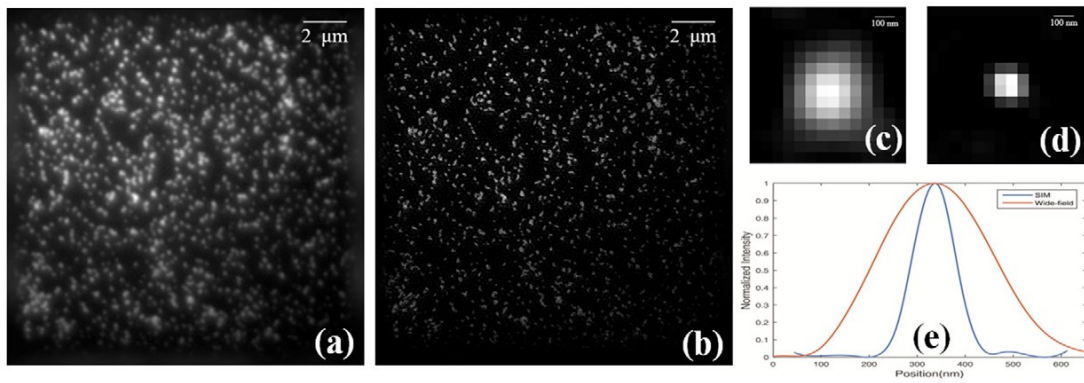


Figure 5. (a) The wide-field image of fluorescence beads (average diameter = 100 nm); (b) the reconstructed SIM image. Average bead size calculated out of 50 selected beads in (c) wide-field and (d) SIM image and (e) their Gaussian fit of the profile with orange and blue line correspond to wide-field and SIM case.

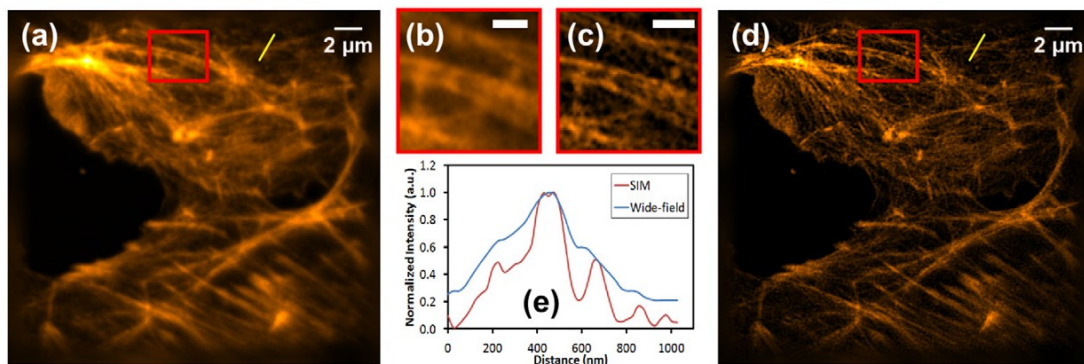


Figure 6. Comparison of (a) the wide-field and (d) SIM image of fluorescence cell. The magnifications of red-boxed region represent the wide-field (b) and SIM (c) results. (e) Normalized intensity profiles along the yellow line in (a) and (d).

the frame are being exposed. After another T_{switch} starting at t_4 , the laser is turned off at t_5 and the SLM is uploading the third segmented frame (F3) within T_{switch} . At time t_6 the last bit of the first full frame raw image has been read, which corresponds to the fully displayed P_1 . While the rest of the frame is being readout (t_5 to t_6) the central part of the second display frame is already being exposed (F3) contributing to the next image to be read out.

The patterned area of the F2 is exactly complementing the first frame to form a full frame with no overlap between them. All areas of an image will experience a same pattern exposure time $T_{exposure}$, which is roughly 1/3 of the frame acquisition time. The readout time for each full frame raw image is equal to $2 \times T_{switch} + 1 \times T_{exposure}$ (or equal to $1 \times T_{switch} + 2 \times T_{exposure}$) as shown in figure 4. It is obvious that such new mode of SLM-based SIM operation for rolling shutter cameras significantly

improves the exposure duty cycle as well as the overall data acquisition speed.

In the supplement material, we show an animation (RunningConfiguration.mp4 (stacks.iop.org/MST/27/055401/mmedia)) to visualize the acquisition process including the displayed SLM frames and the positions of the start-exposure and readout lines.

3. Experimental results and discussion

Adopting the fastSIM system described in reference [18], we first optimize the 9 full-frame grating patterns through a search algorithm. Then we construct the segmented 14 frames out of these 9 full-frame grating patterns. Here we only use the positive images of 14 frames on the SLM. The inverse images, required to prevent damage to the liquid crystal are displayed in the next cycle. The inverse images of 14 frames can be used in the next acquisition cycle since they lead to the identical excitation pattern as the positive images in the sample plane. The synchronization between the SLM, the illuminating laser and the camera is realized with an Arduino Uno board (Arduino, Italy). During the whole process, the laser is turned on when a frame finished uploading and off when the next display frame is being loaded. The 9 raw images are automatically saved in memory for later reconstruction.

To demonstrate the spatial resolution of this system, fluorescent microspheres (PCFP-0252, Kisker Biotech GmbH & Co. KG, Germany) with an average diameter of 100nm are chosen as the sample. The exposure time of each segmented frame on the SLM is 0.5ms and the uploading time for each segmented grating pattern frame onto the SLM is ~0.434ms. The experimental ROI was 256×256 pixels ($16.5 \mu\text{m} \times 16.5 \mu\text{m}$), the objective is a $63 \times /1.4$ oil immersion (alpha Plan-Apochromat $63 \times /1.46$ Oil Corr M27) and the excitation wavelength is 488nm and emission wavelength of 520nm. The corresponding readout time was 12.6ms for all 9 raw images (raw data rate is 714 fps), realizing an acquisition rate of 79 superresolved fps, which is 4 times faster than in reference [18]. This is to our knowledge the fastest SIM acquisition rate so far reported.

Experimentally, 9 full frame raw images were acquired using the fast method as described above. By adding up all these 9 raw images, we obtain the wide-field image as shown in figure 5(a). The corresponding SIM image based on standard reconstruction process is shown in figure 5(b). To evaluate the point spread function (PSF), a 2D Gaussian fit was applied to 50 selected beads in both wide-field and SIM images as shown in figures 5(c) and (d). The mean full width at half maximum (FWHM) was determined to amount to 282nm (wide-field case) and 108 nm (SIM case) as seen in figure 5(e). We verified that this procedure yielded a reliable estimate of the FWHM, even though a PSF is not precisely described by a Gaussian function. The wide-field PSF is 2.6 times wider than the SIM PSF.

We also imaged actin filaments of bovine pulmonary artery endothelial cells (BPAE, Invitrogen) labelled with Alexa Fluor@ 488 phalloidin with excitation wavelength of 488nm

and maximum emission at 510nm. The corresponding wide-field and SIM images, acquired in the described fast acquisition mode, are shown in figures 6(a) and (d). As can be seen from the magnification images (figures 6(b) and (c)) marked with red boxes and intensity profiles in figure 6(e), in the wide-field image the filaments are blurred together (orange line) whereas in the SIM image they are spatially resolved (blue line).

4. Conclusion

An acquisition rate of 79 superresolved fps has been designed and realized experimentally in a two-beam based SIM system by a cyclic update scheme synchronized with a rolling-shutter camera. This segmented frame method avoids non-continuous readout in SIM raw images acquisition and improve the acquisition speed. Such improvement is of vital importance for increasing the time resolution of such a super-resolution technique, enabling the scientists to see and trace processes at video rate while maintaining molecular scale resolution. However, a drawback is that this continuous readout configuration, the exposure time is no longer adjustable. In order to obtain sufficient signal to noise ratio (SNR), a bright sample or a strong excitation laser is required.

Acknowledgments

The authors thank X Xie for useful discussion. We acknowledge the financial support from the German Science Foundation (DFG) under TRR 166 project B5, the Federal Ministry of Education and Research, Germany (BMBF, grant no. 13N13140) and the Chinese National Natural Science Foundation (61575223 & 11534017) and the Pilot Project of SYSU-CMU Shunde International Joint Research Institute (20150101).

References

- [1] Hell S W and Wichmann J 1994 Breaking the diffraction resolution limit by stimulated emission: stimulated-emission-depletion fluorescence microscopy *Opt. Lett.* **19** 780–2
- [2] Hein B, Willig K I and Hell S W 2008 Stimulated emission depletion (STED) nanoscopy of a fluorescent protein-labeled organelle inside a living cell *Proc. Natl Acad. Sci.* **105** 14271–6
- [3] Betzig E, Patterson G H and Hess H F 2006 Imaging intracellular fluorescent proteins at nanometer resolution *Science* **313** 1642–5
- [4] Rust M J, Bates M and Zhuang X 2006 Sub-diffraction-limit imaging by stochastic optical reconstruction microscopy (STORM) *Nat. Methods* **3** 793–6
- [5] Heintzmann R and Cremer C G 1999 Laterally modulated excitation microscopy: improvement of resolution by using a diffraction grating *Proc. SPIE* **3568** 185–96
- [6] Gustafsson M G L 2000 Surpassing the lateral resolution limit by a factor of two using structured illumination microscopy *J. Microsc.* **198** 82–7
- [7] Heintzmann R, Jovin T M and Cremer C 2002 Saturated patterned excitation microscopy (SPEM)—a novel concept

- for optical resolution improvement *J. Opt. Soc. Am. A* **19** 1599–609
- [8] Hirvonen L, Mandula O, Wicker K and Heintzmann R 2008 Structured illumination microscopy using photoswitchable fluorescent proteins *Proc. SPIE* **6861** 68610L
- [9] Rego E et al 2012 Nonlinear structured-illumination microscopy with a photoswitchable protein reveals cellular structures at 50nm resolution *Proc. Natl Acad. Sci. USA* **109** E135–43
- [10] Dong L et al 2015 Extended-resolution structured illumination imaging of endocytic and cytoskeletal dynamics *Science* **349** aab3500
- [11] Yang B, Przybilla F and Lounis B 2014 Large parallelization of STED nanoscopy using optical lattices *Opt. Express* **22** 5581–9
- [12] D’Este E, Kamin D, Goettfert F, El-Hady A and Hell S 2015 STED Nanoscopy reveals the ubiquity of subcortical cytoskeleton periodicity in living neurons *Cell Rep.* **10** 1246–51
- [13] Shroff H, Galbraith C G, Galbraith J A and Betzig E 2008 Live cell photoactivated localization microscopy of nanoscale adhesion dynamics *Nat. Methods* **5** 417–23
- [14] Shim S H et al 2012 Super-resolution fluorescence imaging of organelles in live cells with photoswitchable membrane probes *Proc. Natl Acad. Sci.* **109** 13978–83
- [15] Hirvonen L, Wicker K, Mandula O and Heintzmann R 2009 Structured illumination microscopy of a living cell *Eur. Biophys. J.* **38** 807–12
- [16] Fiolka R, Shao L, Rego E H, Davidson M W and Gustafsson M G L 2012 Time-lapse two color 3D imaging of live cells with doubled resolution using structured illumination *Proc. Natl Acad. Sci.* **109** 5311–5
- [17] Förster R, Lu-Walther H W, Jost A, Kielhorn M, Wicker K and Heintzmann R 2014 Simple structured illumination microscope setup with high acquisition speed by using a spatial light modulator *Opt. Express* **22** 20663
- [18] Lu-Walther H W, Kielhorn M, Förster R, Jost A, Wicker K and Heintzmann R 2015 fastSIM: a practical implement of fast structured illumination microscopy *Methods Appl. Fluoresc.* **3** 014001
- [19] McKnight D J, Johnson K M and Serati R A 1994 256 × 256 liquid-crystal-on-silicon spatial light modulator *Appl. Opt.* **33** 2775–84

Publication 4

Structured illumination microscopy: gaining further resolution improvement by nonlinear photo-response from photoswitchable fluorescent protein

Lu-Walther H-W, Hou W, Kielhorn M, Arai Y, Nagai T, Kessels M M, Qualman B, Heintzmann R.

submitted, 19 April 2016

[HWLW4] Lu-Walther H-W, Hou W, Kielhorn M, Arai Y, Nagai T, Kessels M M, Qualman B, Heintzmann R. Structured illumination microscopy: gaining further resolution improvement by nonlinear photo-response from photoswitchable fluorescent protein. PLoS ONE. submitted, 19 April 2016

Beteiligt an (Zutreffendes ankreuzen)

Author	Lu-Walther H-W
Konzeption des Forschungsansatzes	×
Planung der Untersuchungen	×
Datenerhebung	×
Datenanalyse und -interpretation	×
Schreiben des Manuskripts	×
Vorschlag Anrechnung Publikationsäquivalente	1,0

All authors revised, edited and proof read the final manuscript.

Plos Journal is an open access publisher, no reprinted permission is required.

1 **Structured illumination microscopy: gaining further**
2 **resolution improvement by nonlinear photo-response from**
3 **photoswitchable fluorescent proteins**

4 Hui-Wen Lu-Walther¹, Wenya Hou², Martin Kielhorn^{1, #a}, Yoshiyuki Arai³, Takeharu Nagai³, Michael
5 M. Kessels², Britta Qualmann², Rainer Heintzmann^{1, 4*}

6 1 Leibniz Institute of Photonic Technology, Jena, Germany, 2 Institute of Biochemistry I, Jena
7 University Hospital/Friedrich Schiller University Jena, Jena, Germany, 3 The Institute of Scientific and
8 Industrial Research, Osaka University, Osaka, Japan, 4 Institute of Physical Chemistry, Abbe Center of
9 Photonics, Friedrich-Schiller-University Jena, Jena, Germany

10 ^{#a} Current Address: eZono AG, Jena, Germany

11 * *heintzmann@gmail.com*

12 **Abstract**

13 Structured illumination microscopy is a wide-field technique in fluorescence microscopy that
14 provides fast data acquisition and two-fold resolution improvement beyond the Abbe limit.
15 We succeeded in obtaining a further resolution improvement using the nonlinear emission
16 response of a fluorescent protein. We demonstrated a two-beam nonlinear structured
17 illumination microscope and a simple acquisition method as in linear SIM (LSIM)
18 configurations for nonlinear structured illumination microscopy (NL-SIM) adapted for the
19 innovative fluorophore Kohinoor. Kohinoor is suitable due to its positive contrast
20 photoswitching characteristics. Contrary to other reversibly photoswitchable fluorescent
21 proteins that only have high photostability in living cells, Kohinoor additionally showed
22 strong fluorescence in fixed cells over many switching cycles.

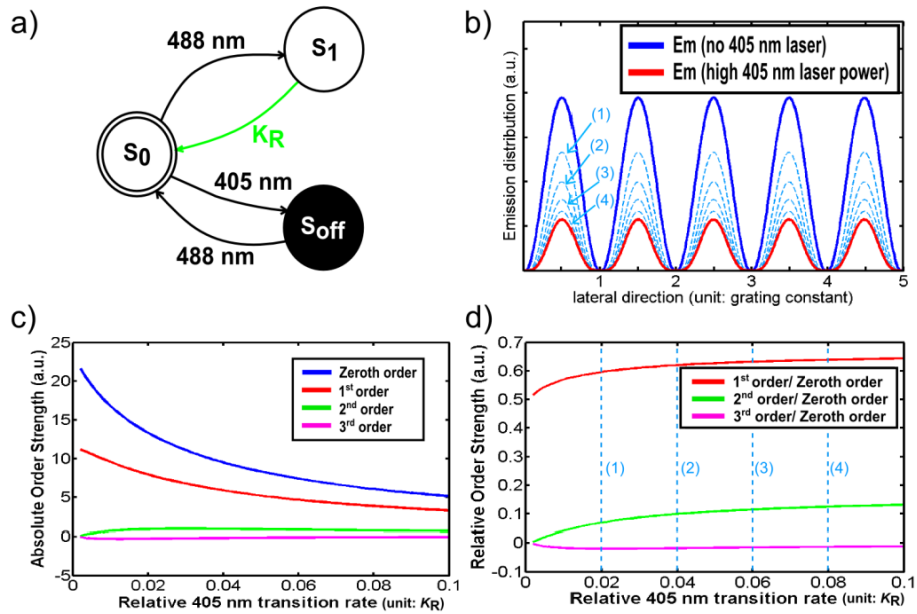
23 **Introduction**

24 In the past few years, the ongoing development of super-resolution imaging techniques
25 has spurred cell biological research world-wide, as previously unresolvable details of
26 cellular structures became visible. Among these methods, structured illumination
27 microscopy (SIM) draws attention to fast super-resolution imaging, as this method does
28 not only provide molecular resolution but is furthermore distinguished by fast
29 acquisition [1-4]. SIM thus has the potential to even explore the molecular dynamics and
30 functions in living cells and tissues at resolutions of a few nanometers. Therefore,
31 various applications have been developed based on the concept of SIM. Fast acquisition
32 is one of the most significant advantages of SIM. Yet, system developers still pursue
33 possibilities to achieve even higher acquisition rates, e.g. by using a programmable
34 spatial light modulator (SLM). SLMs allow for rapid control of the structured
35 illumination pattern in specimens [3-6].

36 Other than improving the acquisition rates of SIM and working in thick
37 specimens [2,5,7], pushing SIM beyond the factor of two in resolution is the most
38 pressing aim of contemporary SIM development efforts. This can be achieved by

39 introducing a non-linear photo-response of the fluorescence emission to the excitation
40 intensity. Saturating the excited state of fluorophores is the possibility to achieve the
41 required nonlinearity to do NL-SIM [9-12]. However, reaching a saturation of the excited
42 state requires high illumination intensities, which photo-damages cells and quickly
43 photo-bleaches fluorophores. NL-SIM can also be experimentally realized by using
44 patterned activation to saturate either a fluorescent on state or off state of reversibly
45 photoswitchable fluorescent proteins (RSFPs) to obtain the desired nonlinear photo-
46 response emission.

47 In the past years, Dronpa used to be the favorite candidate of the RSFPs in
48 NL-SIM experiments [11, 12]. Despite its low photostability after few switching cycles
49 and its long relaxation time Dronpa offers high quantum yields. More recently, rsEGFP
50 attracted a lot of interest due to its high photostability allowing for > 1,200 switching
51 cycles [13]. However, its quantum yield is low and this results in low signal-to-noise
52 ratios (SNRs). Low SNRs are a major problem in acquiring sufficient photons for NL-SIM
53 reconstruction. Recently, Li et al. [3] presented a major break-through by conducting
54 NL-SIM imaging with newly developed RSFP Skylan-NS. The use of Skylan-NS provided
55 resolutions as low as 45 nm [3]. The RSFP Skylan-NS hereby also offers high quantum
56 yield and long photostability [14]14. However, the use of Syklan-NS currently is
57 seriously limited by the need of using a 405 nm laser for activation of RSFP Skylan-NS.
58 Simultaneously, a 488 nm laser was needed to excite and deactivate the fluorophore in a
59 multi-linear mode of operation [15]. However, this design has several serious limitations.
60 First, the activation pattern in the specimen has to be generated by illuminating the SLM
61 with both the 405 nm and the 488 nm laser. Although the 405 nm laser is outside of the
62 recommended safe working range of the SLM and extended use may damage the device.
63 Second, 405 nm is nearly outside the range of supported wavelengths of the objective.
64 Hence producing a perfect illumination pattern that is very precisely aligned to the 488
65 nm illumination pattern at every position is rather quite challenging. We here
66 demonstrate that these limitations can be overcome by a NL-SIM setup using the newly
67 developed fast-switching fluorescent protein, Kohinoor [16]. The excitation maximum of
68 Kohinoor is at 495 nm and its emission maximum is at 514 nm. Further advantage of
69 Kohinoor is the property of positive photoswitchability (Fig 1a) [16]. We achieved
70 NL-SIM by activating Kohinoor with 488 nm patterned illumination to the fluorescent
71 ground state S_0 . In the meantime, the illumination light of 488 nm also excites the
72 fluorophore to the fluorescent excited state S_1 . 405 nm illumination deactivates the
73 fluorophore to the nonfluorescent dark state S_{off} over a large field of view. Since in
74 contrast to the use of Skylan-NS, the 405 nm laser is not used for excitation to generate
75 the nonlinear fluorescent emission response to the illumination intensity, the 405 nm
76 light of the laser does not need to be sent to the SLM. Our NL-SIM design therefore
77 protects the SLM, ensures optimal illumination patterns and yields high SNR. Besides,
78 the data acquisition method is as simple as in linear SIM (LSIM) configurations [6].



79

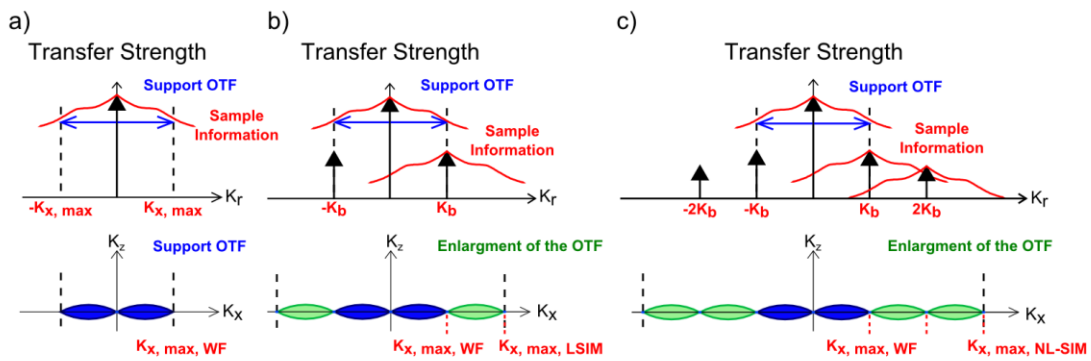
80 **Fig 1. Illustration of switching behavior of Kohinoor photoswitchable proteins and**
 81 **simulation of fluorescent emission distribution in two-beam NL-SIM scheme.** a) The
 82 Kohinoor in our experiment. Excitation: 488 nm, photoactivation: 488 nm, photodeactivation:
 83 405 nm. S_{off} , S_0 , S_1 and k_R denote the nonfluorescent dark state, the fluorescent ground
 84 state, the fluorescent excited state and the rate constant of fluorescence, respectively. b)
 85 Simulated dependence of the lateral fluorescent emission distribution in a steady state
 86 situation with no simultaneous photodeactivation (blue solid line, all activated) and
 87 photodeactivation with high powered 405 nm illumination (red solid line) in which the
 88 relative transition rate of the 405 nm laser is equal to $0.1K_R$. The transition rate is
 89 proportional to the laser intensity. The blue dashed lines of (1) to (4) correspond to lateral
 90 fluorescent emission distribution in a steady state with simultaneous photodeactivation in
 91 which the relative transition rate of the 405 nm laser is $0.02K_R$, $0.04K_R$, $0.06K_R$ and $0.08K_R$,
 92 respectively. c) Absolute diffraction order strength. d) Relative diffraction order strength. In
 93 the steady state the amplitude of 3^{rd} diffraction order is far below the noise level and the 2^{nd}
 94 diffraction order is barely enough to be used for NL-SIM image reconstruction. The blue
 95 dashed lines of (1) to (4) show the corresponding relative order strength at different relative
 96 transition rate of the 405 nm laser.

97 Methods and Materials

98 Principle of NL-SIM

99 In an optical system, the optical transfer function (OTF) defines the maximum
 100 transferable frequency. High frequency information outside the passband of the OTF is
 101 lost and thus fine details in specimens cannot be seen. In linear SIM, fluorophores are

102 illuminated with a sinusoidal illumination pattern resulting in emission pattern
 103 proportional to the illumination intensity. The detected image in the image plane is
 104 described by the convolution of the point spread function and the effective emission
 105 pattern. By unmixing these two components and shifting the object components
 106 attached to the zeroth and $\pm 1^{\text{st}}$ illumination orders (Fig 2b) back to coincide with the
 107 zeroth order in Fourier space the effective OTF is expanded. High-frequency object
 108 information outside the passband of the original OTF is now in the support region of the
 109 effective OTF and hence, a superresolved image with two-fold resolution improvement
 110 can be reconstructed.



111
 112 **Fig 2. Fourier transform components of an emission pattern and corresponding effective**
 113 **OTF.** a) Fourier transform of an emission pattern generated by uniform illumination. Sample
 114 information in Fourier space lying inside the region of support of the OTF defined by a cut-
 115 off frequency of $K_{x,max}$ is detectable. b) Fourier transform of a sinusoidal emission pattern
 116 generated by linear structured illumination. Two $\pm 1^{\text{st}}$ diffraction orders with frequency of $\pm K_b$
 117 are generated and to both the same sample information as also the zero diffraction order is
 118 attached. Hence high-frequency sample information is down shifted into the support region
 119 of the OTF. Accordingly, the effective OTF is enlarged. c) Fourier transform of non-sinusoidal
 120 effective excitation distribution is created due to the nonlinear dependence of the emission
 121 rate on the excitation intensity. This nonlinearity introduces higher-order harmonics in
 122 Fourier space all attaching the same sample information. However, the noise limits the
 123 possible resolution-enhancement and thus the effective OTF cannot be expanded arbitrarily.
 124 Only signal that can be discriminated from noise contributes to the reconstructed image.

125 In NL-SIM, an effective non-sinusoidal emission pattern is generated by
 126 introducing nonlinear emission dependence on the illumination intensity. This can be
 127 done by saturating the state of transition of fluorophores. The non-sinusoidal effective
 128 excitation pattern contains higher-order harmonics that all carry the same object
 129 information in Fourier space. Consequently, separating object information from higher-
 130 order harmonics and rejoining them to the central order in frequency space yields, in
 131 principle, infinite resolution. Practically, however, the resolution remains affected by the
 132 saturation level and only the frequency orders above the noise level are detectable.
 133 These two aspects are the key limiting parameters for the final NL-SIM resolution
 134 (Fig 2c).

135 In this work, we demonstrate an experimental design that achieves NL-SIM by
 136 using RSFP Kohinoor. We activate and excite Kohinoor by 488 nm laser with sinusoidal
 137 illumination pattern and deactivate by wide-field illumination with a 405 nm laser. In
 138 the steady state approximation the population of three transition states of fluorophores,
 139 in dark state $\langle S_{off} \rangle$, in fluorescent ground state $\langle S_0 \rangle$ and in excitation state $\langle S_1 \rangle$
 140 are constant. The temporal derivative of the population of each state is zero.

$$0 = \frac{\partial \langle S_{off} \rangle}{\partial t} = k_{405} \langle S_0 \rangle - k_{488} \langle S_{off} \rangle \quad (1)$$

$$0 = \frac{\partial \langle S_0 \rangle}{\partial t} = k_{488} \langle S_{off} \rangle - k_{405} \langle S_0 \rangle - \varepsilon_{rel} k_{488} \langle S_0 \rangle + k_R \langle S_1 \rangle \quad (2)$$

$$0 = \frac{\partial \langle S_1 \rangle}{\partial t} = \varepsilon_{rel} k_{488} \langle S_0 \rangle - k_R \langle S_1 \rangle \quad (3)$$

$$1 = \langle S_0 \rangle + \langle S_{off} \rangle + \langle S_1 \rangle \quad (4)$$

141 k_R represents the rate constant of fluorescence. k_{405} and k_{488} are the transition rates of
 142 the 405 nm and the 488 nm laser proportional to the laser intensity, respectively and
 143 both are functions of lateral position in specimens. ε_{rel} represents the relative activation
 144 efficiency. We here assumed ε_{rel} to be one as there is apart from an overall sample
 145 brightness effect no change in the general behavior expected in intensity ranges far from
 146 singlet excited state saturation. By combining Eq. (1), Eq. (2), Eq. (3) and Eq. (4), the Eq.
 147 (4) can be rewrite as

$$\begin{aligned} 1 &= \frac{k_R}{k_{488}} \langle S_1 \rangle + \frac{(k_{405} + \varepsilon_{rel} k_{488}) \frac{k_R}{\varepsilon_{rel} k_{488}} \langle S_1 \rangle - k_R \langle S_1 \rangle}{k_{488}} + \langle S_1 \rangle \\ &= (k_{405} + \varepsilon_{rel} k_{488}) \frac{k_R}{\varepsilon_{rel} k_{488}^2} \langle S_1 \rangle + \langle S_1 \rangle \\ &= \left(\frac{1}{k_{488}} + \frac{k_{405}}{\varepsilon_{rel} k_{488}^2} + \frac{1}{k_R} \right) k_R \langle S_1 \rangle \end{aligned} \quad (5)$$

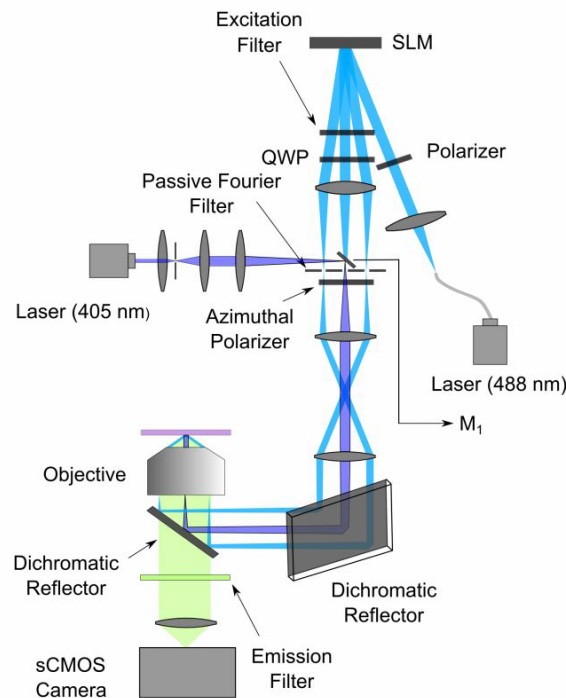
148 The fluorescent emission distribution can be then expressed as

$$k_R \langle S_1 \rangle = \frac{1}{\left(\frac{1}{k_{488}} + \frac{k_{405}}{\varepsilon_{rel} k_{488}^2} + \frac{1}{k_R} \right)} \quad (6)$$

149 Hence, in the steady state emission pattern is no longer sinusoidal and higher-
 150 order harmonics are created (Fig 1b). However, the saturation level by this method is
 151 limited and consequently only the first higher-order harmonics ($\pm 2^{\text{nd}}$ diffraction orders)
 152 can be pushed above the noise level (Fig 1d). In most situations, while the sample is
 153 illuminated by 405 nm and 488 nm lasers simultaneously, this involves activation,

154 excitation and deactivation happening simultaneously. Nevertheless, the acquisition
155 method is as simple as in LSIM as there is no switching time between two lasers and no
156 extra waiting time for deactivation.

157 Our NL-SIM system is adopted from a two-beam fastSIM setup, described in [6] as
158 depicted in Fig 3. A small mirror (see Fig 3, M_1) is used to integrate the 405 nm laser into
159 the system in the Fourier plane of the SLM. The 405 nm can focus to one of the triangular
160 linear polarizers of an azimuthally patterned polarizer resulting in uniform illumination
161 of the specimen. The structured illumination grating patterns, hereafter referred to as
162 the illumination grating, are generated by an SLM (SXGA-3DM, 1280×1024 pixels, Forth
163 Dimension Displays, UK) and are projected into specimens. The illumination grating is
164 rotated to six orientations, separated by $\sim 30^\circ$ to achieve near isotropic resolution
165 improvement. In order to derive high-resolution object information from zeroth, $\pm 1^{\text{st}}$
166 and $\pm 2^{\text{nd}}$ diffraction orders, for each grating orientation, five images at phases $0, 2\pi/5,$
167 $4\pi/5, 6\pi/5$ and $8\pi/5$ are recorded in the NL-SIM system. In total, 30 raw images are
168 used for the reconstruction of a NL-SIM image.



169

170 **Fig 3. Fast nonlinear structured illumination microscope setup.** A 488 nm laser is coupled
171 into a single-mode polarization-maintaining fiber for activation of the fluorophore. A
172 polarizer ensures linear polarization of the light before the SLM. The SLM displays binary
173 grating patterns and offers rapid control in the liquid crystals and thus fast switching of the
174 illumination grating pattern. An excitation filter is used for cleaning up fluorescence
175 generated by the SLM. A quarter wave plate (QWP) together with the azimuthal polarizer
176 ensures azimuthal polarization of the light in all directions of grating orientation to achieve

177 high contrast of grating pattern in the sample plane. The zero diffraction order of 488 nm
178 laser is blocked by the backside of a small mirror (M_1) used to reflect the 405 nm laser into
179 the system near the Fourier plane of the SLM. The $\pm 1^{\text{st}}$ diffraction orders of the 488 nm laser
180 pass through a passive filter at the Fourier plane of the SLM. Both 405 nm and 488 nm lasers
181 are sent to the sample plane through a 63 \times oil immersion microscope objective (NA 1.46,
182 alpha Plan-Apochromat, Korr TIRF, Zeiss, Germany) Fluorescence is focused and collected
183 through an emission filter on the sCMOS camera (Orca Flash 4, Hamamatsu, Japan).

184 **Sample preparation and cell line information**

185 **pcDNA3-Kohinoor-Actin** [16] was amplified using the NucleoBond® Xtra Midi/Maxi
186 kit (MACHERY-NAGEL GmbH & Co. KG).

187 **HeLa cells** were maintained in DMEM medium (Gibco® Life technologies)
188 supplied with 10% fetal bovine serum, 0.1 mM gentamicin and 1 \times penicillin (100
189 units/ml)-streptomycin (100 $\mu\text{g}/\text{ml}$) and cultured at 37°C under 5% CO₂.

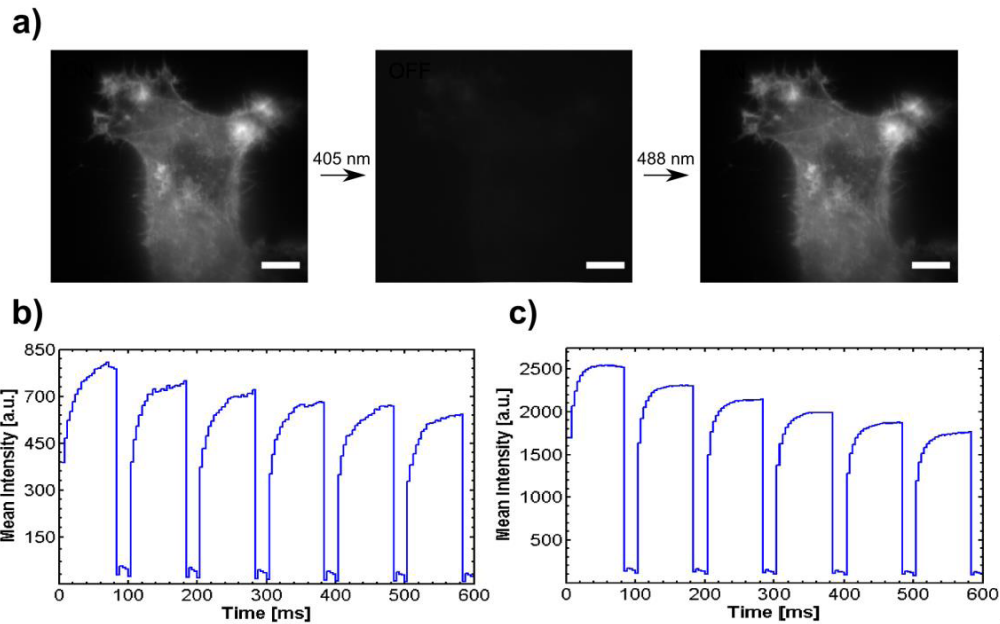
190 **For transfection and fixation**, almost confluent HeLa cells were seeded into a 6
191 well plate and transfected 24 h later following the user manual of the TurboFect
192 transfection reagent (Thermo Scientific, R0531). After 48 h, transfected HeLa cells were
193 seeded (1:3 dilution) onto high precision microscope cover glasses (18 \times 18 mm) and
194 cultured for another 24 h. Afterwards, cells were fixed with 1 ml pre-warmed 4% (w/v)
195 PFA for 15 min at 37°C. After washing with PBS, the coverslips were mounted upside
196 down onto slides using Mowiol® 4-88 (Calbiochem), dried overnight at room
197 temperature and stored at 4°C.

198 **Results and Discussion**

199 **Photoswitching test on Kohinoor**

200 We first tested the photoswitching of Kohinoor on fixed HeLa cells transfected with
201 Kohinoor-actin using alternating uniform laser illuminations at 405 nm and 488 nm
202 (Fig. 4a-c). In each cycle of the photoswitching examination, we acquired 20 images,
203 each with effective 488 nm laser illumination for 4 ms subsequent deactivation with the
204 405 nm laser for ~ 20 ms. Two light intensity combinations of the 488 nm laser and 405
205 nm lasers at the sample were tested, 14 W/cm² (488 nm) and 27 W/cm² (405 nm)
206 (Fig. 4b) and 20 W/cm² and 32 W/cm² (Fig. 4c), respectively. We observed very efficient
207 deactivation even at low powers of the 405 nm laser.

208 In contrast, high illumination intensities of the 488 nm laser made a significant
209 difference and saturated the fluorophore faster and also induced more fluorescence. The
210 increase of photobleaching due to the higher intensities turned out to be minimal
211 (Fig. 4b, c). Additionally, photobleaching turned out to be much slower than the NL-SIM
212 acquisition anyway (Fig. 4b, c). Acquisition of 30 raw images for the reconstruction of an
213 2D NL-SIM image took only ~ 52 ms. Thus, even higher laser intensities can be used for
214 excitation NL-SIM imaging making the use of Kohinoor very powerful.

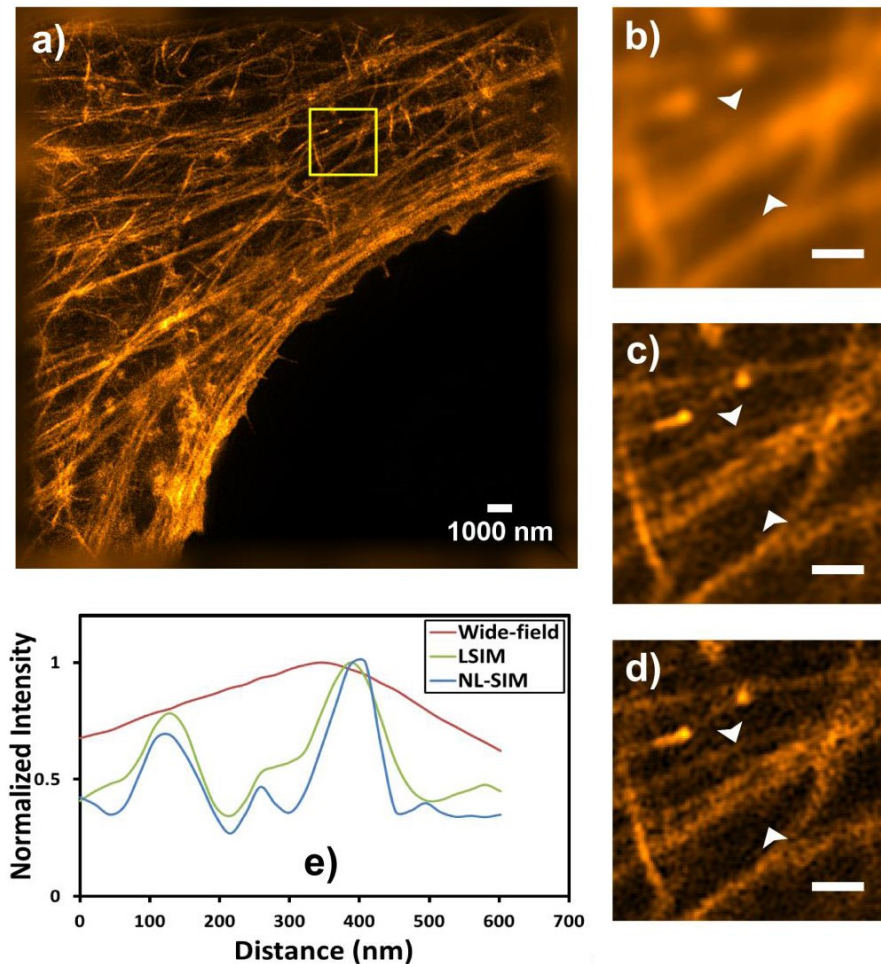


215
 216 **Fig 4. Repeated photoswitching test on Kohinoor-actin expressed in a fixed HeLa cell.** a) A
 217 fixed HeLa cell expressing Kohinoor-actin was switched on and excited by a 488 nm laser. A
 218 405 nm laser was used to switch the fluorophore off. Scale bar: 5 μm . b) Photoswitching of
 219 Kohinoor over time with the light intensity of the 488 nm laser at 14 W/cm^2 and of the 405
 220 nm laser at 27 W/cm^2 at the sample. c) Photoswitching of Kohinoor over time with the light
 221 intensity of the 488 nm laser at 20 W/cm^2 and of the 405 nm laser at 32 W/cm^2 at the
 222 sample.

223 We next imaged the actin filaments in 2D with our two-beam NL-SIM microscope
 224 in which the illumination of the 488 nm laser is under nearly total internal reflection
 225 conditions (Fig 5 a-d). The exposure time of the structured illumination at 488 nm laser
 226 excitation in each raw image was 12 ms. The 405 nm laser was switched on 0.22 seconds
 227 before the acquisition started and was kept on until the end of acquisition. While the
 228 camera reads out each raw image, the 405 nm illumination depletes residual on states
 229 for ~ 2.494 ms. The illumination intensity used was 56 W/cm^2 and 11 W/cm^2 at the
 230 sample for the 488 nm and the 405 nm lasers, respectively. 30 raw images were
 231 acquired in ~ 52 ms for one 2D NL-SIM image reconstruction. The pixel size in
 232 reconstructed NL-SIM image corresponds to 21.5 nm.

233 In contrast to a wide-field image obtained by summing all raw images, which did
 234 not provide resolution of fine F-actin structures at all (Fig 5b), linear SIM already yielded
 235 high resolution images (Fig. 5c). Reconstructing images from NL-SIM with one higher-
 236 order harmonic even increased this resolution further (Fig 5d). The actin filaments
 237 detected by Kohinoor-actin became less blurry and the more discrete appearance of
 238 these fine structures in HeLa cells allowed for visualization of details that were invisible
 239 in wide-field images (Fig 5b) and less clear in LSIM images (Fig 5c).

240 Quantitative analyses of actin filaments by line scans confirmed that the
241 impression that filamentous actin structures obtained by NL-SIM were thinner and more
242 discrete than in wide field and LSIM analyses (Fig. 5e).



243 **Fig 5. NL-SIM imaging of a fixed HeLa cell expressing Kohinoor-actin.** a) NL-SIM image in a
244 large field of view. Magnified view of the yellow-boxed region represent conventional wide-
245 field microscopy image b), LSIM image c), and NL-SIM image d). Scale bar in magnified
246 images is 500 nm. e) Normalized intensity profiles between the white triangles in b)-d).
247

248 In LSIM and NL-SIM the underlying assumption is that the sample always
249 behaves predictably. In stark contrast to localization-based methods such as dSTORM,
250 the single-molecule switching is deviating from the continuity assumption. This
251 molecular switching leads to artefacts in the SIM reconstruction, even if many photons
252 can be detected from a single fluorophore. Since the concentration of fluorophores is not
253 very far from the single-molecule regime, we solved this problem by opting for several
254 switching cycles contributing to a single detected image by applying both activation and

255 deactivation simultaneously. This greatly simplifies the acquisition configuration and
256 also prevented our image acquisition from drowning in the noise of molecular switching
257 but a disadvantage of this choice is that the achievable level of non-linearity remained
258 relatively low (see Figure 1d). The final resolution in NL-SIM is improved better than
259 two-fold beyond LSIM.

260 **Conclusion**

261 We confirmed the high photostability and strong fluorescence of Kohinoor in fixed HeLa
262 cells. We used a positively reversibly photoswitchable fluorescent protein Kohinoor to
263 acquire data for nonlinear structured illumination microscopy (NL-SIM) using a fast
264 acquisition system. Thus, the attainable acquisition speed in fast NL-SIM is well suited to
265 follow fast dynamics in biological samples in sub-nanoscale.

266 In order to fully exploit the shown advantages of the NL-SIM set-up with
267 Kohinoor as RSFP for analyses of molecular structures and dynamics in cells, future
268 work will have to focus on accounting for the effect of single-molecule switching. Solving
269 this problem in the future would further increase the resolution improvement achieved
270 beyond standard SIM. A direction of future research to improve the super-resolution
271 method we here describe even further may thus be iterative schemes with preparation
272 steps (activation, depletion) interleaved with detection ideally all contributing to the
273 same camera exposure. This may be achievable with very fast mechanical shutters. Such
274 and other future improvements will help to fully explore dynamic interactions of specific
275 molecular assemblies in living cells in sub-nanoscale with NL-SIM.

276 **Acknowledgements**

277 We thank Robert Kretschmer for comprehensive support with electronics and general
278 practical help; Walter Müller for the useful discussion on image processing; Elen Tolstik,
279 Tatiana Tolstik and Liyan Song for assistance in the biology lab; Aurélie Jost, Ronny
280 Förster and Kai Wicker for helpful advice on experimental design of the NL-SIM
281 microscope.

282 **Author Contributions**

283 Conceived and designed the experiments: HWLW MK MMK BQ RH. Performed the
284 experiments: HWLW WH MK. Analyzed the data: HWLW RH. Contributed reagents/
285 materials/analysis tools: WH YA TN MMK BQ. Wrote the paper: HWLW WH MK MMK BQ
286 RH.

287 **References**

- 288 1. Kner P, Chhun B B, Griffis E R, Winoto L, Gustafsson M G L. Super-resolution video microscopy of
289 live cells by structured illumination. *Nat. Methods*. 2009; 6: 339-342

- 290 2. Shao L, Kner P, Rego E, Gustafsson M. Super-resolution 3d microscopy of live whole cell using
291 structured illumination. *Nature methods*. 2011; 1734: 1–5
- 292 3. Li D, Shao L, Chen B-C, Zhang X, Zhang M, Moses B, et al. Extended-resolution structured
293 illumination imaging of endocytic and cytoskeletal dynamics. *Science*. 2015; 349: aab3500. DOI:
294 10.1126/science.aab3500
- 295 4. Hirvonen L M, Wicker K, Mandula O, Heintzmann R. Structured illumination microscopy of a
296 living cell. *Eur Biophys J*. 2009; 38:807–812. DOI: 10.1007/s00249-009-0501-6
- 297 5. Fiolka R, Shao L, Rego E G, Davidson M W, Gustafsson M. Time-lapse two-color 3D imaging of
298 live cells with doubled resolution using structured illumination. *Proc. Natl Acad. Sci*. 2012; 109:
299 5311–5315
- 300 6. Lu-Walther H W, Kielhorn M, Förster R, Jost A, Wicker K, Heintzmann R. fastSIM: A practical
301 implement of fast structured illumination microscopy. *Methods Appl. Fluoresc*. 2015; 3: 014001
- 302 7. Mandula O, Kielhorn M, Wicker K, Krampert G, Kleppe I, Heintzmann R. Line scan - structured
303 illumination microscopy super-resolution imaging in thick fluorescent samples. *Opt. Exp*. 2012;
304 20: 24167–24174
- 305 8. Song L, Lu-Walther H W, Förster R, Jost A, Kielhorn M, Zhou J, et al. Fast structured illumination
306 microscopy using rolling shutter cameras. *Meas. Sci. Technol*. 2016; 27: 055401
- 307 9. Heintzmann R, Jovin T M, Cremer C. Saturated patterned excitation microscopy - a concept for
308 optical resolution improvement. *J. Opt. Soc. Am. A*. 2002; 19: 1599–1609
- 309 10. Gustafsson M G L. Nonlinear structured-illumination microscopy: Wide-field fluorescence
310 imaging with theoretically unlimited resolution. *Proc. Natl Acad. Sci*. 2005; 102(37): 13081–
311 13086
- 312 11. Hirvonen L, Mandula O, Wicker K, Heintzmann R. Structured illumination microscopy using
313 photoswitchable fluorescent proteins. *Proc. Of SPIE*. 2008; 6861: 68610L. DOI:
314 10.1117/12.763021
- 315 12. Rego E H, Shao L, Macklin J J, Winoto L, Johansson G A, Kamps-Hughes N, et al. Nonlinear
316 structured-illumination microscopy with a photoswitchable protein reveals cellular structures at
317 50-nm resolution. *Proc. Natl. Acad. Sci*. 2012; 109: E135–E143. DOI: 10.1073/pnas.1107547108;
318 pmid: 22160683
- 319 13. Grotjohann T, Testa I, Leutenegger M, Bock H, Urban N T, Lavoie-Cardinal F, et al. Diffraction-
320 unlimited all-optical imaging and writing with a photochromic GFP. *Nature*. 2011; 478: 204-208.
321 DOI:10.1038/nature10497
- 322 14. Zhang X, Chen X, Zeng Z, Zhang M, Sun Y, Xi P, et al., Development of a reversibly switchable
323 fluorescent protein for super-resolution optical fluctuation imaging (SOFI). *ACS Nano* 2015; 9:
324 2659–2667 DOI: 10.1021/nn5064387; pmid: 25695314
- 325 15. Heintzmann R, Cremer C. Verfahren zur Erhöhung der Auflösung optischer Abbildung; German
326 Patent Nr. 199 08 883 A1, September 7, 2000, priority Mar. 2nd, 1999; Heintzmann R, Cremer C.
327 Method and Device for Representing an Object, WO 0052512, Patent Applicant: Max-Planck
328 Society, priority (see above), 1999.
- 329 16. Tiwari D K, Arai Y, Yamanaka M, Matsuda T, Agetsuma M, Nakano M, et al. A fast- and
330 positively photoswitchable fluorescent protein for ultralow-laser-power RESOLFT nanoscopy.
331 *Nat. Methods*. 2015; 12: 515–518. DOI:10.1038/nmeth.3362

Publication 5

Shedding light on host niches: label-free in situ detection of *Mycobacterium gordonae* via carotenoids in macrophages by Raman microspectroscopy

Silge A, Abdou E, Schneider K, Meisel S, Bocklitz T, Lu-Walther H-W, Heintzmann R, Rösch P, Popp J.

[HWLW5] Silge A, Abdou E, Schneider K, Meisel S, Bocklitz T, Lu-Walther H-W, Heintzmann R, Rösch P, Popp J. Shedding light on host niches: label-free in situ detection of *Mycobacterium gordonae* via carotenoids in macrophages by Raman microspectroscopy. *Cellular Microbiology*. 2015; 17:832-842.

doi: <http://dx.doi.org/10.1111/cmi.12404>

Beteiligt an (Zutreffendes ankreuzen)

Author	Silge A	Lu-Walther H-W
Konzeption des Forschungsansatzes	×	
Planung der Untersuchungen	×	
Datenerhebung	×	×
Datenanalyse und -interpretation	×	×
Schreiben des Manuskripts	×	
Vorschlag Anrechnung Publikationsäquivalente	1,0	0,5

All authors revised, edited and proof read the final manuscript.

Reprinted with kind permission from the John Wiley & Sons, Inc.

Copyright © 1999-2016 John Wiley & Sons, Inc. All Rights Reserved.

Shedding light on host niches: label-free *in situ* detection of *Mycobacterium gordonae* via carotenoids in macrophages by Raman microspectroscopy

Anja Silge,^{1,2} Elias Abdou,^{1,2,4} Kilian Schneider,^{1,2}
Susann Meisel,^{1,2} Thomas Bocklitz,^{1,2}
Hui-Wen Lu-Walther,³ Rainer Heintzmann,^{1,3,5}
Petra Rösch^{1,2} and Jürgen Popp^{1,2,3*}

¹Institute of Physical Chemistry and Abbe Center of Photonics, Friedrich-Schiller-University Jena, Helmholtzweg 4, Jena D-07743, Germany.

²InfectoGnostics Research Campus Jena, Center for Applied Research, Philosophenweg 7, Jena D-07743, Germany.

³Leibniz Institute of Photonic Technology, Albert-Einstein-Strasse 9, Jena D-07745, Germany.

⁴Center for Sepsis Control and Care, University Hospital Jena, Erlanger Alee 101, Jena D-07747, Germany.

⁵Randall Division of Cell and Molecular Biophysics, King's College London, London SE1 1UL, UK.

Summary

Macrophages are the primary habitat of pathogenic mycobacteria during infections. Current research about the host–pathogen interaction on the cellular level is still going on. The present study proves the potential of Raman microspectroscopy as a label-free and non-invasive method to investigate intracellular mycobacteria *in situ*. Therefore, macrophages were infected with *Mycobacterium gordonae*, a mycobacterium known to cause inflammation linked to intracellular survival in macrophages. Here, we show that Raman maps provided spatial and spectral information about the position of bacteria within determined cell margins of macrophages in two-dimensional scans and in three-dimensional image stacks. Simultaneously, the relative intracellular concentration and distributions of cellular constituents such as DNA, proteins and lipids

provided phenotypic information about the infected macrophages. Locations of bacteria outside or close to the outer membrane of the macrophages were notably different in their spectral pattern compared with intracellular once. Furthermore, accumulations of bacteria inside of macrophages exhibit distinct spectral/molecular information because of the chemical composition of the intracellular microenvironment. The data show that the connection of microscopically and chemically gained information provided by Raman microspectroscopy offers a new analytical way to detect and to characterize the mycobacterial infection of macrophages.

Introduction

Intracellular bacteria are capable of inducing persistent infections in their hosts. Those infections can manifest as acute or chronic disease as well as being clinically asymptomatic with the potential to get reactivated (Monack *et al.*, 2004). Mycobacterial infections are characterized by intracellular survival and a tight interaction between the bacterium and the host cells (Nguyen and Pieters, 2005). The genus *Mycobacterium* includes *Mycobacterium tuberculosis*, the causative agent of tuberculosis (TB). However, diseases caused by mycobacteria other than TB are also of interest (Mazumder *et al.*, 2010; Izaguirre Anariba *et al.*, 2014). The level one non-tuberculous *Mycobacterium gordonae* was reported to cause necrotizing inflammation in immunosuppressed and immunocompetent individuals (Mazumder *et al.*, 2010; Izaguirre Anariba *et al.*, 2014). In a peritonitis case report in 2011, the miss-detection of *M. gordonae* by conventional identification methods in the primary diagnosis, caused a reminiscence of the symptoms after 2 weeks of effective treatment (Hirohama *et al.*, 2011). The pathogenicity of those mycobacteria relies on their capacity to survive and to multiply in professional or non-professional cells of the host immune system. In absence of treatment and during infection, the bacteria tend to disseminate in the host organs where granulomas are formed (Wayne and Sohaskey, 2001). Granulomas are organized

Received 21 October, 2014; revised 1 December, 2014; accepted 3 December, 2014. *For correspondence. E-mail juergen.popp@uni-jena.de; juergen.popp@ipht-jena.de; Tel. (+49) 364194 8320; Fax (+49) 36 4194 8302.

© 2014 John Wiley & Sons Ltd

structures rich in macrophages and lymphocytes that act as functional units modulated by the microorganisms themselves and the immune status of the host (Mattila *et al.*, 2013). They either restrain the bacterial growth and support the intracellular persistence (anti-inflammatory phenotype) or they become necrotic granuloma (pro-inflammatory phenotype) having a bactericidal function (Lugo-Villarino *et al.*, 2012). Macrophages represent the primary habitat of mycobacteria and play a key role in the formation and function of granulomas. The microenvironment of the granuloma is characterized by different phenotypes of the macrophages like epithelioid forms, multinucleated giant cells or foamy macrophages with a high content of intracellular lipids (Lugo-Villarino *et al.*, 2012).

The diagnosis and investigation of a mycobacterial infection in its early stages is important, as this allows a prompt treatment. It highly avoids the transformation of granulomatous bodies and furthermore reduces the risk of progression to necrosis and diseases like TB. The broad spectrum of mycobacterial infections, especially the multiple microenvironments that support bacterial replication, persistence or killing on the cellular level and within granulomatous structures required series of detailed investigations. Thus, different perspectives are needed to build up a multidimensional image of the heterogeneous biological processes in this context. The diversity of possible investigations provided by microscopic methods, biochemical assays and genome-based techniques are desperately required to analyse the bimodal distribution between active and latent mycobacterial infections and their numerous subsets (Barry *et al.*, 2009). All possible analytical tools have to be arranged such that strong synergies of individual analytical contributions identify new targets for therapies.

Raman microspectroscopy is a valuable analytical technique element to provide complementary insights in the field of mycobacterial infections. Especially, as Raman microspectroscopy can proceed on a single-cell level. This is important for the biochemical characterization of the individual infection stages and events represented by a subset of heterogeneous cell populations after infection, which are observed by fluorescence and electron microscopy. The chemical composition of cells or tissue sections, for example the cellular lipid homeostasis, which changes after infection, is mainly investigated by electron microscopy or complex biochemical assays and HPTLC (High Performance Thin Layer Chromatography) from a whole cell population of one preparation (Caceres *et al.*, 2009; Melo and Dvorak, 2012; Mattos *et al.*, 2014). Raman microspectroscopy could provide additional and more detailed information on the single-cell level without any further labelling or preparation by probing the spectral character of cellular struc-

tures space-resolved and *in situ* (Diem *et al.*, 2004; Krafft *et al.*, 2005; Hartmann *et al.*, 2012; Schie and Huser, 2013a). This method is non-invasive and therefore provides an application that can easily be combined with other microscopical, histopathological and biochemical methods (Diem *et al.*, 2004; Matthäus *et al.*, 2012; Ramoji *et al.*, 2012; Bräutigam *et al.*, 2013; Schie and Huser, 2013a; Stiebing *et al.*, 2014). Because of the provided chemical contrast and molecular selectivity, Raman microspectroscopy is able to analyse the chemical dynamics of subcellular habitats even in living cells (Pully *et al.*, 2011; Bräutigam *et al.*, 2013; Schie *et al.*, 2014).

The principle of this method is the non-invasive illumination of a biological specimen with a monochromatic laser, and the subsequent analysis of the inelastically scattered light. In doing so, individual cells can be measured applying a mapping approach resulting in a two-dimensional array of 'pixels' (spatial elements). Each recorded Raman spectrum contains information about the pixel coordinates and signal intensities that can be used to construct a chemical image of the sample. Raman maps can be acquired from different sample layers along the z-direction and thus display a three-dimensional space. Because of these capabilities, Raman microspectroscopy is suited for the localization of foreign matter directly in the cellular microenvironment with a spatial resolution of approximately 1 μm (Matthäus *et al.*, 2008; Bräutigam *et al.*, 2014).

The scope of the present study was to demonstrate the potential of Raman microspectroscopy as a label-free technique for the *in situ* detection and localization of *M. gordonae* in macrophages. *M. gordonae* was used as a model organism for bacteria that cause persistent infections linked to intracellular survival in macrophages and granuloma formation (Mazumder *et al.*, 2010; Izaguirre Anariba *et al.*, 2014). The mouse macrophage cell line J774 was chosen for the infection experiment, as it is a widely used and established model from which to study intracellular bacteria including mycobacteria (Kuehnel *et al.*, 2001). Applying a mycobacterial-specific fluorescence staining kit and plate count proved the positive infection and the intracellular survival of *M. gordonae* in J774 cells. The acquired Raman data were used to construct colour-coded maps of the macrophages by an expert knowledge method via the integration over relevant Raman bands. By doing so, the spectral characteristics of intra- and extracellular bacterial positions were determined and the spectral phenotype of the infected macrophages was analysed. Based on the findings of the present work, the facilities and the prospects of Raman microspectroscopy to study the microenvironment of intracellular bacilli, and thus the host pathogen interaction, are discussed.

Methods

Bacteria and cell lines

M. gordonae were obtained from the DSMZ (Deutsche Sammlung von Mikroorganismen und Zellkulturen GmbH, Braunschweig, Germany) and cultivated at 37°C in Middlebrooks 7H10 media supplemented with oleic acid, dextrose and catalase for 9 days. The murine macrophage cell line J774.A1 were obtained from DSMZ and cultivated at 37°C under 5% of CO₂ in Dulbecco's Modified Eagle medium (DMEM) supplemented with 10% heat-inactivated foetal bovine serum.

Sample preparation – cell infection

A 1 µl inoculation loop was used to scrap *M. gordonae* from the agar plate. The bacteria were suspended and washed twice in 100 µl distilled water. One microlitre of the bacterial suspension was applied on a CaF₂ slide for single-cell Raman measurements of *M. gordonae*.

Macrophages were grown on calcium fluoride (CaF₂) slides (Crystal, Berlin, Germany) in 35 mm petri dishes (5 × 10⁵ cells) for 24 h. Infection was performed with 2 ml pure DMEM plus 1 mL of bacterial suspension in the late log phase of growth (DMEM), corresponding to a multiplicity of infection of 30. After 3 h, the infection was stopped by removing the bacterial suspension and washing the cells twice with phosphate-buffered saline (PBS, VWR International, Dresden, Germany). Cells were further incubated for a post-infection phase of 24 h with 50 µg ml⁻¹ of amikacin (Fluka, Buchs, Switzerland). This concentration was found to affect only the viability of extracellular bacteria. For negative control, cells were grown under the conditions mentioned earlier without bacteria in the medium. After 24 h, cells were fixed with 4% paraformaldehyde (Sigma-Aldrich, Buchs, Switzerland) and stored in PBS with 0.05% sodium azide (Sigma-Aldrich, Buchs, Switzerland) at 4°C until further use. The fixation maintains the shape and the height of the cells. For fluorescence microscopy, the macrophages were treated as described, but grown on normal glass slides.

To determine the number of cultivable intracellular bacteria, macrophages were treated as described earlier, but without CaF₂-slides. At 3, 24 and 48 h post-infection, cells were washed twice with PBS and lysed in 3 ml 0.2% triton X-100 (Sigma-Aldrich, Buchs, Switzerland). Cellular lysates were serially diluted with PBS and plated on Middlebrook agar in order to determine the number of cultivable bacteria (CFU/ml). All experiments were performed in duplicate.

Fluorescence microscopy (structured illumination)

For fluorescence microscopy, the fixed macrophages were stained according the procedure of the TB Fluores-

cent Stain Kit M (BD, Heidelberg, Germany) and mounted with Mowiol (Sigma-Aldrich, Buchs, Switzerland). Imaging was done with an Elyra S1 (Zeiss, Oberkochen, Germany), applying an excitation wavelength of 488 nm with the following set-up parameters: filter: BP495-550 + LP750, laser power: 2.2%, exposure time: 100 ms, electron multiplying charge-coupled device (EMCCD) EMCCD gain: 80.

Raman spectroscopic measurements

For Raman measurements a WITec (Ulm, Germany) Model CRM 300, combined with a Zeiss microscope equipped with a Nikon Fluor water immersion objective (60×/1.00, Nikon GmbH, Düsseldorf, Germany) was used. A diode laser provided the excitation wavelength of 785 nm (ca. 45 mW onto the sample). The sample was placed onto a piezo-electrically driven scanning stage and moved through the laser focus in a raster pattern. The back-scattered light was diffracted using a 300 lines per mm grating and detected with a Peltier-cooled electron-multiplying charge-coupled device (–65°C) camera (Andor, Belfast). Spectra were collected with an acquisition time of 1s per measurement position. For each macrophage three 25 × 25 µm Raman maps (step size 0.5 µm = 2500 spectra per Raman map) were acquired with a distance of 2 µm in the z-direction, defined as the apical, the middle and the bottom cell layers. Thus, for each macrophage, a dataset of 7500 spectra was collected (3 × 2500 spectra per layer). In total, 10 infected macrophages were analysed derived from two independent preparations. Data from five non-infected control macrophages were collected from one preparation.

Data analysis

Preprocessing of Raman spectra and the analysis of the sum intensity of characteristic Raman bands (an expert knowledge method) was previously described (Bräutigam *et al.*, 2014). However, in the Supporting Information Fig. S1 the determination of the sum intensity is summarized. In hierarchical cluster analysis, spectra are divided into groups (or cluster) according to their spectral similarities. A detailed description is given in the literature (Diem *et al.*, 2004; Bonifacio *et al.*, 2010). All computations were performed in the statistical language R (R Development Core Team, 2010).

Results and discussion

Performance of infection

For this first Raman measurement of intracellular mycobacteria, we selected the opportunistic pathogen

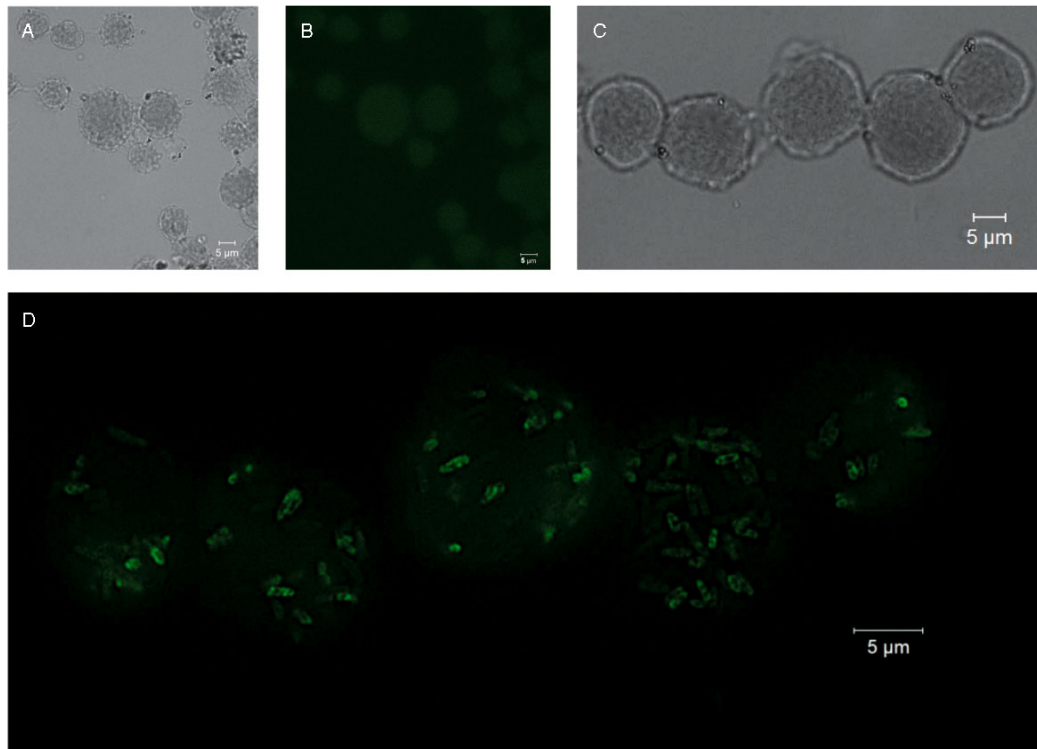


Fig. 1. Macrophages with and without mycobacterial infection stained with auramin O. Bright-field (A) and corresponding fluorescence image (B) of non-infected macrophages is depicted. For macrophages infected with *Mycobacterium gordonae* the bright field and corresponding fluorescence image are shown in panel C and D respectively.

M. gordonae as a mycobacterium that can cause persistent infections linked to the intracellular survival in macrophages and granuloma formation (Mazumder *et al.*, 2010; Izaguirre Anariba *et al.*, 2014). *M. gordonae* produces carotenoids, a bioactive compound used by bacteria against oxidative damage and for membrane rigidity (Liaaen-Jensen and Andrewes, 1972). Its carotenoids are expressed regardless of the presence of light, therefore they can also be produced by intracellular bacteria (Park and DeCicco, 1974). Carotenoids are known to exhibit intensive Raman signals and are therefore particularly suited as biomarkers to study the bacterial distribution in the cell (Jehlicka *et al.*, 2014).

As the mode of infection with *M. gordonae* might be cell line specific, the performance of infection and the intracellular viability of the bacilli were evaluated. The experiment was subdivided into an infection phase of 3 h and post-infection phase of 21 h. Macrophages were allowed to phagocytose the bacteria for three consecutive hours. During the 21 h post-infection period, the macrophages were treated with an antibiotic, making sure that no bacteria survive in the extracellular environment. As control, an aliquot of the antibiotic-containing culture medium from the post-infection period was incubated on an agar

plate and observed for 4 weeks, showing no bacterial growth.

In the next step, a well-established mycobacterial-specific staining procedure was applied to verify via fluorescence microscopy that bacteria were in the macrophages. In contrast to the non-infected control cells that did not show any specific fluorescence (see Fig. 1A bright-field and 1B corresponding fluorescence image) the infected macrophages exhibited specific fluorescence, highlighting the intracellular bacilli (Fig. 1C bright-field and 1D corresponding fluorescence image). These results prove the successful performance of the infection *in situ*. The clearly visible rod shape of the bacilli is evidence that bacteria were not destroyed by intracellular mechanisms. However, to verify the intracellular viability of the bacilli during the experiment, lysates of macrophages 3, 24 and also 48 h after infection with *M. gordonae* were incubated on agar plates. Colonies were observed and counted for each time point (for details see the Supporting Information Fig. S2). Thus, the applied experimental conditions provided a successful uptake of the bacteria by the macrophages and their survival within the host cell, which is of high relevance to study intracellular bacteria.

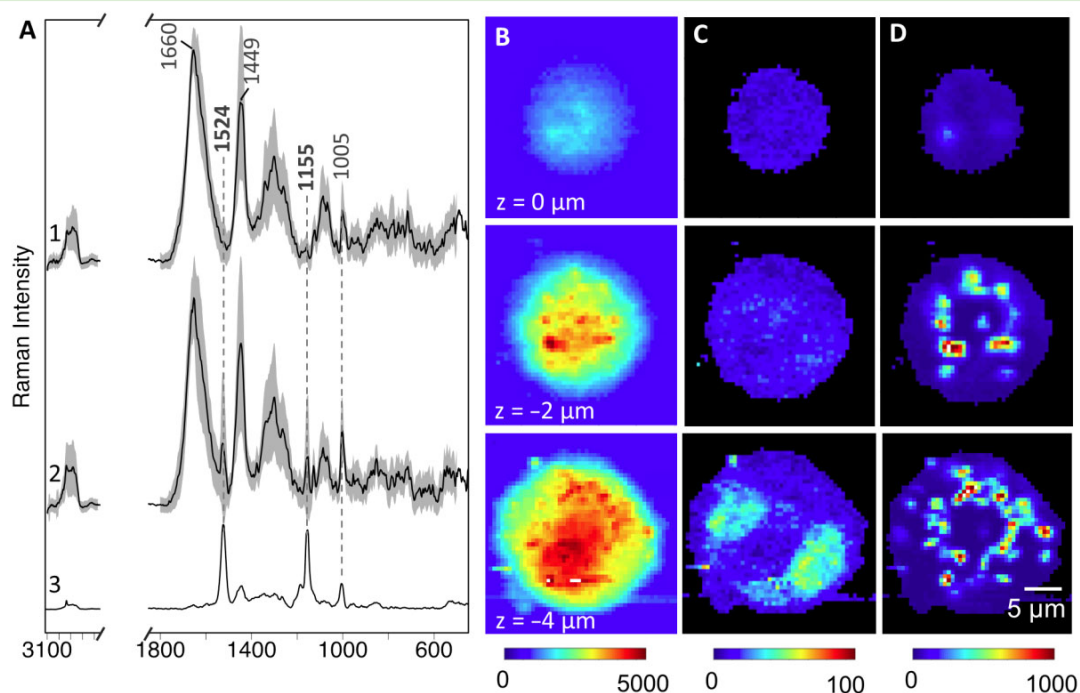


Fig. 2. Raman spectroscopic investigation of macrophages. Left side: Representative spectral profiles from the Raman maps of a non-infected control (1) and an infected macrophage (2) are plotted (A). The grey zone around each spectrum visualizes the standard deviation referring to each individual spectrum of the Raman map ($n = 2500$ spectra). A Raman spectrum of *Mycobacterium gordonae* is plotted for comparison (3). Right side: Raman false colour images of the three cell layers of one single infected macrophage. B. The intensity distributions of typical cell signals at 1449 and 1660 cm^{-1} for $z = 0, -2$ and $-4 \mu\text{m}$ are plotted. C. The intensity of the Raman signal at 785 cm^{-1} for each cell layer within the determined cell margins. D. The sum intensity of the bacterial carotenoid signals at 1524 and 1155 cm^{-1} for each cell depth are shown within the determined cell margins. The sum intensity of the respective signals is represented by the colour scales.

Raman microspectroscopy of infected macrophages

The intracellular survival of bacteria in special host niches poses several fundamental biological questions, e.g. the host–pathogen interaction during persistent infection (Monack *et al.*, 2004). In order to localize *M. gordonae* *in situ* without any labelling or preparation techniques, the whole macrophage was mapped by grid-defined Raman measurements. In Fig. 2A, spectral profiles of a non-infected and an infected macrophage (spectra 1 and 2, respectively) were determined by calculating the mean spectra of the cell layer where the highest contribution of the nucleus Raman signal was detectable. Within this cell layer, the highest variation on biochemical components in the cell is expected. The standard deviation for each map is visualized as a grey zone around the mean spectra. Both spectra exhibit Raman signals (1660, 1449 cm^{-1}), which are ubiquitous distributed all over the cell because they result from a strong overlap of Raman signals of general cell components. The signal at 1660 cm^{-1} can be assigned to the C = C stretching vibration of unsaturated fatty acids and the amid I band of proteins. The signal at

1449 cm^{-1} is assigned to the CH_2 deformation vibration, which occur in lipids and proteins. Depending on the lipid to protein ratio, those Raman bands can shift in their wavenumber position (about $\pm 10 \text{cm}^{-1}$) or varies in their band shape, for further details see Krafft *et al.* (2005). The ring-breathing mode of phenylalanine (Phe) at 1005 cm^{-1} (Movasaghi *et al.*, 2007) is also visible in both spectra. Distinct differences between the two spectra can be explained with the Raman signals of *M. gordonae* (spectrum 3). The single-cell Raman spectrum of *M. gordonae* is dominated by three specific Raman bands at 1005, 1155 and 1524 cm^{-1} , that can be assigned to carotenoids (Jehlicka *et al.*, 2014). Consequently, specific bacterial Raman features distinguishes non-infected from infected macrophages.

Furthermore, Raman maps are acquired in different cell depths. For each cell layer, two-dimensional chemical maps are reconstructed by calculating the sum intensity of typical cell signals (1660 + 1449 cm^{-1}) for each measurement point, and plotted according to the x and y -coordinates from $z = 0 \mu\text{m}$ to $z = -4 \mu\text{m}$. The determined cell profile of the respective layer is displayed in

Fig. 2B for one single infected macrophage. The sum intensity distribution of prominent Raman bands was further used to determine the cell borders as previously described (Bräutigam *et al.*, 2013). Regions outside the defined cell area of the same macrophage are shown in black in Fig. 2C and D. This analysing method facilitates the visualization of signal contributions from chosen chemical targets that are located within the determined cell borders. This is shown in Fig. 2C for the sum intensity of the Raman signal at 785 cm^{-1} , assigned to DNA/RNA modes (ring-breathing mode of cytosin, thymine and uracil and the O-P-O⁻ stretching mode of the phosphate backbone). The intensity distribution of this Raman signal allows to detect the position and shape of the cell nucleus as has been shown in a previous study (Hartmann *et al.*, 2012).

To demonstrate that bacterial-specific Raman signals are detected from within the cell matrix of the macrophages and not only from the cell surface, the sum intensity of the Raman bands at 1524 and 1155 cm^{-1} (assigned to the bacterial carotenoid) were plotted within the determined margins of the cell (Fig. 2D). The carotenoid signal at 1005 cm^{-1} was not used for the calculation, because the Phe Raman signal is detected within the same wavenumber region and therefore makes the signal ambiguous. The three-dimensional Raman map reveals the biodistribution of the bacteria in different cell depths and within the determined cells margins. Raman maps of other infected macrophages with different distribution patterns of the intracellular bacteria are shown in the Supporting Information Fig. S3. The non-infected control macrophages do not exhibit any intensity distribution of carotenoid bands. For comparison, the chemical map of a representative control cell is shown in the Supporting Information Fig. S4. However, both cell types (the eukaryotic macrophages and the prokaryotic intracellular bacterium) can exhibit carotenoids (Liaaen-Jensen and Andrewes, 1972; Puppels *et al.*, 1993; Ramanauskaitė *et al.*, 1997; Ramoji *et al.*, 2012; Jehlicka *et al.*, 2014). The main difference is that the carotenoid level in macrophages is dependent on an external β -carotene supplementation (Fotouhi *et al.*, 1996). *M. gordonae* produce carotenoids by itself (Liaaen-Jensen and Andrewes, 1972; Park and DeCicco, 1974). Carotenoids are therefore an intrinsic Raman biomarker for chromogenic bacteria in the present study. In future, it has to be determined to what extent does accumulated carotenoids in macrophages after supplementation interfere with the here described Raman microspectroscopic detection and localization of *M. gordonae* via the bacterial carotenoid Raman signal in subcellular structures.

Nevertheless, the cell profile, cell morphology and the biodistribution of the bacterial signal in different cell layers or depths were recorded using a confocal Raman set-up

(Fig. 2B-D). By applying an expert knowledge analysing method via plotting the sum intensity of relevant Raman bands, the bacterial Raman signal can be localized within determined cell margins. The results show, that Raman microspectroscopy is a strong *in vitro* diagnostic tool for the localization of bacilli *in situ* beside cell compartments such as the nucleus without any additional preparation or labelling techniques. In this first Raman spectroscopy-based study of single macrophages infected by mycobacteria, we observed different shapes and numbers of cell nuclei, by plotting the sum intensity of the Raman band at 785 cm^{-1} . Examples are depicted in the Supporting Information Fig. S5. Here, macrophages with a well-defined round nucleus, elongated nuclei and a cell with three cell nuclei are shown. It is known that the phenotype of macrophages changes during infection depending on the immune response of the host. The shape and number of the cell nuclei is an important marker in histopathology to categorize the macrophages in granulomas and therefore the state of infection (Lugo-Villarino *et al.*, 2012; Mattila *et al.*, 2013). The ease of visualizing the cell nucleus in Raman maps, as shown in the present study and previously described in the literature (Krafft *et al.*, 2005; Hartmann *et al.*, 2012; Bräutigam *et al.*, 2013), can prospectively be used as a biomarker to study the phenotype of macrophages during mycobacterial infection.

Microenvironment of intracellular bacteria

Beside the detection and localization of the intracellular bacteria (Fig. 2) and the visualization of the macrophages nuclei, the acquired spectral information of the intracellular bacteria exhibit also distinct chemical information. One of the investigated macrophages shows a well-defined compartment that exhibits high intensities of bacterial Raman signal (Fig. 3A, arrow). A cluster analysis of the Raman map assigns the indicated compartment as a separate cluster, distinct from the other bacterial locations in the cell map (Fig. 3B, arrow). The mean spectrum of the cluster exhibits, beside the bacterial carotenoid signal and protein features, relatively high contributions of lipids (Fig. 3C). Here, the high intensities at 1296 cm^{-1} [assigned to $\delta(\text{CH}_2)$ twisting vibration of isolated saturated fatty acids] and in particular the C = O stretching vibration at 1743 cm^{-1} , which is due to the lipid ester bond, is noticeable (De Gelder *et al.*, 2007). At 1743 cm^{-1} , no spectral contribution of other biochemical contents is observed, and therefore, it is used as a lipid marker band. Plotting the sum intensity of the Raman signal at 1743 cm^{-1} (Fig. 3D) shows that the highest intensities of this signal coincide with the indicated cluster (Fig. 3B) and the highest intensity of the bacterial Raman signal (Fig. 3A). We suggest that the comparative high contribu-

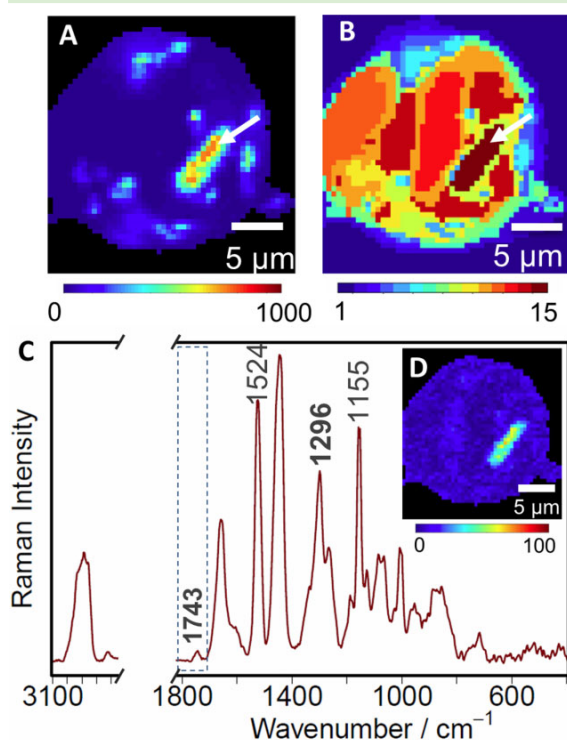


Fig. 3. Raman map of an infected macrophage with noticeable compartmentalization.

- A. Sum intensity of the bacterial Raman signal at 1524 and 1155 cm^{-1} within the cell matrix.
 B. Corresponding plot of a hierarchical cluster analysis with 15 clusters. The cell compartment of interest is indicated by an arrow in both panels.
 C. Mean spectrum of the indicated cluster.
 D. Sum intensity of the Raman signal at 1743 cm^{-1} within the determined cell margins.

tion of lipids differentiate the indicated bacterial location in Fig. 3B from other intracellular bacterial clusters. A lipid-filled phagosome that contain bacteria might be an explanation for this observation. Such cell compartments are the primary habitat of intracellular persistent mycobacteria (Mattila *et al.*, 2013). Lipid-rich droplets or lipid bodies (LBs) play an important role during the infection with mycobacteria and the formation of granuloma. They are considered as key organelles involved in experimental and clinical infections with different intracellular pathogens. The formation of LBs starts after the phagocytosis of the pathogen and during the course of phagosome maturation. The progression and the modulation of phagosomes by pathogens are connected with accentuated formation of LBs. These organelles are described as dynamic and functionalized active organelles involved in intracellular trafficking and signalling processes (Nguyen and Pieters, 2005; Melo and Dvorak, 2012). The chemical and physical properties of the LBs vary with time and lead to the accu-

mulation of cholesterol (Caceres *et al.*, 2009). The cholesterol accumulation is linked to the intracellular survival of mycobacteria (Mattos *et al.*, 2014). It is proposed, that the investigation of LBs biology is crucial for applying new therapies (Steinberg and Grinstein, 2008; Melo and Dvorak, 2012; Mattos *et al.*, 2014). Raman microspectroscopy offers a potential analytic tool to investigate the lipid content of single cells by combining the spatial information of the reconstructed chemical image and the spectral profile and therefore, the lipid composition in different cell compartments. This has been shown in different studies, where for example, the uptake and storage behaviour of arachidonic acid in human macrophages (Stiebing *et al.*, 2014), the concentration of palmitic and oleic acid in lipid droplets of hepatocytes (Schie *et al.*, 2013b), the spatially resolved investigation of the oil composition in single intact hyphae of *Mortierella spp.* (Münchberg *et al.*, 2013), or the non-invasive imaging of intracellular lipid metabolism in macrophages have been investigated by Raman microspectroscopy (Matthäus *et al.*, 2012).

However, mycobacteria are known to have a lipid-rich cell wall (Kieser and Rubin, 2014). The conglomeration of bacteria inside the macrophage could also be responsible for higher lipid contributions in the Raman signal of intracellular bacterial locations. In order to verify that the lipid signal comes from the cell compartment of the macrophage itself and not from the bacteria, another cell with high signal intensities of intracellular bacteria was investigated. After the cluster analysis of the Raman map, the areas with the highest carotenoid signals were not assigned to distinct clusters by the algorithm. A lipid contribution comparable with the lipid intensities in Fig. 3 because of the signal intensity at 1743 cm^{-1} is not detectable in this Raman map (for details, see Supporting Information Fig. S6A–C). This result is evidence that the detected lipid enrichment within the indicated cell compartment in Fig. 3 is probably due to a cellular reaction of the macrophage in response to the mycobacterial infection and not due to the bacteria itself.

The present study investigates the infection of individual macrophages with *M. goodii* under standardized *in vitro* conditions. Even though the growth and infection conditions were the same for each macrophage, the randomly selected cells show individual differences concerning their morphology, size, cell adhesion on the substrate, etc. Also, the quantity of intracellular bacteria and the degree of compartmentalization varies among the individual cells. The cellular response after infection is not synchronic at the single-cell level and during the experimental time window. This complies with the literature. For example, the lipid droplet formation in macrophages, infected with *Mycobacterium leprae* after 48 h, was reported as twofold higher compared with the control cells

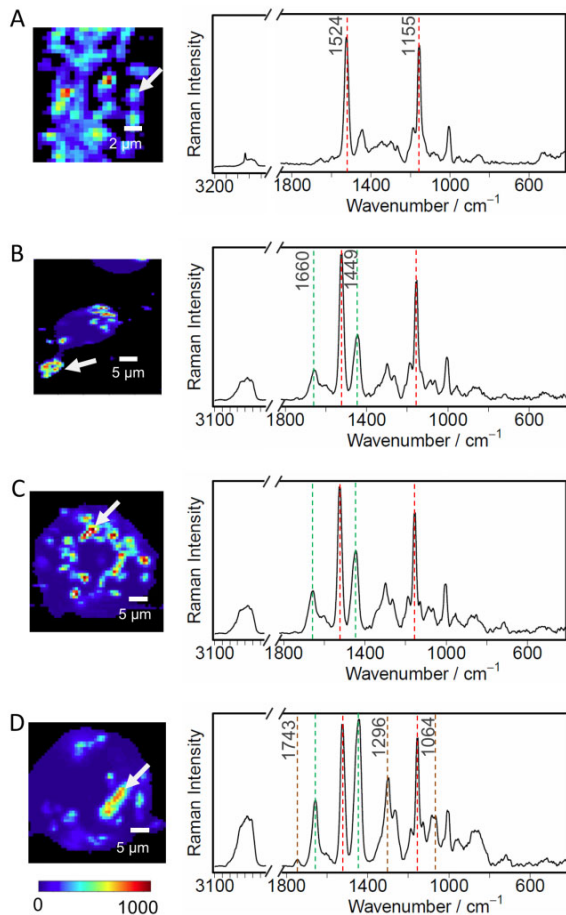


Fig. 4. Raman maps of bacterial cells of *Mycobacterium gordonae* in different states of uptake by macrophages and their corresponding mean Raman spectra.

- A. Single bacterial cells of extracellular *M. gordonae* were mapped in the absence of macrophages.
 B. Bacteria attached to a cell extension (white arrow).
 C. Intracellular bacteria.
 D. Macrophage with a well-defined cell compartment (white arrow), which exhibits high signal intensities of the bacterial carotenoid.

(Mattos *et al.*, 2014). In the present study, 1 of 10 analysed macrophages exhibit a lipid-filled droplet 24 h after infection with *M. gordonae*. Although both studies cannot be compared directly, more macrophages with LBs can be expected even on the single-cell level at later time points. However, the detailed investigation of the compartmentalization was beyond the scope of this first Raman spectroscopic investigation of intracellular mycobacteria.

The spectral patterns of different intra- and extracellular bacterial locations observed in the present study are compared in Fig. 4. Extracellular bacteria (*M. gordonae* directly spread on CaF₂) exhibit strong signal intensities of the bacterial carotenoid and lower contributions from pro-

teins, lipids and DNA (Fig. 4A). Bacteria attached to a cell extension and therefore located close to the determined cell margin are depicted in Fig. 4B (indicated by an arrow). The corresponding Raman spectrum of these bacteria shows increased signal intensities 3000–2800, 1660 and 1449 cm⁻¹ because of the contribution of the macrophage–cell matrix (spectrum Fig. 4B). In Fig. 4C, intracellular bacteria are shown. The respective Raman spectrum shows high similarity to the spectrum in Fig. 4B. However, slightly different intensity ratios among the bacterial signals and the typical cell signals can be observed. In contrast, the spectrum of the bacteria-containing compartment in Fig. 4D is distinct from the bacterial positions in 4B and 4C because of the higher lipid contributions. These results show that the Raman spectroscopic profiles of bacteria can be used to distinguish different microenvironments related with the host cell. Therefore, Raman microspectroscopy has the capability to follow the uptake of extracellular bacteria via their adhesion to the cell membrane, the intracellular distribution and the detection of bacteria in cell compartments with a distinct chemical composition.

In summary, we investigated *M. gordonae* in macrophages with Raman microspectroscopy. A mycobacterial-specific staining method in combination with fluorescence microscopy was used as a reference method to verify the performance of the infection experiment. The viability of the investigated intracellular *M. gordonae* at 24 h post-infection was insured and verified until Raman measurements initiation. As this was the first investigation of intracellular mycobacteria based on Raman microspectroscopy, we clarified some fundamental aspects for the critical evaluation of the introduced method to complement the future investigations of intracellular mycobacteria from a spectroscopic point of view. Without any label, the bacterial cells out, inside and close to the cell membrane of the macrophages were not visible in the present study, which is expected, in native samples. Therefore, we successfully proved the ability to differentiate between bacterial locations relative to the host cell because of distinct spectral patterns. Here, the cellular margins of the macrophages were determined by visualizing the chemical contrast acquired in a Raman map in different cell depths, which led to an established classification of different bacterial locations and associations to different cellular components. Thus, we could reconstruct Raman false colour images, which reveal reliable spectral information about *M. gordonae* surrounded by the cellular environment of the macrophage. The presented results confirm the potential of Raman microspectroscopy as a non-invasive and label-free technique for the detection of intracellular bacteria *in situ*. Based on the present results, the Raman microspectroscopic investigations of mycobacterial infections can go into detail.

In the context of the current understanding of the host-pathogen interaction, this method offers new possibilities for investigations of the host niches dynamics. Raman microspectroscopy is able to reduce the complexity of cellular analysis by providing spatial information of intracellular bacteria relative to host cell compartments in combination with chemical contrast and molecular selectivity. The spectral investigations of the bacteria-associated lipid-filled bodies are especially promising in this context. Therefore, the present work paves the way for Raman microspectroscopy as a diagnostic tool to improve the knowledge about the pathophysiology of acute and persistent infections.

For future investigations, the application of Raman microspectroscopy can be expanded to identify the biochemical make-up and the range of phenotypic diversity of bacilli from cellular microenvironments that support bacterial replication, persistence or death. The differentiation between the replicative and metabolic state of the bacteria still poses an analytical challenge in persistence bacterial infections (Monack *et al.*, 2004; Fonseca and Swanson, 2014). A comprehensive characterization of those intracellular bacterial subpopulations is important to establish new drugs for efficient eradication at the different stages of infection. Several studies showed that Raman-based methods are very sensitive regarding the detection of metabolic changes, growth phase characteristics and environmental influences on microorganisms (Neugebauer *et al.*, 2007; Walter *et al.*, 2012; Silge *et al.*, 2014). Beside the LBs discussed earlier, trace elements and metals have a great influence on the molecular status, and subsequently, on the pathophysiology of mycobacteria inside macrophages (Soldati and Neyrolles, 2012). The sensitivity of Raman microspectroscopy regarding spectral changes of *Pseudomonas* species adapted to different types of natural mineral water, and furthermore, to different contents of minerals and salts, was evident (Silge *et al.*, 2014). We suggest that Raman microspectroscopy is a powerful tool to support the investigation of the intracellular phenotypes of bacteria either *in situ* or directly after isolation from the host microenvironment. The versatile possibilities of using Raman microspectroscopy to complement standard microscopic methods, biochemical assays and genome-based techniques, offers new diagnostic means to push the improvements for therapeutics against mycobacterial infections forward.

Acknowledgements

This work was supported by the Free State of Thuringia and the European Union (EFRE) in the project Fast-TB (grant number 2013FE9057). We thank Dr. Ute Münchberg for her critical reading the paper.

Conflicts of interest statement

We certify that there is no conflict of interest with any financial or non-financial organization regarding the material discussed in the paper.

References

- Barry, C.E., Boshoff, H.I., Dartois, V., Dick, T., Ehrt, S., Flynn, J., *et al.* (2009) The spectrum of latent tuberculosis: rethinking the biology and intervention strategies. *Nat Rev Microbiol* **7**: 845–855.
- Bonifacio, A., Beleites, C., Vittur, F., Marsich, E., Semeraro, S., Paoletti, S., and Sergo, V. (2010) Chemical imaging of articular cartilage sections with Raman mapping, employing uni- and multi-variate methods for data analysis. *Analyst* **135**: 3193–3204.
- Bräutigam, K., Bocklitz, T., Schmitt, M., Rösch, P., and Popp, J. (2013) Raman spectroscopic imaging for the real-time detection of chemical changes associated with docetaxel exposure. *Chemphyschem* **14**: 550–553.
- Bräutigam, K., Bocklitz, T., Silge, A., Dierker, C., Ossig, R., Schnekenburger, J., *et al.* (2014) Comparative two- and three-dimensional analysis of nanoparticle localization in different cell types by Raman spectroscopic imaging. *J Mol Struct* **1073**: 44–50.
- Caceres, N., Tapia, G., Ojanguren, I., Altare, F., Gil, O., Pinto, S., *et al.* (2009) Evolution of foamy macrophages in the pulmonary granulomas of experimental tuberculosis models. *Tuberculosis* **89**: 175–182.
- De Gelder, J., De Gussem, K., Vandenabeele, P., and Moens, L. (2007) Reference database of Raman spectra of biological molecules. *J Raman Spectrosc* **38**: 1133–1147.
- Diem, M., Romeo, M., Boydston-White, S., Miljkovic, M., and Matthaus, C. (2004) A decade of vibrational microspectroscopy of human cells and tissue (1994–2004). *Analyst* **129**: 880–885.
- Fonseca, M.V., and Swanson, M.S. (2014) Nutrient salvaging and metabolism by the intracellular pathogen *Legionella pneumophila*. *Front Cell Infect Microbiol* **4**: 1–14.
- Fotouhi, N., Meydani, M., Santos, M.S., Meydani, S.N., Hennekens, C.H., and Gaziano, J.M. (1996) Carotenoid and tocopherol concentrations in plasma, peripheral blood mononuclear cells, and red blood cells after long-term beta-carotene supplementation in men. *Am J Clin Nutr* **63**: 553–558.
- Hartmann, K., Becker-Putsche, M., Bocklitz, T., Pachmann, K., Niendorf, A., Rösch, P., and Popp, J. (2012) A study of Docetaxel-induced effects in MCF-7 cells by means of Raman microspectroscopy. *Anal Bioanal Chem* **403**: 745–753.
- Hirohama, D., Ishibashi, Y., Kawarazaki, H., Kume, H., and Fujita, T. (2011) Successful treatment of *Mycobacterium gordonae* exit-site and tunnel infection by partial catheter reimplantation of the Tenckhoff catheter. *Perit Dial Int* **31**: 368–370.
- Izagirre Anariba, D., Lanza, J., Mina, B., and Lessnau, K. (2014) A 34-year-old Californian surfer with a right upper lung mass. *Chest* **145**: 101A–101A.
- Jehlicka, J., Edwards, H.G., and Oren, A. (2014) Raman spectroscopy of microbial pigments. *Appl Environ Microbiol* **80**: 3286–3295.

- Kieser, K.J., and Rubin, E.J. (2014) How sisters grow apart: mycobacterial growth and division. *Nat Rev Microbiol* **12**: 550–562.
- Krafft, C., Knetschke, T., Funk, R.H.W., and Salzer, R. (2005) Identification of organelles and vesicles in single cells by Raman microspectroscopic mapping. *Vib Spectrosc* **38**: 85–93.
- Kuehnel, M.P., Goethe, R., Habermann, A., Mueller, E., Rohde, M., Griffiths, G., and Valentin-Weigand, P. (2001) Characterization of the intracellular survival of *Mycobacterium avium* ssp paratuberculosis: phagosomal pH and fusogenicity in J774 macrophages compared with other mycobacteria. *Cell Microbiol* **3**: 551–566.
- Liaaen-Jensen, S., and Andrewes, A.G. (1972) Microbial carotenoids. *Annu Rev Microbiol* **26**: 225–248.
- Lugo-Villarino, G., Hudrisier, D., Benard, A., and Neyrolles, O. (2012) Emerging trends in the formation and function of tuberculosis granulomas. *Front Immunol* **3**: 405.
- Matthäus, C., Kale, A., Chermenko, T., Torchilin, V., and Diem, M. (2008) New ways of imaging uptake and intracellular fate of liposomal drug carrier systems inside individual cells, based on Raman microscopy. *Mol Pharm* **5**: 287–293.
- Matthäus, C., Krafft, C., Dietzek, B., Brehm, B.R., Lorkowski, S., and Popp, J. (2012) Noninvasive imaging of intracellular lipid metabolism in macrophages by Raman microscopy in combination with stable isotopic labeling. *Anal Chem* **84**: 8549–8556.
- Mattila, J.T., Ojo, O.O., Kepka-Lenhart, D., Marino, S., Kim, J.H., Eum, S.Y., et al. (2013) Microenvironments in tuberculous granulomas are delineated by distinct populations of macrophage subsets and expression of nitric oxide synthase and arginase isoforms. *J Immunol* **191**: 773–784.
- Mattos, K.A., Oliveira, V.C.G., Berredo-Pinho, M., Amaral, J.J., Antunes, L.C.M., Melo, R.C.N., et al. (2014) *Mycobacterium leprae* intracellular survival relies on cholesterol accumulation in infected macrophages: a potential target for new drugs for leprosy treatment. *Cell Microbiol* **16**: 797–815.
- Mazumder, S., Hicks, A., and Norwood, J. (2010) *Mycobacterium gordonae* pulmonary infection in an immunocompetent adult. *N Am J Med Sci* **2**: 205–207.
- Melo, R.C.N., and Dvorak, A.M. (2012) Lipid body-phagosome interaction in macrophages during infectious diseases: host defense or pathogen survival strategy? *PLoS Pathog* **8**: 1–13.
- Monack, D.M., Mueller, A., and Falkow, S. (2004) Persistent bacterial infections: the interface of the pathogen and the host immune system. *Nat Rev Microbiol* **2**: 747–765.
- Movasaghi, Z., Rehman, S., and Rehman, I.U. (2007) Raman spectroscopy of biological tissues. *Appl Spectrosc Rev* **42**: 493–541.
- Münchberg, U., Wagner, L., Spielberg, E.T., Voigt, K., Rösch, P., and Popp, J. (2013) Spatially resolved investigation of the oil composition in single intact hyphae of *Mortierella* spp. with micro-Raman spectroscopy. *Biochim Biophys Acta Mol Cell Biol Lipids* **1831**: 341–349.
- Neugebauer, U., Schmid, U., Baumann, K., Ziebuhr, W., Kozitskaya, S., Deckert, V., et al. (2007) Towards a detailed understanding of bacterial metabolism – spectroscopic characterization of *Staphylococcus epidermidis*. *Chemphyschem* **8**: 124–137.
- Nguyen, L., and Pieters, J. (2005) The Trojan horse: survival tactics of pathogenic mycobacteria in macrophages. *Trends in Cell Biol* **15**: 269–276.
- Park, S.S., and DeCicco, B. (1974) Autotrophic growth with hydrogen of *Mycobacterium gordonae* and another scotochromogenic mycobacterium. *Int J Syst Bacteriol* **24**: 338–345.
- Pully, V.V., Lenferink, A.T.M., and Otto, C. (2011) Time-lapse Raman imaging of single live lymphocytes. *J Raman Spectrosc* **42**: 167–173.
- Puppels, G.J., Garritsen, H.S.P., Kummer, J.A., and Greve, J. (1993) Carotenoids located in human lymphocyte subpopulations and natural killer cells by Raman microspectroscopy. *Cytometry* **14**: 251–256.
- R Development Core Team (2010) *R: A Language and Environment for Statistical Computing*. Vienna, Austria: R Foundation for Statistical Computing.
- Ramanauskaite, R.B., SegersNolten, I., de Grauw, K.J., Sijtsma, N.M., van der Maas, L., Greve, J., et al. (1997) Carotenoid levels in human lymphocytes, measured by Raman microspectroscopy. *Pure Appl Chem* **69**: 2131–2134.
- Ramaji, A., Neugebauer, U., Bocklitz, T., Foerster, M., Kiehnopf, M., Bauer, M., and Popp, J. (2012) Toward a spectroscopic hemogram: Raman spectroscopic differentiation of the two most abundant leukocytes from peripheral blood. *Anal Chem* **84**: 5335–5342.
- Schie, I.W., and Huser, T. (2013a) Methods and applications of Raman microspectroscopy to single-cell analysis. *Appl Spectrosc* **67**: 813–828.
- Schie, I.W., Nolte, L., Pedersen, T.L., Smith, Z., Wu, J., Yahiatene, I., et al. (2013b) Direct comparison of fatty acid ratios in single cellular lipid droplets as determined by comparative Raman spectroscopy and gas chromatography. *Analyst* **138**: 6662–6670.
- Schie, I.W., Alber, L., Gryshuk, A.L., and Chan, J.W. (2014) Investigating drug induced changes in single, living lymphocytes based on Raman micro-spectroscopy. *Analyst* **139**: 2726–2733.
- Silge, A., Schumacher, W., Rösch, P., Da Costa, P.A., Gerard, C., and Popp, J. (2014) Identification of water-conditioned *Pseudomonas aeruginosa* by Raman microspectroscopy on a single cell level. *Syst Appl Microbiol* **37**: 360–367.
- Soldati, T., and Neyrolles, O. (2012) Mycobacteria and the intraphagosomal environment: take it with a pinch of salt(s)!. *Traffic* **13**: 1042–1052.
- Steinberg, B.E., and Grinstein, S. (2008) Pathogen destruction versus intracellular survival: the role of lipids as phagosomal fate determinants. *J Clin Invest* **118**: 2002–2011.
- Stiebing, C., Matthäus, C., Krafft, C., Keller, A.-A., Weber, K., Lorkowski, S., and Popp, J. (2014) Complexity of fatty acid distribution inside human macrophages on single cell level using Raman micro-spectroscopy. *Anal Bioanal Chem* **406**: 7037–7046.
- Walter, A., Kuhri, S., Reinicke, M., Bocklitz, T., Schumacher, W., Rosch, P., et al. (2012) Raman spectroscopic detection of Nickel impact on single Streptomyces cells – possible

bioindicators for heavy metal contamination. *J Raman Spectrosc* **43**: 1058–1064.

Wayne, L., and Sohaskey, C. (2001) Nonreplicating persistence of *Mycobacterium tuberculosis*. *Annu Rev Microbiol* **55**: 139–163.

Supporting Information

Additional Supporting Information may be found in the online version of this article at the publisher's web-site:

Fig. S1. Determination of the sum intensity of characteristic Raman bands for one representative cell map.

A. The wavenumber regions of the Raman cell bands are coloured green (spectrum 1), 1640–1680 cm^{-1} [amide I at 1662 cm^{-1} (Krafft *et al.*, 2005; Harz *et al.*, 2009)], 1430–1470 cm^{-1} [CH_2 -deformation mode at 1449 cm^{-1} (Krafft *et al.*, 2005; Harz *et al.*, 2009)], from 990 to 1010 cm^{-1} [symmetric ring-breathing mode of phenylalanine at 1005 cm^{-1} (Krafft *et al.*, 2005; Harz *et al.*, 2009)]. The resultant sum intensity plot for the cell signals is depicted in panel D. The cell nucleus is determined by calculating the sum intensity between 780 and 790 cm^{-1} [785 cm^{-1} symmetric stretch vibration of the O-P-O of DNA/RNA (Krafft *et al.*, 2005; Harz *et al.*, 2009; Hartmann *et al.*, 2012)] coloured blue (spectrum 2). The sum intensities of the Raman nucleus band are plotted in panel C. The sum intensity of the carotenoid signal was calculated between 1152 and 1158 cm^{-1} [$\nu(\text{C}-\text{C})$ at 1155 cm^{-1} (Jehlicka *et al.*, 2014)] and 1530 and 1510 cm^{-1} [$\nu(\text{C}=\text{C})$ at 1524 cm^{-1} (Jehlicka *et al.*, 2014)]. The sum intensities of the Raman carotenoid bands are plotted in panel B.

Fig. S2. Intracellular viability of the bacilli. The cfu ml^{-1} was determined by plate count. Cell lysate of the infected

macrophages were incubated on agar plates after infection (different time points). Bacterial growth is evident by colony formation (CFU ml^{-1}). Experiments were done in triplicates, the mean value is plotted.

Fig. S3. Raman maps of representative infected macrophages with different distribution patterns of the intracellular bacteria. The sum intensity of the bacterial carotenoid signals at 1524 and 1155 cm^{-1} within the determined cell margins are plotted. The intensity range is represented by the colour scale. Raman maps were acquired from two independent batches.

Fig. S4. Raman spectroscopic analysis of a non-infected macrophage.

A. Intensity distribution of typical cell signals at (1449 and 1660 cm^{-1}) from $z = 0 \mu\text{m}$ to $z = -4 \mu\text{m}$ are plotted.

B. Sum intensity of the Raman signal at 785 cm^{-1} within the determined cell margin.

C. Sum intensity of the bacterial carotenoid signals at 1524 and 1155 cm^{-1} . The sum intensity range of the respective signals is represented by the colour scales.

Fig. S5. Different shapes and numbers of cell nuclei observed during the Raman microscopic studies of macrophages infected with *M. gordonae*.

A–C. sum intensity of the Raman signal at 785 cm^{-1} within the determined cell margins is plotted.

D–F. Sum intensity of the bacterial carotenoid signals at 1524 and 1155 cm^{-1} . The sum intensity range of the respective signals is represented by the colour scales.

Fig. S6. Raman map of an infected macrophage without noticeable compartmentalization.

A. Sum intensity of the bacterial Raman signal at 1524 and 1155 cm^{-1} within the determined cell matrix.

B. Corresponding plot of a hierarchical cluster analysis with 15 clusters.

C. Sum intensity of the Raman signal at 1743 cm^{-1} .

Publication 6

A Metabolic Probe-Enabled Strategy Reveals Uptake and Protein Targets of Polyunsaturated Aldehydes in the Diatom *Phaeodactylum tricornutum*

Wolfram S, Wielsch N, Hupfer Y, Mönch B, Lu-Walther H-W, Heintzmann R, Werz O, Svatoš A, Pohnert G.

[HWLW6] Wolfram S, Wielsch N, Hupfer Y, Mönch B, Lu-Walther H-W, Heintzmann R, Werz O, Svatoš A, Pohnert G. A Metabolic Probe-Enabled Strategy Reveals Uptake and Protein Targets of Polyunsaturated Aldehydes in the Diatom *Phaeodactylum tricornutum*. PLoS ONE. 2015; 10(10): e0140927. doi: <http://dx.doi.org/10.1371/journal.pone.0140927>

Beteiligt an (Zutreffendes ankreuzen)

Author	Wolfram S	Lu-Walther H-W
Konzeption des Forschungsansatzes	×	
Planung der Untersuchungen	×	×
Datenerhebung	×	×
Datenanalyse und -interpretation	×	×
Schreiben des Manuskripts	×	
Vorschlag Anrechnung Publikationsäquivalente	1,0	0,25

All authors revised, edited and proof read the final manuscript.

Plos Journal is an open access publisher, no reprinted permission is required.

RESEARCH ARTICLE

A Metabolic Probe-Enabled Strategy Reveals Uptake and Protein Targets of Polyunsaturated Aldehydes in the Diatom *Phaeodactylum tricornutum*

Stefanie Wolfram¹, Natalie Wielsch², Yvonne Hupfer², Bettina Mönch³, Hui-Wen Lu-Walther⁴, Rainer Heintzmann^{4,5}, Oliver Werz³, Aleš Svatoš², Georg Pohnert^{1*}

1 Bioorganic Analytics, Institute for Inorganic and Analytical Chemistry, Friedrich Schiller University, Jena, Germany, **2** Department Mass Spectrometry/Proteomics, Max Planck Institute for Chemical Ecology, Jena, Germany, **3** Department of Pharmaceutical and Medicinal Chemistry, Institute of Pharmacy, Friedrich Schiller University, Jena, Germany, **4** Biomedical Imaging, Department Microscopy, Leibniz Institute of Photonic Technology e.V., Jena, Germany, **5** Institute for Physical Chemistry, Abbe Center of Photonics, Friedrich Schiller University, Jena, Germany

* Georg.Pohnert@uni-jena.de



CrossMark
click for updates

OPEN ACCESS

Citation: Wolfram S, Wielsch N, Hupfer Y, Mönch B, Lu-Walther H-W, Heintzmann R, et al. (2015) A Metabolic Probe-Enabled Strategy Reveals Uptake and Protein Targets of Polyunsaturated Aldehydes in the Diatom *Phaeodactylum tricornutum*. PLoS ONE 10(10): e0140927. doi:10.1371/journal.pone.0140927

Editor: Tilmann Harder, Universität Bremen, GERMANY

Received: July 16, 2015

Accepted: October 1, 2015

Published: October 23, 2015

Copyright: © 2015 Wolfram et al. This is an open access article distributed under the terms of the [Creative Commons Attribution License](https://creativecommons.org/licenses/by/4.0/), which permits unrestricted use, distribution, and reproduction in any medium, provided the original author and source are credited.

Data Availability Statement: All relevant data are within the paper and its Supporting Information files.

Funding: Support was provided by the Deutsche Forschungsgemeinschaft, German Research Foundation (DFG) and Studienstiftung des deutschen Volkes.

Competing Interests: The authors have declared that no competing interests exist.

Abstract

Diatoms are unicellular algae of crucial importance as they belong to the main primary producers in aquatic ecosystems. Several diatom species produce polyunsaturated aldehydes (PUAs) that have been made responsible for chemically mediated interactions in the plankton. PUA-effects include chemical defense by reducing the reproductive success of grazing copepods, allelochemical activity by interfering with the growth of competing phytoplankton and cell to cell signaling. We applied a PUA-derived molecular probe, based on the biologically highly active 2,4-decadienal, with the aim to reveal protein targets of PUAs and affected metabolic pathways. By using fluorescence microscopy, we observed a substantial uptake of the PUA probe into cells of the diatom *Phaeodactylum tricornutum* in comparison to the uptake of a structurally closely related control probe based on a saturated aldehyde. The specific uptake motivated a chemoproteomic approach to generate a qualitative inventory of proteins covalently targeted by the $\alpha,\beta,\gamma,\delta$ -unsaturated aldehyde structure element. Activity-based protein profiling revealed selective covalent modification of target proteins by the PUA probe. Analysis of the labeled proteins gave insights into putative affected molecular functions and biological processes such as photosynthesis including ATP generation and catalytic activity in the Calvin cycle or the pentose phosphate pathway. The mechanism of action of PUAs involves covalent reactions with proteins that may result in protein dysfunction and interference of involved pathways.

Introduction

Oceans accommodate numerous coexisting microalga species in the plankton. Their community is shaped by different factors including nutrient limitation, predation and chemical signaling. Diatoms, a class of unicellular algae, are key players in the marine food web as they are responsible for about 40% of global marine primary productivity [1]. Some diatom species release biologically active metabolites as mediators of interactions. An intensively studied compound class in this context are oxylipins, which derive from the oxidative transformation of polyunsaturated fatty acids [2]. Of considerable interest among oxylipins are polyunsaturated aldehydes (PUAs), which have been reported to mediate various inter- and intraspecific interactions (reviewed in [2–5]). 2,4-Decadienal (DD) is the best studied metabolite of the group of PUAs, with attributed roles in grazer defense [6], allelopathy [7], cell to cell signaling [8], antibacterial activity [7,9] and bloom termination initiation [10,11]. PUA-mediated allelopathy [5,7,12,13] is impairing different phyla regarding growth and physiological performance. Sensitivity against PUAs has been reported for the prymnesiophyte *Isochrysis galbana* [7], the chlorophyte *Dunaliella tertiolecta* [7] as well as the centric diatom *Thalassiosira weissflogii* [14]. A synchronized release of PUAs from intact *Skeletonema marinoi* cells transiently before the culture changes to the decline phase supports the idea that PUAs play a role as infochemicals in mediating bloom termination [10]. Despite the well-documented biological functions of PUAs, their mechanism of action and their molecular targets are almost unknown [3,4]. Only few impaired biological processes and functions are recognized mainly involving disruption of intracellular calcium signaling, cytoskeletal instability and induction of apoptosis (reviewed in [2–4]).

PUA activity is structure-specific, since saturated aldehydes, like decanal that lack the conjugated $\alpha,\beta,\gamma,\delta$ -unsaturated aldehyde motive of PUA, are not active [15,16]. Conjugated unsaturated aldehydes are reactive compounds belonging to the class of Michael acceptors. They act as electrophiles and react with proteins [17,18] and DNA [19–21]. Model investigations revealed that DD covalently modifies proteins by formation of imines (Schiff bases), pyridinium adducts and 1,4-addition products with nucleophiles [17,18]. Thus, proteins are putative targets of the electrophilic PUAs. PUAs also react with DNA resulting in apoptosis in copepods (reviewed in [22]). In algae [7], sea urchin embryos [23] and copepod embryos and nauplii [6,24] DNA laddering and chromatin dispersal or complete DNA fragmentation and dislocation is observed after PUA exposure.

The diatoms *Phaeodactylum tricornerutum* [25] and *Thalassiosira pseudonana* [26] have emerged as model organisms since these were the first species with sequenced genome. *P. tricornerutum* is a producer of the oxylipins 12-oxo-(5Z,8Z,10E)-dodecatricienoic acid and 9-oxo-(5Z,7E)-nonadienoic acid [27] and was reported to be affected by DD [8,28]. Exposure to this aldehyde altered the mitochondrial glutathione redox potential by oxidation of glutathione and induced cell death of *P. tricornerutum* [28]. DD also triggers intracellular calcium transients and nitric oxide generation [8]. There is evidence for a sophisticated stress surveillance system in which individual diatom cells sense local DD concentration thereby monitoring the stress level of the entire population. An ortholog of the plant enzyme AtNOS1 was predicted as molecular target of PUAs [8]. Transcriptome analysis revealed that *PtNOA*, a gene with similarities to AtNOS1 [8], is upregulated in response to DD [29]. *PtNOA* overexpressing cell lines are hypersensitive to this PUA with altered expression of superoxide dismutase and metacaspases; both protein classes are involved in activation of programmed cell death [29]. Other studies on gene regulation in response to PUAs focused on copepods. In *Calanus helgolandicus* tubulin expression [30] and primary defense systems [31] were downregulated whereas detoxification genes

like glutathione S-transferase, superoxide dismutase, and catalase remained unaffected [31] in response to a diet of the PUA producer *S. costatum* compared to a control.

We report here on the uptake, accumulation and molecular targets of a molecular probe containing a DD-derived head group and a 5-tetramethylrhodamine carboxamide fluorophore (TAMRA) reporter in *P. tricornutum* using an activity-based protein profiling (ABPP) strategy (Fig 1). Such chemical probe-enabled proteome strategies have been successfully applied with mechanism-based inhibitors [32] or protein-reactive natural products [33,34]. The utilized probe consists of a reactive group mimicking DD and a fluorescent reporter tag for detection [35]. By applying 2D gel electrophoresis (GE) followed by liquid chromatography/tandem mass spectrometry (LC-MS/MS) we found specific probe-labeled proteins having important roles regarding catalytic activity and biological functions in the alga including fucoxanthin chlorophyll *a/c* proteins, ATP synthases, a ribulose-phosphate-3-epimerase (RPE) and a phosphoribulokinase (PRK).

Materials and Methods

Uptake experiments

Growth of *P. tricornutum*. *P. tricornutum* (strain UTEX 646, Segelskär, Finland) was cultivated in artificial seawater prepared as described in Maier and Calenberg [36] under a 14/10 hours light/dark cycle, at 32 to 36 mmole photons $s^{-1} m^{-2}$ and 13°C in 580 mL Weck jars (Weck, Wehr, Germany). The 4-(2-hydroxyethyl)-1-piperazineethanesulfonic acid (HEPES)-buffered medium was adjusted to a pH of 7.8 before autoclaving. Nutrient levels were 14.5 mM phosphate, 620 mM nitrate and 320 mM silicate. Incubation experiments were done under the same conditions.

Sample preparation. A *P. tricornutum* culture (100 μ L) was pipetted on ethanol pre-cleaned cover slips (Marienfeld 474030-9010-000, 18x18 mm², D = 0.17 mm +/- 0.005 mm; Carl Zeiss Canada, Toronto, ON). To prevent evaporation cover slips were placed in a Petri dish, which contained a seawater wetted filter paper and were covered. Incubation for 8 hours allowed cells to adhere to the cover slips. Subsequently, 10 μ M of the substances DDY coupled to TAMRA (TAMRA-PUA), 5-hexynal (SA) coupled to TAMRA (TAMRA-SA) or azide modified TAMRA (TAMRA-N₃) were added to the cell suspensions (each 0.5 mM stocks in DMSO), mixed gently with a pipette and incubated for one hour. Afterwards, the cell suspensions were removed and the cover slips were washed seven times by carefully pipetting 200 μ L artificial seawater and incubated with 100 μ L 4% [w/v] para-formaldehyde in artificial seawater for 25 min. The cover slips were washed twice with 200 μ L artificial seawater and finally the

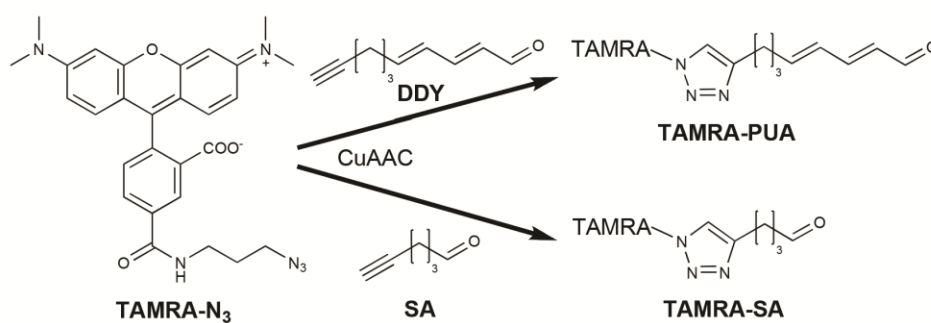


Fig 1. Synthesis of the probe TAMRA-PUA and the control TAMRA-SA. For details on the synthesis see [35].

doi:10.1371/journal.pone.0140927.g001

liquid was removed. A control with the same washing and fixation steps was prepared as well. Due to extensive washing steps a part of algae cells detach from cover slips. 4 μL of 2,2'-thio-diethanol were pipetted on an ethanol pre-cleaned object slide and the treated side of the cover slip was placed on top of the object slide and slightly pressed down. Edges were fixed with nail polish and the slides were stored at 4°C until measurements on the next day. For each treatment three individual cover slips (biological replicates) were prepared out of three different *P. tricornerutum* cultures. Those cultures have been prepared out of the same stock and kept under identical growth condition.

Fluorescence microscopy and analysis. *P. tricornerutum* cells were observed with a structured illumination microscope (SIM), Zeiss Elyra S1 system (Carl Zeiss, Jena, Germany). Imaging was performed with an oil immersion objective lens (Plan-Apo, 63X, 1.4NA, Carl Zeiss, Jena, Germany). A 561 nm laser was used for excitation and fluorescence was filtered by a band pass filter (BP 570–620 nm) which opens up above 750 nm. 2D wide field images were acquired to compare fluorescence intensity of the different probes and treatments (TAMRA-PUA, TAMRA-SA, TAMRA-N₃, no probe), whereas all cells were measured using the same settings (laser intensity, gain, exposure time). 12 cells were observed per treatment distributed over three biological replicates (microscope slides), four cells each. Three dimensional SIM images of treated *P. tricornerutum* providing twofold resolution improvement were taken from selected samples to confirm, that TAMRA-PUA and TAMRA-SA were taken up in the cells and did not exclusively stick onto their surfaces. 15 raw images are required for reconstructing one 2D SIM image. 3D SIM images were taken with z steps of 110 nm. All SIM images were reconstructed on ZEN software 2010 (black edition, Carl Zeiss, Jena, Germany).

For fluorescence analysis bright field and wide field fluorescence images at 561 nm excitation were exported in TIF format with the ZEN software and processed with ImageJ2x 2.1.4.7 (freeware, <http://www.rawak.de/ij2x/Download.html>) as follows: tonal correction of the bright field image of each cell was optimized (see [S1 Folder](#) for unmodified images), the cell was circled by hand and this selection was laid on the corresponding fluorescence picture using the ROI manager. The mean gray value, which is defined in this software as the sum of the gray values of all the pixels in the selection divided by the number of pixels, and the mean gray value of the background were measured and subtracted. For the previously described issue we use the term mean gray value per pixel. For background analysis a region of at least 1000 pixels was used.

Probe labeling, 1D and 2D gel electrophoresis and identification of target proteins

In vivo labeling of *P. tricornerutum* and sample preparation for gel electrophoresis. *P. tricornerutum* cultures were grown for 13 days in 580 mL Weck jars (1.0×10^6 to 1.5×10^6 cells mL^{-1}) without shaking as described before, which resulted in cells mainly sticking to the glass bottom. The overlaying artificial seawater was almost quantitatively removed with a pipette and cells were transferred into centrifuge tubes with the remaining medium.

For 1D GE samples were incubated with 100 μM DDY or 100 μM SA (each 50 mM stocks in DMSO) or DMSO for one hour.

For 2D GE the concentrated algae suspension was treated with 14 μL (250 μM) DDY stock solution (50 mM), which was added to 2.8 mL concentrated cell suspension (total cell number 48.7×10^6 resulting in 14 fmol DDY cell^{-1}) and incubated for 1 hour. During this incubation period no change in cell viability compared to untreated cells was observed by microscopy after application of Evan's Blue [37]; however, we observed that incubation of several hours increases the amount of non-viable cells. The undiluted samples were centrifuged for 2 min at

1,800 g immediately after incubation to remove DDY and salts; the supernatant was removed and the cells were washed twice with 1 mL buffer A (10 mM HEPES and 250 mM sucrose, pH 7.4) and twice with 1 mL buffer B (10 mM HEPES and 250 mM sucrose, pH 8.2). After each washing step the tubes were centrifuged at 1,800 g for 2 min and the supernatant was discarded. Application of Evan's Blue [37] and microscopy ensured that cells stayed intact during this procedure. The pellet was resuspended in buffer B and cells were treated with 1 mM dithiothreitol (20 mM stock in buffer B) to react with possibly unremoved DDY. Cells were lysed by sonication (ultrasonic probe: Bandelin sonotronic HD2070, power supply: Bandelin UW2070; Bandelin electronic, Berlin, Germany) twice for 15 s on ice.

The protein concentration was determined with the Roti[®]-Quant universal assay (Carl Roth, Karlsruhe, Germany) based on the biuret test using a microplate reader (Mithras LB 940, Berthold Technologies, Bad Wildbad, Germany) and bovine serum albumin as reference.

Copper(I)-catalyzed azide-alkyne cycloaddition (CuAAC). *P. tricornutum* protein samples (30 μ L, 30 to 50 μ g proteins μ L⁻¹) were diluted with 270 μ L buffer B and incubated with 6 μ L (0.09 mM) TAMRA-N₃ solution (5 mM stock in DMSO), 18 μ L (0.09 mM) ligand tris [(1-benzyl-1H-1,2,3-triazol-4-yl)methyl]amin solution (1.7 mM stock in DMSO/*tert*-butanol, 1/4, v/v) and 12 μ L (35 mM) of a freshly prepared ascorbic acid solution (1.00 M in water). Samples were vortexed and 6 μ L (0.88 mM) copper sulfate solution (50 mM in water) were added. Samples were vortexed again and stored on ice for 1 hour. 1% Triton[™] X-100 and protease inhibitor cocktail (M221, Amresco Inc., Solon, OH, USA) were added according to the manufacturer's protocol and after 30 min on ice samples were centrifuged at 15,000g and 3°C for 20 min. The supernatant was transferred into centrifugal filter units (vivaspin[®]500, 5,000 MWCO, PES, Sartorius, Göttingen, Germany) and the sample volume was reduced by centrifugation at 15,000g and 3°C. 100 μ L buffer B was added three times and the volume was reduced by centrifugation after each addition to give a final protein concentration of 10 to 20 μ g proteins μ L⁻¹.

Sodium dodecyl sulfate polyacrylamide gel electrophoresis (SDS-PAGE) and in-gel fluorescence detection. 20 μ g of protein samples were mixed with 2 \times loading buffer [38] and heated to 95°C for 6 min. A protein ladder (PageRuler unstained protein ladder, Thermo Fischer Scientific Inc., Waltham, MA, USA) and the protein sample were loaded on a SDS mini gel containing 12% acrylamide resolving gel and 5% stacking gel prepared according to [39]. The gel was separated in a Mini-Protean[®] Tetra gel cell (Bio-Rad, Hercules, CA, USA) by applying 80 V for 30 min followed by 180 V for 65 min. A fluorescent picture was taken at 312 nm irradiation using a UV transilluminator (UV star, Bio-Rad), a PowerShot A640 camera (Canon, Tokyo, Japan) and a 520 nm long pass filter. The gel was stained with RAPIDstain[™] (G-Biosciences, St. Louis, MO, USA).

Difference gel electrophoresis (DIGE). DIGE was conducted in triplicates. 440 to 880 μ g protein of the probe-treated sample (incubated with DDY and connected with TAMRA-N₃ by CuAAC as described before) and 50 μ g protein of a control sample incubated with the N-hydroxysuccinimide ester of the cyanine 5 fluorophore (Cy5 NHS ester) were loaded on each of the isoelectric focusing (IEF) strips (Immobiline DryStrip, 24 cm, pH 3–11 NL, GE Healthcare Bio-Sciences, Piscataway, NJ, USA). For Cy5 labeling of the whole proteome 20 μ L of the control sample were diluted with 48 μ L buffer B. 3 μ L Cy5 NHS ester (2 mM in DMSO) were added and the mixture was incubated with shaking at 4°C for 45 min. To stop labeling 5 μ L of a 10 mM solution of L-lysine in water were added.

The IEF strip was rehydrated overnight (7 M urea, 2 M thiourea, 2% [w/v] CHAPS, 0.002% [w/v] bromophenol blue, 0.5% [v/v] IPG buffer (GE Healthcare Bio-Sciences), 10 mM dithiothreitol). Isoelectric focusing of the strips with the Ettan IPGphor II (GE Healthcare Bio-

Sciences) was carried out according to the following protocol: 4 h at 300 V (gradient), 4 h at 600 V (gradient), 4 h at 1,000 V (gradient), 4 h at 8,000 V (gradient) and 3 h at 8,000 V (step).

After isoelectric focusing the IEF strips were equilibrated for 15 min in 10 mL of equilibration buffer (6 M urea, 30% [v/v] glycerol, 2% [w/v] SDS, 75 mM tris(hydroxymethyl)amino-methane, 0.002% [w/v] bromophenol blue) containing 1% [w/v] dithiothreitol and subsequently for 15 min in 10 mL of equilibration buffer containing 2.5% [w/v] iodoacetamide. For separation of proteins in the second dimension, the Ettan DALT System (GE Healthcare Bio-Sciences) was used. SDS polyacrylamide gels 12% [w/v] of 1.0 mm thickness were casted via the Ettan DALTsix Gel caster (GE Healthcare Bio-Sciences). The separation conditions were as follows: 1 W/gel for 1 h followed by 15 W/gel for 5 h. Proteins were visualized by analyzing the gels with a Typhoon 9410 scanner (GE Healthcare Bio-Sciences) using a resolution of 100 μ m. Proteins were fixed (10% [v/v] acetic acid, 50% [v/v] methanol in water), stained (0.025% [w/v] Coomassie R 250, 10% [v/v] acetic acid in water) and the gels were destained (10% [v/v] acetic acid in water; see [S3 Folder](#) for unmodified Coomassie and fluorescence images of the gels). Gels were merged with Delta2D (DECODON, Greifswald, Germany).

Protein isolation, LC-MS/MS analysis and data processing. Fluorescent TAMRA-PUA protein spots were in-gel reduced, alkylated with iodoacetamide and digested as described by Shevchenko et al. [40]. Tryptic peptides were extracted, dried down in a vacuum centrifuge and dissolved in 10 μ L of water containing 0.1% formic acid.

LC-MS/MS analysis and data processing were conducted as described in [S1 Information](#).

Results

Probe design and labeling strategy

The fluorescent $\alpha,\beta,\gamma,\delta$ -unsaturated aldehyde-derived probe TAMRA-PUA ([Fig 1](#)) could be used successfully to investigate uptake and accumulation of PUAs in *P. tricornutum* and to monitor protein targets of these natural products. TAMRA-PUA was recently developed in our group to monitor accumulation of PUAs in copepods [35]. The probe consists of DDY as reactive group that mimics DD. The alkyne functionality allows to couple the commercially available azide modified tetramethylrhodamine TAMRA-N₃ ([Fig 1](#)). To identify protein targets, DDY was incubated with *P. tricornutum* cells. After work-up CuAAC allowed to covalently link the reporter TAMRA-N₃ to DDY (Figs 1 and 2). For uptake studies we employed the probe as already coupled construct TAMRA-PUA. For comparison of the activity of $\alpha,\beta,\gamma,\delta$ -unsaturated aldehyde-derived probes with structurally related saturated-aldehyde-derived ones we also applied the probe TAMRA-SA ([Fig 1](#)).

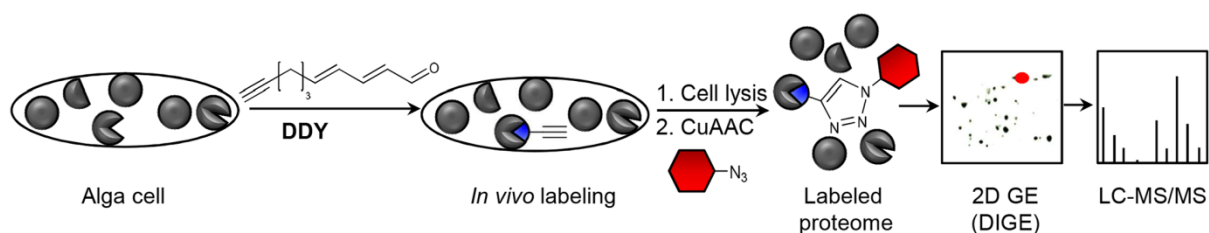


Fig 2. Schematic *in vivo* application of the probe. Living cells of *P. tricornutum* were incubated with the PUA-derivative DDY. After removal of excess DDY cell lysis followed by CuAAC enables attachment of the fluorescent reporter to covalently labeled proteins. 1D GE quickly allows detection of labeled proteins (not shown). Identification of protein targets is enabled by 2D GE. Therefore, a second *P. tricornutum* sample was treated with Cy5 NHS ester to label the whole proteome. The combined samples were separated using DIGE, labeled proteins were digested using trypsin and the resulting peptides were separated and analyzed by LC-MS/MS.

doi:10.1371/journal.pone.0140927.g002

TAMRA-PUA accumulates in *P. tricornutum*

Cell permeability and uptake of the probes by *P. tricornutum* was investigated by wide field fluorescence microscopy. Living cells were treated with TAMRA-PUA, TAMRA-SA or TAMRA-N₃ for labeling or kept as control without additional treatment. After one hour incubation probes were removed by washing seven times with artificial seawater, once with artificial seawater containing 4% paraformaldehyde for cell fixation and twice with artificial seawater. Cells were embedded in 2,2'-thiodiethanol and measured with an epifluorescence microscope in wide field mode. Images were processed with ImageJ. Cells were encircled by hand and the background corrected average mean gray value per pixel within each alga cell was calculated (Fig 3). The aldehyde containing probes TAMRA-PUA and TAMRA-SA were significantly enriched in the cells compared to TAMRA-N₃ or the control. Interestingly, TAMRA-PUA accumulation was significantly higher compared to TAMRA-SA, despite being similar in physicochemical properties.

Results were verified in additional independent experiments, also using a different embedding medium (S1 Fig). To confirm that the probes do not only appear on the surface we conducted 3D SIM showing that TAMRA-PUA and TAMRA-SA accumulate within the cells (Fig 4). Distribution of label revealed local maxima but in general nearly the entire cellular content was affected by the probe.

DDY covalently modifies proteins of *P. tricornutum*

We next tested for protein targets of PUAs in living cells using DDY as well as the saturated aldehyde derivative SA. After incubation with the probes followed by cell lysis, TAMRA-N₃ was coupled to the alkyne groups of DDY as well as SA via CuAAC (Fig 2). Proteins were

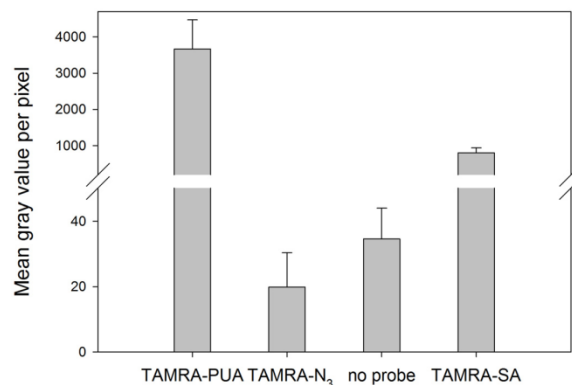


Fig 3. Fluorescence intensity of *P. tricornutum* cells treated under different conditions. Cells were either incubated with TAMRA-PUA, TAMRA-N₃, TAMRA-SA for one hour or kept under identical conditions without probe. For each treatment three microscope slides with four cells each were measured. Unmodified raw data are available in S1 and S2 Folders. Fluorescence intensities were recorded as mean gray value per pixel after data treatment as described in the main text. Averaged mean gray values per pixel of cells of each treatment are presented as bars ±SD. One way Anova comparing results of different microscope slides within one treatment revealed no statistical difference ($p > 0.05$). Kruskal-Wallis one way analysis of variance on ranks revealed differences in the median values among the treatment groups ($H = 42.436$, $p < 0.001$) and Tukey's HSD test ($p < 0.05$) allowed classification into three groups: (a) TAMRA-PUA with the highest mean gray value per pixel of 3661 ± 809 , (b) TAMRA-SA with 800 ± 140 and (c) TAMRA-N₃ and control with almost no emission signals (20 ± 10 and 35 ± 9); these controls were not significantly different to each other (Tukey's HSD test $p > 0.05$).

doi:10.1371/journal.pone.0140927.g003

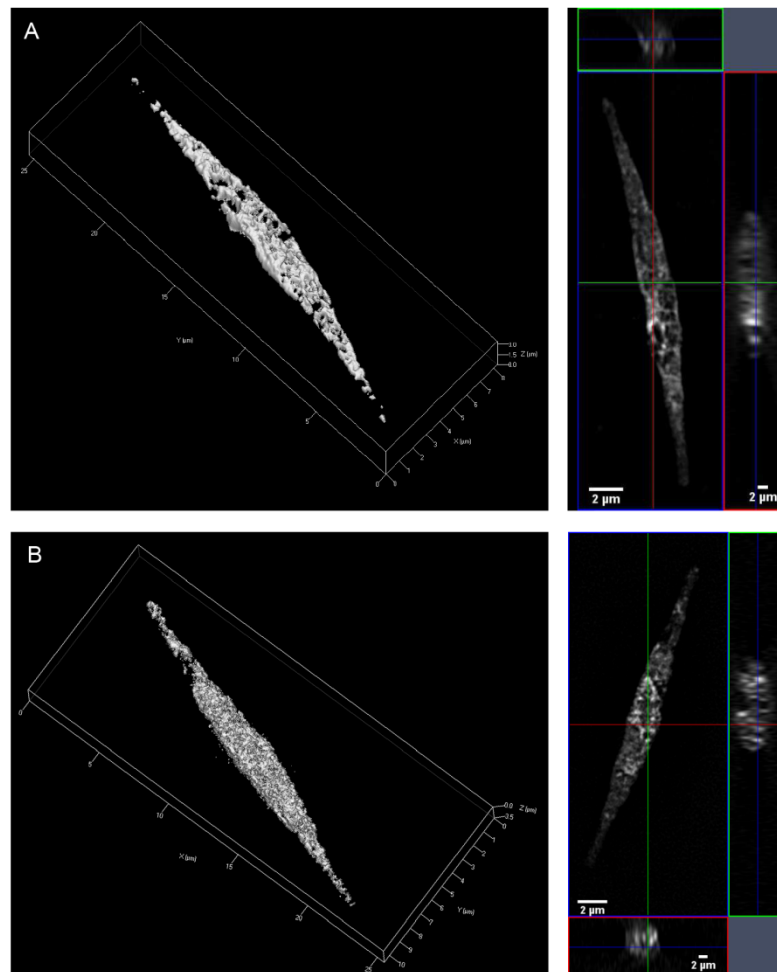


Fig 4. Fluorescence microscopy of *P. tricornutum* cells. 3D (left) and 2D (right) images of a TAMRA-PUA (A) and a TAMRA-SA (B) treated cell. Images were taken in 3D SIM mode. A 561nm laser was used for excitation, and fluorescence was filtered by a band pass filter (BP 570-620nm) which opens up above 750nm. Fluorescence is visible in the entire cells, which confirms that both probes were taken up.

doi:10.1371/journal.pone.0140927.g004

separated by 1D GE and monitored for fluorescent labeling. UV-illumination revealed exclusive labeling of proteins in DDY treated cells while SA and DMSO treatments did not result in any fluorescent bands (S2 Fig).

To unravel protein targets of DDY, protein extracts obtained after incubation of *P. tricornutum* with the probe as described above were separated by DIGE in three replicates (S3 Fig, S3 Folder for unmodified pictures). For comparison samples without probe addition were incubated with the Cy5 NHS ester to label the whole proteome. Separation was performed by isoelectric focusing and SDS-PAGE as second dimension and DDY-TAMRA labeled proteins were excised and tryptically digested. Digested peptides were separated and analyzed by LC-MS/MS (Fig 2). More precisely separation was conducted with a nano Ultra Performance

Liquid Chromatography (nanoUPLC) and analysis by tandem mass spectrometry using data-independent acquisition (MS^E analysis). In data-independent analysis the mass spectrometer cycles between low and high energy acquisition of data resulting in high sampling rate.

A list of confident target proteins classified according to their biological processes and molecular functions is shown in Table 1. Two ATP synthases, four different chlorophyll *a/c* binding proteins, different catalytic active enzymes and some predicted proteins were found to be modified by the probe. A full list of confident, probable and putative proteins (for evaluation see S1 Information) as well as an overview of all protein hits for each gel is given in S1 Table.

Discussion

While previous research mainly has reported the teratogenic and allelochemical effects of PUAs as well as their role in cell to cell signaling (reviewed in [2–5]) and PUAs influence on

Table 1. Confident target proteins found by 2D GE. ¹

Protein	Gene name	Accession No.	Mass (kDa)	Gel 1	Gel 2	Gel 3
1) Biological process						
ATP biosynthetic process						
ATP synthase subunit alpha, chloroplastic	<i>AtpA</i>	A0T0F1	54621.6	X	OO	O
ATP synthase subunit beta	<i>AtpB</i>	B7FS46	53619.2	X	OO	O
Photosynthesis						
Fucoxanthin chlorophyll <i>a/c</i> protein	<i>Lhcf10</i>	B7G5B6	21352.7	X	OOO	O
Fucoxanthin chlorophyll <i>a/c</i> protein	<i>Lhcf9</i>	B7G955	22100.5	OOO	O	X
Fucoxanthin chlorophyll <i>a/c</i> protein	<i>Lhcx2</i>	B7FR60	21177.4	OO	O	X
Fucoxanthin chlorophyll <i>a/c</i> protein	<i>Lhcf4</i>	B7FRW2	21328.5	OO	O	X
2) Molecular function						
Catalytic activity, isomerase activity						
Ribulose-phosphate 3-epimerase	<i>Rpe</i>	B7FRG3	27812.0	OO	O	O
Catalytic activity, ligase activity						
Predicted protein, family: Aspartate-ammonia ligase	<i>PHATRDRAFT_44902^a</i>	B7FW24	43206.1	X	OO	O
Catalytic activity, oxidoreductase activity						
Predicted protein, domains: Thioredoxin-like fold, Thioredoxin domain	<i>PHATRDRAFT_42566^a</i>	B7FNS4	24136.3	X	OOO	OOO
Predicted protein, domain: Rieske [2Fe-2S] iron-sulphur domain	<i>PHATRDRAFT_9046^a</i>	B7FPI8	17010.4	X	OO	O
Catalytic activity, transferase activity						
Phosphoribulokinase	<i>Prk</i>	B5Y5F0	43325.4	X	OO	O
3) Predicted proteins without assignable function						
Predicted protein	<i>PHATRDRAFT_42612^a</i>	B7FNX7	24938.5	O	OOO	OOO
Predicted protein	<i>PHATRDRAFT_45465^a/PHATRDRAFT_50215^a</i>	B7FXS8	37645.2	O	X	OOO
Predicted protein, family: SOUL haem-binding protein	<i>PHATRDRAFT_37136^a</i>	B7G284	46049.4	O	OOO	OOO
Predicted protein	<i>PHATRDRAFT_49286^a</i>	B7GA37	32141.6	OO	O	O
Predicted protein, domain: NAD(P)-binding domain	<i>PHATRDRAFT_49287^a</i>	B7GA38	126885.6	X	OO	O
Predicted protein, family: Protein of unknown function DUF1517	<i>PHATRDRAFT_32071^a</i>	B7FQ47	33258.8	OO	X	O

¹Proteins in this table were found in at least two of the three gels, a full list of labeled proteins can be found in S1 Information. OOO—only one protein per excised gel spot was found, OO—identification of probe labeled protein besides other unlabeled proteins in a gel spot, O—more than one labeled protein per excised gel spot, X—no hit.

^aNames are temporarily ascribed to an open reading frame (ORF) by a sequencing project [41].

doi:10.1371/journal.pone.0140927.t001

gene regulation [30,31], almost nothing is known about underlying mechanistic aspects regarding covalent protein interactions. Therefore, we applied a PUA-derived as well as control probe to *P. tricornutum*.

Probe design and labeling strategy

PUAs are known to have diverse effects on planktonic organisms but defined molecular targets are hitherto almost unidentified. Especially their function in cell to cell communication of diatoms has attracted much attention [7,8,10,14]. We undertook a labeling study to obtain a deeper insight into the mechanism of action of these metabolites to reveal potential PUA-uptake of phytoplankton and to identify protein targets of the compounds. Following previous structure activity studies we addressed the specific activity of PUAs by comparison of probes derived from the active unsaturated aldehyde (TAMRA-PUA) and the inactive saturated aldehyde (TAMRA-SA) [16,35]. The design of the probes allowed to employ them in two different modes. For uptake studies we could use the TAMRA coupled molecules as described earlier for the monitoring of PUA-targeting in copepods [35]. Interestingly, the different effects of unmodified saturated aldehydes and PUAs observed in previous studies [16] were also mirrored in the effect of our different TAMRA-constructs. This indicates that the TAMRA substitution has no significant influence on the action of the aldehydes. However we cannot exclude that permeability is altered by the substitution.

Probe concentration was set to 10 μ M, a value for which different algae showed response to DD regarding cell membrane permeability of SYTOX Green [7], but *P. tricornutum* did not [8]. For identification of protein targets we developed a two-step protocol involving incubation with unmodified SA or DDY and, after work-up, coupling with the TAMRA-N₃. This approach allows to minimize the influence of bulky groups during *in vivo* interaction with target proteins. The well-established CuAAC coupling allowed to covalently link the dye to DDY-labeled proteins [42,43]. As fluorescent reporter we selected the tetramethylrhodamine fluorophore as it is relatively cheap, pH insensitive, photostable, cell permeable and easily excitable with common lasers and filter sets [44]. Compared to experimental design of fluorescence microscopy where physiological conclusions were relevant, probe concentration in the mechanistic gel electrophoretic experiments was increased to 250 μ M DDY ensuring an adequate detection of labeled proteins.

TAMRA-PUA accumulates in *P. tricornutum*

Fluorescence microscopy clearly shows an uptake and accumulation of the DD derived probe by *P. tricornutum* (Fig 3). In contrast, TAMRA-SA, the probe derived from an almost inactive aldehyde with otherwise similar physicochemical properties, compared to TAMRA-PUA, did not substantially accumulate in the cells. Apparently the $\alpha,\beta,\gamma,\delta$ -unsaturated structure element found in PUAs is responsible for uptake and/or accumulation within diatom cells. A potential mechanism explaining the accumulation could be an inhibited exfiltration due to covalent adduct formation with cellular components such as proteins [17,18] as verified below or DNA [19–21]. In contrast, the weaker fluorescence signal of TAMRA-SA is consistent with the much lower reactivity of the underlying structure hexanal for which only few covalent reactions with proteins have been reported [45,46]. By applying the hexanal derived TAMRA-SA to a *P. tricornutum* culture we did not observe any covalently modified proteins in the corresponding 1D gel (S2 Fig).

The intracellular accumulation can explain the specific elicitation of effects by PUAs [8]. We can exclude that the dye itself accumulates unspecifically in cells since TAMRA-N₃ treated *P. tricornutum* showed no different fluorescence signals compared to untreated controls

(Tukey's HSD test $p > 0.05$ between TAMRA- N_3 and no probe), confirming the effective washing procedure to remove TAMRA [47]. 3D SIM images (Fig 4) reveal that fluorescence after application of the TAMRA-PUA probe is distributed over almost the entire cell. The lack of intracellular compartmentation can be explained with the high reactivity of such types of electrophilic Michael acceptors [16,48,49]. Apparently no preferred shuttling of the probe into specific compartments occurs but also the cell walls and membranes do not represent a barrier for this compound class. PUA-uptake might thus be a way to facilitate diatoms' perception of this compound class. Efficient uptake of essential metabolites has been earlier observed in diatoms but specific uptake mechanisms of primary and secondary metabolites involving transporters are not yet identified [50]. However, transporters of glucose that can support mixotrophic growth of *P. tricornutum* are known, supporting the note of the capability of the alga to actively take up organic metabolites from its environment [51]. This further supports the notion of a possible cell to cell communication mechanism based on PUAs that requires cellular uptake. To unravel potential molecular targets within the proteome of *P. tricornutum* we undertook further labeling studies.

DDY covalently modifies proteins of *P. tricornutum*

We performed an *in vivo* labeling of *P. tricornutum* with a PUA-derived probe to identify target proteins and to deduce affected molecular functions and biochemical pathways. We hypothesize that modified proteins may lose their function and that PUAs thereby interrupt or disturb metabolic pathways. These changes on a molecular level probably lead to observed effects of PUAs like growth inhibition and cell death [4,8].

Whereas Vardi et al. used a transcriptome analysis to search for DD affected genes and gene products by screening for up- and downregulated transcripts [29], we performed a direct investigation on the covalent modification of the proteome by DDY. Thus, we discover interactions with proteins, which do not necessarily have an influence on the transcript level but a direct influence on the functionality of these proteins.

Although the unsaturated aldehyde group of PUAs is universally reactive against nucleophilic amino acid side chains, we received moderate specific labeling of proteins (Table 1). This agrees with previous findings that DD preferentially attacks distinct proteins and specific nucleophilic sites if incubated with isolated purified proteins [17]. Underneath the confident target proteins we found four fucoxanthin chlorophyll *a/c* proteins, which are part of the light harvesting complex (LHC), responsible for the delivery of excitation energy between photosystem I and II [52]. Compared to higher plants, LHCs of diatoms named fucoxanthin-chlorophyll-proteins bind chlorophyll *c* instead of *b* and fucoxanthin instead of lutein [53]. Three groups of LHCs regarding their sequence and function are known, the found target proteins (see Table 1) belong to two groups of them: *Lhcx* gene products are needed for protection against surplus light and thus photoprotection and *Lhcf* gene products, the main antenna proteins, function in light harvesting (reviewed in [54]). Effects of DD on photosystem efficiency have already been shown for the diatoms *Thalassiosira weissflogii* [14] and a transgenic *P. tricornutum* [29] and our findings now provide a mechanistic explanation for this action of PUAs.

The energy harvested during light reaction is mainly stored by forming adenosine triphosphate (ATP). We identified two probe labeled ATP synthase subunits (see Table 1) belonging to the extrinsic catalytic sector, CF1 [55] of the chloroplastic ATP synthase. ATP synthase, located either in the mitochondria inner membrane or chloroplast thylakoid membrane, are responsible for cellular ATP production from adenosine diphosphate and inorganic phosphor in the presence of a proton gradient across the membrane [56]. The two PUA-targets ATP

synthase subunit alpha (*AtpA*) and ATP synthase subunit beta (*AtpB*) are located in the water soluble CF1 complex of the chloroplastic ATP synthase. In the green algae *Chlamydomonas reinhardtii* in the absence of the mitochondrial beta-subunit (gene name *Atp2*), ATP synthase could not be assembled into an enzyme complex leading to decreased mitochondrial respiration [57]. In conjunction with the finding of impairment of enzymes involved in light harvesting the identified ATP synthase targets support the notion of a profound modulation of the energy household under the influence of PUAs.

Enzymes from the Calvin cycle are also PUA-targets connected to photosynthetic activity. Two PUA-targets, the kinase PRK and the epimerase RPE were found to be labeled after DDY incubation. These enzymes are involved in carbon dioxide assimilation during the dark reaction. RPE reversibly catalyzes the reaction of D-xylulose 5-phosphate to D-ribulose 5-phosphate in the Calvin cycle and pentose phosphate pathway [58]. The product D-ribulose-5-phosphate is under ATP consumption further converted by PRK to D-ribulose-1,5-bisphosphate, which acts as acceptor for CO₂ in photosynthetic carbon assimilation [59]. In the Calvin cycle glyceraldehyde-3-phosphate dehydrogenase, the small protein CP12 and PRK form a multi-enzyme complex, the redox state of PRK is regulated by thioredoxin-mediated thiol-disulfide exchange in a light-dependent manner [59,60]. PRK is not active in the oxidized form where cysteine residues at positions 16 and 55 in land plants and green algae form an intramolecular disulfide bridge [61]. By reaction of those thiols with a PUA inactivation of PRK due to spatial changes and loss of redox behavior is conceivable. Also labeling on other sites, such as Lys may lead to loss of activity. Examples for alkylations were shown for PRK of different origin [62,63] and accordingly, alkylation of thiols and other nucleophilic residues by PUAs might change activity of enzymes.

It is striking that metabolic pathways such as the pentose phosphate pathway, photosynthesis including photophosphorylation and Calvin cycle that are involved in the energy household are specifically affected by PUA-treatment. The response is more immediate than transcriptional regulation since proteins are the direct target of a covalent modification.

Conclusion

In this study we investigate the structure specificity of the uptake of PUA-derived probes and analogues in *P. tricornutum*. We could also reveal PUA probe targets within the proteome of the alga. Uptake experiments show a clear enrichment of TAMRA-PUA within the cells compared to TAMRA-SA. Chemoproteomics allowed the identification of target proteins of TAMRA-PUA. Interestingly, preferential targets have important roles in biological processes covering photosynthesis including ATP generation, conversion in Calvin cycle or the pentose phosphate pathway. Besides three *Lhcf*- and one *Lhcx*-coding proteins important for light harvesting and photoprotection we found two ATP synthases. Generation of ATP is of major importance since it supports nearly all cellular activities that require energy and its synthesis is the most frequent chemical reaction in the biological world [56]. PRK, another PUA target catalyzes the only reaction by which intermediates in the Calvin cycle can be contributed for further CO₂ assimilation [64]. RPE is important for both, the Calvin cycle and the reverse pentose phosphate pathway. Loss of molecular functions of these proteins as it might occur through covalent reactions of the nucleophilic protein residues with a PUA would immediately interfere with the homeostasis of algae cells, explaining the fast adverse effect of PUAs.

Supporting Information

S1 Fig. Relative fluorescence intensity of *P. tricornutum* cells treated under different conditions in two independent experiments. Cells were either incubated with TAMRA-PUA,

TAMRA-N₃, TAMRA-SA (only experiment 2) for one hour or kept under identical conditions without probe. For each experiment one microscope slide per treatment with five cells (experiment 1) or seven cells (experiment 2) was measured. For experiment 1, all microscope slides were embedded in 2,2'-thiodiethanol as described in the materials and methods section, for experiment 2 a poly (vinyl alcohol)/ n-propyl gallate antifade embedding medium [See Lu-Walther H-W, Kielhorn M, Förster R, Jost A, Wicker K, Heintzmann R. fastSIM: a practical implementation of fast structured illumination microscopy. *Methods Appl Fluoresc.* 2015;3(1):014001] was used. Fluorescence intensities were recorded as mean gray value per pixel after data treatment as described in the main text. To compare both experiments results were normalized to "no probe". Normalized averaged mean gray values per pixel of cells of each treatment are presented as bars \pm SD. Kruskal-Wallis one way analysis of variance on ranks revealed differences in the median values among the treatment groups of each experiment (No. 1 H = 12.500, No. 2 H = 22.902; p < 0.05). Tukey's HSD test (p < 0.05) attested significant differences between TAMRA-PUA and all other treatments within each experiment. (TIF)

S2 Fig. SDS-PAGE of *in vivo* treated samples of *P. tricornutum*. *P. tricornutum* was incubated with 100 μ M of the reactive group (RG) DDY or SA or DMSO as control. After one hour incubation cells were lysed, CuAAC with TAMRA-N₃ was applied and SDS-PAGE and in-gel fluorescence detection were accomplished (see also Fig 2). Only the DDY treated sample shows specific fluorescent bands. (TIF)

S3 Fig. 2D GE images. Position of excised spots with identified proteins in the three 2D gels (1, 2 and 3) presented in the Coomassie stained gels (A) and fluorescence images excited at 532nm for TAMRA-PUA detection (B). The positions of the spots were computed by Delta 2D for each image by considering the Coomassie stained gel image as well as TAMRA-PUA and Cy5 fluorescence images (for raw data of each image see S3 Folder). Slightly shifted positions of spots between Coomassie and fluorescence images of each gel are due to change of gel dimensions during Coomassie staining. (TIF)

S1 Folder. Unmodified wide field fluorescence images of *P. tricornutum* treated with TAMRA-PUA, TAMRA-SA, TAMRA-N₃ or without addition of a substance as control for uptake experiments. Cells were measured with a Zeiss Elyra S1 system in wide field mode. A 561 nm laser was used for excitation, and fluorescence was filtered by a band pass filter (BP 570–620 nm) which opens up above 750 nm. WF—wide field. (ZIP)

S2 Folder. Unmodified bright field images of *P. tricornutum* treated with TAMRA-PUA, TAMRA-SA, TAMRA-N₃ or without addition of a substance as control for uptake experiments. Cells were measured with a Zeiss Elyra S1 system in bright field mode. Before data analysis tonal correction was optimized. BF—bright field. (ZIP)

S3 Folder. Unmodified 2D GE images. Fluorescence images of TAMRA-PUA and Cy5 labeled protein gels and images of Coomassie stained gels. (ZIP)

S1 Information. LC-MS/MS analysis and data processing. (DOCX)

S1 Table. Target proteins found by 2D GE. Proteins were classified into confident, labeled and putative proteins subject to guidelines described in [S1 Information](#) and separated according to their biological processes and molecular functions. (XLSX)

Acknowledgments

Kathrin Klehs, Ivana Šumanovac-Šestak and Martin Reifarth are acknowledged for helpful advice on experimental design of fluorescence microscopy and choice of embedding medium.

Author Contributions

Conceived and designed the experiments: SW GP BM OW. Performed the experiments: SW NW YH BM HWLW. Analyzed the data: SW NW GP. Contributed reagents/materials/analysis tools: SW NW RH OW AS. Wrote the paper: SW GP.

References

1. Nelson DM, Tréguer P, Brzezinski MA, Leynaert A, Quéguiner B. Production and dissolution of biogenic silica in the ocean: Revised global estimates, comparison with regional data and relationship to biogenic sedimentation. *Global Biogeochem Cycles*. 1995; 9(3):359–72.
2. Pohnert G. Diatom/Copepod interactions in plankton: The Indirect chemical defense of unicellular algae. *ChemBioChem*. 2005; 6(6):946–59. PMID: [15883976](#)
3. Caldwell G. The influence of bioactive oxylipins from marine diatoms on invertebrate reproduction and development. *Mar Drugs*. 2009; 7(3):367–400. doi: [10.3390/md7030367](#) PMID: [19841721](#)
4. Ianora A, Bentley MG, Caldwell GS, Casotti R, Cembella AD, Engström-Öst J, et al. The relevance of marine chemical ecology to plankton and ecosystem function: An emerging field. *Mar Drugs*. 2011; 9(9):1625–48. doi: [10.3390/md9091625](#) PMID: [22131962](#)
5. Ianora A, Miralto A. Toxicogenic effects of diatoms on grazers, phytoplankton and other microbes: a review. *Ecotoxicology*. 2010; 19(3):493–511. doi: [10.1007/s10646-009-0434-y](#) PMID: [19924531](#)
6. Ianora A, Miralto A, Poulet SA, Carotenuto Y, Buttino I, Romano G, et al. Aldehyde suppression of copepod recruitment in blooms of a ubiquitous planktonic diatom. *Nature*. 2004; 429(6990):403–7. PMID: [15164060](#)
7. Ribalet F, Berges JA, Ianora A, Casotti R. Growth inhibition of cultured marine phytoplankton by toxic algal-derived polyunsaturated aldehydes. *Aquat Toxicol*. 2007; 85(3):219–27. PMID: [17942163](#)
8. Vardi A, Formiggini F, Casotti R, De Martino A, Ribalet F, Miralto A, et al. A stress surveillance system based on calcium and nitric oxide in marine diatoms. *PLoS Biol*. 2006; 4(3):411–9.
9. Balestra C, Alonso-Sáez L, Gasol JM, Casotti R. Group-specific effects on coastal bacterioplankton of polyunsaturated aldehydes produced by diatoms. *Aquat Microb Ecol*. 2011 Mar 31; 63(2):123–31.
10. Vidoudez C, Pohnert G. Growth phase-specific release of polyunsaturated aldehydes by the diatom *Skeletonema marinoi*. *J Plankton Res*. 2008; 30(11):1305–13.
11. Vidoudez C, Casotti R, Bastianini M, Pohnert G. Quantification of dissolved and particulate polyunsaturated aldehydes in the adriatic sea. *Mar Drugs*. 2011; 9(4):500–13. doi: [10.3390/md9040500](#) PMID: [21731545](#)
12. Ribalet F, Wichard T, Pohnert G, Ianora A, Miralto A, Casotti R. Age and nutrient limitation enhance polyunsaturated aldehyde production in marine diatoms. *Phytochemistry*. 2007; 68(15):2059–67. PMID: [17575990](#)
13. Casotti R, Mazza S, Ianora A, Miralto A. Growth and cell cycle progression in the diatom *Thalassiosira weissflogii* is inhibited by the diatom aldehyde 2-trans-4-trans-decadienal. ASLO Aquatic Sciences 2001 Meeting, Special Session 22—Strategies to reduce mortality in marine and freshwater phytoplankton; 2001 Oct 24–27, Albuquerque, USA.
14. Casotti R, Mazza S, Brunet C, Vantrepotte V, Ianora A, Miralto A. Growth inhibition and toxicity of the diatom aldehyde 2-trans,4-trans-decadienal on *Thalassiosira weissflogii* (bacillariophyceae) *J Phycol*. 2005; 41(1):7–20.
15. Adolph S, Poulet SA, Pohnert G. Synthesis and biological activity of $\alpha,\beta,\gamma,\delta$ -unsaturated aldehydes from diatoms. *Tetrahedron*. 2003; 59(17):3003–8.

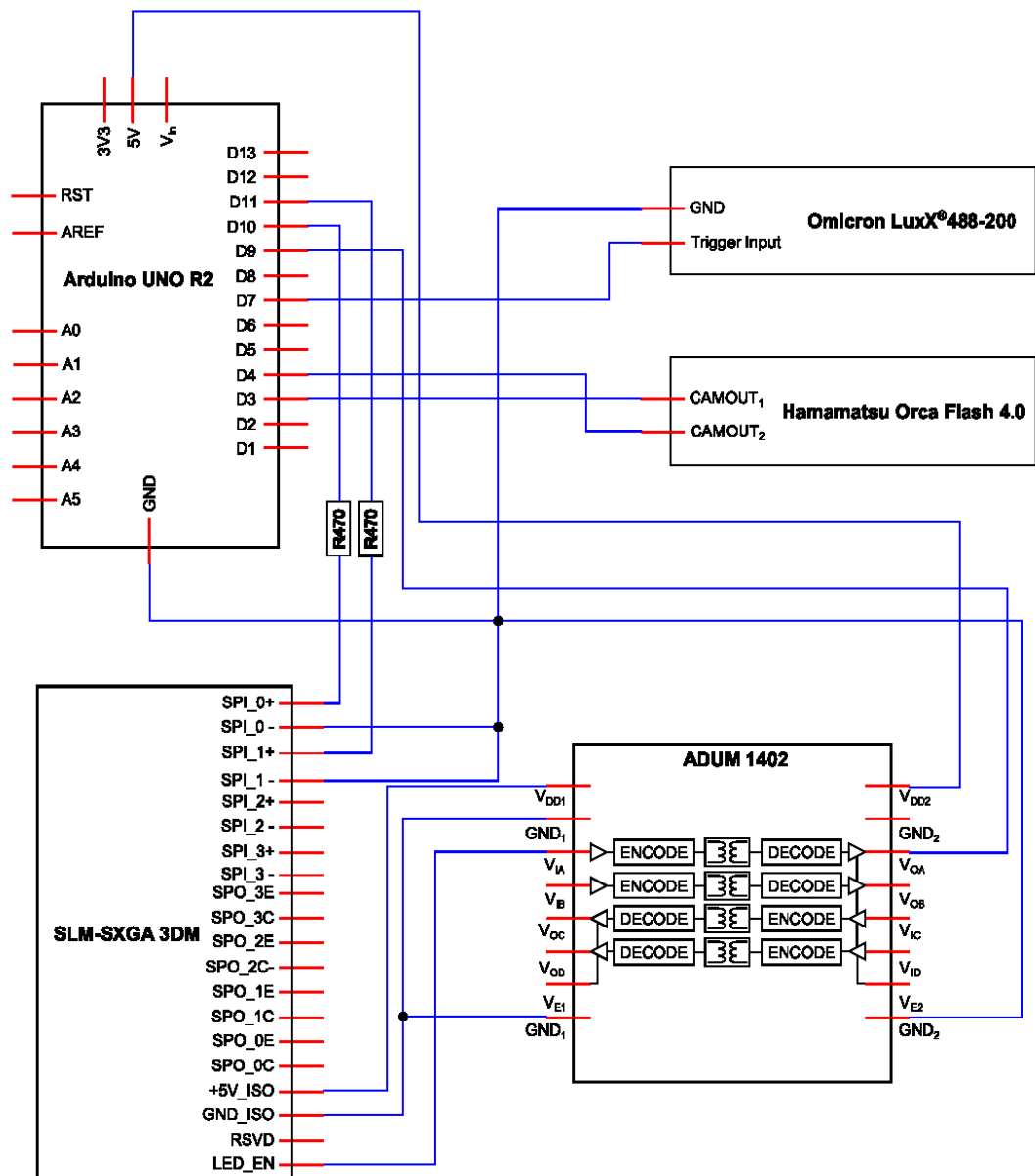
16. Adolph S, Bach S, Blondel M, Cueff A, Moreau M, Pohnert G, et al. Cytotoxicity of diatom-derived oxylipins in organisms belonging to different phyla. *J Exp Biol*. 2004; 207(17):2935–46.
17. Zhu X, Tang X, Zhang J, Tochtrop GP, Anderson VE, Sayre LM. Mass spectrometric evidence for the existence of distinct modifications of different proteins by 2(E),4(E)-decadienal. *Chem Res Toxicol*. 2010; 23(3):467–73. doi: [10.1021/bx900379a](https://doi.org/10.1021/bx900379a) PMID: [20070074](https://pubmed.ncbi.nlm.nih.gov/20070074/)
18. Sigolo CAO, Di Mascio P, Medeiros MHG. Covalent modification of cytochrome c exposed to *trans*, *trans*-2,4-decadienal. *Chem Res Toxicol*. 2007; 20(8):1099–110. PMID: [17658762](https://pubmed.ncbi.nlm.nih.gov/17658762/)
19. Carvalho VM, Asahara F, Di Mascio P, de Arruda Campos IP, Cadet J, Medeiros MHG. Novel 1,*N*⁶-etheno-2'-deoxyadenosine adducts from lipid peroxidation products. *Chem Res Toxicol*. 2000; 13(5):397–405. PMID: [10813657](https://pubmed.ncbi.nlm.nih.gov/10813657/)
20. Loureiro APM, Di Mascio P, Gomes OF, Medeiros MHG. *trans*,*trans*-2,4-Decadienal-induced 1,*N*²-etheno-2'-deoxyguanosine adduct formation. *Chem Res Toxicol*. 2000; 13(7):601–9. PMID: [10898592](https://pubmed.ncbi.nlm.nih.gov/10898592/)
21. Loureiro APM, de Arruda Campos IP, Gomes OF, Di Mascio P, Medeiros MHG. Structural characterization of diastereoisomeric ethano adducts derived from the reaction of 2'-deoxyguanosine with *trans*, *trans*-2,4-decadienal. *Chem Res Toxicol*. 2004; 17(5):641–9. PMID: [15144221](https://pubmed.ncbi.nlm.nih.gov/15144221/)
22. Buttino I, Hwang J-S, Sun C-K, Hsieh C-T, Liu T-M, Pellegrini D, et al. Apoptosis to predict copepod mortality: state of the art and future perspectives. *Hydrobiologia*. 2011; 666(1):257–64.
23. Hansen E, Even Y, Genevière A-M. The $\alpha,\beta,\gamma,\delta$ -unsaturated aldehyde 2-*trans*-4-*trans*-decadienal disturbs DNA replication and mitotic events in early sea urchin embryos. *Toxicol Sci*. 2004; 81(1):190–7. PMID: [15201434](https://pubmed.ncbi.nlm.nih.gov/15201434/)
24. Romano G, Russo GL, Buttino I, Ianora A, Miralto A. A marine diatom-derived aldehyde induces apoptosis in copepod and sea urchin embryos. *J Exp Biol*. 2003; 206(19):3487–94.
25. Bowler C, Allen AE, Badger JH, Grimwood J, Jabbari K, Kuo A, et al. The *Phaeodactylum* genome reveals the evolutionary history of diatom genomes. *Nature*. 2008 Nov 13; 456(7219):239–44. doi: [10.1038/nature07410](https://doi.org/10.1038/nature07410) PMID: [18923393](https://pubmed.ncbi.nlm.nih.gov/18923393/)
26. Armbrust EV, Berges JA, Bowler C, Green BR, Martinez D, Putnam NH, et al. The genome of the diatom *Thalassiosira pseudonana*: Ecology, evolution, and metabolism. *Science*. 2004 Oct 1; 306(5693):79–86. PMID: [15459382](https://pubmed.ncbi.nlm.nih.gov/15459382/)
27. Pohnert G, Lumineau O, Cueff A, Adolph S, Cordevant C, Lange M, et al. Are volatile unsaturated aldehydes from diatoms the main line of chemical defence against copepods? *Mar Ecol Prog Ser*. 2002; 245:33–45.
28. Graff van Creveld S, Rosenwasser S, Schatz D, Koren I, Vardi A. Early perturbation in mitochondria redox homeostasis in response to environmental stress predicts cell fate in diatoms. *The ISME Journal*. 2015 Feb; 9(2):385–95. doi: [10.1038/ismej.2014.136](https://doi.org/10.1038/ismej.2014.136) PMID: [25083933](https://pubmed.ncbi.nlm.nih.gov/25083933/)
29. Vardi A, Bidle KD, Kwityn C, Hirsh DJ, Thompson SM, Callow JA, et al. A diatom gene regulating nitric-oxide signaling and susceptibility to diatom-derived aldehydes. *Curr Biol*. 2008; 18(12):895–9. doi: [10.1016/j.cub.2008.05.037](https://doi.org/10.1016/j.cub.2008.05.037) PMID: [18538570](https://pubmed.ncbi.nlm.nih.gov/18538570/)
30. Lauritano C, Borra M, Carotenuto Y, Biffali E, Miralto A, Procaccini G, et al. First molecular evidence of diatom effects in the copepod *Calanus helgolandicus*. *J Exp Mar Biol Ecol*. 2011; 404(1–2):79–86.
31. Lauritano C, Borra M, Carotenuto Y, Biffali E, Miralto A, Procaccini G, et al. Molecular evidence of the toxic effects of diatom diets on gene expression patterns in copepods. *PLoS ONE*. 2011; 6(10):e26850. doi: [10.1371/journal.pone.0026850](https://doi.org/10.1371/journal.pone.0026850) PMID: [22046381](https://pubmed.ncbi.nlm.nih.gov/22046381/)
32. Evans MJ, Cravatt BF. Mechanism-based profiling of enzyme families. *Chem Rev*. 2006; 106(8):3279–301. PMID: [16895328](https://pubmed.ncbi.nlm.nih.gov/16895328/)
33. Gersch M, Kreuzer J, Sieber SA. Electrophilic natural products and their biological targets. *Nat Prod Rep*. 2012; 29(6):659–82. doi: [10.1039/c2np20012k](https://doi.org/10.1039/c2np20012k) PMID: [22504336](https://pubmed.ncbi.nlm.nih.gov/22504336/)
34. Böttcher T, Pitscheider M, Sieber SA. Natural products and their biological targets: Proteomic and metabolomic labeling strategies. *Angew Chem Int Ed*. 2010; 49(15):2680–98.
35. Wolfram S, Nejtgaard JC, Pohnert G. Accumulation of polyunsaturated aldehydes in the gonads of the copepod *Acartia tonsa* revealed by tailored fluorescent probes. *PLoS One*. 2014; 9(11):e112522. doi: [10.1371/journal.pone.0112522](https://doi.org/10.1371/journal.pone.0112522) PMID: [25383890](https://pubmed.ncbi.nlm.nih.gov/25383890/)
36. Maier I, Calenberg M. Effect of extracellular Ca²⁺ and Ca²⁺-antagonists on the movement and chemotaxis of male gametes of *Ectocarpus siliculosus* (Phaeophyceae). *Bot Acta*. 1994; 107(6):451–60.
37. Gaff DF, Okong'o-Ogola O. The use of non-permeating pigments for testing the survival of cells. *J Exp Bot*. 1971; 22(3):756–8.
38. Laemmli UK. Cleavage of structural proteins during the assembly of the head of bacteriophage T4. *Nature*. 1970; 227(5259):680–5. PMID: [5432063](https://pubmed.ncbi.nlm.nih.gov/5432063/)

39. Carl Roth GmbH. Karlsruhe: Polyacrylamide gel electrophoresis (PAGE). Available: http://www.carlroth.com/website/fr-fr/pdf/PAGE_E.pdf. Accessed 2012 Sep 15.
40. Shevchenko A, Tomas H, Havlis J, Olsen JV, Mann M. In-gel digestion for mass spectrometric characterization of proteins and proteomes. *Nat Protoc.* 2006; 1(6):2856–60. PMID: [17406544](#)
41. UniProt consortium [Internet]. Universal Protein Resource consortium; 2002–2015 [updated 2015 Feb 5]; Gene names. Available: http://www.uniprot.org/help/gene_name. Accessed 2015 Mar 30.
42. Baskin JM, Bertozzi CR. Bioorthogonal click chemistry: Covalent labeling in living systems. *QSAR Comb Sci.* 2007; 26(11–12):1211–9.
43. Best MD. Click chemistry and bioorthogonal reactions: Unprecedented selectivity in the labeling of biological molecules. *Biochemistry.* 2009 Jul 21; 48(28):6571–84. doi: [10.1021/bi9007726](#) PMID: [19485420](#)
44. Haugland RP. Handbook of fluorescent probes and research products. 9th ed. Eugene: Molecular Probes Inc; 2002.
45. Meynier A, Rampon V, Dalgalarondo M, Genot C. Hexanal and 1,2-hexenal form covalent bonds with whey proteins and sodium caseinate in aqueous solution. *Int Dairy J.* 2004; 14(8):681–90.
46. O'Keefe SF, Wilson LA, Resurreccion AP, Murphy PA. Determination of the binding of hexanal to soy glycinin and β -conglycinin in an aqueous model system using a headspace technique. *J Agric Food Chem.* 1991; 39(6):1022–8.
47. Cunningham CW, Mukhopadhyay A, Lushington GH, Blagg BSJ, Prinszano TE, Krise JP. Uptake, distribution and diffusivity of reactive fluorophores in cells: Implications toward target identification. *Mol Pharm.* 2010; 7(4):1301–10. doi: [10.1021/mp100089k](#) PMID: [20557111](#)
48. Schwöbel JAH, Wondrusch D, Koleva YK, Madden JC, Cronin MTD, Schüürmann G. Prediction of Michael-type acceptor reactivity toward glutathione. *Chem Res Toxicol.* 2010; 23(10):1576–85. doi: [10.1021/tx100172x](#) PMID: [20882991](#)
49. Witz G. Biological interactions of α,β -unsaturated aldehydes. *Free Radic Biol Med.* 1989; 7(3):333–9. PMID: [2673948](#)
50. Spielmeier A, Gebser B, Pohnert G. Investigations of the uptake of dimethylsulfoniopropionate by phytoplankton. *ChemBioChem.* 2011 Oct 17; 12(15):2276–9. doi: [10.1002/cbic.201100416](#) PMID: [21853511](#)
51. Zheng Y, Quinn A, Sriram G. Experimental evidence and isotopomer analysis of mixotrophic glucose metabolism in the marine diatom *Phaeodactylum tricornutum*. *Microb Cell Fact.* 2013 Nov 14; 12(1):1–17.
52. Liu XD, Shen YG. NaCl-induced phosphorylation of light harvesting chlorophyll a/b proteins in thylakoid membranes from the halotolerant green alga, *Dunaliella salina*. *FEBS Lett.* 2004 Jul 2; 569(1–3):337–40.
53. Veith T, Büchel C. The monomeric photosystem I-complex of the diatom *Phaeodactylum tricornutum* binds specific fucoxanthin chlorophyll proteins (FCPs) as light-harvesting complexes. *Biochim Biophys Acta (BBA)—Bioenergetics.* 2007 Dec; 1767(12):1428–35.
54. Gundermann K, Schmidt M, Weisheit W, Mittag M, Büchel C. Identification of several sub-populations in the pool of light harvesting proteins in the pennate diatom *Phaeodactylum tricornutum*. *Biochim Biophys Acta.* 2013 Mar; 1827(3):303–10. doi: [10.1016/j.bbabi.2012.10.017](#) PMID: [23142526](#)
55. Groth G, Strotmann H. New results about structure, function and regulation of the chloroplast ATP synthase (CF₁CF₀). *Physiol Plant.* 1999; 106(1):142–8.
56. Yoshida M, Muneyuki E, Hisabori T. ATP synthase—a marvellous rotary engine of the cell. *Nat Rev Mol Cell Biol.* 2001; 2:669–77. PMID: [11533724](#)
57. Lapaille M, Thiry M, Perez E, Gonzalez-Halphen D, Remacle C, Cardol P. Loss of mitochondrial ATP synthase subunit beta (Atp2) alters mitochondrial and chloroplastic function and morphology in *Chlamydomonas*. *Biochim Biophys Acta.* 2010 Aug; 1797(8):1533–9. doi: [10.1016/j.bbabi.2010.04.013](#) PMID: [20416275](#)
58. Sprenger GA. Genetics of pentose-phosphate pathway enzymes of *Escherichia coli* K-12. *Arch Microbiol.* 1995 Nov; 164(5):324–30. PMID: [8572885](#)
59. Brandes HK, Hartman FC, Lu T-YS, Larimer FW. Efficient expression of the gene for spinach phosphoribulokinase in *Pichia pastoris* and utilization of the recombinant enzyme to explore the role of regulatory cysteinyl residues by site-directed mutagenesis. *J Biol Chem.* 1996; 271(11):6490–6. PMID: [8626451](#)
60. Graciet E, Lebreton S, Gontero B. Emergence of new regulatory mechanisms in the Benson—Calvin pathway via protein—protein interactions: a glyceraldehyde-3-phosphate dehydrogenase/CP12/phosphoribulokinase complex. *J Exp Bot.* 2004; 55(400):1245–54. PMID: [15047759](#)

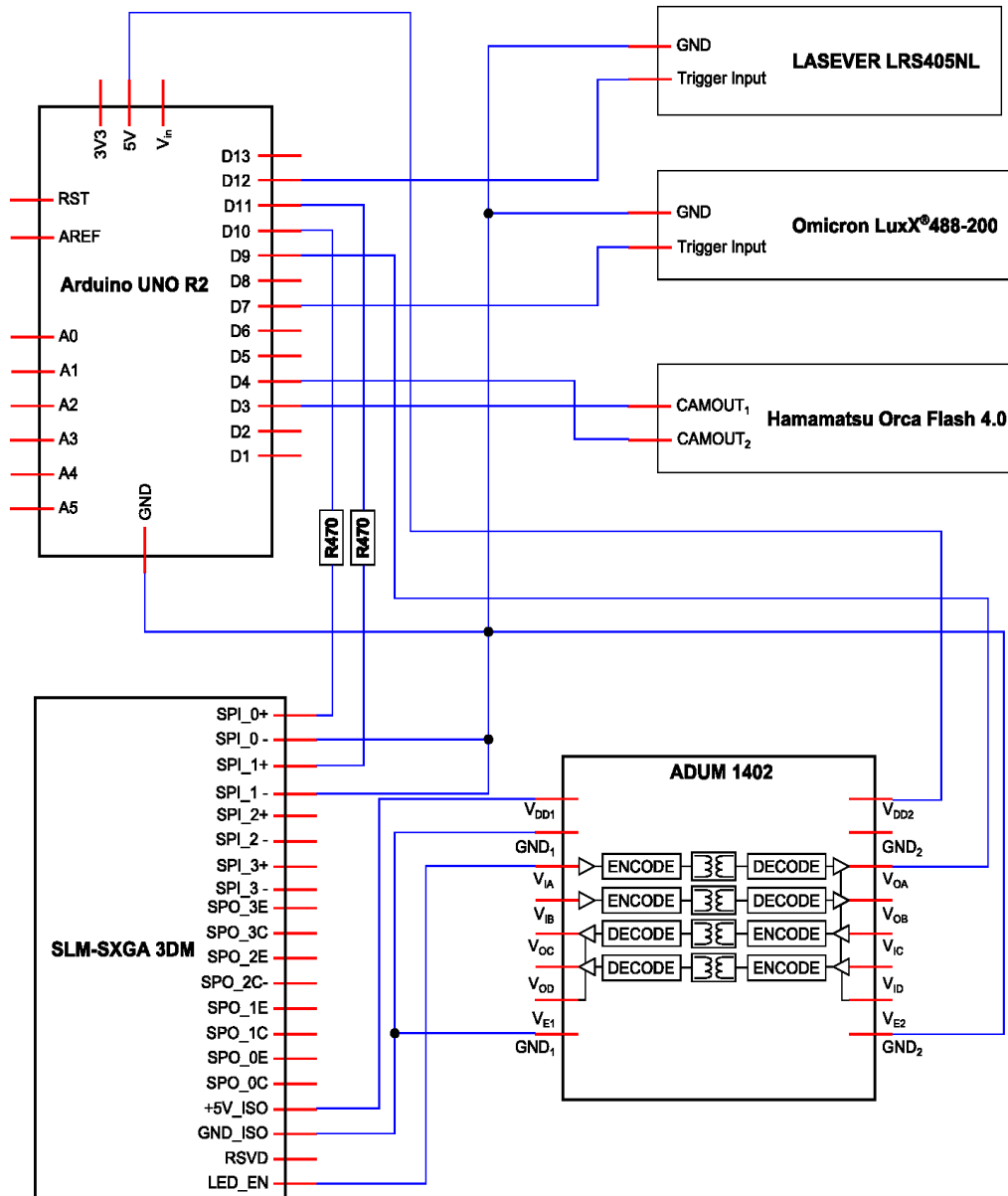
61. Maberly SC, Courcelle C, Groben R, Gontero B. Phylogenetically-based variation in the regulation of the Calvin cycle enzymes, phosphoribulokinase and glyceraldehyde-3-phosphate dehydrogenase, in algae. *J Exp Bot*. 2010 Mar, 2010; 61(3):735–45. doi: [10.1093/jxb/erp337](https://doi.org/10.1093/jxb/erp337) PMID: [19926682](https://pubmed.ncbi.nlm.nih.gov/19926682/)
62. Porter MA, Hartman FC. Commonality of catalytic and regulatory sites of spinach phosphoribulokinase: Characterization of a tryptic peptide that contains an essential cysteinyl residue. *Biochemistry*. 1986 Nov; 25(23):7314–8.
63. Lebreton S, Graciet E, Gontero B. Modulation, via protein-protein interactions, of glyceraldehyde-3-phosphate dehydrogenase activity through redox phosphoribulokinase regulation. *J Biol Chem*. 2003; 278(14):12078–84. PMID: [12556449](https://pubmed.ncbi.nlm.nih.gov/12556449/)
64. Michels AK, Wedel N, Kroth PG. Diatom plastids possess a phosphoribulokinase with an altered regulation and no oxidative pentose phosphate pathway. *Plant Physiol*. 2005; 137(3):911–20. PMID: [15734914](https://pubmed.ncbi.nlm.nih.gov/15734914/)

Appendix

A.1 Electronic circuit sketch in the first prototype of fastSIM setup



A.2 Electronic circuit sketch in nonlinear fastSIM setup



B.1 Arduino_Code: fastSIM_main_ArduinoProgram

```
/* In this InternalRunningMode, the ExposureTime has to be given on Camera
Software.
In order to get proper GlobalExposureTime for different Rep the "real" Readout
Timing and Shutter Open Timing have to be tested.
*/
// variables needed to be defined depends on cases
int rep = 1; // repetition of images
int NLSIM = 0;
int NLcycle = 6; // 6 means one 405, one DeEx, one Measure 3 Clear images
int KohinoorNLSIM = 0; // 405 nm always on and do LSIM with 488 nm.
int DoZstack = 0; // "1" enable trigger to Zstack-Arduino,
// "0" disable Zstack-Arduino trigger
int NumSlices = 15; // # of slices for z-scanning; should be the same as in the
// Zstack-Arduino
int DoLASER = 2; /* processes one SLM cycle on-switch-off-switch,
DoLASER==0 mean Laser always off,
DoLASER==1 means Laser on only Frame
DoLASER==2 means Laser on Frame and Antiframe, */
int conllu = 0; // for continuous illumination;
int NLSwitch = 0; // for Photoswitchable fluorophore swtiching test
int KNLSwitch = 0; // for Kohinoor Photoswitchable fluorophore swtiching test
int KSwitch405 = 0; // for Kohinoor Photoswitchable fluorophore, swtiching test
// with 405
// on/off cycle by cycle
// define variables for SLM repertoire
int NumDirs = 3; // number of directions of grating
int NumPhases = 3; // number of phases of grating
int TriggerR = 1; // check Camera Trigger_ready output
int Shot = 10; // 405 nm activated illu.
int captures = 20; // 488nm deactivated illu.
int Clear405 = 1;
int t fastR = 0; // Liyan's rolling SLM project
int LSIMwith405 = 0; // take LSIM data with 405 nm laser.
// w1: 405 nm always on, w2: 405 nm on when the camera
// readout.
/*
Trigger for the Hamamatsu C11440 in both LiveMode and TimeSeriesMode
Trigger Mode: External Level Trigger,set exposure time and exposure length
*/
// define pin on Arduino (all variables)
int cam_in = 2; // trigger to camera. (ie. start exposure)
int cam_out_G = 3; // Global exposure trigger from camera.
int cam_out_R = 4; // Trigger ready output from camera (signal is high if camera is
// ready
//for next exposure)
```

```

int laser_enable = 7; // Trigger laser on/off, blanking mode
int slm_out = 9; // SLM LED enable signal, "HIGH" indicates SLM is displaying images
int slm_ext_run = 10; // starts hardware, activate running orders
int slm_trigger = 11; // if high start showing image
int DoActLaseer = 12; // trigger 405 nm laser
int DoGLaser = 8; // trigger 532 nm laser
int zstackarduino = 5; // to zstack arduino board

// define variables for TestLASER()
int blinks = 3; // number of blinks at the beginning
int countblinks = 0;
// define variables for z-stage
int Slice = 0;
int mindelay = 100; // time for delay

int debug = 1;
#define D(x) do{if(debug){x;}}while(0)

void setup() {
  // allocate names to pins on arduino
  //DIGITAL SIGNALS
  Serial.begin(9600); // opens serial port, sets data rate to 9600 bps
  Serial.println("waiting for input. Enter 'h' to see all the current paremeters.");
  Serial.print("\n");
  Serial.println ("Or enter 'H' to see introduction of all paremeters.");
  // CAMERA
  pinMode(cam_in, OUTPUT); // exposure while signal is high
  pinMode(cam_out_R, INPUT); // Camera Trigger ready signal
  pinMode(cam_out_G, INPUT); // Global exposure signal
  // LASER
  pinMode(laser_enable, OUTPUT); // Luxx 488nm can be triggered in 10 ns
  pinMode(DoActLaseer, OUTPUT); // trigger 405 nm laser
  pinMode(DoGLaser, OUTPUT); // trigger 532 nm laser
  // SLM
  pinMode (slm_ext_run, OUTPUT);
  pinMode (slm_trigger, OUTPUT);
  pinMode (slm_out, INPUT); // LED_EN
  // z-stage
  pinMode (zstackarduino, OUTPUT);
  digitalWrite (slm_ext_run, HIGH); //starts running order of SLM (Hardward Mode)
  TestLASER();
}
//test if Laser is working (try blinking)
void TestLASER() {
  countblinks = 0;
  while (countblinks < blinks) {
    digitalWrite (laser_enable, LOW);

```

```

    delay(200); // millisecond
    digitalWrite (laser_enable, HIGH);
    delay(200);
    countblinks = countblinks + 1;
}
digitalWrite (laser_enable, LOW); // after 3 blinks, Laser is set to low = off
}

void SLMCycle(int DoLASER) {
    while (digitalRead(slm_out) == LOW) {
        delayMicroseconds(mindelay); // this delay is for checking digitalRead not so
often
    }
    if (DoLASER > 0) digitalWrite (laser_enable, HIGH);
    while (digitalRead(slm_out) == HIGH) {
        delayMicroseconds(mindelay); // positive image on SLM
    }
    if (DoLASER > 0) digitalWrite(laser_enable, LOW); // Now SLM is under switching
// process,
// stop illumination the SLM,
// camera still integrating!

    while (digitalRead(slm_out) == LOW) {
        delayMicroseconds(mindelay);
    }
    if (DoLASER > 1) digitalWrite(laser_enable, HIGH); // illuminate the SLM again
    while (digitalRead(slm_out) == HIGH) {
        delayMicroseconds(mindelay); // SLM shows negative image
    }
    if (DoLASER > 1) digitalWrite(laser_enable, LOW); // Now SLM is under switching
// process,
// stop illumination the SLM
}

void fastRSLMCycle() {
    while (digitalRead(slm_out) == LOW) {
        delayMicroseconds(mindelay);
    }
    digitalWrite(laser_enable, HIGH);
    while (digitalRead(slm_out) == HIGH) {
        delayMicroseconds(mindelay); // positive image on SLM
    }
    digitalWrite(laser_enable, LOW); // Now SLM is under switching process, stop
// illumination the SLM
}

void loop() {
    checkinput:
    // send data only when you receive data:

```

```

while (Serial.available() > 0) {
  //D(Serial.println("waiting for input"));

  switch (Serial.read()) {
    case 'r': rep = Serial.parseInt(); Serial.print("# rep:"); Serial.println(rep, DEC);
      break;
    case 'z': { DoZstack = Serial.parseInt ();Serial.print ("z1/z0 DoZstack:");
      Serial.println (DoZstack, DEC); break; }
    case 's': { NumSlices = Serial.parseInt ();Serial.print ("s# NumSlices:");
      Serial.println (NumSlices, DEC); break; }
    case 'c': { conIllu = Serial.parseInt (); NLSIM = 0; NLSwitch = 0; KohinoorNLSIM = 0;
      fastR = 0; KNLSwitch = 0; Serial.print ("c1/c0 conIllu:");
      Serial.println (conIllu, DEC); break;}
    case 'l': { DoLASER = Serial.parseInt ();Serial.print ("l1/l0 DoLASER:");
      Serial.println (DoLASER, DEC); break;}
    case 'o': { NumDirs = Serial.parseInt ();Serial.print ("o# NumDirs:");
      Serial.println (NumDirs, DEC); break;}
    case 'p': { NumPhases = Serial.parseInt ();Serial.print ("p# NumPhases:");
      Serial.println (NumPhases, DEC); break;}
    case 'K': { KohinoorNLSIM = Serial.parseInt (); conIllu = 0; NLSwitch = 0; NLSIM = 0;
      NumDirs = 6; NumPhases = 5; Serial.print ("K1/K0 KohinoorNLSIM:");
      Serial.println (KohinoorNLSIM, DEC); Serial.println ();
      Serial.print ("conIllu=0; NLSIM=0; NLSwitch=0; NumDirs=6; NumPhases=5");
      Serial.print ("\n"); break;}
    case 'P': { KSwitch405 = Serial.parseInt (); conIllu = 0; NLSIM = 0; NumDirs = 6;
      NumPhases = 5; Serial.print ("P1/P0 KSwitch405:");
      Serial.println (KSwitch405, DEC); Serial.println ();
      Serial.print ("conIllu=0; NLSIM=0; NLSwitch=0"); Serial.print ("\n"); break;}
    case 'N': { NLSIM = Serial.parseInt (); conIllu = 0; NLSwitch = 0; NumDirs = 6;
      NumPhases = 5; Serial.print ("N1/NO NLSIM:"); Serial.println (NLSIM, DEC);
      Serial.parseInt ();break;}
    case 'S': { NLSwitch = Serial.parseInt (); NLSIM = 0; conIllu = 0;
      Serial.print ("S# NLSwitch:"); Serial.println (NLSwitch, DEC); break;}
    // case 'k':{ KNLSwitch=Serial.parseInt();Serial.print("# KNLSwitch:");
    // Serial.println(KNLSwitch,DEC);break;}
    case 'C': { NLCycle = Serial.parseInt ();Serial.print ("C# NLCycle:");
      Serial.println (NLCycle, DEC); break;}
    case 't': { Shot = Serial.parseInt ();Serial.print ("t# Shot:"); Serial.println (Shot, DEC);
      break;}
    case 'u': { captures = Serial.parseInt ();Serial.print ("u# captures:");
      Serial.println (captures, DEC); break;}
    case 'e': { Clear405 = Serial.parseInt ();Serial.print ("e# Clear405:");
      Serial.println (Clear405, DEC); break;}
    case 'A': Serial.print ("405 nm laser ON"); digitalWrite(DoActLaseer, HIGH); break;
    case 'a': Serial.print ("405 nm laser OFF"); digitalWrite(DoActLaseer, LOW); break;
    case 'G': Serial.print ("532 nm laser ON"); digitalWrite(DoGLaser, HIGH); break;
    case 'g': Serial.print ("532 nm laser OFF"); digitalWrite(DoGLaser, LOW); break;
  }
}

```

```

case 'f': { fastR = Serial.parseInt ();Serial.print ("f# fastR:");
          Serial.println (fastR, DEC); break;}
// case 'w': { LSIMwith405=Serial.parseInt(); Serial.print ("w2/w1/w0'
LSIMwith405:");
// Serial.println(LSIMwith405,DEC);break;}
// case 't': { DoTimeSeries=Serial.parseInt(); Serial.print ("t' DoTimeSeries:");
// Serial.println(DoTimeSeries,DEC);break;}
case 'h':
Serial.print ("c1/c0' conllu: "); Serial.println (conllu, DEC);
Serial.print ("r# rep:"); Serial.println (rep, DEC);
Serial.print ("o# NumDirs:"); Serial.println (NumDirs, DEC);
Serial.print ("p# NumPhases:"); Serial.println (NumPhases, DEC);
Serial.print ("f# fastR:"); Serial.println (fastR, DEC);
Serial.print ("K1/K0' KohinoorNLSIM:"); Serial.println (KohinoorNLSIM, DEC);
Serial.print ("P1/PO' KSwitch405:"); Serial.println (KSwitch405, DEC);
Serial.print ("N1/NO' NLSIM:"); Serial.println (NLSIM, DEC);
Serial.print ("C# NLcycle:"); Serial.println (NLcycle, DEC);
Serial.print ("S1/SO' NLSwitch:"); Serial.println (NLSwitch, DEC);
// Serial.print ("k1/k0' KNLSwitch:"); Serial.println(KNLSwitch,DEC);
Serial.print ("t# Shot:"); Serial.println (Shot, DEC);
Serial.print ("u# captures:"); Serial.println (captures, DEC);
Serial.print ("e# Clear405:"); Serial.println (Clear405, DEC);
Serial.print ("z1/z0' DoZstack:"); Serial.println (DoZstack, DEC);
Serial.print ("s# NumSlices:"); Serial.println (NumSlices, DEC C);
Serial.print ("A' 405 nm laser ON;'a' 405 nm laser OFF ");
Serial.print ("G' 532 nm laser ON;'g' 532 nm laser OFF ");
Serial.print ("l1/IO' DoLASER:"); Serial.println (DoLASER, DEC);
// Serial.print ("w2/w1/w0' LSIMwith405:"); Serial.println(LSIMwith405,DEC);
break;

case 'H':
Serial.print ("(countinue 488 nm illumination)'c1/c0' conllu:"); Serial.print ("\n");
Serial.print (" (longer exposure time, r=3, 5, 10, 15, 20)'r# rep: "); Serial.print
("\n");
Serial.print (" (number of grating orientation)'o# NumDirs:"); Serial.print ("\n");
Serial.print (" (number of grating phase shift)'p# NumPhases:"); Serial.print ("\n");
// Serial.print ("(Liyan's project)'f# fastR:"); Serial.print ("\n");
Serial.print (" (Do Kohinoor LSIM with 405 nm laser on all the time)'K1/K0'
KohinoorNLSIM:");
Serial.print ("\n");
Serial.print (" (Do NLSIM with rsEGFP or mIrisGFP)'N1/NO' NLSIM:"); Serial.print
("\n");
Serial.print ("(Do NLSIM with rsEGFP or mIrisGFP, #=Deact+Measure+Clear)'C#
NLcycle:");
Serial.print ("\n");
Serial.print ("(Do photoswitching experiment)'S1/SO' NLSwitch:"); Serial.print ("\n");
Serial.print (" (# of 405 nm shot for doing photoswitching experiment)'t# Shot:");

```

```

Serial.print ("\n");
Serial.print (" (# of 488 nm shot for doing photoswitching experiment)'u#'
    captures:");
Serial.print ("\n");
Serial.print (" (# of 405 nm shot for doing Kohinoor photoswitching)'e#'
    Clear405:");
Serial.print ("\n");
Serial.print (" (Do z-scanning)'z1/z0' DoZstack:"); Serial.print ("\n");
Serial.print (" (# of slice of doing z-scanning, should be the same as ");
Serial.print (" in z-scanning Arduino code.)'s#' NumSlices:");
Serial.print ("\n");
Serial.print (" 'A' 405 nm laser ON;'a' 405 nm laser OFF ");
Serial.print (" 'G' 532 nm laser ON;'g' 532 nm laser OFF ");
Serial.print (" (I0: no 488 nm, I1: 488 nm on with + SLM image, ");
Serial.print (" I2: 488 nm on with both +- SLM images)DoLASER:");
Serial.print ("\n");
// Serial.print("'w2/w1/w0' LSIMwith405:");Serial.print('\n');
break;
}
//D(Serial.println("maybe new input"));
Serial.println ();
Serial.print ("maybe new input, eg. 'r1'. Or enter 'h' to see all the current paremeters.
    ");
Serial.print ('\n');
Serial.print ("Or enter 'H' to see introduction of all paremeters.");
Serial.print ("*****");
}

if (conllu) {
    digitalWrite(laser_enable, HIGH);
}
else if (NLSwitch) {
    int camwaitcount = 0;
    int wasreset;
    int i;
    int j;
    int t;

    if (TriggerR) {
        while (digitalRead (cam_out_R) == LOW) {
            camwaitcount++;
            if (camwaitcount == 10000) {
                goto checkinput;
            }
        }
    }
    TriggerR = 0;
}

```

```

digitalWrite (DoActLaseer, HIGH);
while (digitalRead (cam_out_R) == HIGH) {
}
digitalWrite (DoActLaseer, LOW);
wasreset = 0;

cli(); // disable global interrupts for the time that precise timing is needed
for (i = 0; i < Shot; i++) {
  for (j = 0; j < captures; j++) {
    if (!wasreset) {
      int countb = 0;
      while (!wasreset && digitalRead (cam_out_G) == LOW) {
        for (int i = 0; i < 200; i++) {
          asm ("" );
        }
        countb ++;
        if (countb > 14341) {
          wasreset = 1;
          TriggerR = 1;
        }
      }
    }
    digitalWrite (slm_trigger, HIGH);
    SLMCycle(DoLASER);
    digitalWrite (slm_trigger, LOW);
    if (wasreset) {
      for (int i = 0; i < 3275; i++) {
        asm ("" );
      }
    }
    while (digitalRead (cam_out_G) == HIGH) {
    }
    if (!wasreset) {
      for (int i = 0; i < 3275; i++) {
        asm ("" );
      }
    }
  }
  if (!wasreset) {
    digitalWrite (DoActLaseer, HIGH);
    for (int i = 0; i < 20000; i++) {
      asm ("" );
    }
    for (t = 0; t < Clear405 - 2; t++) {
      while (digitalRead (cam_out_G) == HIGH) {
      }
      while (digitalRead (cam_out_G) == LOW) {

```

```

    }
    }
    while (digitalRead (cam_out_G) == HIGH) {
    }
    digitalWrite (DoActLaseer, LOW);
    }
}
if (wasreset) {
    for (int i = 0; i < 3275; i++) {
        asm ("" );
    }
}
sei(); // enable global interrupts
}

else if (KNLSwitch) {
    int camwaitcount = 0;
    int wasreset;
    int i;
    int j;

    if (TriggerR) {
        while (digitalRead (cam_out_R) == LOW) {
            camwaitcount++;
            if (camwaitcount == 10000) {
                goto checkinput;
            }
        }
        TriggerR = 0;
    }
    wasreset = 0;

    cli();
    for (i = 0; i < Shot; i++) {
        for (j = 0; j < captures; j++) {
            if (!wasreset) {
                int countb = 0;
                while (!wasreset && digitalRead (cam_out_G) == LOW) {
                    for (int i = 0; i < 200; i++) {
                        asm ("" );
                    }
                    countb ++;
                    if (countb > 14341) {
                        wasreset = 1;
                        TriggerR = 1;
                    }
                }
            }
        }
    }
}

```



```

    }
    digitalWrite (DoActLaseer, HIGH);
    while (digitalRead (cam_out_G) == HIGH) {
    }
    digitalWrite (DoActLaseer, LOW);
}
if (!wasreset) {
    int countb = 0;
    for (int i = 0; i < 20000; i++) {
        asm ("");
    }
    while (!wasreset && digitalRead (cam_out_G) == LOW) {
        for (int i = 0; i < 200; i++) {
            asm ("");
        }
        countb ++;
        if (countb > 14341) {
            wasreset = 1;
            TriggerR = 1;
        }
    }
    digitalWrite (slm_trigger, HIGH);
    SLMCycle(DoLASER);
    digitalWrite (slm_trigger, LOW);
    if (wasreset) {
        for (int i = 0; i < 3275; i++) {
            asm ("");
        }
    }
    while (digitalRead (cam_out_G) == HIGH) {
    }
}
if (wasreset) {
    for (int i = 0; i < 3275; i++) {
        asm ("");
    }
}
sei();
}

else if (KSwitch405) {
    int camwaitcount = 0;
    int wasreset;
    int i;
    int j;
    int t;

```

```

if (TriggerR) {
  while (digitalRead (cam_out_R) == LOW) {
    camwaitcount++;
    if (camwaitcount == 10000) {
      goto checkinput;
    }
  }
  TriggerR = 0;
}
digitalWrite (DoActLaseer, HIGH);
while (digitalRead (cam_out_R) == HIGH) {
}
digitalWrite (DoActLaseer, LOW);
wasreset = 0;
cli();
for (i = 0; i < Shot; i++) {
  for (j = 0; j < captures; j++) {
    if (!wasreset) {
      int countb = 0;
      while (!wasreset && digitalRead (cam_out_G) == LOW) {
        for (int i = 0; i < 200; i++) {
          asm ("" );
        }
        countb ++;
        if (countb > 14341) {
          wasreset = 1;
          TriggerR = 1;
        }
      }
    }
  }
  digitalWrite (slm_trigger, HIGH);
  SLMCycle(DoLASER);
  digitalWrite (slm_trigger, LOW);
  if (wasreset) {
    for (int i = 0; i < 3275; i++) {
      asm ("" );
    }
  }
  while (digitalRead (cam_out_G) == HIGH) {
  }
  if (!wasreset) {
    for (int i = 0; i < 3275; i++) {
      asm ("" );
    }
  }
}

```

```

}
unsigned int odd = 0;
odd = i % 2;
if (!wasreset && !odd) {
    digitalWrite (DoActLaseer, HIGH);
    for (int i = 0; i < 200; i++) {
        asm (""");
    }
}
else {
    digitalWrite (DoActLaseer, LOW);
    for (int i = 0; i < 200; i++) {
        asm (""");
    }
}
}
if (wasreset) {
    for (int i = 0; i < 3275; i++) {
        asm (""");
    }
}
sei();
}
else if (!NLSIM) {
    int wasreset;
    digitalWrite (slm_trigger, LOW);
    digitalWrite (laser_enable, LOW);
    if (DoZstack) {
        digitalWrite (zstackarduino, LOW);
    }
    int camwaitcount = 0;
    if (TriggerR) {
        while (digitalRead (cam_out_R) == LOW) {
            camwaitcount++;
            if (camwaitcount == 10000) {
                goto checkinput;
            }
        }
    }
    TriggerR = 0;
    if (DoZstack) {
        digitalWrite (zstackarduino, HIGH);
    }
}
if (fastR) {
    while (digitalRead (cam_out_R) == HIGH) {
    }
    digitalWrite (slm_trigger, HIGH);
}

```

```

cli();
for (int d = 0; d < 14; d++) {
    fastRSLMCycle();
    digitalWrite (slm_trigger, LOW);
}
TriggerR = 1;
sei();
}
if (!fastR) {
    wasreset = 0;
    if (DoZstack) {
        NumSlices = NumSlices;
    }
    if (!DoZstack) {
        NumSlices = 1;
    }
    cli();
    for (Slice = 0; Slice < NumSlices; Slice++) {
        for (int d = 0; d < NumDirs; d++) {
            for (int p = 0; p < NumPhases; p++) {
                if (!wasreset && LSIMwith405 > 0) {
                    digitalWrite (DoActLaseer, HIGH);
                }
                if (!wasreset && KohinoorNLSIM == 1) {
                    digitalWrite (DoActLaseer, HIGH);
                }
                if (!wasreset) {
                    int countb = 0;
                    while (!wasreset && digitalRead (cam_out_G) == LOW) {
                        for (int i = 0; i < 200; i++) {
                            asm ("" );
                        }
                        countb ++;
                        if (countb > 14341) {
                            wasreset = 1;
                            TriggerR = 1;
                        }
                    }
                }
            }
        }
        if (LSIMwith405 > 1) {
            digitalWrite (DoActLaseer, LOW);
        }
        digitalWrite (slm_trigger, HIGH);
        if (DoZstack) {
            digitalWrite (zstackarduino, LOW);
        }
        for (int i = 0; i < rep; i++) {

```

```

    SLMCycle(DoLASER);
    digitalWrite (slm_trigger, LOW);
  }
  if (wasreset) {
    for (int i = 0; i < 3275; i++) {
      asm ("" );
    }
    digitalWrite (DoActLaseer, LOW);
  }
  while (digitalRead (cam_out_G) == HIGH) {
  }
}
}
if (wasreset && KohinoorNLSIM == 1) {
  digitalWrite (DoActLaseer, LOW);
}
if (!wasreset && DoZstack) {
  digitalWrite (zstackarduino, HIGH);
  for (int i = 0; i < 29500; i++) { //wait for the stage reaches the given position
    asm ("" );
  }
}
digitalWrite (zstackarduino, LOW);
while (digitalRead (cam_out_G) == HIGH) {
}
}
sei();
}
}

else if (NLSIM) {
  int wasreset;
  digitalWrite (slm_trigger, LOW);
  digitalWrite (laser_enable, LOW);
  digitalWrite (DoActLaseer, LOW);
  if (DoZstack) {
    digitalWrite (zstackarduino, LOW);
  }
  int camwaitcount = 0;
  if (TriggerR) {
    while (digitalRead (cam_out_R) == LOW) {
      camwaitcount++;
      if (camwaitcount == 10000) {
        goto checkinput;
      }
    }
  }
  TriggerR = 0;
}

```

```

if (DoZstack) {
    digitalWrite (zstackarduino, HIGH);
}
}
wasreset = 0;
if (DoZstack) {
    NumSlices = NumSlices;
}
if (!DoZstack) {
    NumSlices = 1;
}

cli();

for (Slice = 0; Slice < NumSlices; Slice++) {
    for (int d = 0; d < NumDirs; d++) {
        for (int p = 0; p < NumPhases; p++) {
            for (int v = 0; v < NLcycle; v++) {
                if (!wasreset) {
                    int countb = 0;
                    while (!wasreset && digitalRead (cam_out_G) == LOW) {
                        for (int i = 0; i < 200; i++) {
                            asm ("" );
                        }
                        countb ++;
                        if (countb > 14341) {
                            wasreset = 1;
                            TriggerR = 1;
                        }
                    }
                }
                if (DoZstack) {
                    digitalWrite (zstackarduino, LOW);
                }
                if (v < 1) {
                    digitalWrite (DoActLaseer, HIGH);
                    while (!wasreset && digitalRead (cam_out_G) == HIGH) {
                    }
                    digitalWrite (DoActLaseer, LOW);
                    while (!wasreset && digitalRead (cam_out_G) == LOW) {
                    }
                }
                digitalWrite (slm_trigger, HIGH);
                SLMCycle(DoLASER);
                digitalWrite (slm_trigger, LOW);

                if (wasreset) {

```

```

    for (int i = 0; i < 3275; i++) {
        asm ("" );
    }
}
while (digitalRead (cam_out_G) == HIGH) {
}
}
}
}
if (!wasreset && DoZstack) {
    digitalWrite (zstackarduino, HIGH);
    for (int i = 0; i < 29500; i++) {
        asm ("" );
    }
}
digitalWrite (zstackarduino, LOW);
while (digitalRead (cam_out_G) == HIGH) {
}
}
sei();
}
}

```

B.2 Arduino_Code: fastSIM_Zstage_ArduinoProgram

```

/*****
/* !!!Define the correct Board!!! */
/*Arduino Maga 2560 or Maga ADK*/
*****/

// variables needed to be defined depends on cases
int Dofocus=1;
int DoZstack=0; //"1" enable Z scanning; "0" disable
int NumSlices=15;
unsigned int IntervalBit=72; // 36 Bit corresponds to ~110 nm in z direction
enum {MAX=65500}; // 16 Bit=65535, 0 to 200 µm in Z direction; 1 bit = 3.053 nm;
// 36 bit = 110 nm
//unsigned int givenpos=32750; //Midpos=MAX/2=32750; when you disable DoZstack "0"
//int Midpos=32750;
/* Include headers */

/*****
/* Define constants in the program */
*****/
// define pins
int main_Ardu=21;
int z_Ardu_DAC=13;

/*****
/* Define variables in the program */
*****/

// Immediate Z position
//volatile unsigned char stop=1;
unsigned int Zpos=0;
unsigned int HZpos=0;
unsigned int Midpos=32750;
unsigned int odd=0;
int Slice=0;

void setup(){
  Serial.begin(9600); // opens serial port, sets data rate to 9600 bps
  Serial.println ("waiting for input. Press 'h' to see all the current paremeters.");
  Serial.print("\n");
  Serial.println ("small f: more into sample");
  Serial.println ("Current Midpos is 32750 for 63X Objective and 54800 for 40X Objective.");
  Serial.println ("If you use life cell chamber, you have to use a smaller Midpos.");
  Serial.println (" i.g. 64800~65150");

  Serial.println("*****
");
  pinMode(main_Ardu, INPUT); // pin 21, from main arduino board
  pinMode(z_Ardu_DAC, OUTPUT); // pin 13, to DAC
  ioinit(); //initialize I/O
}

```



```

void ioinit (void)
{
  /******
  /* Define 16-bit data port for DACs */
  /******
  PORTA = B00000000; // lower byte LSB(PA0, digital pin 22),MSB(PA7, digital pin 29)
  DDRA = B11111111; // data direction register A
  PORTC = B00000000; // upper byte LSB(PC0, digital pin 37),MSB(PC7, digital pin 30)
  DDRC = B11111111; // data direction register C
  DDRL = B11111111; // data direction register L
  PORTL = B11111111; // LDAC (PL0, digital pin 49), CS(PL7,digital pin 42)
}

void movZ(unsigned int pos)
{
  PORTA=lowByte(pos);
  PORTC=highByte(pos);
  PORTL=B11001111; // CS = 1 and LDAC = 1 and A0,A1,A2 = 100 W26.1
  PORTL=B01001111; // CS = 0 and LDAC = 1 and A0,A1,A2 = 100 W26.1
  PORTL=B11111110; // CS = 1 and LDAC = 0 and A0,A1,A2 = 111 W26.1
  PORTL=B11111111; // CS = 1 and LDAC = 1 and A0,A1,A2 = 111 W26.1
}

void loop(){
  checkinput:
  while(Serial.available(>0){
    switch(Serial.read()){
      case 'f': { DoZstack=0; Midpos=Serial.parseInt(); Serial.print("#' DofocusAt:");
        Serial.println(Midpos, DEC);movZ(Midpos);break;}
      // case 'f':{ DoZstack=0; movZ(Midpos); Serial.print ("f' Dofocus:");
      // Serial.print("#' DoZstack:"); Serial.println(DoZstack, DEC);break;}
      case 'z': { DoZstack= Serial.parseInt (); Serial.print("z1/z0' DoZstack:");
        Serial.println(DoZstack, DEC);break;}
      case 's': { NumSlices=Serial.parseInt(); Serial.print("s#' NumSlices:");
        Serial.println(NumSlices, DEC);break;}
      case 'h':
        Serial.print("z1/z0' DoZstack:"); Serial.println (DoZstack, DEC);
        Serial.print ("s#' NumSlices:"); Serial.println (NumSlices,DEC);
        Serial.print ("f#' DofocusAt:");Serial.println(Midpos,DEC);
        break;
    }
    Serial.println ("maybe new input, eg. 'f0'. Or enter 'h' to see all the current paremeters. ");
    Serial.println ("small f: more into sample");
    Serial.println ("Current Midpos is 32750 for 63X Objective and 54800 for 40X Objective.");
    Serial.println ("If you use life cell chamber, you have to use a smaller Midpos.");
    Serial.println (" i.g. 60000~65150");
    Serial.println
    ("*****");
  }

  if (DoZstack){

```

```

odd = NumSlices % 2;
if (digitalRead(main_Ardu)==LOW){
  goto checkinput;
}

if (!odd){
  HZpos=Midpos+((NumSlices)*(IntervalBit/2)); // 36 bit corresponding to 108 nm;
                                           // (NumSlices/2)*36= NumSlices*18
  Zpos=Midpos-((NumSlices)*(IntervalBit/2)); // Lowest position of z-stage for z direction
                                           // scanning

  cli();
  for(Slice=0; Slice<(NumSlices+1); Slice++) {
    while(digitalRead(main_Ardu)==LOW){
      for(int i=0;i<100;i++) { // wait 72 us
        asm("");
      }
    }
    movZ(Zpos);
    while(digitalRead(main_Ardu)==HIGH){ // 512*512 takes 5,12 ms
      for(int i=0;i<100;i++) { // wait 72 us
        asm("");
      }
    }
    if(Slice<(NumSlices)){
      Zpos=Zpos+IntervalBit;
    }
    else break;
  }
  Zpos=Midpos;
  movZ(Midpos);
  DoZstack=0;
  sei();
}

if (odd){
  HZpos=Midpos+((NumSlices-1)*(IntervalBit/2));
  Zpos=Midpos-((NumSlices-1)*(IntervalBit/2)); //Lowest position of z-stage for z direction
                                           // scanning

  cli();
  for(Slice=0; Slice<(NumSlices+1); Slice++) {
    while(digitalRead (main_Ardu)==LOW){
      for(int i=0;i<100;i++) { // wait 72 us
        asm("");
      }
    }
    movZ(Zpos);
    while(digitalRead (main_Ardu)==HIGH){
      for(int i=0;i<100;i++) { // wait 72 us
        asm("");
      }
    }
  }
}

```

```
        if(Slice<(NumSlices)){
            Zpos=Zpos+IntervalBit;
        }
        else break;
    }
    Zpos=Midpos;
    movZ(Midpos);
    DoZstack=0;
    sei();
}
Serial.println("*****");
goto checkinput;
}
}
```

Selbständigkeitserklärung

Ich erkläre, dass ich die vorliegende Arbeit selbstständig und unter Verwendung der angegebenen Hilfsmittel, persönlichen Mitteilungen und Quellen angefertigt habe.

	Datum	Ort	Unterschrift
Hui-Wen Lu-Walther	_____	_____	_____

Erklärungen

Erklärung zu den Eigenanteilen des Promovenden sowie der weiteren Doktoranden/Doktorandinnen als Koauthoren an den Publikationen und Zweitpublikationsrechten bei einer kumulativen Dissertation

Für alle in dieser kumulativen Dissertation verwendeten Manuskripte liegen die notwendigen Genehmigungen der Verlage ("Reprint permissions") für die Zweitpublikation vor.

Die Co-Autoren der in dieser kumulativen Dissertation verwendeten Manuskripte sind sowohl über die Nutzung, als auch über die oben genannten Eigenanteile informiert und stimmen dem zu.

	Datum	Ort	Unterschrift
Hui-Wen Lu-Walther	_____	_____	_____

Einverständniserklärung des Betreuers

Ich bin mit der Abfassung der Dissertation als publikationsbasiert, d.h. kumulativ, einverstanden und bestätige die vorstehenden Angaben. Eine entsprechend begründete Befürwortung mit Angabe des wissenschaftlichen Anteils des Doktoranden an den verwendeten Publikationen werde ich parallel an den Rat der Fakultät der Chemisch-Geowissenschaftlichen Fakultät richten.

Name Erstbetreuer

Datum

Ort

Unterschrift

Prof. Dr. Rainer Heintzmann
